Rui Montenegro Val-do-Rio Pinto

M. Sc. in Physics Engineering

Photoelectron Spectroscopy of Nitrogen Containing Molecules of Biological and Industrial Interest

A thesis submitted for the degree of
Ph. D. in Physics

Supervisor: Maria de Lourdes Santos Lourenço Costa,
Associate Professor, Physics Department
Co-supervisor: António Alberto Dias,
Assistant Professor, Physics Department

Examining Committee:

Chair: Professor Maria Adelaide de Almeida Pedro de Jesus
External Examiner: Professor Rui Fausto Martins Ribeiro da Silva Lourenço
Internal Examiner: Professor Orlando Manuel Neves Duarte Teodoro

Other Members: Professor John Malcolm Dyke
Professor Ana Maria Botelho do Rego
Professor António Alberto Dias
Professor Maria de Lourdes Santos Lourenço Costa

FACULDADE DE CIÊNCIAS E TECNOLOGIA
UNIVERSIDADE NOVA DE LISBOA

December 2011

Photoelectron Spectroscopy of Nitrogen Containing Molecules of Biological and Industrial Interest

Rui Montenegro Val-do-Rio Pinto

December 2011

Acknowledgements

The work presented herein would not be possible without the scientific supervision and patient guidance of Prof. Maria Lourdes Costa and Prof. António Dias, to whom a word of sincere acknowledgement is given. My potential offspring as a scientific researcher is mainly due to them. The friendship and confidence demonstrated towards me throughout this years are on the basis of my own trust and achievements, and our successful operation as a team. Thank you both!

To Prof. José Paulo dos Santos a very respectful thank you, for the first insights into quantum physics during my undergraduate years, to the support and help provided during the course of this thesis. The computational resources made available for the group were indispensable for completing this work.

Prof. John Dyke and Dr. Grant Copeland are also acknowledged for the indispensable support in the work performed in collaboration with the historical PES group, in the School of Chemistry of the University of Southampton. Their contribution was priceless and deeply appreciated. The University of Southampton is of course also acknowledged for the hosting conditions and research facilities.

A special thanks to Dr. Marcello Coreno, Dr. Monica de Simone and Dr. Barbara Michela Giuliano, without whom the work performed at Elettra (in Trieste, Italy) would not be possible. Thank you for sharing the opportunity of making science in a totally different environment, in a large-scale open-lab, boiling from intense scientific activity. Thanks to the technical staff at Elettra, for providing good light conditions.

A very special thanks to Prof. Maria Teresa Barros, Prof. Christopher Maycock and Dr. Paula Rodrigues, from Requimte-ITQB, FCT-UNL, for synthesizing the azido compounds, with renowned efficiency and improved ability.

The work on the azides also benefited from the expertise and analysis of Prof. Maria Teresa Fernandez, Prof. Maria Filomena Duarte and Dr. Filipa Martins, from CQB, FC-UL. To Prof. Teresa Fernandez a special thanks for enlightening me with some important concepts behind mass spectrometry and radical formation.

The majority of the work was performed at the Photoionisation Laboratory in the Department of Physics of FCT-UNL, therefore a great deal of respect and acknowledgement is due to this institution and all academic staff lecturing there, with special emphasis to the head of the department, Prof. Adelaide de Jesus.

A special thanks to the people who indirectly contributed in various forms to this thesis, by occasionally clarifying my many questions: Prof. Augusto Moutinho, Prof. Orlando Teodoro, Prof. António Paiva, Dr. André Wemans, Dr. Cláudia Quaresma, Juscelino Ferreira and João Faustino.

To the masterful Mr. José Carlos Mesquita and the skilful Mr. Eduardo Jobling a very big thanks, for all the technical help provided, regarding the construction of electronic circuits and the machining of scientific equipment. To all the students who worked in the lab with me, specially João Franco and Carolina Matias.

To all my colleagues and working comrades – Mauro Guerra, Diana Guimarães, Pedro Amaro, and Susana Gomes, Diogo Almeida, Gonçalo Martins, and Rodrigo Antunes – who struggle(d) to make a living out of making science, I express a very joyful thanks. You represent the second-order perturbation effect in a charge-transfer process, arising from the vibronic coupling of a $\pi\pi^*$ transition, mediated by the "bofião" elementary particle in a ubiquitously spread Pb compound, deposited on a PCL matrix, a problem only treatable with the modified BEB approach in a two-photon transition framework; without you, things would not be as interesting or as funny as they were. Sincere thanks!

To all my friends and family. To both my grandparents with whom I had the luck to grow and absorb history and inspiration. A warm embrace to my mother, for showing me how to put one's heart in place of one's head, at all the right times. A big hug to my father who, by example, taught me how to be curious and rationale in approaching and resolving life's problems, and for his immense support. A special thanks to the shark princess for all the love and moments shared.

Finally, I would also like to express my gratitude to Fundação para a Ciência e Tecnologia (FCT) for the doctoral grant SFRH/BD/40308/2007 that allowed me to continue with my education.

FCT Fundação para a Ciência e a Tecnologia
MINISTÉRIO DA EDUCAÇÃO E CIÊNCIA

Abstract

The work presented herein is based on the gas-phase spectroscopic characterization of several molecules of high nitrogen content which are relevant to organic synthesis, industry and fundamental research on molecular physics. It is mainly an experimental enterprise on selected organic azides and tetrazoles, with heavy support on theoretical results from readily available computational methods. Part of the work relies on the design and construction of scientific apparatus, which substantially improve the existing equipment and extend the limits of the experiment.

The electronic structure and gas-phase thermal decomposition of methyl 2-azidopropionate (M2AP, $N_3CH_3CHCO_2CH_3$), benzyl azide (BA, $C_6H_5CH_2N_3$), 2-, 3- and 4-methyl benzyl azide (2-, 3- and 4-MBA, $CH_3C_6H_4CH_2N_3$), 5-aminotetrazole (5ATZ, NH_2CN_4H), and 5-methyltetrazole (5MTZ, CH_3CN_4H) are investigated through photoelectron spectroscopy, using either He(I) (21.22 eV) or synchrotron radiation in the X-ray range. Relevant information obtained from mass spectrometry and matrix-isolation infrared spectroscopy is used to complement characterization of the samples.

Regarding each molecules' thermal decomposition, pathways are proposed which account for the observed end products. Conformational analysis is performed, and the special case of annular tautomerism is addressed in the tetrazole compounds. High-temperature pyrolysis work is performed in collaboration with the University of Southampton, and XPS analysis using synchrotron radiation is performed at Elettra, the multidisciplinary synchrotron light laboratory in Trieste, Italy.

Experimental findings are rationalized using different computational methods, based on post-Hartree-Fock approaches: many-body perturbation theory (MPn), configuration interaction (CI) and Green's function methods (OVGF, P3), as well as density functional theory (DFT), are used extensively to obtain optimized molecular geometries, ionization energies, orbital contours, relative energies, vibrational frequencies, and to assess possible pathways for thermal or electron impact fragmentation. Composite methods (Gn and CBS) are used to estimate to kcal mol^{-1} accuracy the energy balance between reactants, transition structures and products in the overall decomposition process of the specified molecules.

Keywords: *azides*; *tetrazoles*; *molecular physics*; *electronic structure*; *UVPES*; *XPS*.

Resumo

O trabalho apresentado no âmbito desta tese incide sobre a caracterização espectroscópica de diferentes moléculas com grande quantidade de azoto, relevantes na síntese química de compostos orgânicos, na indústria e em investigação fundamental na área da física molecular. Baseia-se, fundamentalmente, numa abordagem experimental à caracterização de algumas azidas orgânicas e tetrazóis, com vasto recurso a métodos computacionais. Parte do trabalho consiste no dimensionamento e construção de equipamento científico que melhora substancialmente o equipamento existente e amplia os limites da experiência.

A estrutura electrónica e a decomposição térmica em fase gasosa do metil 2-azidopropionato (M2AP, $N_3CH_3CHCO_2CH_3$), benzil azida (BA, $C_6H_5CH_2N_3$), 2-, 3- e 4-metil benzil azida (2-, 3- and 4-MBA, $CH_3C_6H_4CH_2N_3$), 5-aminotetrazol (5ATZ, NH_2CN_4H) e 5-metiltetrazol (5MTZ, CH_3CN_4H), são investigados através da espectroscopia de fotoelectrões, recorrendo a radiação He(I) (21.22 eV) ou de sincrotrão na gama dos raios-X. As técnicas de espectrometria de massa e de espectroscopia de infravermelhos em matriz-isolada são utilizadas como técnicas complementares à caracterização dos compostos.

Relativamente à decomposição térmica de cada molécula, são apresentados trajectos de decomposição que explicam a formação dos produtos detectados. É realizada a análise conformacional dos compostos, com especial enfâse para o tautomerismo anular exibido pelos compostos tetrazólicos. O processo de pirólise a alta-temperatura é investigado, em colaboração com a Universidade de Southampton. A análise das moléculas com XPS, utilizando radiação de sincrotrão, é também levada a cabo no laboratório multidisciplinar Elettra, em Trieste, Itália.

Os resultados experimentais são racionalizados usando diferentes métodos computacionais, baseados em aproximações pós-Hartree-Fock: teoria da perturbação a vários corpos (MPn), interacção de configuração (CI), métodos baseados na função de Green (OVGF, P3) e teoria do funcional de densidade (DFT) são utilizados recorrentemente com o intuito de obter geometrias moleculares optimizadas, energias de ionização, contornos das orbitais moleculares, energias relativas e frequências vibracionais, e com o objectivo de averiguar possíveis trajectos de fragmentação térmica e de dissociação por impacto electrónico. O balanço de energia entre os reagentes, estruturas de transição e produtos envolvidos no processo de decomposição é estimado com uma precisão de kcal mol^{-1} recorrendo a métodos computacionais compostos (Gn and CBS).

Palavras-chave: *azidas*; *tetrazóis*; *física molecular*; *estrutura electrónica*; *UVPES*; *XPS*.

Contents

List of Figures

Page

List of Tables

Page

List of Acronyms

2MBA 2-Methyl benzyl azide.

3MBA 3-Methyl benzyl azide.

3MBA 4-Methyl benzyl azide.

5ATZ 5-Aminotetrazole.

5MTZ 5-Methyltetrazole.

AES Auger electron spectroscopy.

AIE Adiabatic ionization energy.

AO Atomic orbital.

B3LYP Becke's three-parameter functional coupled to the Lee-Yang-Parr functional

BA Benzyl azide

BE Binding energy

BL Beamline

BM Bending magnet

BO Born-Oppenheimer

BPR Boltzmann population ratio

CBS Complete basis set

CEBE Core-electron binding energy

CGTO Contracted Gaussian-type orbital

cc correlation-consistent

CI Configuration interaction

CIS Configuration interaction including single excitations

CISD Configuration interaction including single and double excitations

CSV Comma separated values

DC Direct current

DFT Density functional theory

DIIS Direct inversion in the iterative subspace

EIMS Electron impact mass spectrometry

EPT Electron propagator theory

ES Experimental station

ESCA Electron spectroscopy for chemical analysis

FAT Fixed analyser transmission

FTIR Fourier-transform infrared

FWHM Full-width at half-maximum

GF Green's function

G*n* Gaussian-n methods

GTO Gaussian-type orbital

HF Hartree-Fock

HFGF Hartree-Fock Green's function

HLC Higher-level correction

IE Ionization energy

IR Infrared

IRC Intrinsic reaction coordinate

KS Kohn-Sham

KT Koopmans' theorem

LINAC Linear accelerator

M2AP Methyl 2-azidopropionate

MAD Mean absolute deviation

MBGF Many-body Green's function

MBPT Many-body perturbation theory

MEP Minimum-energy path

MO Molecular orbital

MP*n* Møller-Plesset perturbation theory up to n-order

MPPT Møller-Plesset perturbation theory

m.r.t. Mean residence time

MS Mass spectrometry

MSDS Material safety data sheet

NEXAFS Near-edge X-ray absorption fine-structure spectroscopy

NIM Nuclear instrumentation module

NIST National Institute of Standards and Technology

NMR Nuclear magnetic resonance

OVGF Outer-valence Green's function

P3 Partial third-order approximation

PE Photoelectron

PES Photoelectron spectroscopy

PGTO Primitive Gaussian-type orbital

PID Proportional-integral-differential

PIMS Photoionization mass spectrometry

PSU Power supply unit

PTFE Polytetrafluoroethylene

QCSCF Quadratically convergent self-consistent-field

QM Quantum chemistry

RF Radio-frequency

RHF Restricted Hartree-Fock

SCEM Single-channel electron multiplier

SCF Self-consistent-field

SD Slater determinant

SO Spin-orbit

SSR Solid state relay

STO Slater-type orbital

TC Thermocouple

TOF Time-of-flight analyzer

TS Transition structure

TST Transition state theory

TTL Transistor-transistor logic

UHF Unrestricted Hartree-Fock

UHV Ultra-high vacuumm

UV Ultraviolet

VASGM Variable angle spherical grating monochromator

VIE Vertical ionization energy

XPS X-ray photoelectron spectroscopy

ZEKE Zero kinetic energy spectroscopy

Part I
Introduction and Methods

Chapter 1

Introduction

1.1 Gas-phase study of nitrogen containing molecules

Nitrogen (N) constitutes the majority of Earth's atmosphere, with approximately 78% of the atmospheric mixture being nitrogen. This element is essential in so many different ways that life on Earth would not be possible without it.

A simple but definitive example regarding the presence of this element in natural occurring biological structures are the porphyrins macrocycles. The nitrogen atoms in these heterocyclic structures functionalize the compound to a degree that trapping magnesium (Mg) or iron (Fe) leads to the formation of two essential biological molecules: chlorophyll and haem. Hence, photosynthesis and oxygen transport through blood – two essential processes in life – are only possible due to the unique electronic structure of nitrogen.

The ground-state electronic configuration of the N atom is $1s^2 2s^2 2p^3$, with five outer-shell electrons. The triple bond established between two nitrogen atoms to form molecular nitrogen (Fig. 1.1 (a), N≡N) is one of the strongest chemical bonds known ($\Delta H_{diss.} = 944.7$ kJ mol^{-1}). This makes N_2 practically non-reactive. Energetically speaking, however, it is extremely advantageous for molecular systems containing N atoms to fragment and form N_2. Throughout the centuries, the high energy release accompanying this fragmentation process constituted the fundamental interest in nitrogen containing molecules. An interest which has not faded with time...

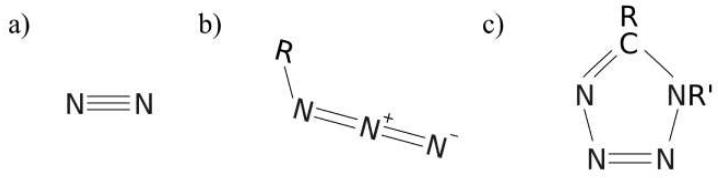

Figure 1.1: Structure of N_2 (a), generic azide R-N_3 (b), and tetrazole R-CN_4-R' (c).

Two classes of synthetic nitrogen based molecules have been continuously studied over time: compounds of the form R–N_3, termed *azides*[1,2], and heterocyclics of the form R–CN_4–R′, termed *tetrazoles*[3–5] (see Fig. 1.1 (b) and (c) respectively). These compounds are widely spread among distinct areas of research and development: pyrotechnics, drug synthesis, automobile industry, propellants, and explosives are just a hand-full of examples from several available applications.

The work presented here relies on a classical experimental technique aimed at gas-phase studies – *photoelectron spectroscopy*[6], to obtain fundamental knowledge regarding

the electronic structure and thermal stability of selected azides and tetrazoles.

A concise general description and up-to-date review of the existing literature concerning gas-phase studies on molecules containing the azido group and the tetrazole moiety will be given in the following sections. Specific literature data regarding each analysed molecule will not be given in this Chapter; instead, updated information concerning what is already known about the compounds will be followed in each chapter dealing with the specified compound.

1.1.1 Azides

The synthesis of the first azide recalls to 1858, with the experiments of Griess[7] on aromatic diazonium salts. The azo-compounds were latter explored by Curtius[8], who managed to successfully synthesise benzoyl ($C_7H_5N_3O$) and sodium (NaN_3) azides. The well-known $-N{=}N^{+}{=}N^{-}$ resonance description of the R-N_3 group was only established in 1931, by Sutton[9], who confirmed the open-chain formula of azides.

Azides participate in several ubiquitous reactions, like the Curtius rearrangement[8] or the Schmidt reaction[10]. A very extensive and useful review on azide's synthetic use was written by Scriven and Turnbull[11], and before them by L'Abbe[12]. The book by Patai[1], in the 1970's, and the more recent review and book by Bräse *et al.*[13], and Bräse and Banert[2], respectively, written in the first decade of the new millennium, accumulate an extensive amount of information regarding azido compounds synthesis, properties and applications. More recently, azides gained a renewed interest among worldwide chemistry R&D labs due to the emerging concept of "click-chemistry"[14] and its banner reaction: the copper catalyzed 1,3-dipolar cycloaddition of azides to alkynes, to yield 1,2,3-triazoles[15,16].

Even at early times, the explosive character of azides was not overlooked[2]: Curtius described a sample of aqueous hydrogen azide on local heating giving rise to a "formidable detonation and disintegration of the thick-walled glass tube to dust".

However, the consistent study of photodegradation and thermal decomposition of azides only began in the 1960's, with the work of Reiser[17–20] on the photolysis of aromatic azides and with the work of Smolinsky[21] on the pyrolysis of vinyl azide. The possibility of forming a nitrene intermediate through either light sensitisation or controlled heating was launched.

The fate of alkyl azides when subject to controlled heating, in the gas-phase, under vacuum, was further studied by Bock and Dammel[22–24], in the 1980's, using real-time gas analysis and photoelectron spectroscopy. For the first time, the unimolecular thermal decomposition of alkyl azides was unveiled: N_2 extrusion was showed to occur synchronously with the imine formation via 1,2-H or 1,2-CH_3 shifts.

In the mid-1990's, following the basis laid by Costa and co-workers on aliphatic azides[25–27], the photoelectron spectroscopy group in the University of Southampton, started to work on the thermal decomposition of organic azides, together with the photoionisation group from Universidade Nova de Lisboa.

Using matrix-isolation infrared (IR) spectroscopy[28] as a complementary technique, Dyke and co-workers successfully characterised both the electronic structure and gas-phase thermal decomposition of an extensive set of newly synthesised azido compounds: 2-azidoacetic acid[29], azidoacetone[30], 2-azidoethanol and 2-azidoethyl acetate[31], 2-azidoacetamide[32], and methyl/ethyl-azidoformate and 2-azido-N, N-dimethylacetamide[33]. The experiments were accompanied by studies performed with high-resolution mass spectrometry, trying to cross-link the decomposition patterns obtained via pyrolysis and the fragmentation arising from electron ionization[34–37].

From these studies, a general mechanistic behaviour describing the thermal decomposition of organic azides was derived, which complemented the original proposal by

Bock and Dammel of N_2 extrusion synchronous with the 1,2-H shift onto the electron deficient N atom. In azides where the central C atom was not bound to any H or alkyl donor i.e. in azides where the carbon atom was incapable of liberating any atom or group to stabilize the electron-deficient nitrogen, a cyclic intermediate was formed rather than an 1,2-H shift imine. Bock's mechanism was termed "type 1" and the mechanism discovered by Dyke and co-workers was termed "type 2". The general schemes for the two mechanisms are shown in Fig. 1.2.

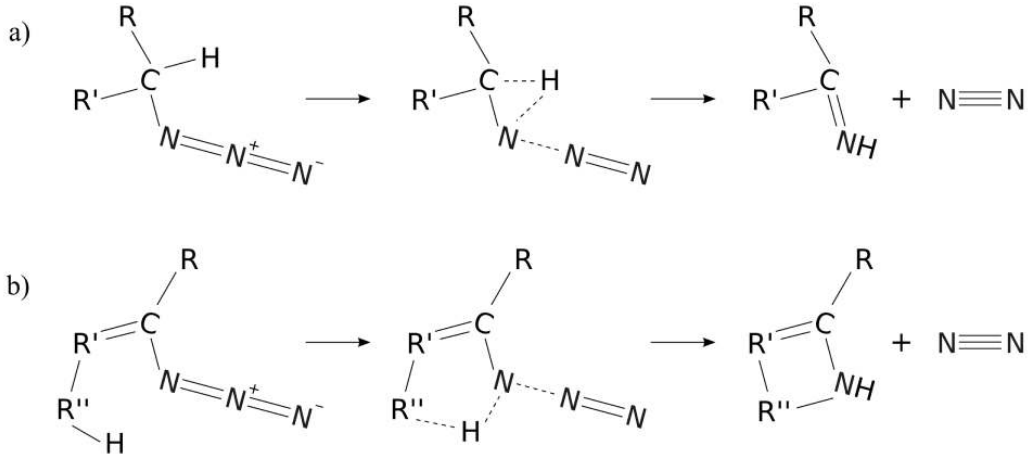

Figure 1.2: General "type 1" (a) and "type 2" (b) thermal decomposition mechanisms of organic azides.

An enormous research potential collates to the thermal decomposition of azides and its gas-phase study: new intramolecular mechanisms can be discovered, mediated by unknown reactive intermediates which can be used as building blocks in high yield synthetic applications. This makes fundamental study of organic azides a very interesting research subject.

A question is utterly launched: will potentially interesting physico-chemical properties appear if an extra nitrogen and carbon atoms are added to the N_3 chain, closing it in a stable pentagonal structure?

1.1.2 Tetrazoles

Tetrazoles are characterized by a five-membered, doubly unsaturated ring consisting of one carbon and four nitrogen atoms. The first tetrazole was synthesized in 1885 by Bladin[38], at the University of Upsala during his experiments with dicyanophenylhydrazine[3]. Bladin managed to prepare the simplest form of tetrazole (HCN_4H) a few years later[39], before retiring completely from the field.

Since Bladin's original experiments, several other researchers continued to work on tetrazoles. Among them, Thiele[40] was successful in synthesizing 5-aminotetrazole (NH_2-CN_4H) for the first time. In 1910, the simplest synthesis of tetrazole was achieved by Dimroth[41] by the direct combination of hydrogen cyanide and hydrogen azide.

The review of Benson[3], in 1947, compiles most extensively the information regarding the first fifty years of prolific research on tetrazoles. As with azides, the tetrazoles potential as high-energy materials was soon recognized, with the majority of the new compounds either decomposing or exploding when heated above their melting point.

Equilibrium between annular isomeric forms, mediated by migrations of the H atom between nitrogens in the ring moiety – *tautomerism* (Fig. 1.3, (a)⇌(b)), appears emphatically described also in those early days. In addition, review work by Mihina

and Herbst[42] on the 5-substituted tetrazoles synthesized according to the primordial HCN + HN_3 reaction[41] strongly pointed to the existence of an intermediate azide, clearly indicating some sort of tetrazole-azide equilibrium, also known as ring-chain isomerism (Fig. 1.3, (b)⇌(c)).

The recent analysis of Raczyńska[43] relating π electron delocalization and tautomerism in a series of organic molecules, devotes part of its attention to tetrazoles: tautomeric forms of tetrazoles are related to an aromaticity index[44] for π electron delocalization in the ring system, connecting ground-state electronic structure and chemical properties.

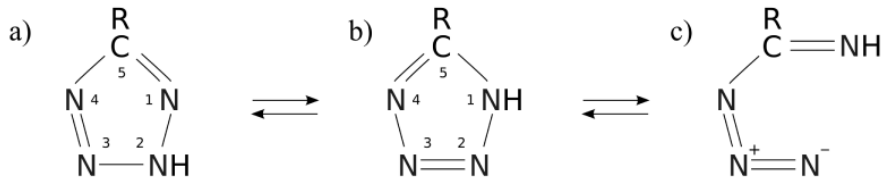

Figure 1.3: Annular tautomerism between 1H- and 2H- tautomers of generic 5-substituted tetrazoles (a⇌b). Tetrazole-azide ring-chain isomerism (b⇌c).

Since Benson's review, tetrazoles only appeared in comprehensive heterocyclic chemistry compendiums[45,46]. No major periodic revisions referring to the physico-chemical properties of tetrazoles were put on before the continuity analysis of Koldobskii, Ostrovskii and co-workers[4,47,48]. In 1994, a major revision by Wittenberger[5] covering synthesis and applications of tetrazoles and derivatives, emphasized the role of the tetrazole moiety in several medicinal applications.

More recently, the "click chemistry" concept was also applied to tetrazoles by the team of K. B. Sharpless[49]: several 5-substituted 1H-tetrazoles were prepared from the addition of NaN_3 to nitriles, in a water reflux with zinc salts as catalysts. The presence of water obviously mitigates the risk of explosion hazards from groups such as aromatic azides and nitro compounds[49], and eases the industrial scale production of tetrazoles.

Experiments with the decomposition of organic tetrazoles via photolysis or pyrolysis started as early as the first synthetic preparations. However, the study of gas-phase photofragmentation of the simple tetrazole molecule was only achieved in the 1990's, by Maier *et al.*[50], using matrix-isolation IR spectroscopy. In addition, flash vacuum pyrolysis of tetrazole was performed.

In recent years, the research group of Fausto, in Coimbra, studied the vibrational behaviour and gas-phase photochemistry of an extensive set of fundamental tetrazoles, using matrix-isolation IR techniques and UV-irradiation of the samples. Their studies included molecules like tetrazole[51], 5-chlorotetrazole[52] and 1-phenyltetrazole[53]. A complete description of all the tetrazoles analysed by this group and an up-to-date analysis of the photochemical transformations of tetrazole derivatives and its applications in organic synthesis can be found in the review by Frija *et al.*[54].

Photoelectron spectroscopy was used recurrently by Palmer and co-workers[55–57] to study the electronic structure of the azoles, and further utilized by Guimon[58] to monitor the gas-phase flash pyrolysis of tetrazole. A thorough analysis of the thermal decomposition of the tetrazole molecule was also performed in the 1990's, by Lesnikovich and co-workers[59–61], using several approaches, including modern calorimetry techniques. Years later, the same approach was again used by Lesnikovich[62] to characterize the thermal decomposition of other ubiquitous tetrazole: the 5-aminotetrazole.

Many enterprises later by several authors[50,58,63,64], and the only apparently unanimous answer is the elimination of N_2: experimental evidences regarding other products

are not consistent. Fig. 1.4 accounts for already proposed pathways, involving the general gas-phase thermal decomposition of tetrazole and 5-substituted derivatives.

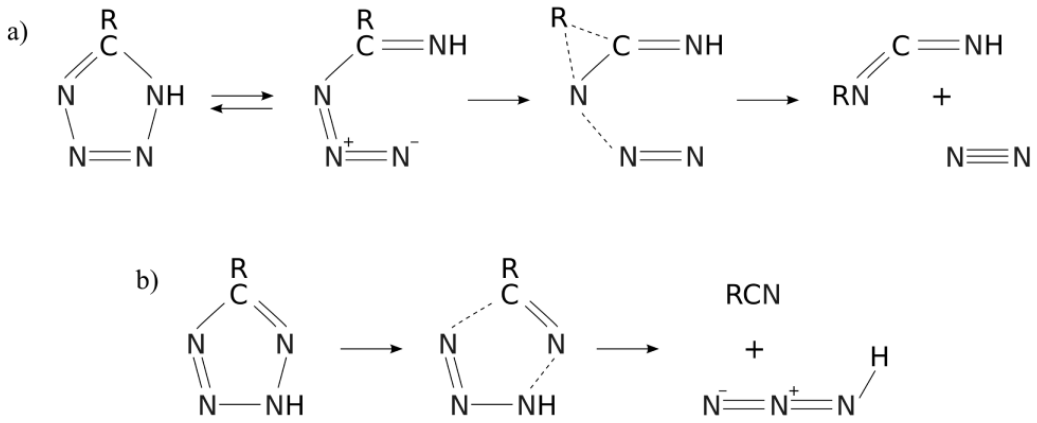

Figure 1.4: General thermal decomposition pathways for 1H-5-substituted tetrazoles leading to N_2 (a), and 2H-5-substituted tetrazoles leading to HN_3 (b).

Most studies of gas-phase thermal decomposition of tetrazoles deal with the question of tautomerism because the initial tautomeric ratio governs which decomposition pathways will be preferentially followed, in the initial stages of a pyrolysis process. It is also a matter of common agreement that the nature of the 5-substituents affects the gas-phase tautomeric ratio, and hence the pyrolysis process. It is clear by now that the 2H-form governs almost all tetrazoles in the gas-phase[65,66], but is deprecated over the 1H-tautomer in the solid state.

In summary, the thermal decomposition of tetrazoles (and azides) acts as a powerful source of the almost inert N_2 gas, which can be employed in a myriad of interesting applications. In addition, the degradation of tetrazole (and azides) can also act as a rich source of intermediates and radical species, useful in the development of new and promising drugs. What are then the main areas of application of these two nitrogen containing compounds?

1.1.3 Applications

Azido compounds find their use sparsely disseminated from the industrial need of foaming gas for plastic modelling to the synthesis of drugs for AIDS treatment[67].

They can act as isosteric substituents of other functional groups of biological interest, such as methylsulfonyl and aminosulfonyl. The smaller azide group is slightly more lipophilic than these two groups, hence it can interact more efficiently with some biological units (as arginine). The azide group can also be used in photoaffinity labelling of proteins: photolysis liberates N_2, leaving the remaining N atom free to form a nitrene with the protein, marking the latter for detection[68].

They are widely used in the synthesis of 1,2,3-triazoles, through copper-catalysed 1,3-dipolar cycloaddition reactions with alkynes, and in the synthesis of tetrazoles, through zinc-catalysed [3+2] dipolar cycloaddition reactions with nitriles, under water reflux[14–16,49]. Extensive information regarding fundamental characteristics of organic azides chemistry with its "explosive" diversity in modern synthetic chemistry can be found in the review by Bräse *et al.*[13].

Azides are potential high-energy density materials[69] and are also used in the generation of electrically conducting polymers and in the covalent modification of polymer surfaces[70].

Sodium azide was, until recently, the main component used in the inflation of airbags in automobiles and in emergency stopping parachutes in aeroplanes. Upon impact, an electromechanical trigger fires an initiator squib that causes the NaN_3 to thermally decompose yielding the N_2 gas that inflates the airbag momentarily[71], following the reaction

$$NaN_3 \rightarrow Na + 3/2\ N_2 \qquad \Delta G\text{=-93.76 kJ/mol.}$$

Due to the formation of toxic products from the thermal disintegration of NaN_3 and eventual interaction of the azide with oxide metals and further increase of explosion risk, sodium azide as been progressively substituted by tetrazoles, which are more stable, and yield less quantities of toxic decomposition products, but maintain a similar energetic behaviour.

Tetrazoles are widely used for both their biological function and their energetic characteristics. The tetrazole moiety possesses similar pH value as that of the carboxylic acid (-CO_2H), but its metabolically more stable than the later[72]. In fact, when coupled to the drug molecular structure it grants the overall molecular system some protection from degradation arising from metabolic processes. Several antihypertensive, antiallergic and antibiotic activity drugs include the tetrazole ring in its composition[73].

Tetrazoles are also used in agriculture as plant growth regulators, herbicides and fungicides. In addition, molecules containing the tetrazole ring present appealing tribological functionalities if coupled to some active elements, functioning as an additive to liquid paraffin, in applications where anti-wear and friction reduction oils are needed[74]. Its use as corrosion inhibitors in copper polishing has also been reported[75].

More recently, resurgence of tetrazole based compounds and molecules of higher nitrogen content has been verified, mainly due to the work of chemical synthesis by Klapötke and co-workers[76]. The thermal stability and pyrotechnic potential of several tetrazoles and bistetrazoles have been investigated by Klapötke, leading to the conclusion that tetrazoles salts present a new and environment friendly way of producing propellant materials for use in fireworks.

In summary, azides and tetrazoles are applied in similar areas of research and industry, due to the resemblance in their physico-chemical properties. In general, synthetic chemistry processes which involve elimination of N_2 and molecular design through intermediate nitrenes are based either in azido or tetrazole groups. Moreover, in industrial processes where a large amount of energy is utilized to generate heat or where a large amount of inert gas needs to be quickly generated, azides and tetrazoles are used.

1.1.4 Safety measurements

The safety measurements adopted when working with organic azides can be estimated by either the carbon-to-nitrogen ratio or the more general "rule of six". The former uses the $(C + O)/N \geq 3$ ratio as a guideline for handling and storing organic azides. If below 1, the azide should never be isolated and a maximum 1 g can be synthesized only if it is a transient intermediate species in some reaction. If between 1 and 3, the azide has to be stored below room temperature, at no more than 1M concentration and at a maximum of 5 g of material.

The "rule of six" says that 6 or more carbon atoms (or atoms of about the same size) per energetic functional group (azide, diazo or nitro) should provide enough dilution to render the compound relatively safe to work with given appropriate controls and safety procedures.

In general, synthesized organic azides should be stored below room temperature and away from sources of heat, light, pressure, and shock.

Although tetrazoles have a higher nitrogen content than most azides, the majority will only decompose or explode upon heating above its melting point or by extreme mechanical stress. Depending on the specific characteristics of each tetrazole based compound, storage at room temperature in a dry and cool place, inside a tightly closed plastic or glass bottle is enough. However, for high purity ($\geq$99%) or very high nitrogen content species ($\geq$85%), desensitization (phlegmatization) of the compounds with appropriate solvents is necessary.

In general, for handling small amounts of stable organic azides and tetrazoles at room temperature, gloves, lab coat, safety glasses (or a face protection shield) are needed at all times. Handling of the substances should be done under the fume cupboard, and the substances should be safely transferred to the spectrometer and pumped to primary vacuum conditions. This also minimizes the risk of any untoward occurrence.

The synthesized azides studied in this work (see Section 1.2) have a carbon-to-nitrogen ratios between 2.0 and 2.7, so they can be securely handled and stored in a fridge with some precautions. As they are stored in solution, at low concentrations, the risk of of explosion at room temperature is practically non-existent. To prevent photo degradation, the samples are protected from light at all times.

The tetrazoles studied in this work are not risk free, but they are not explosive nor dangerous at normal storage conditions. They are sold commercially by Sigma-Aldrich and shipped in a properly sealed plastic bottle. At all times, the handling procedures and safety measures on the material safety data sheet (MSDS) supplied by the company were followed.

1.2 Objectives

A set of model systems was chosen from the azido and tetrazole groups, with no specific relation between them. Choice criteria for the organic azide systems were the ready availability and the fact that they were anew, not-previously synthesized or extensively studied molecules. Benzyl azide and its methylated compounds (BA and 2-, 3-, 4-MBA) and methyl 2-azidopropionate (M2AP) fit the profile (Fig. 1.5, (a) and (b)). Neither electronic structure or gas-phase thermal decomposition of these molecules was ever studied.

In the case of tetrazoles, several flavours were available commercially, most of them as solids. In order to test the limits of application of the photoelectron spectroscopy technique to the study of simple 5-substituted tetrazoles, two molecules were chosen: 5-methyltetrazole (5MTZ) and 5-aminotetrazole (5ATZ) (Fig. 1.5, (c) and (d)). Choice criteria for these two molecules were the wide range of application of 5ATZ, the high thermal stability of 5MTZ and the lack of information regarding the electronic structure of both molecules extracted from its study in a free molecular environment (as it occurs in photoelectron spectroscopy). The fact that these molecules are known to exhibit tautomerism is also a strong point of interest.

The objectives of this work can be summarized as follows:

1. Obtain information regarding the electronic structure and other molecular properties of all the compounds under study.
2. Obtain information regarding the gas-phase thermal decomposition of all the compounds under study.
3. Assess which mechanisms are behind the thermal decomposition of the azido compounds, specifically if the schemes depicted in Fig. 1.2 apply.
4. Assess which mechanisms are behind the thermal decomposition of the tetrazole compounds, specifically if the schemes depicted in Fig. 1.4 occur.

5. Evaluate the tautomeric forms adopted by the different tetrazoles under study, following the general isomeric structures depicted in Fig. 1.3.
6. Design and construct the equipment necessary to perform the above tasks, exploring the advantages of the photoelectron spectroscopy technique.
7. Lay the framework for future similar studies, employing the photoelectron spectroscopy technique.

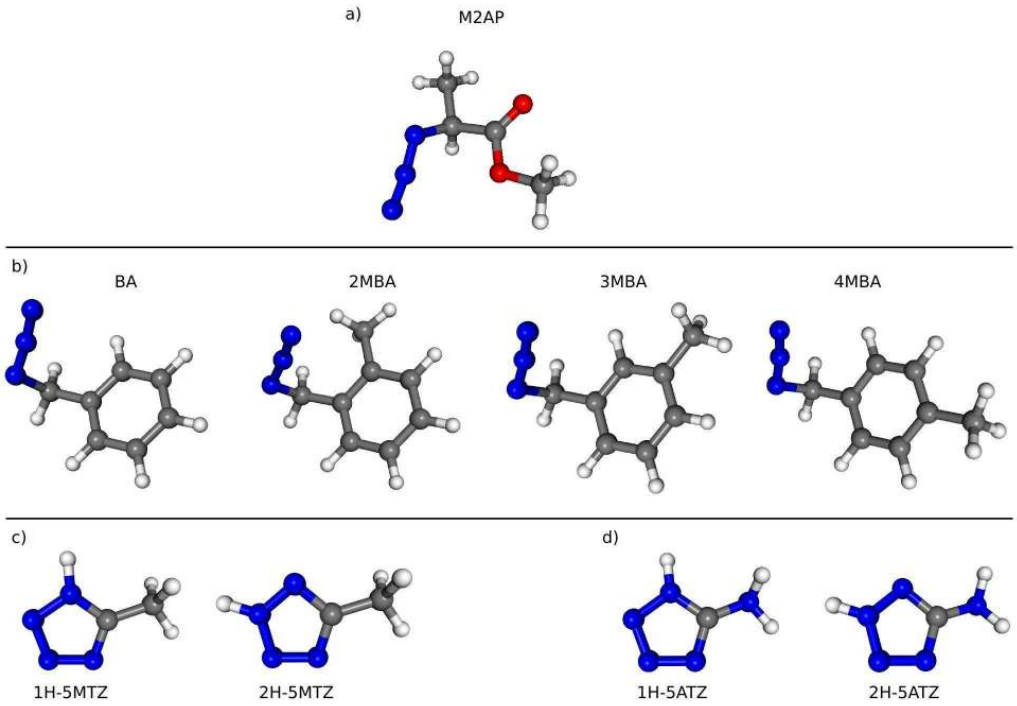

Figure 1.5: Azides and tetrazoles under study: methyl 2-azidopropionate (M2AP) (a), benzylazide and 2-, 3- and 4-methyl-benzylazide (BA and 2-,3-,4-MBA) (b), 5-methyltetrazole (1H-5MTZ and 2H-5MTZ tautomers) (c), and 5-aminotetrazole (1H-5ATZ and 2H-5ATZ tautomers) (d).

1.3 Thesis outline

This thesis is divided into two parts: Part I, *Introduction and Methods*, introduces the research subject and explains the experimental and theoretical methods used; Part II, *Case Studies*, compiles the work carried out with each of the molecular systems and ends up with a summary of the major conclusions.

Part I is divided into three chapters. Chapter 1, *Introduction*, deals with the theme under study, with some general information regarding the electronic structure and gas-phase thermal decomposition of organic azides and tetrazoles, and presents the molecules under study.

Chapter 2, *Experimental Methods*, introduces the reader to the main technique used during the course of this work – photoelectron spectroscopy, using He(I) and synchrotron radiation. Details regarding the instrumentation used in gas-phase thermal decomposition studies are presented thoroughly. A word for complementary techniques – matrix-isolation infrared spectroscopy and mass spectrometry – is also presented.

Chapter 3, *Theoretical Framework and Methods*, yields information regarding the theoretical methods covering photoionisation and general molecular electronic structure

calculations. In addition, the modelling of thermal decomposition pathways, and the software used to perform the calculations are analysed.

Part II is divided into nine chapters, all based in work already published or in preparation.

Chapter 4 deals with the electronic structure and thermal decomposition of M2AP. Chapters 5, 6 and 7 cover all the work achieved with BA and 2-, 3- and 4-MBA. Chapter 5 reports the computational work performed to describe the electronic structure of the benzyl and methyl benzylazide compounds. Chapter 6 reports the experimental results obtained on these molecules with the photoelectron spectroscopy technique, complemented with information from mass spectrometry analysis. Chapter 7 provides information regarding the gas-phase thermal decomposition of BA and 2-, 3-, and 4-MBA, obtained in collaboration with the PES group of University of Southampton

Chapters 8 and 9 refer to the electronic structure and thermal decomposition of 5ATZ and 5MTZ, respectively.

Chapters 10 and 11 cover the x-ray photoelectron spectroscopy (XPS) studies performed on 5MTZ and 5ATZ, respectively, using synchrotron radiation, with the aim of further understanding the tautomerism in tetrazoles. These studies were performed in the Elettra synchrotron facilities, in Trieste, Italy, in collaboration with the Gas Phase beamline group.

Chapter 12 summarizes the findings from all the above studies, regarding azides and tetrazoles electronic structure, mechanisms of thermal decomposition and tautomerism.

The list of publications *in print*, included as chapters in this thesis, is as follows:

1. R. M. Pinto, A. A. Dias, M. L. Costa, P. Rodrigues, M. T. Barros, J. S. Ogden, J. M. Dyke "Thermal decomposition of methyl 2-azidopropionate studied by UV photoelectron spectroscopy and matrix isolation IR spectroscopy: heterocyclic intermediate vs. imine formation" *J. Phys. Chem. A* **2011**, *115*, 8447-8457. **(Chapter 4)**
2. R. M. Pinto, A. A. Dias, M. L. Costa, J. P. Santos, "Computational study on the ionization energies of benzyl azide and its methyl derivatives" *J. Mol. Struct. (THEOCHEM)* **2010**, *948*, 15-20. **(Chapter 5)**
3. R. M. Pinto, R. I. Olariu, J. Lameiras, F. T. Martins, A. A. Dias, G. J. Langley, P. Rodrigues, C. D. Maycock, J. P. Santos, M. F. Duarte, M. T. Fernandez, M. L. Costa "Study of selected benzyl azides by UV photoelectron spectroscopy and mass spectrometry" *J. Mol. Struct.* **2010**, *980*, 163-171. **(Chapter 6)**
4. R. M. Pinto, A. A. Dias, M. L. Costa "Electronic structure and thermal decomposition of 5-aminotetrazole studied by UV photoelectron spectroscopy and theoretical calculations" *Chem. Phys.* **2011**, *381*, 49-58. **(Chapter 8)**
5. R. M. Pinto, A. A. Dias, M. L. Costa "Electronic structure and thermal decomposition of 5-methyltetrazole studied by UV photoelectron spectroscopy and theoretical calculations" *Chem. Phys.* **2012**, *392*, 21-28. **(Chapter 9)**
6. R. M. Pinto, A. A. Dias, M. Coreno, M. de Simone, B. M. Giuliano, J. P. Santos, M. L. Costa "Tautomerism in 5-methyltetrazole investigated by core-level photoelectron spectroscopy and ΔSCF calculations" *Chem. Phys. Lett.* **2011**, *516*, 149-153. **(Chapter 10)**
7. R. M. Pinto, A. A. Dias, M. Coreno, M. de Simone, B. M. Giuliano, J. P. Santos, M. L. Costa "Tautomerism in 5-aminotetrazole investigated by core-level photoelectron spectroscopy and ΔSCF calculations" *J. Electron Spectrosc. Relat. Phenom.* **2012**, *185*, 13-17. **(Chapter 11)**

The following work is *in preparation* and is also included as a chapter in this thesis:

1. R. M. Pinto, G. Copeland, A. A. Dias, P. Rodrigues, M. T. Barros, M. L. Costa,

J. M. Dyke "Thermal decomposition of benzyl azide studied by UV photoelectron spectroscopy and theoretical calculations" *J. Phys. Chem. A* **2012**, *in preparation.* **(Chapter 7)**

Chapter 2

Experimental Methods

2.1 Ultraviolet photoelectron spectroscopy

One of the most straightforward ways of experimentally probing the valence electronic structure of a single molecule or atom is by using the ultraviolet photoelectron spectroscopy technique (UVPES).

Originally developed by Turner and Al-Joboury[77], in 1962, at the Imperial College, and further celebrated in the seminal book *Molecular Photoelectron Spectroscopy*[6], this technique is nowadays the launching pad for numerous other experiments. Zero kinetic energy (ZEKE) photoelectron spectroscopy[78] and other (more recent) techniques[79], all drove its inspiration somewhere from the roots of UVPES. By promoting the interaction of ionizing radiation with molecules and analysing the energy of the ejected photoelectrons, the UVPES technique allows for the characterization of the molecular electron cloud that surrounds the nuclei and, in some cases, can even lead to fundamental information regarding the molecular geometry.

The ease-of-operation and implementation of this technique, allows it to be coupled to other complementary methods for studying species in the gas-phase, such as matrix-isolation infrared spectroscopy (matrix-isolation IR)[28] and mass spectrometry (MS)[80]. Characterization of short-lived reactive species or reaction intermediates in the gas-phase, which otherwise would be impossible to produce and retain intact in solution or solid medium, often appears collated to the UVPES technique[81–84].

In fact, most medium-sized molecules can be readily identified and distinguished by the corresponding photoelectron bands appearing in a UVPES spectra. This "fingerprint" spectroscopy is therefore a powerful technique for studying molecules and atoms, free of any interaction with the surrounding medium, in both a fundamental and qualitatively manner.

2.1.1 Principles

Photoelectron spectroscopy can be envisioned essentially as a special case of electronic absorption spectroscopy in which the electron is given enough energy to take it beyond any of the bound orbitals. The underlying physical process is the widely recognized photoelectric effect, in which photons of a given energy interact with an atom or molecule, resulting in the ejection of an electron from the sample[85,86].

We can define the term *ionization energy* (*IE*) as the minimum energy needed for an electron in a given orbital to exceed the *ionization limit* i.e. to escape the attractive force of the atom or molecule. In UV photoelectron spectroscopy, this energy is provided by a photon whose energy falls in the ionizing UV range i.e. from the near UV (400-300

nm, 3-4 eV) to the extreme UV (121-10 nm, 10-124 eV).

On interaction, only part of the energy $h\nu$ carried by the photon is used to ionize the atom or molecule. Another part of it is transferred to the ion (T_{ion}) and the remainder is taken away by the ejected electron (T_e), both in the kinetic form. Hence, from conservation of energy, the following relationship holds,

$$h\nu = IE_i + T_e + T_{ion} \tag{2.1}$$

where IE_i is the ionization energy of an electron in orbital i. The kinetic energy T_{ion} imparted to the ion is usually neglected due to the large disparity of mass between the electron and the ion.

The basic idea behind conventional photoelectron spectroscopy resides in measuring the electron current (also termed *intensity*) as a function of the electron kinetic energy, using a source of monoenergetic radiation i.e. of fixed frequency. The data can then be plotted as a 2D graph, *intensity* vs. IE, or *intensity* vs. T_e, assuming the typical form of a spectrum.

2.1.1.1 Direct photoionisation and autoionisation processes

For the purpose of this work, ejection of a valence shell electron from a molecule will be considered via two processes: *direct photoionisation* (or simply *photoionisation*) and *autoionisation*. Experimentally, however, only direct ionisation will be accounted for.

The first process, *photoionisation*, consists on the removal of a single electron from the neutral molecule without changing the quantum number of any other electrons, independently of the orbital where this electron is in. The electron is ejected from a molecule $\mathrm{M}(X; v'')$ in its ground electronic state X and vibrational level v'' to form the corresponding molecular ion $\mathrm{M}^+(x, a, b, c, ...; v' = 0, 1, ...)$ in either its ground electronic state x or any of its excited electronic states $a, b, c, ...$ and vibrational levels v', according[87] to the following expression

$$\mathrm{M}(X; v'') + h\nu \rightarrow \mathrm{M}^+(x, a, b, c, ...; v' = 0, 1, ...) + e^- \tag{2.2}$$

or, suppressing the electronic and vibrational states notation, to

$$\mathrm{M} + h\nu \rightarrow \mathrm{M}^+ + e^- \tag{2.3}$$

Which transitions are therefore allowed (i.e. more probable) in the *photoionisation* process? Since electronic transitions are mostly of the electric dipole type (E1), they are mediated by the the *electric dipole selection rules*. The photon carries itself a spin angular momentum of 1, therefore a change of $\Delta l{=}\pm 1$ should be observed upon interaction with the neutral molecule. The change in total angular momentum ΔL from the neutral molecule to the ion is given by

$$\Delta L = 0, \pm 1 \qquad . \tag{2.4}$$

Given that the final state wave function is an antisymmetrized product of the ionic wave function and the unbound electron wave function, it is clear that the free electron can leave the ion carrying whatever angular momentum is needed to satisfy the above selection rule, even a mixed character of angular momentum. In effect, the outgoing photoelectron can be described by a wave function which encompasses s, p, d or f waves in order to obey rule 2.4. Therefore, regarding angular momentum, *all one-electron photoionisation transitions are allowed*[87].

If the spin-orbit coupling is weak, then the total spin of the system S is conserved between the initial state (the neutral molecule) and the final state (ion + photoelectron). This means that a photoelectron with $m_s = \pm 1/2$, ejecting from a closed-shell system, leaves an ion in a doublet spin state. Therefore, the *spin selection rule*

$$\Delta S = 0 \quad , \tag{2.5}$$

also dictates which transitions are allowed in the photionisation process. In spectroscopy, the term *spin multiplicty* $(2S + 1)$ is used to coin the degeneracy of the spin part of an electronic state. Most common photoelectron spectra consist of transitions from the singlet molecular ground states $(2S+1 = 1)$ to the doublet states $(2S+1 = 2)$ of the positive ion[87].

Autoionization also leads to the formation of a ionic species but it is preceded by photoexcitation of the neutral molecule to a highly excited $\mathrm{M}(A, B, C, ...; v'' \neq 1)$ electronic state, frequently a Rydberg state above the *ionization limit*, according to the expression

$$\mathrm{M}(X; v''') + h\nu \rightarrow \mathrm{M}(A, B, C, ...; v'' \neq 1) \rightarrow \mathrm{M}^+(x, a, b, c, ...; v' = 0, 1, ...) + e^- \tag{2.6}$$

or, simply put

$$\mathrm{M} + h\nu \rightarrow \mathrm{M}^* \rightarrow \mathrm{M}^+ + e^- \tag{2.7}$$

The process of *autoionization* is effectively the radiationless transition of the second step, the first step being simply a resonance process. The autoionizing states can only be detected in experiments which involve variation of the energy of the ionizing photon source, such as photoabsorption studies or photoelectron spectra obtained at different excitation wave lengths.

2.1.1.2 Franck–Condon principle and the origin of vibrational structure

At this point of the discussion, it is mandatory to introduce a common graphical crutch, frequently found in most molecular physics textbooks: the potential energy curves associated with the several electronic states of a given polyatomic molecule (Fig. 2.1).

Usually these curves are presented as 2D plots, without referring the important fact that they are slices of a multidimensional surface, which spans over 3N independent coordinates (N equals the number of atoms). There is an enormous amount of information which can be retrieved from Fig. 2.1, hence we will analyse it in some detail.

The abscissa scale is represented in generalized coordinates, q_i, which means that a set of independent variables can be used to describe the molecular system. These coordinates can be the vibrational modes of a molecule, a set of bond lengths and angles or any minimum number of coordinates which represent an irreducible set of spatial parameters needed to correctly describe the physical state.

For a diatomic molecule, such as CO, we would need six of such parameters: three for the translation of the centre of mass, one for the vibrational mode and two for the rotational motion. For a non-linear triatomic molecule, such as H_2O, we would require nine free parameters: three for the translation, three for the vibrational modes and three for the rotational motion. Any polyatomic molecule, with N atoms (N>2), requires 3N degrees of freedom to be correctly described.

In the XY plane, a nicely set of well-defined curves are associated with the potential energy of the neutral ground-state $\mathrm{M}(X)$ and several ionic states $\mathrm{M}^+(x, a, b, c, ...)$. In spite its illustrative purpose, these curves are actually based on the Morse potential[88], which are analytical expressions for the potential energy of diatomic molecules. Each of these potentials describes the total electronic energy of the molecule, in a given

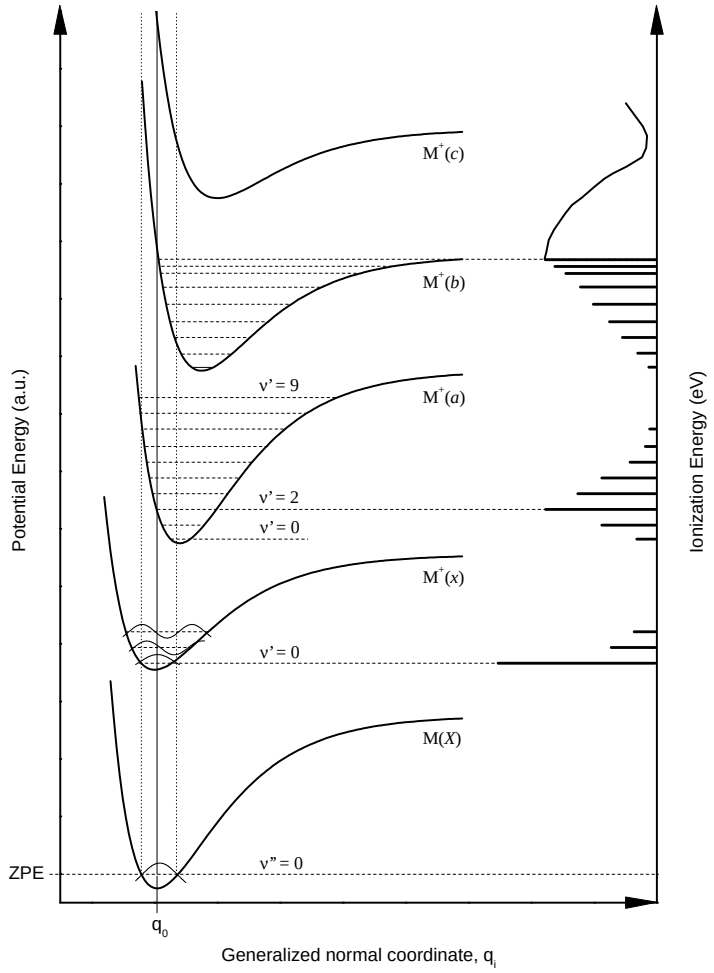

Figure 2.1: Potential energy curves for the molecule M in its ground-state and the corresponding cation M^+ in several ionic states.

electronic state, as a function of q_i. If we insert one of these potentials in the vibrational Schrödinger equation and solve it, we gain access to a set of stationary solutions, corresponding to the vibrational levels ν' shown in Fig. 2.1.

The potential curves $M^+(x, a, b, c, ...)$ are shifted with respect to the equilibrium coordinate q_0 i.e. relatively to the q_i value at which the potential curve $M(X)$ has its absolute minimum. This means that removal of an electron from the valence electronic structure changed the molecular electrostatic distribution in such a way that a different geometry is now associated with the new minimum of energy.

Where does it all link to the subject of photoelectron spectroscopy? Precisely at the *Franck–Condon principle*[89–91]:

> *Classically, the Franck–Condon principle is the approximation that an electronic transition is most likely to occur without changes in the positions of the nuclei in the molecular entity and its environment. The resulting state is called a Franck–Condon state, and the transition involved, a vertical transition.*
>
> *The quantum mechanical formulation of this principle is that the intensity of a vibronic transition is proportional to the square of the overlap integral between the vibrational wave functions of the two states that are involved in the transition.*

In 1926, Franck elaborated a semi-classical interpretation of how light interacts with atoms and molecules, in a photochemical process. For the first time, a plot like the one portrayed in Fig. 2.1 was sought, in order to connect the relative position of the nuclei before and after excitation with the probability of that excitation to occur. Also in 1926, Condon extended the work of Franck, analysing a photoabsorption spectrum of CO at the light of Franck's ideas[92], confirming that "an electronic transition is most likely to occur without changes in the positions of the nuclei".

The Franck-Condon region is drawn in Fig. 2.1, defined by the area between the two vertical dashed lines. The most probable transition is the one for which the overlap between final and initial vibrational wave functions is the largest. This is indicated by the full vertical line drawn from the maximum value of the square of molecular wave function for the state $\mathrm{M}(X;\nu''=0)$. Outside the Franck-Condon region, no overlap between wave functions exists and therefore the transition probability is very low (i.e. a forbidden transition).

The spectral band shape of a typical photoelectron spectrum is intimately related to the Franck-Condon region and the so-called *Franck-Condon envelope*. This can be seen in the right side of Fig. 2.1.

For a given electronic transition, the highest probability transition to the group of final vibrational states will be the one with the highest overlap with the initial wave function. As higher probabilities mean higher chances of populating a state, there will be more electron counts at the energy of that given state, than for other states. The photoelectron spectrum reflects this fact, in a series of closely spaced peaks, often called vibrational progressions, whose intensities follow a *Franck-Condon envelope*. If the vibrational structure is well resolved, information regarding the molecule's equilibrium structure can be extracted from the vibrational progressions.

If we consider a wave function Ψ' for the final state M^+ (ion+photoelectron), and a wave function Ψ'' for the initial neutral state M, which can be written as products of separable electronic, vibrational and spin parts i.e. $\Psi = \Psi_e\Psi_v\Psi_s$, then the *photoionisation transition probability* P can be considered, to a good approximation, as

$$\mathrm{P} \propto \int (\Psi'_v)^* \Psi''_v \, d\mathrm{q}_i \qquad , \tag{2.8}$$

where the integral is evaluated over the generalized coordinate q_i. The rotational part of the wave function, Ψ_r, is neglected since it usually cannot be probed with the UVPES technique.

The above equation represents the quantum formulation of the Franck-Condon principle, and the square of the overlap integral is called the *Franck-Condon factor*. As stated before, the value for this integral largely rules the relative intensity of the vibrational lines in a progression, often appearing in photoelectron spectra. This approximation rests on the validity of the Born-Oppenheimer framework which will be discussed in more detail in Chapter 3.

The energy of the highest intensity peak in each vibrational progression is termed *vertical ionization energy* (VIE) and corresponds to the energy involved in transitions of the type

$$\mathrm{M}(X;v''=0) + h\nu \rightarrow \mathrm{M}^+(x,a,b,c,...;v'=n) + e^- \tag{2.9}$$

where n is the vibrational level whose wave function gives the largest overlap with the initial state wave function.

The energy of the first peak appearing in each vibrational progression is termed *adiabatic ionization energy* (AIE), and is associated with the energy involved in transitions of the type

$$\mathrm{M}(X;v''=0) + h\nu \rightarrow \mathrm{M}^+(x,a,b,c,...;v'=0) + e^- \qquad . \tag{2.10}$$

At the light of these concepts and looking at Fig. 2.1, one can rewrite Eq. 2.1 as[87]

$$T_e = h\nu - IE_i \qquad , \tag{2.11}$$

with

$$IE_i = \mathrm{AIE}_i + E^+_{vib} + E^+_{rot} \equiv \mathrm{VIE}_i \qquad , \tag{2.12}$$

where the ion recoil energy T_{ion} is neglected, and E^+_{vib} and E^+_{rot} represent the vibrational and rotational energies of the molecule in the ionic state M^+; the VIE is just the sum of the AIE plus the vibrational/rotational energy levels. The term E^+_{vib} can often be distinguished within the resolving power of the UVPES technique, but not the rotational term E^+_{rot}.

We have learned the main qualitative features of photoelectron spectroscopy and of a typical photoelectron spectrum...yet, an additional question arises: what instruments do we need to acquire such spectra?

2.1.1.3 Overview of a general purpose UV photoelectron spectrometer apparatus

Typically, a conventional UV photoelectron spectrometer is based on five items: a radiation source, a sample introduction system, an energy analyser, an electron detector and a vacuum system.

The *radiation source* has to be able to produce ionizing UV radiation of fixed wavelength. This radiation is usually created by making a DC discharge in a rare gas (helium, neon, argon, krypton or xenon), and populating an excited state whose radiative decay is well-defined. A classical example of the design and construction of this type of sources is given by Schönhense and Heinzmann[93]. Alternatively, synchrotron radiation can be employed as ionizing source for better resolution, intensity and custom-polarization characteristics.

The *sample introduction system* is a very important part of the spectrometer, as it defines the range of analysis of the apparatus: direct pumping from the liquid phase is only possible with samples of sufficiently high vapour pressure, whereas for solid samples it is mandatory the use of some type of oven or furnace to evaporate the samples. Design overview and construction requirements for molecular ovens can be found in the review by Ross and Sonntag on high temperature metal atom beam sources[94].

After promoting the interaction between the object of study (molecule or atom) and the probe (photons), the devised result (photoelectrons) has to be analysed. This is often performed using an electrostatic *energy analyser*, whose performance characteristics vary profoundly with geometry and mode of operation. The seminal article by Purcell[95], and the reference works by Kuyatt and Simpson[96], and Roy and Tremblay[97], give fundamental insight regarding the subject of design and construction of such analysers, defining two important figures of merit: resolution and transmission. A good example of precise fabrication of an electrostatic energy analyser and full characterization of its electron-optics capabilities is the recent work of Sise and co-workers[98].

The detection limits and sensitivity are ultimately established by the *electron detector* device. Usually, its construction is based on the properties of a semiconductor material. After travelling through the analyser, the photoelectron collides with this material and promotes the ejection of two other electrons, and so forth, in a successive cascade of current build-up. At the end, the charge of one electron is converted into a 10 mV negative pulse with ca. 20 ns of width. The number of pulses detected at a given pass-energy of the analyser are summed and stored in a computer or directly drawn by a XY plotter.

Finally, the experiment cannot at all be accomplished at atmospheric pressure, so a *vacuum system* is needed to evacuate the ionization and analyser chambers. A simple

rotary vane pump coupled to an oil diffusion pump are enough to reach the high vacuum region in a medium sized chamber i.e. an ultimate base pressure of approximately 1×10^{-4} Pa (1×10^{-6} mbar). This low pressure is necessary for the electron detector to work and to assure that only the sample to be analysed is in fact interacting with the probing photons.

A schematic view of a general purpose photoelectron spectrometer is given in Fig. 2.2. A good source of information regarding the overall design and construction of photoelectron spectrometers can be found in the literature[99–102].

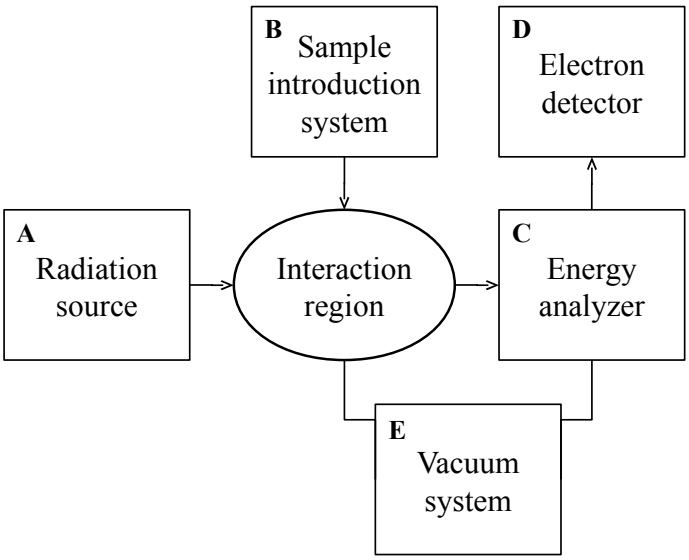

Figure 2.2: Diagram of the main components of a general purpose photoelectron spectrometer.

2.1.2 Experimental details

The photoelectron spectrometer presently located at the Physics Department, FCT-UNL, Lisbon, was originally constructed at the University of Southampton, by John Dyke's research group, under a Science Twinning Project with Universidade Nova de Lisboa. Its design and original mode of operation are described by Morris, Dyke and co-workers, in a 1983 article[99]. During the last decade, the spectrometer has been modified and updated, but no drastic changes have been introduced regarding the main components. A gross illustration of the relative position of the several elements of the spectrometer is shown in Fig. 2.3.

In the following sections, concise technical information on each main component of our photoelectron spectrometer will be given, together with some general modes of operation. The subject of calibration of the energy scale will also be analysed. Whenever possible, real figures regarding the contribution of each component to the overall working resolution will be estimated and discussed.

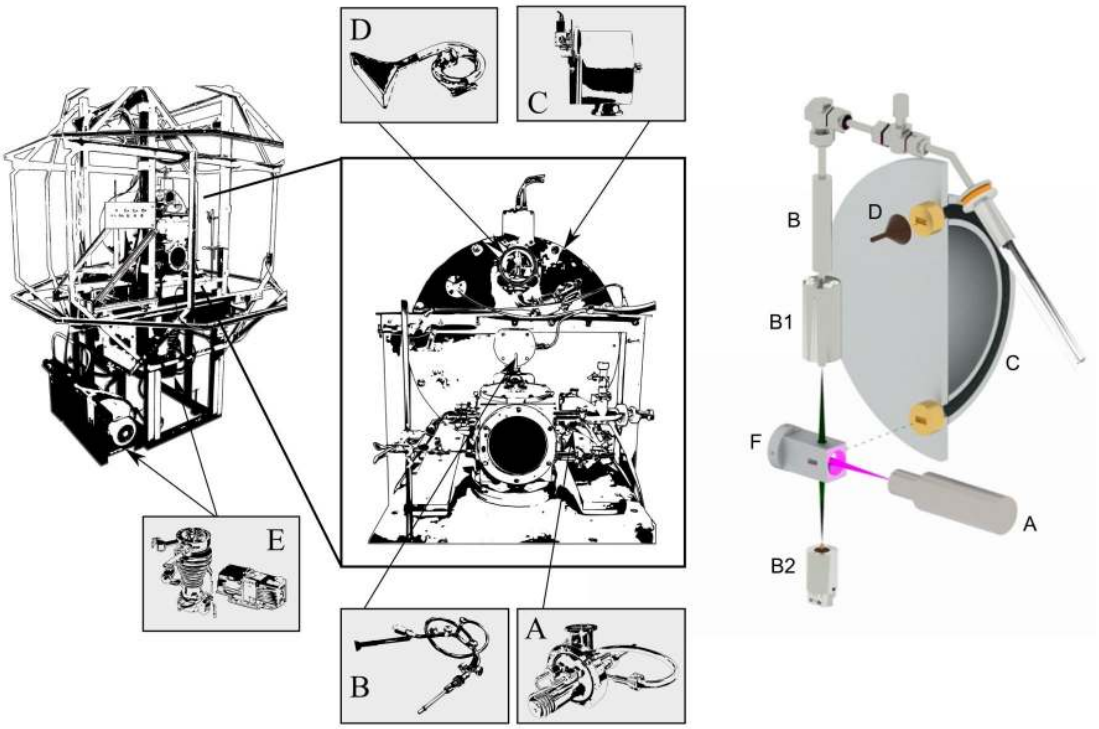

Figure 2.3: Illustration of the main components of the UV photoelectron spectrometer located in Lisbon. A - radiation source, B - sample introduction system, B1 - pyrolysis system, B2 - over for organic samples, C - energy analyser, D - electron detector, E - vacuum system, F - reaction cell.

2.1.2.1 Radiation source – A

The resonance radiation in the ionizing UV range can be produced by a microwave or current discharge through a rare-gas, typically helium, in a small 1-2 mm diameter capillary. An initial spark initiates the production of a confined plasma which, depending on the experimental conditions and gas used, can draw 30 to 200 mA current, at ca. 600-1000 V, after the discharge.

The most important resonance lines are listed in Table 2.1, where the roman numerals next to the element symbol define either the neutral (I) or the singly ionized (II)

Table 2.1: Principal resonance lines (wavelength in Å, energy in eV) for the rare gases helium, neon, argon and xenon.

Gas	Transition	Wavelength[a]	Energy
He(I)	$1s^2 \rightarrow 1s2p$	584.334357	21.218022
	$1s^2 \rightarrow 1s3p$	537.029918	23.087018
	$1s^2 \rightarrow 1s4p$	522.213086	23.742069
He(II)	$1s^2 \rightarrow 1s2p$	303.785815	40.813029
	$1s^2 \rightarrow 1s3p$	256.317703	48.371295
	$1s^2 \rightarrow 1s4p$	243.026877	51.016659
Ne(I)	$2s^22p^6 \rightarrow 2s^22p^53s$	743.7195	16.6708
	$2s^22p^6 \rightarrow 2s^22p^53s$	735.8962	16.8481
Ar(I)	$3s^23p^6 \rightarrow 3s^23p^54s$	1066.660	11.624
	$3s^23p^6 \rightarrow 3s^23p^54s$	1048.220	11.828
Xe(I)	$5p^6 \rightarrow 5p^56s$	1469.610	8.437
	$5p^6 \rightarrow 5p^56s$	1295.588	9.570

[a]Retrieved fromt the NIST Atomic Spectra Database[103].

species emitting radiation. Usually, the most intense line is produced by the transition from the first excited state to the ground state of the atom or ion.

In this work, only the first resonance line of He(I) was used, with an energy of ca. 21.22 eV, which represents almost 99% of the radiation being emitted. The presence of the other two resonance lines can sometimes be detected in the spectra of small molecules or atoms, in the form of a twin spectra of negligible intensity, shifted towards low ionization energy values.

As no material is completely transparent to the UV range below 584 Å, all discharge lamps are based in a windowless design. This implies the use of some sort of differential pumping system when operating the lamp, in order to minimize the leakage of the rare-gas into the main interaction chamber. For high-vacuum systems, only one stage maintained at primary vacuum is enough; for pressures below 10^{-4} Pa, a two-stage differential pumping system is advisable.

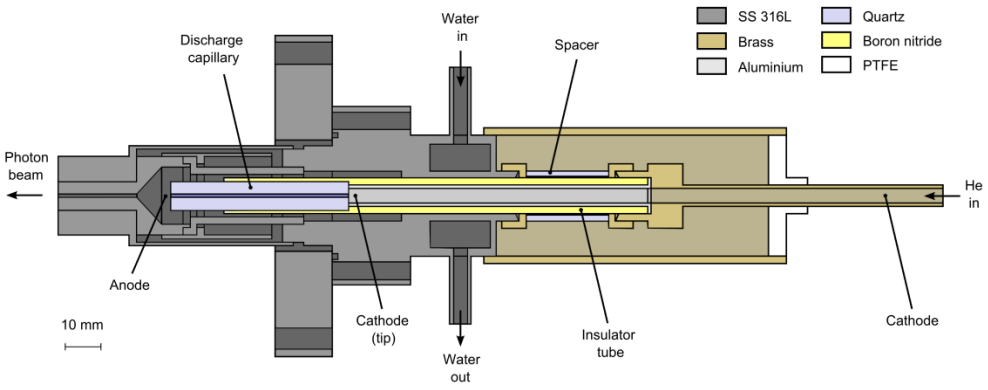

Figure 2.4: Schematic diagram of the water-cooled discharge lamp, for producing resonance radiation of rare gases. The gas pumping port and the water-cooled serpentine tip were omitted for the sake of clarity.

The radiation source from our system is based on an original design by Perkin-Elmer, one of the first companies to produce and sell a commercial photoelectron spec-

trometer. Fig. 2.4 shows such a design, where the water-cooled DC discharge lamp can be seen. The discharge occurs through the capillary, between the anode and the cathode's tip, and the rare-gas is introduced from a brass tube maintained at high voltage. The insulating sieve surrounding the thin aluminium conducting tube is usually made of machinable glass ceramic (Macor®), aluminium oxide (Al_2O_3) or boron nitride (BN).

A few important physical parameters are the length and internal diameter of the discharge capillary, and the distance between the cathode and the anode. This last figure is crucial in obtaining a stable discharge, and depends on the geometric parameters of the source apparatus. The tip of the discharge capillary is placed $\approx$ 10 mm away from the concave end of the discharge chamber, which means the discharge actually occurs along the capillary, with a cathode to anode distance of approximately 50-60 mm.

The collimating capillary and cathode's end are surrounded by a water-cooled serpentine and jacket, respectively, which lowers the temperature near the discharge region to room temperature values. A typical discharge procedure is described as follows:

1. Open the valve to the water cooling system.
2. Evacuate the discharge region by opening the valve to the pumping port.
3. Admit helium into the lamp until a pressure of $\approx$ 30 Pa (0.3 mbar) is reached.
4. Slowly increase the voltage between the cathode and the anode, to a maximum of 3.5 kV, until the discharge ignites.
5. Adjust the voltage until the current drops to 30–50 mA.

The width of the ionizing radiation contributes to the width of the ionization lines seen in the spectra, and depends mainly on two phenomena: *self-absorption* and *Doppler broadening* caused by the motion of the atoms or ions in the radiating plasma[101]. The *Doppler broadening*[104] is given by

$$\Delta\lambda_{\mathrm{D}} = 1.67 \left(\frac{\lambda}{c}\right) \sqrt{\frac{2RT}{M}} \qquad [\text{Å}] \ , \tag{2.13}$$

where R is the universal gas constant, T is the temperature of the plasma, M is the molar mass, and λ is the wavelength of the radiation being emitted. Considering He(I) radiation with 584 Å, M=0.004 kg/mol, and T=300 K, then $\Delta\lambda_{\mathrm{D}} = 3.6 \times 10^{-3}$ Å, which is equivalent to 1.3×10^{-4} eV.

Equation 2.13 can be rearranged as a function of the radiation energy E (eV), the temperature of the plasma T (K) and the molar mass of the rare-gas M (kg/mol), to yield directly $\Delta\mathrm{E_D}$ as follows

$$\Delta\mathrm{E_D} = 2.272 \times 10^{-8} \ E \ \sqrt{\frac{T}{M}} \qquad [\text{eV}] \ . \tag{2.14}$$

Fig. 2.5 shows the variation of the Doppler broadening with temperature, for rare-gases and radiative transitions typically used in resonance lamps (He, Ne and H).

The second main cause of width broadening arises from the process of *self-absorption*. It consists in the absorption of the emitted radiation by part of the unexcited gas lying between the end of the discharge capillary and the slit to the interacting region.

If the frequency distribution of the radiant flux is given by $I_0(\nu) = C(1 - e^{-\sigma(\nu)nl})$, then the profile of resonant radiation after self-absorption decays exponentially:

$$I(\nu) = I_0(\nu) \times e^{-\sigma(\nu)nl} = C(1 - e^{-\sigma(\nu)nl}) \ e^{-\sigma(\nu)nL} \qquad , \tag{2.15}$$

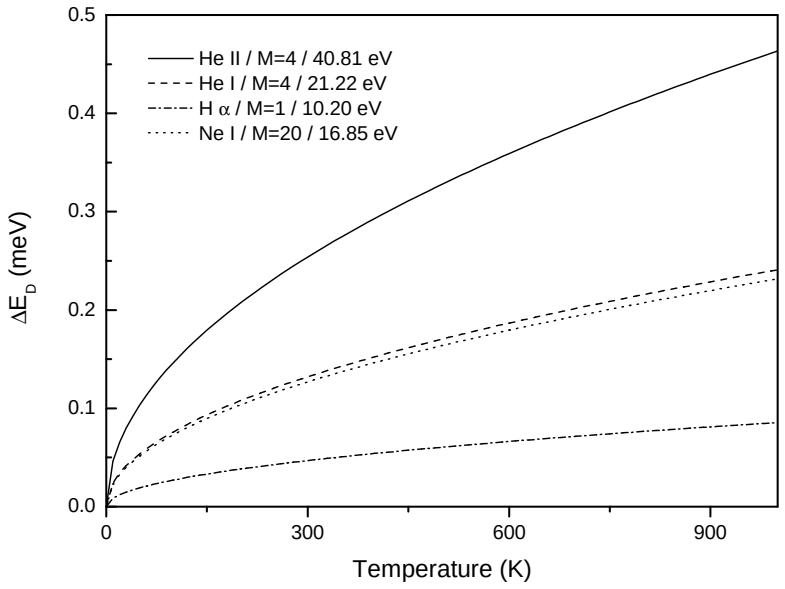

Figure 2.5: Thermal Doppler broadening as a function of temperature, for the principal resonance lines of the helium, neon and hydrogen rare gases.

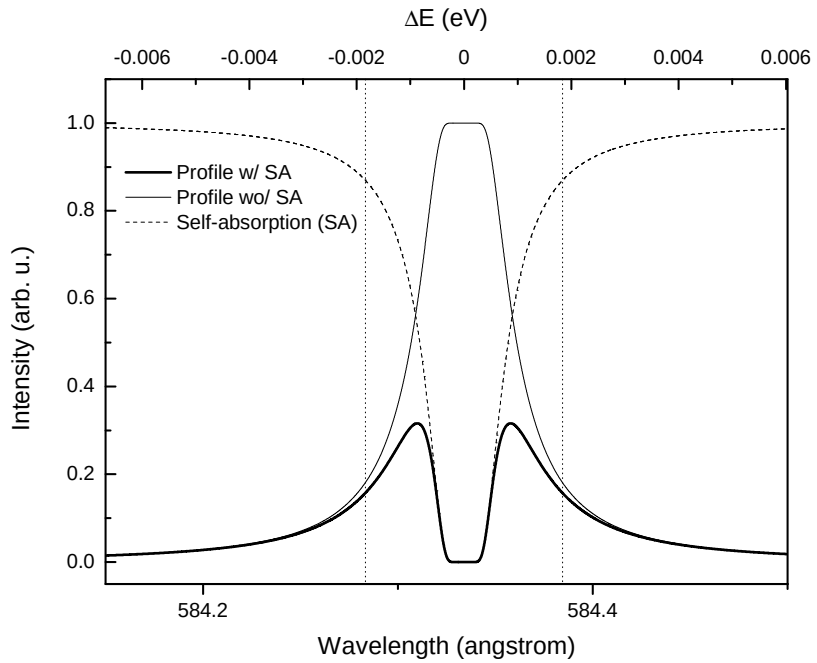

Figure 2.6: Example intensity profile of the ionizing radiation, with and without the effect of self-absorption.

where C is a constant for given conditions of pressure and temperature, n is the gas density, l is the length of the discharge column, L is the length of unexcited gas, and $\sigma(\nu)$ is the frequency dependent absorption cross-section of the gas.

The profile in Fig. 2.6 was simulated assuming that the Doppler effect governs the absorption cross-section, which follows a Lorentzian profile with a FWHM of 3.6×10^{-3} Å, and that $L = 3.5$ cm, $l = 5$ cm,$n = 0.1664$ kg/m^3.

At our experimental conditions, the predicted contribution to overall width brodening due to self-absorption is approximately 3.7×10^{-3} eV. However, this value can be reduced by pumping the zone immediately after the discharge.

2.1.2.2 Sample introduction system – B

Admittance of the sample into the spectrometer is processed by the introduction system. Liquid samples are pumped directly from a glass vial outside the spectrometer, through the use of a needle valve connected to a stainless steel tube.

The tube is positioned along the axis transversal to both the ionizing beam axis and the plane of entrance to the analyser. The position of this tube relatively to the axis of the ionizing beam can be adjusted, but its end is usually kept 3-5 mm above the photon beam.

From the length of the tube L and its internal radius r, 195 and 2 mm, respectively, one can estimate its transmission probability α and conductance C. The latter is computed considering the tube's entrance as an aperture. Hence, the conductance of the tube's entrance, in the molecular flow regime, is given by[105] $C_A = A(R_0T/2\pi M)^{1/2}$, where A is the cross-sectional area of the tube, R_0 is the universal gas constant, T is the temperature, and M is the molar mass of the particle travelling through the tube.

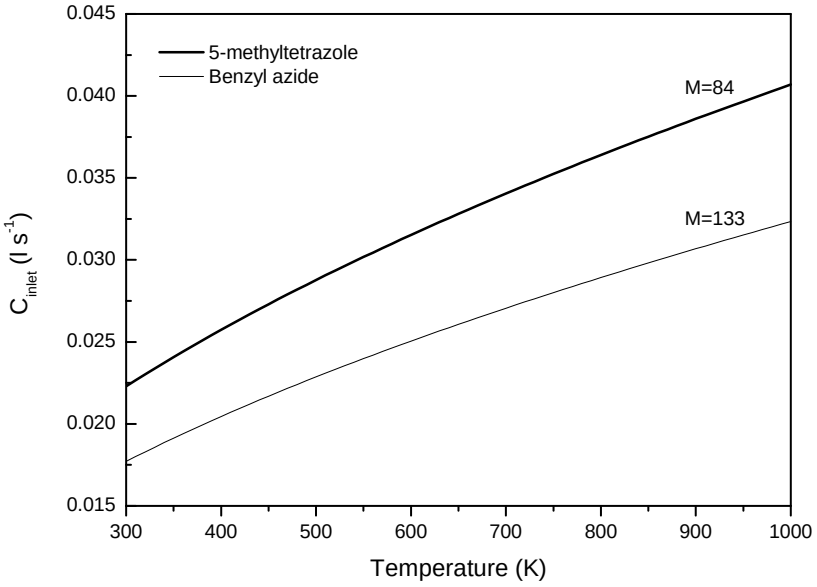

Figure 2.7: Conductance of the inlet tube of the sample introduction system, as a function of temperature, evaluated for samples with M = 84 (5-methyltetrazole) and 133 (benzyl azide). The Clausing transmission probability is 0.0258, estimated for $L/r \approx 100$

.

The conductance of the introduction system's tube is just the product of C_A with the transmission probability α. The latter term is also known as Clausing factor and arrives from the numerical solution of an integral equation first established by Clausing[106], and

with solutions further approximated by Berman[107] and Cole[108]. For our tube, with the L/r ratio being approximately 100, α is estimated as 0.0258.

Using $\alpha \approx 0.0258$, $M = 0.084$ and 0.133 kg/mol, $A = 2.5 \times 10^{-5}$ m^2, the conductance of the introduction tube was computed for different temperature values, for the molecular flow regime. The results are shown in Fig. 2.7.

If the liquid sample has a vapour pressure value of the same order of magnitude of the working pressure inside the spectrometer (ca. 10^{-3} Pa, with the radiation source fully operational), then it will evaporate and travel downstream the steel tube, colliding with the photon beam, in the interaction region.

If the sample needs to be heated, a baking heater band can be wrapped around the glass vial in order to raise the temperature until the sample can be directly pumped.

The introduction system has to be versatile enough to allow for the study of samples in any initial physical state, whether being gas, liquid or solid states. Furthermore, its dismount and cleansing procedures should also be easily performed.

2.1.2.3 Electron energy analyser – C

An extremely important part of any photoelectron spectrometer is the electron kinetic energy analyser: among the several types of electrostatic analysers, the *spherical sector electrostatic analyser* finds its use widely disseminated due to its double focusing capability, and transmission and sensitivity properties.

Geometrically, it consists on two concentric stainless steel bowls, of different internal diameters, electrically insulated from each other. When a voltage difference is applied between these two semi-spheres, it behaves like a curved condenser. Only charged particles with a specific initial kinetic energy will travel across this condenser without colliding with its walls.

The 150° spherical sector electrostatic analyser is a truncated hemispherical electrostatic analyser[95,109,110], but maintains approximately the same electron-optical properties of the 180° version. The space made available is used to accommodate the entrance and exit slits, the reaction cell and the electron detector. In this way, the focusing plane of the analyser (termed Barber's plane[111]) simultaneously allocates the point at which the photoelectrons are detected and the point at which they are produced. Fig. 2.8 shows a schematic diagram of the experimental spatial disposition of the analyser and slits, relatively to the interaction region.

The scan of the energy of the photoelectrons travelling through the analyser is performed by scanning the voltage established between the spherical sectors. The pass energy E_0 for an electron entering the analyser can be defined as[112–114]

$$E_0 = Cq\Delta V = \frac{R_1 R_2}{\frac{\gamma}{\xi}(1+\xi)R_0\Delta R} q\Delta V \quad , \tag{2.16}$$

where C is the calibration constant, $\Delta V = V_2 - V_1$ is the potential between the sectors, q is the charge of the electron, R_1 and R_2 are the radii of the sectors, $\Delta R = R_2 - R_1$ is the difference between radii, R_0 is the mean radius between the two sectors, and γ and ξ are parameters regarding paracentricity and biasing of the analyser entrance. The indexes 1 and 2 regard the inner and outer sectors, respectively.

Considering only a central unbiased analyser entry ($\gamma = 1$ and $\xi = 1$) and using the geometric parameters of our analyser – $R_2 = 0.22$ m, $R_1 = 0.18$ m, $R_0 = 0.2$ m, then Eq. 2.16 can be rearranged to

$$\Delta V = \frac{E_0}{2.475q} \quad , \tag{2.17}$$

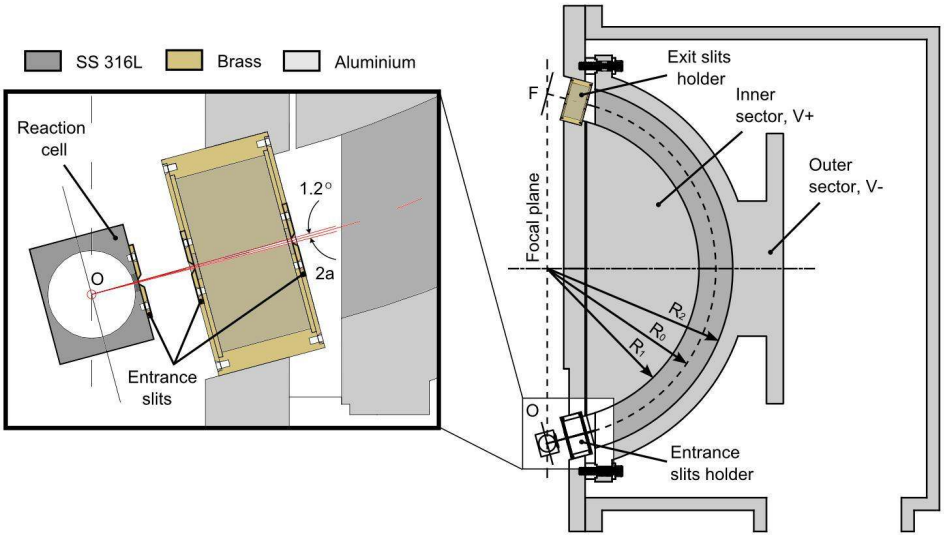

Figure 2.8: Schematic diagram of the 150° electrostatic analyser, and exit and entrance slits. A close-up view of the interaction region and analyser entrance is shown at the left-hand side. α is the angle done by the initial trajectory with the normal to the entrance plane. Definitions regarding R_1, R_2, R_0, O and F are given in the text.

where ΔV is expressed in volts and E_0 in eV. If one wishes to select only electrons with 5 eV kinetic energy, a potential difference of 2.020 V has to be set between the sectors of the analyser, with V_2 being negative and V_1 positive with respect to ground potential. The voltage applied to each sector, for a central unbiased entry[114], should follow the expression $V_i = (2 - 2R_0/R_i)E_0/q$, where $i = 1, 2$.

The base resolution ΔE i.e. the maximum energy spread of the analysed particles at a given energy E, can be defined as

$$\frac{\Delta E}{E} = \frac{s_i + s_f}{2R_0} + \alpha^2 \quad , \tag{2.18}$$

where s_i and s_f are the widths of the entrance and exit slits, and α is the angle of the photoelectron's initial trajectory with respect to the entrance of the analyser.

Assuming that the response function of the analyser follows a Gaussian distribution then the resolution measured at FWHM is usually equal or smaller than half the base width i.e. $\Delta E_{\mathrm{FWHM}} \leq \Delta E/2$. Using real values from of our set-up – $s_i = s_f = 1 \times 10^{-3}$ m and $R_0 = 0.2$ m, a 5 eV photoelectron entering the analyser at α=0° will give rise to a Gaussian response function with a maximum FWMH of 12.5×10^{-3} eV, at the exit.

Even though Eq. 2.18 yields the precise value for the energy resolution of a hemispherical analyser, a more precise equation can be derived for the case of a concentric spherical-sector analyser.

Let ϕ be the angle subtended by the sector analyser and l the distance between the entrance/exit boundary and the focal plane, then

$$\frac{\Delta E_{\mathrm{FWHM}}}{E} = \frac{s_i + s_f}{2[R_0(1 - cos\phi) + lsin\phi]} + \frac{\alpha^2}{2} \quad , \tag{2.19}$$

where R_0, s_i and s_f are defined as before. Considering l equal to ca. 0.05 m, then a 5 eV photoelectron entering the analyser at α=0° will have an energy dispersion (FWHM) of 12.6×10^{-3} eV, which is identical to the value obtained with the 180° analyser.

According to Eq. 2.19, as the pass energy E_0 is scanned, the resolution at FWHM also varies. Using the aforementioned experimental parameters, a plot for this variation can be seen in Fig. 2.9, with and without considering the effect of angular dispersion.

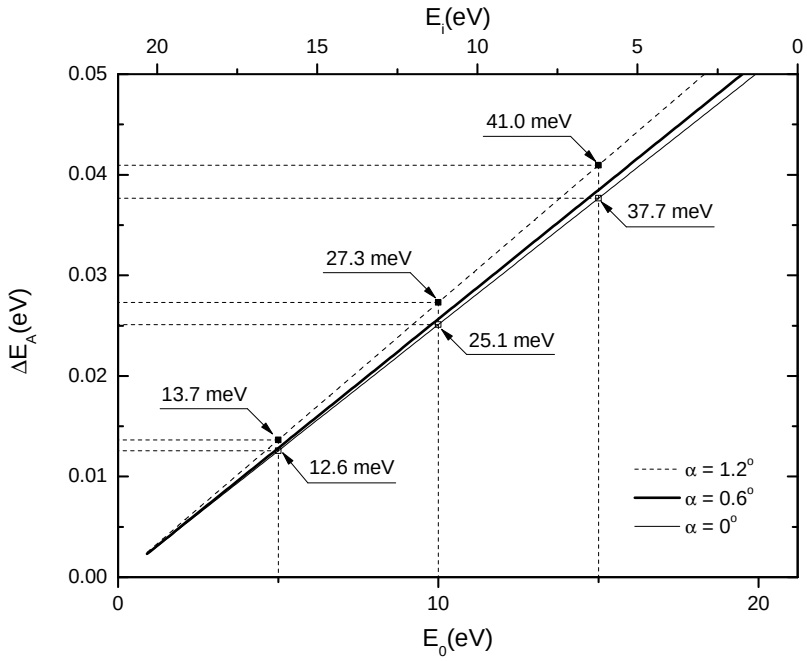

Figure 2.9: Energy dispersion of the analyser ΔE_{A} (FWHM, in eV), as a function of the pass energy E_0. Results for $\alpha = 0$ (thin), 0.6 (thick) and 1.2° (dashed) are presented.

2.1.2.4 Detector system – D

The electron detector system is based on a single channel electron multiplier (SCEM), often named by its commercial term Channeltron®. The detector is a small, curved, glass tube, with an inside wall coated with high-resistance material.

A potential applied between the ends of the tube, turns the resistive surface into a continuous dynode. Any electron entering the low-potential end of the multiplier generates secondary electrons on collision with the walls of the tube. These secondary electrons are accelerated, and strike the walls of the tube again, generating further secondary electrons. This avalanche phenomena leads to the production of a large number of electrons at the end of the tube.

The response of a SCEM to the input of one electron is a negative charge pulse, whose height is proportional to the detector gain and the electron charge, and whose width is about 10 ns. Thus, the charge of the electron is typically multiplied by 10^8, leading to a pulse height of ca. 1.6×10^{-11} C. If an incoming swarm of 10^4 electrons per second strike the detector, then the cumulative height of the negative pulse will be approximately 0.16 μA.

The electron multiplier coupled to the analyser is a Phillips device, model X914AL, with an open end and rectangular section entrance (17×5 mm, w×h). Its plane of entrance is parallel to the plane containing the analyser exit slits, 3 to 5 mm away from the latter. It is kept in place by two insulating PTFE plates, and biased through two Inconel strips driven outside vacuum using electrical feedthroughs. In order to collect the generated end cloud of electrons, a positively biased copper plate is place 2 mm next to the open end and connected outside vacuum.

For negative charged particles detection, the mouth of the detector is kept at a low positive voltage (100-200 V) and the end of the detector is kept at positive high voltage (2500-3000 kV). The collector is usually biased 200 V higher than the end of the detector, in order to increase the collection efficiency by accelerating the electron cloud.

The optimal value for the operating voltage can be found experimentally by using a fixed energy electron beam or narrow ionization line to drive the photoelectrons through the analyser and to the detector. By slowly increasing the voltage and registering the count rate values, a plateau region can be encountered, where the count rate is approximately constant. In order to extend the detector's lifetime, working at +500 V than the plateau's starting voltage is advisable.

The detector is operated in pulse-counting mode, or space charge saturation mode. In this mode, knowing the number of particles reaching the analyser is the main purpose, disregarding of their energy profile. An electronic circuit, which decouples from high voltage and converts the accumulated charge into a voltage pulse is necessary, before the signal is treated. Details of this circuitry will be given in Sec. 2.1.2.8.

2.1.2.5 Vacuum system – E

A schematics of the vacuum system is shown in Fig. 2.10. The high-vacuum pressure conditions inside the spectrometer are created and maintained through a differential pumping system i.e. two independent sets of pumps are used to evacuate two chambers – a reaction chamber (see Fig. 2.10) and an analyser chamber (C) – which are connected through a very small slit (ca. 1 mm x 15 mm). The chamber housing the detector (D) is evacuated through a bellow tube, connected to the analyser chamber. Thus, both analyser and detector operate at the same pressure.

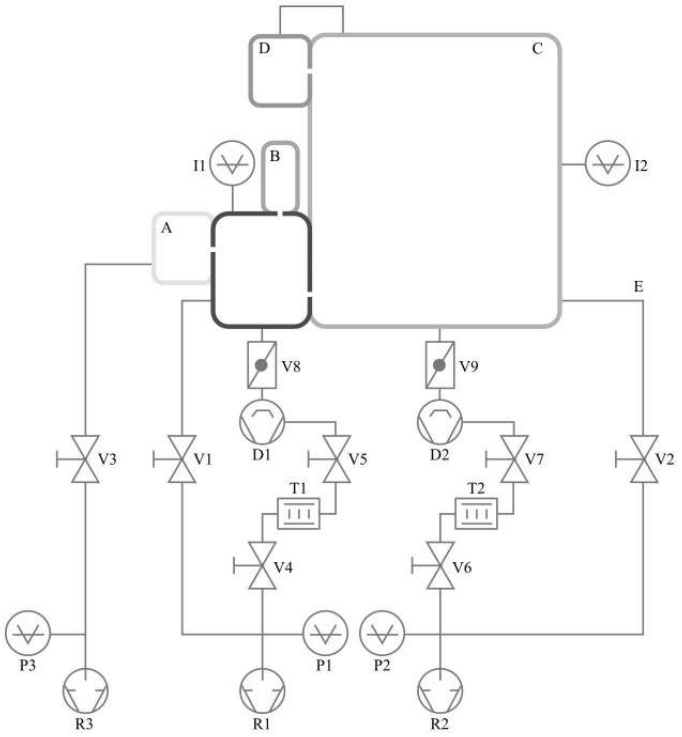

Figure 2.10: Schematics of the vacuum system used with the photoelectron spectrometer: R1, R2, R3 – rotary pumps; D1, D2 – diffusion pumps; V1,..., V9 – valves; P1, P2, P3 – Pirani gauges; I1, I2 – ion gauges; T1, T2 – absorption traps.

Two Edwards E2M28 rotary vane pumps (32.3 m^3/h), R1 and R2, are used to reach primary vacuum inside the chambers and to back the diffusion pumps D1 and D2. The latter consists of two Edwards Diffstak 160/700M oil diffusion pumps (700 l/s). Given the fact that our system is sealed mostly with Viton® O-rings, an ultimate base pressure of 4×10^{-4} Pa can be achieved in approximately 3 hours. An additional R3 rotary pump (Edwards RV12, 14.2 m^3/h) is used to evacuate the radiation source (A) to primary vacuum conditions ($\approx 5 \times 10^{-1}$ Pa).

The pressure values are read from a total of three Pirani gauges (P1, P2 and P3) and two ion gauges (I1 and I2), for values between $1\times10^{5} - 1\times10^{-1}$ and $1\times10^{-1} - 6.6\times10^{-8}$ Pa, respectively. The quality of the vacuum is very important due to the fact that a dirty system (high base pressure) can impair the sensitivity of the spectrometer. Also, a high pumping flux is necessary when dealing with very reactive species, because it lowers the residence time of those species in zones where local potentials could build-up and alter the surface contact potential, degrading the overall resolution.

2.1.2.6 Interaction region and reaction cell

The photon beam crosses the molecular beam at the interaction region, inside a stainless steel reaction cell. Only photoelectrons ejected at 90° with respect to the two beams are analysed. The distance between the centre of the interaction and the entrance of the analyser at mean radius R_0 is approximately 50 mm. If no potential is applied to the reaction cell, the photoelectron then travels this distance in a field-free region, until it meets the analyser.

The reaction cell serves the purpose of restringing the analysed gas near the interaction region, effectively increasing the local pressure by a factor of 10-100. The reaction cell becomes very advantageous in the study of low quantity species formed through *in situ* reactions (by pyrolysis, discharge,...), by increasing its concentration and, therefore, its signal intensity. The obvious drawback is that some reactive samples can deposit inside the walls of the cell, which leads to build-up of local charges which alter the resolution and signal intensity.

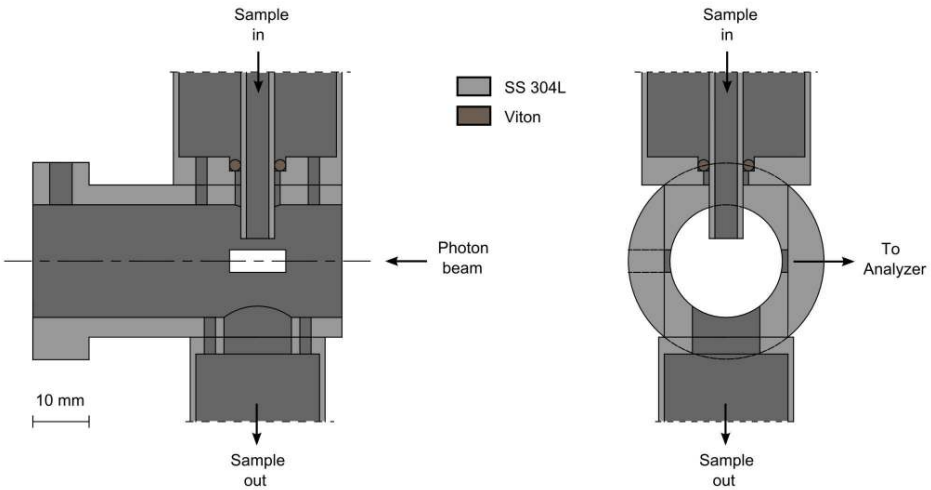

Figure 2.11: Schematic diagram of the reaction cell (front and side view), showing the (perpendicular) axis for the propagation of the photon, molecular and photoelectron beams.

An illustration of the cell design is presented in Fig. 2.11. In its standard form and mode of operation, the reaction cell follows a cross-like design, with the sample being

admitted from above and the pumping being performed from below, through a 10-15 mm exit to the ionization chamber. Aligned with the entrance of the analyser, there is also an adjustable slit, which is usually maintained opened at 1 mm.

No cooling of the cell is performed; therefore, the sample gas agitates in thermal motion, at room temperature. Hence, the kinetic energy of the photoelectron ejected from the molecule is modified. This is also a factor that contributes to the energy dispersion and decreases the overall resolution of the technique. The FWHM energy dispersion ΔE_{T} arising from the thermal motion of the sample gas[104] is given by

$$\Delta E_{\mathrm{T}} = 723 \times 10^{-6} \left(\frac{ET}{M} \right)^{1/2} \qquad [eV], \tag{2.20}$$

where E is the photoelectron kinetic energy, expressed in eV, T is the temperature of the sample and M is the mass of the analysed molecules, expressed in atomic mass units. For $M = 28$ (N_2, CO,...), $T = 300$ K, a 5 eV photoelectron will give rise to a FWHM energy spread of ca. 5.3×10^{-3} eV.

In this study we are mainly concerned with tetrazoles and azides: 5-methyltetrazole ($M = 84$), 5-aminotetrazole ($M = 85$), benzylazide ($M = 133$) and methyl 2-azidopropionate ($M = 129$). A plot which shows the variation of the thermal energy dispersion with the photoelectron kinectic energy, for $M = 84$ and 133, can be seen in Fig. 2.12.

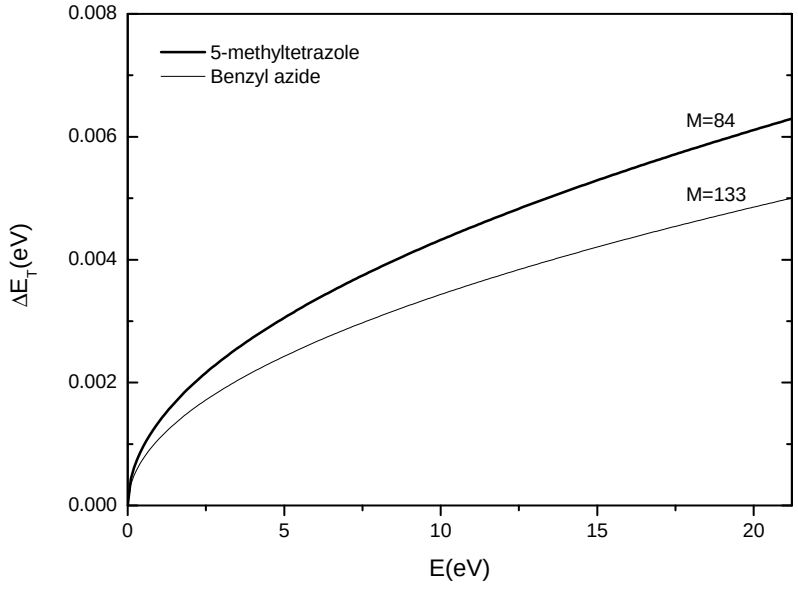

Figure 2.12: Thermal broadening as a function of photoelectron kinetic energy, due to the motion of target molecules. Curves obtained for $T = 300$ K, and M=84 (5-methyltetrazole) and 133 (benzylazide).

2.1.2.7 Magnetic field compensation

Photoelectrons travelling through the analyser experience the influence of the earth's magnetic field, as well as other transient/permanent fields in the surroundings of the apparatus (cell phones, variable transformers).

It is necessary to minimize the influence of undesirable permanent magnetic fields, in order to preserve the viability of the analyser as an effective energy filtering device. Therefore, three perpendicular pairs of Helmholtz coils are fixed around the equipment, which allow for the fine-tuning of the magnetic field inside them in three directions:

north-south, east-west and vertical (altitude). By passing current through each pair, a magnetic field in the normal direction of the coils plane is created and used to counterbalance the effect of the earth's magnetic field in that direction.

Tuning of the current values can be achieved on-the-fly by looking at the shape of known ionization peaks of rare gases (for resolution) and of oxygen (for transmission), and adjusting the values according to the best compromise between resolution and transmission. This should be done prior to any experience with the sample to be analysed.

2.1.2.8 Electronics and acquisition system

Operation and control of the vacuum system, Helmholtz coils, radiation source, and detector system are performed by several units, joined together at the same rack, in a seamless design developed by Alan Morris[99].

The power system that drives the rotary and diffusion pumps receives a signal from a bi-metal sensor, which informs the user when to open the diffusion pump valves to the chambers. In this way, only when the heating resistance from the diffusion pumps is hot enough, will the user start pumping the ionization and detection chambers, minimizing the risk of oil migration to the chamber.

The Pirani and ionization gauges are also driven by a rack unit (Edwards, ACG control/power unit) which enables the user to turn on/off the ionization gauges, and to simultaneous read the pressure from three different measurement sites. The three pairs of Helmholtz coils are powered by a constant current power supply (DC), with outputs between 0.5 and 1.2 A, adjustable by fine-tuning resistance knobs.

The radiation source is powered by a constant voltage power supply, capable of delivering 150 mA at 4000 V max. (ca. 600 W). Its circuit design revolves around a variable transformer, and a set of resistances and condensers in series (voltage ladder). When the lamp is fully operational, it draws approximately 30 W from the power supply.

The detector power supply and signal processing electronics consist in three nuclear instrumentation modules (NIM), assembled together in a power bin: a 5 kV detector bias supply (Ortec®, model 659), an amplifier/single-channel analyser (Ortec®, model 590A) and a standard ratemeter (Ortec®, model 661).

The detector high voltage decoupler and preamplifier electronics are placed outside the spectrometer, but as close as possible to the detector chamber, in order to minimize noise pick-up or bad transmittance in the cables. The corresponding schematics are given in Fig. 2.13. The high-voltage decoupler converts the accumulate charge in a negative voltage pulse, whereas the preamplifier only filters the signal (voltage follower with unity gain).

The negative voltage pulse is fed to the amplifier/single-channel analyser which inverts and amplifies the signal (gain=10-500), and discriminates between electron and noise-generated pulses through an adjustable voltage threshold value. The module 590A then generates an active TTL logic signal for each pulse between threshold values. The ratemeter can be used to give a fast indication of the number of counts.

The acquisition system was developed by Pedro Cristo[115], and is based on a National Instruments® PCI acquisition board (model NI-6601) and two 12 bit digital-to-analogue converters (DACs) from Analog Devices® (model AD7845JN). The acquisition board is driven by a LabVIEW program, termed PSAS (Photoelectron Spectroscopy Acquisition System). A block circuit for the acquisition system can best be seen in Fig. 2.14 and a screenshot of the acquisition program is shown in Fig. 2.15.

Briefly, the program instructs the acquisition board to output a binary value corresponding to a given voltage, which is converted to its analogue value (by the DACs)

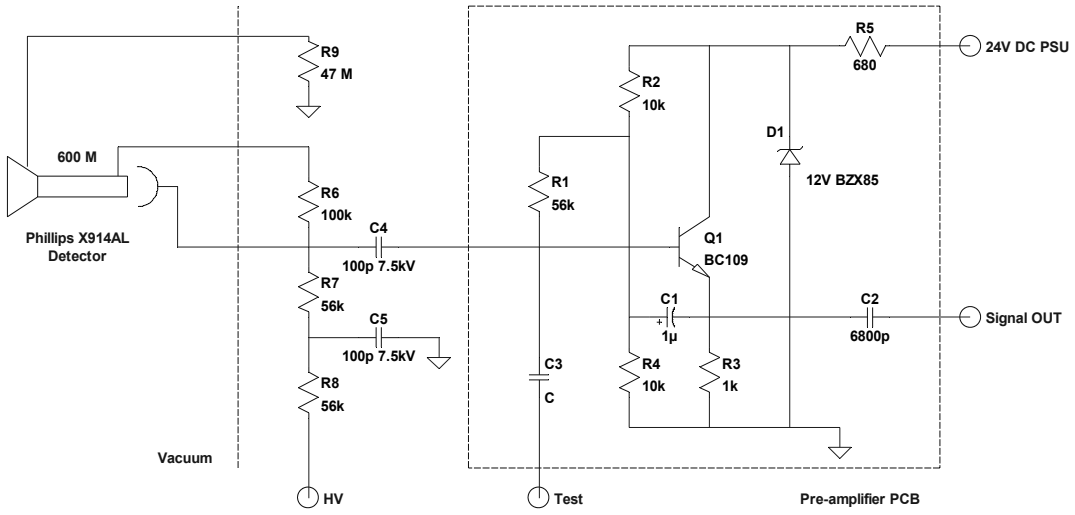

Figure 2.13: Detector high-voltage decoupler and preamplifier circuit used to convert and filter the incoming pulses from the electron detector.

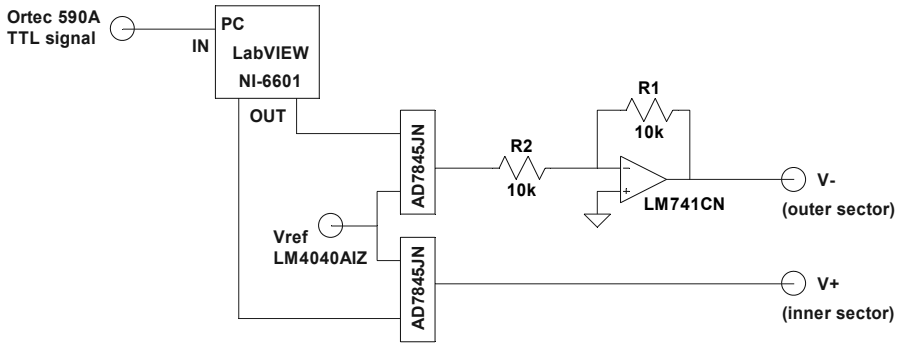

Figure 2.14: Representative electronic circuit of the acquisition system.

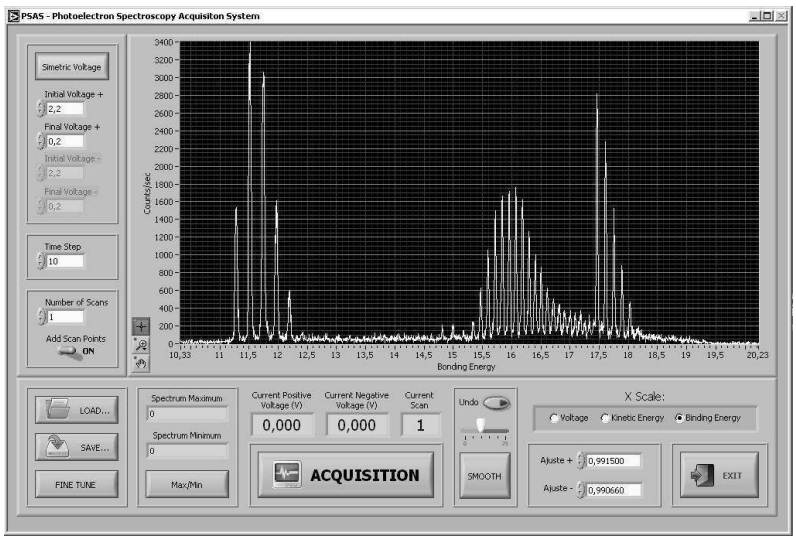

Figure 2.15: Screenshot of the *Photoelectron Spectrometer Acquisition System* (PSAS).

and applied to the sectors of the analyser. During a given period of time, set by the user, the acquisition board counts the TTL pulses coming from the Ortec 590A module, and saves the number of pulses per second. The information needed to construct the spectra comes from repeating this cycle in each step of increasing voltage ($\Delta V = 1$ mV), between a voltage range defined by the user. At the end, the program saves the spectra to disk, in comma-separated values (CSV) format.

The program empowers the user with some extra functionalities: it can sum the counts from a pre-defined number of acquisitions, it lets the user choose the acquisition time (0.01 s - 9 s) at each output voltage, it allows for the calibration of the voltage output (by multiplying it by an adjustable m factor), and it can output asymmetric voltage values. The program allows loading and analysis of the spectra, and it also possesses an adjustable smooth filter (adjacent-averaging).

2.1.2.9 Resolution and calibration

Resolution of a photoelectron spectrometer is the smallest difference between two groups of electrons that will result in separate bands in the spectrum[87].

The overall experimental contribution to the broadening of a given ionization line, arising from the analyser dispersion, intrinsic properties of the discharge and thermodynamic conditions inside the reaction cell, can be approximated by using Eqs. 2.15, 2.19, 2.20 and estimating the effect of self-absorption in the lamp.

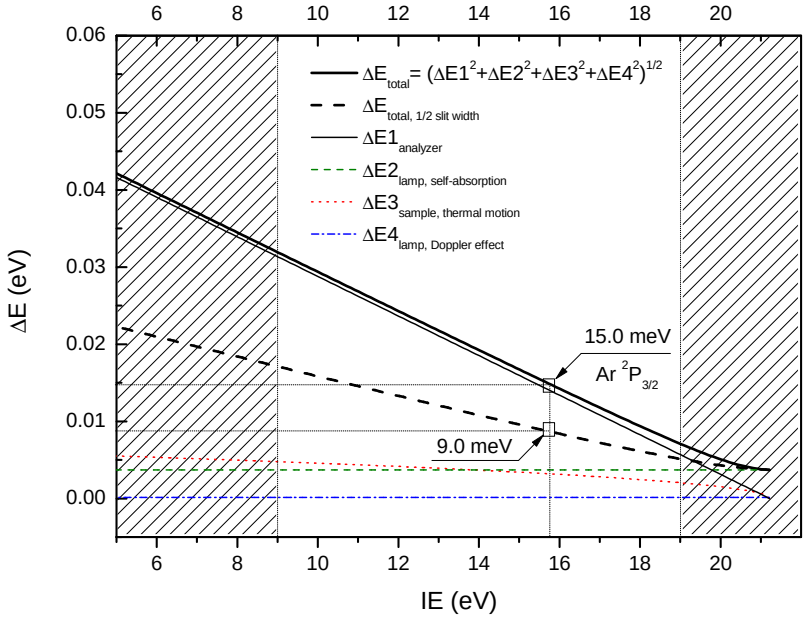

Figure 2.16: Total and partial contributions for the experimental broadening (FWHM) in a photoelectron spectrum, acquired with our spectrometer in a set of well-defined experimental conditions (see text for details). For reference purposes, the predicted experimental broadening for the Ar $^2P_{3/2}$ $(3p)^{-1}$ ionization line is presented.

The plot in Fig. 2.16 shows the experimental contribution to the total FWHM energy dispersion of a ionization line found in the photoelectron spectrum, in addition to the natural width of the state. It was constructed assuming $M = 84$, $T = 300$ K, helium as the discharge gas and self-absorption path length of ca. 50 mm, $\alpha = 0.6°$, slit widths of 1 mm, $R_0 = 200$ mm, $l = 50$ mm, and a spherical sector of 150° (see prior sections for details).

In normal working conditions with the aforementioned parameters and without serious contaminations of the reaction cell by deposited sample, one can record a photoelectron spectrum of argon and find the FWHM measured at the $^2P_{3/2}$ peak to be ca. 21 meV. This value is sufficient to distinguish between peaks arising from vibrational structure of small molecules, and is even below the rotational energy at room temperature ($k_BT \approx 24$ meV).

For high-resolution studies, both entrance and exit slit widths can be reduced to half (≈0.5 mm), effectively halving the resolution of the analyser. In that case, we can achieve a theoretical working resolution of 14 meV (see Fig. 2.16, thick dashed line).

The linearity of the analyser's voltage ΔV with respect to the pass energy E_0, expressed by Eq. 2.17, can be slightly altered during the course of the experiment, due to fluctuations in the pressure inside the analyser's chamber, and the build up of charges in the analyser's surface. Therefore, an internal standard is usually used for calibration of the energy scale.

In order to surpass this effect, *calibration* is achieved by admitting a small amount of the calibration gas into the ionization region, along with the sample gas, and simultaneous measuring the peaks of both calibrator and sample[87]. Table 2.2 collects a set of commonly used calibration lines.

Table 2.2: Common vertical ionization lines used in the internal calibration process of UV photoelectron spectra, using radiation from a He(I) source[116].

Gas	Ionic State	VIE
Ar	$^2P_{3/2}$	15.759
Ar	$^2P_{1/2}$	15.937
Xe	$^2P_{3/2}$	12.130
Xe	$^2P_{1/2}$	13.436
N_2	$^2\Sigma_g^+$	15.60
N_2	$^2\Pi_u$	16.98
N_2	$^2\Sigma_u^+$	18.78
H_2O	$^2B_1$	12.62
CH_3I	$^2E_{3/2}$	9.54
CH_3I	$^2E_{1/2}$	10.16

In principle, all gases can be used as calibrators as long as they do not interact with the sample gas, to the extent of altering permanently their electronic distribution. In practical terms, rare gases (Ar, Xe, Kr) and small molecules (N_2, O_2) exhibiting sharp ionization peaks, are the most frequently used. When performing experiments where fragmentation of the molecule is induced (like thermal decomposition studies), sharp ionization peaks of known decomposition products can also be used.

2.1.3 Gas-phase thermal decomposition studies

Apart from studying the valence electronic structure of molecules and atoms, one of the main applications of photoelectron spectroscopy is the study of chemical reactions in their most fundamental form: in gas-phase, free from the influence of the surrounding medium.

Usually, an extra equipment is added to the standard photoelectron spectrometer, depending on the type of reaction studied: crossed-beam flow tubes for the study of chemi-ionization reactions[117], supersonic expansion devices for the study of cluster formation[118,119], and microwave discharge tubes for the study of radical formation[120–122].

Alongside with the aforementioned reactions, a great deal of interest also revolves around the way gases react when heated, in the absence of oxygen (pyrolysis). Important questions immediately come to mind: will the gas molecules rearrange into more stable structures, will they isomerise, will they break apart and if so, at what temperature and in how many different fragments?

The next sections follow the technical aspects regarding the instruments needed to perform gas-phase thermal decomposition studies with the UVPES technique.

Accurate descriptions of the pyrolysis system and oven apparatus, designed and constructed to be coupled to the Lisbon photoelectron spectrometer, will be given. In addition, a more concise description of the inductively heated pyrolysis system, also coupled to a photoelectron spectrometer of similar design, located in Southampton, will be put forward.

2.1.3.1 Standard pyrolysis system

The spectrometer was already equipped with a pyrolysis system, where the sample was heated before entering the ionization region, to a maximum temperature of 700 K[123]. A furnace quartz tube was heated resistively, using a variable transformer to power a molybdenum resistance, non-inductively wound around the tube.

Although the system was fully operational, the process of mounting and cleaning was very cumbersome, due to the all glass-design and the use of vacuum grease to seal the system. Furthermore, the system which powered the resistance did not offer the required temperature stability and control over the heating process.

In order to extend the range of operational temperature and to gain full control of the heating process, a more easy-to-use system was designed and fabricated. The glass was deprecated in favour of stainless steel, copper and ceramics (boron nitride and alumina), but the resistively heating principle was maintained.

One of the design principles was the possibility of removing the sample introduction tube maintaining the pyrolysis furnace mounted, without misaligning the reaction cell. This was accomplished by fixing the furnace to the top of the reaction cell. A technical illustration of the pyrolysis furnace can be seen in Fig. 2.17.

The furnace is supported by the stainless steel heat shield that surrounds the heating zone. The heating shield has the double purpose of restringing the amount of heat transferred to the remainder of the chamber and of reflecting part of the radiation emanating from the heating resistance back to the central heating zone.

The top support has four symmetrical holes of 5 mm. From two adjacent holes, stainless steel rods drive the current to the heating resistance. These rods are insulated by alumina bushes. From one of the other holes, a type K thermocouple (TC) is inserted. The TC is protected by an alumina rod until it reaches the temperature measurement point illustrated in Fig. 2.17.

The heating resistance is made of molybdenum wire (Mo, 99% purity, 1 mm diameter), a refractory metal capable of supporting a maximum temperature of 2100 K.

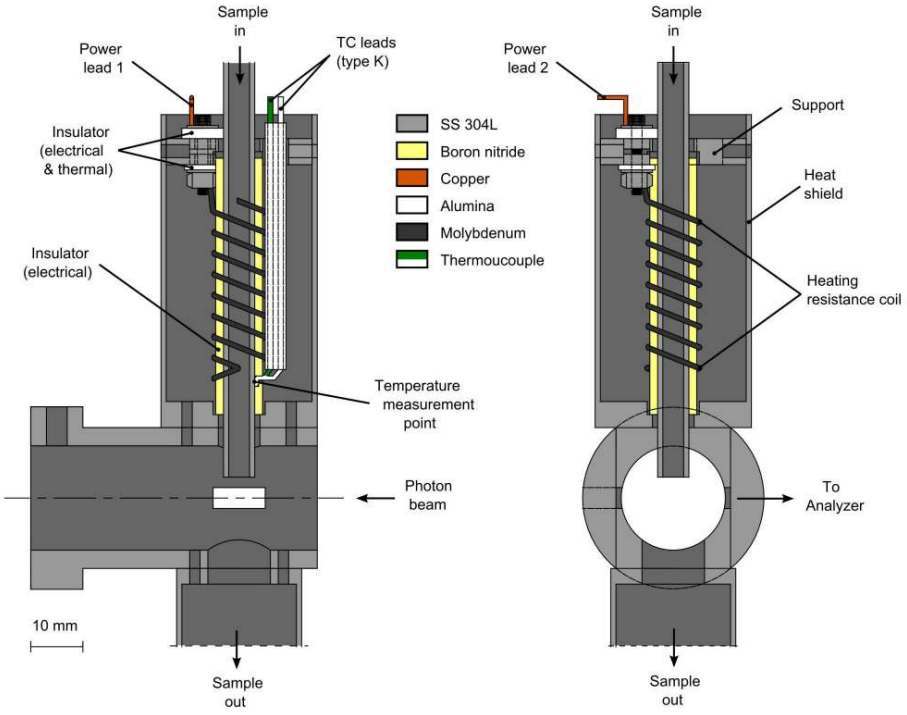

Figure 2.17: Schematic diagram of the pyrolysis furnace coupled to the reaction cell (front and side view). Some details regarding the top support were omitted for clarity.

Molybdenum has the advantage of withstanding higher temperatures than standard Inconel heating wires, but being less brittle than tantalum (Ta) or tungsten (W), after being heated.

The heating wire is non-inductively wounded around a boron nitride (BN) tube with a wall thickness of approximately 1.5 mm and an external diameter of 10 mm. Boron nitride has the advantage of being both an excellent thermal conductor and a very effective electrical insulator, with a compact crystalline structure, with a melting point of 3246 K. Hexagonal boron nitride (h-BN) possesses a thermal conductivity k of 6 $\mathrm{Wcm^{-1}K^{-1}}$ (at 300 K) and an electrical resistivity ρ of 5×10^{13} Ωcm (at 1000 K). Drilled at the lower part of the BN insulator, there is a hole to allow contact between the heated inner tube and the TC tip.

The molybdenum wire and the boron nitride tube can react, but only at a sustained temperature above 1800 K. Regarding this aspect, the materials used to insulate and heat the furnace are well adjusted for the purpose of the experiment. The type K thermocouple is also well adjusted for the experimental needs: it can read values from well below room temperature to ca. 1600 K.

The bottom part of the heat shield and the top support have recesses where the BN tube is held. The whole furnace assembly is fixed on top of the reaction cell by two M3 stainless steel screws. After mounting and alignment of the reaction cell, the stainless steel tube is ready to be inserted through the furnace.

Considering the maximum length of the heating resistance in contact with the BN tube, L=40 mm, and a mean free path higher than the furnace length, $\lambda >> L$, then for a molecule entering the hot region in a central trajectory normal to the plane of entrance, the mean residence time ($m.r.t.$) inside the heating region will be

$$m.r.t. = \frac{L}{\langle v \rangle} = \left(\frac{L^2 M \pi}{8RT} \right)^{1/2} \qquad [s], \tag{2.21}$$

where $\langle v \rangle$ is the mean speed of the molecule, and M is its molar mass (expressed in Kg mol^{-1}). At 300 K, the benzyl azide molecule (M=133) is expected to spend at least 0.18 ms in the pyrolysis zone, whereas at 1000 K, this values lowers to 0.10 ms. A plot for the MRT as a function of temperature is shown in Fig. 2.18

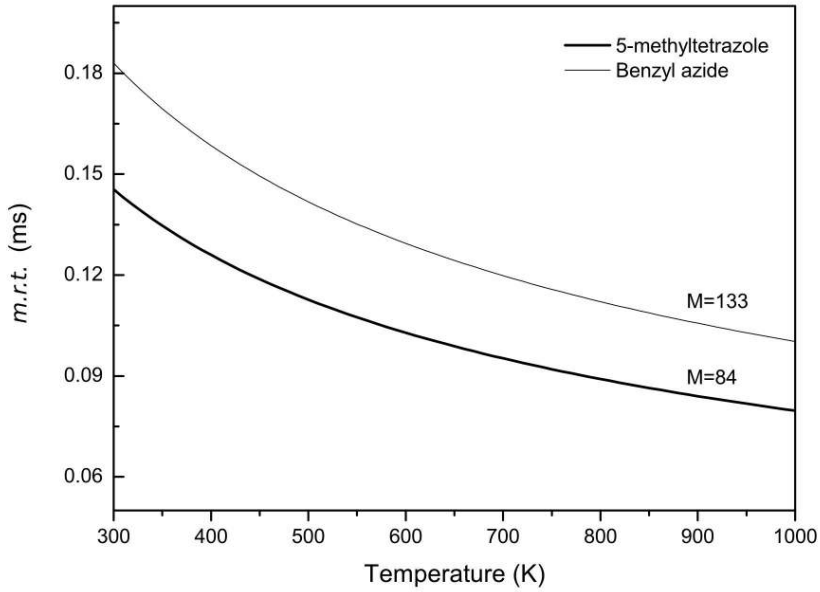

Figure 2.18: Mean residence time (*m.r.t.*) in the pyrolysis zone, as a function of temperature, for M=84 (5-methyltetrazole) and 133 (benzylazide).

After leaving the pyrolysis volume, the molecule enters the ionization region. Considering the distance between the end of the heating region and the ionization point ($l \approx 20$ mm) and a mean temperature in the non-heated region of 300 K, the MRT in the non-heated zone is approximately 0.09 ms (90 μs).

The detection limit for a transient species created in the pyrolysis process is limited by this value. In principle, if an intermediate is formed due to pyrolysis, it will only be detectable in the photoelectron spectra if it does not fragment or recombine in a 90 μs time period.

2.1.3.2 Oven for organic molecules

The motivation for the construction of the oven arose from the necessity of evaporating 5-aminotetrazole, after failing in pumping a solution directly from a glass vial.

The design and construction of the oven were based on few principles: the oven **(1)** would be resistively heated, **(2)** it would have cylindrical symmetry, **(3)** it would be fixed to the reaction cell, and **(4)** it would be made out of stainless steel, ceramics and copper only. Also, the oven would have to be able to evaporate solid organic samples with melting points up to 700 K, with no water-cooling support.

Several prototypes were machined and tested before the optimum solution was found. The seminal review by Ross and Sonntag[94] on atom beam sources was consulted during the whole design process. The final design is illustrated in Fig. 2.19.

The crucible and support form an unique piece, machined from stainless steel, grade 304L (non-magnetic). The piece is held to the bottom cylinder of the reaction cell, through M3 stainless steel screws. The support has a rectangular protrusion in its lower side, with two holes. These holes are traversed by two insulated power leads which drive the current through the heating resistance. In the base of the support,

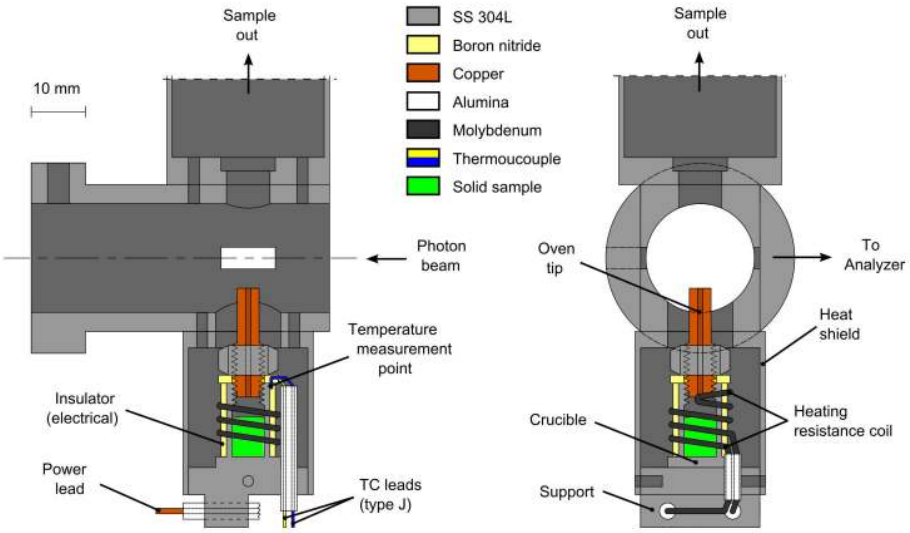

Figure 2.19: Schematic diagram of the evaporation oven coupled to the reaction cell (front and side view). Some details regarding the bottom support were omitted for clarity.

two other holes are drilled, through where bored Al_3O_2 ceramics pass. These ceramics insulate both the resistance wire and the thermocouple from the base of the support.

The heating strategy is similar to the one employed in the pyrolysis furnace, detailed in Sec. 2.1.3.1. The crucible is electrically insulated by a hollow BN cylinder. Both crucible and insulated sheath are 1 mm thick. The heating resistance is made out of molybdenum, and wound non-inductively around the BN cylinder. A small BN washer restrains the coil, in the top.

Several tips of different internal diameters (i.d. = 0.5, 1, 1.5 and 2 mm) were machined out of copper. They are screwed to the top of the crucible (M6 thread), and further fixed by a M6 stainless steel nut. The length (L = 20 mm) to diameter ratio (L/D) of the tips ranges from 40 to 10, for the one with the smallest to the largest i.d., respectively.

The possibility of using tips of different internal diameters is crucial in the study of species with diversified thermal stability characteristics. It can serve the purpose of restraining the flux of downstream gas into the ionization region, extending the lifetime of the experiment. For thermally stable species with very low ionization cross-sections, the widest tip can be used in order to increment the signal.

The end of the oven's tip is usually located 5 mm below the interaction point. However, the proximity of the tip to the photon beam axis can be adjusted by changing the insertion depth of the tip into the crucible. The length of the tip allows for collimation of the downstream vapour, effectively forming a molecular beam with confined spatial characteristics. The maximum available space for the evaporating charge is ca. 0.38 cm^3, with an open end crucible. With the copper tip positioned at the typical insertion depth, the space available is reduced to two thirds, ca. 0.25 cm^3.

2.1.3.3 Furnace/oven power supply and temperature control

Although the design of the furnace/oven is of extreme importance, the design of the power supply and temperature control system should be regarded as equally important.

Some principles of merit, regarding the way resistively heating devices should be

powered, can be considered as follows: **(1)** when possible, all resistance wires should be non-inductively wound and properly shielded; **(2)** line transmission losses (through Joule heating) should be minimized by the use of high conductivity materials to drive the current to the heating resistance; **(3)** if stray magnetic field affects adversely the experiment, AC currents should be avoided; **(4)** in order to optimize the heating procedure, some type of feedback control is advisable.

Bearing this in mind, a very simple but robust system was designed and mounted. The power system revolves around three essential components: a 500 W ATX power supply unit (PSU), a DC solid state relay (SSR) and a proportional-integral-differential (PID) controller. In addition, an extra AC SSR device and the option to use the power from a variable transformer unit was also included.

The 500 W ATX PSU is capable of delivering DC current at constant voltage. The maximum allowed current can be extracted from the 12 V rails, at 18 A. This effectively represents a maximum power of 216 W, which is more than enough to feed the heating resistance and reach the desirable temperature values. Due to the fact that an ATX unit is designed to power sensitive computer components, the clean DC output is an obvious advantage regarding other custom designed power supplies, where the output is regulated to a lesser extent. Another advantage is that ATX PSUs can be found everywhere at a relatively low cost, when compared with other dedicated PSU designed for process control applications.

The DC SSR device serves the purpose of toggling on/off the power to the heating resistance. It acts like a very responsive valve, of literally infinite working cycles due to the opto-coupling design it is based on. A small DC voltage is applied to the SSR gate, which opens or closes the line connecting the 12V output from the ATX PSU to the heating resistance. The amount of time and frequency at which the SSR switch closes the line is defined by the PID device.

The PID feedback control is assured by a CAL Controls® temperature controller, model 3300 – that reads the signal from a temperature sensor and controls the output frequency of the SSR device. The controller provides the user with a autotuning option, which derives the best PID parameters according with the thermal inertia of the system being heated. In addition, it can be connected to the RS232 serial port and controlled via computer.

The integration of the heating system power supply and temperature control can be seen in the schematics of Fig. 2.20. All the components, with the exception of the variable transformer and the computer, are mounted inside a small metal case, two times the volume of a typical ATX power supply. Venting of the components is performed by the 140 mm fan of the PSU and aided by holes drilled on top of the metal case.

A computer program was written in LABView in order to control the heating process of the furnace/oven apparatus via the PID controller. The protocol for communicating with the CAL 3300 controller is based on the ModBus protocol, which is more complex than the more frequently found NI-VISA serial protocol. The code was initially written by R. Antunes, and further refined by J. Franco and the author of this thesis.

Two versions of the program were created. In the simplest version (named *PyroControl*), the user can set the desired temperature, start/stop the heating process, and visualize the temperature behaviour over time. In the more complete version (which was not used due to some yet to be resolved programming issues), the user can also insert the PID values for a specific application in mind, among other options provided by the CAL 3300 controller (heating rate, transducer type, maximum usable power). A view of *PyroControl*'s interface can be seen in Fig. 2.21.

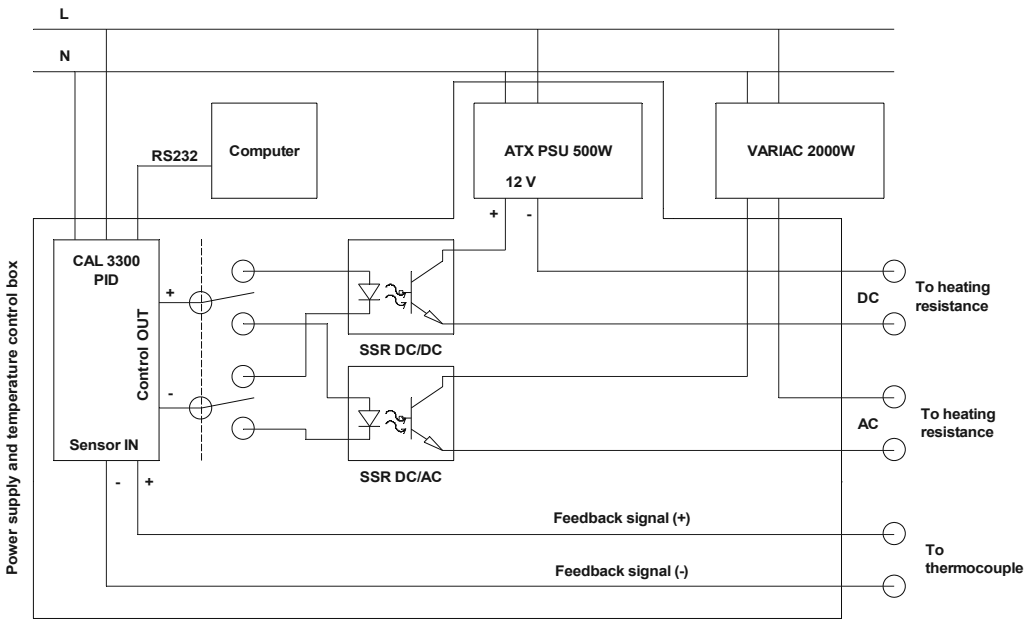

Figure 2.20: Representative electronic circuit of the heating system power supply and temperature control.

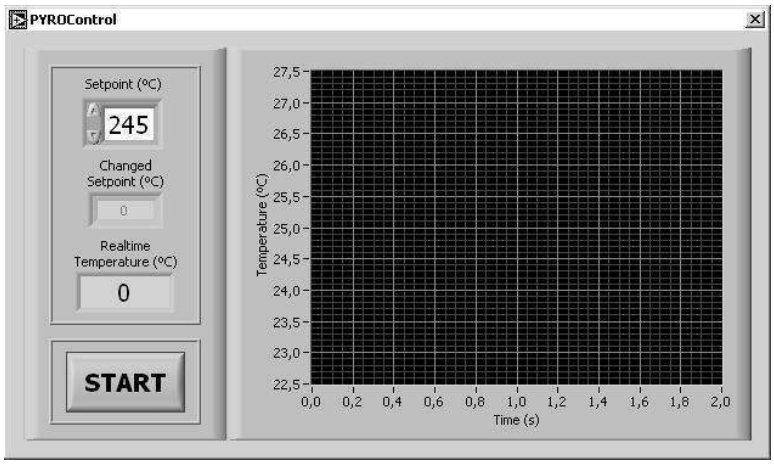

Figure 2.21: Screenshot of the *PyroControl* interface, written in LabView, running in Windows environment.

2.1.3.4 Thermal distribution: numerical simulations

In order to assess the thermal distribution upon heating in the pyrolysis and oven systems, numerical simulations using the open-source finite-element multi-physics analysis program Elmer[124] were performed.

Only energy transport through conduction was evaluated; thus, radiation heat transfer was not modelled. Convection heat transfer does not play an important role in the overall thermal distribution given the fact that the heating process takes place in vacuum. The specific properties of each material – stainless steel, Cu and BN, used in the construction of the pyrolysis furnace and oven, were used in the simulations.

Briefly, the Elmer finite-element package[124] solves the heat-conduction equation in a discretized triangular mesh (produced with the open-source program Gmsh[125]), portraying the cross-sectional area of the heating system. Boundaries between different

materials are defined by a non-zero heat flux condition and the boundaries at the axis of cylindrical symmetry are defined by a zero flux condition.

The Joule heating (heating through current dissipation) in the Mo heating resistance was not modelled, because the real system was powered in a non-linear way; instead, the outside boundary of the BN sheath was defined by a Dirichlet condition of constant temperature. For each system, the outside wall of the insulator sheath was fixed at the approximate maximum working temperature: ca. 1000 and 773 K for the pyrolysis and oven systems, respectively. The triangular meshes used and the simulations at T_{heat} = 1000 and 773 K can be seen in Figs. 2.22 and 2.23, respectively.

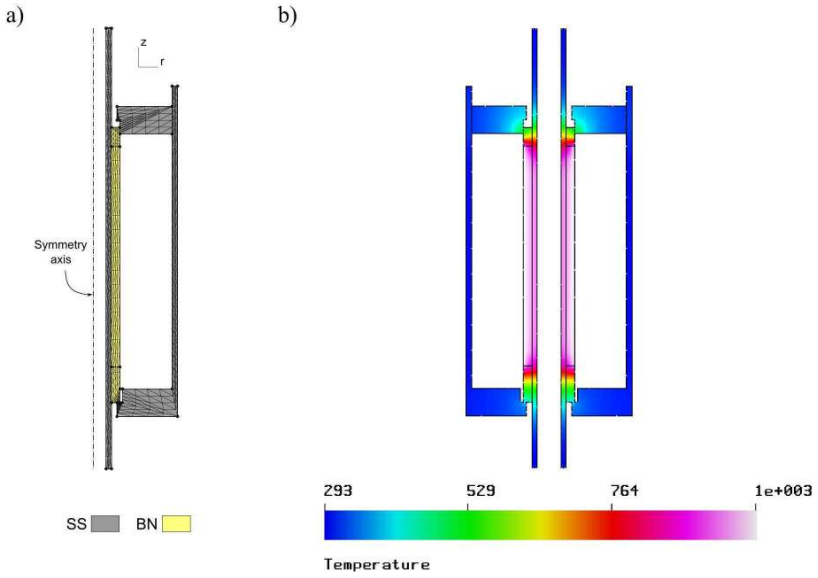

Figure 2.22: Triangular mesh created with the Gmsh program (a) and simulated thermal distribution of the pyrolysis system at 1000 K heating temperature (b).

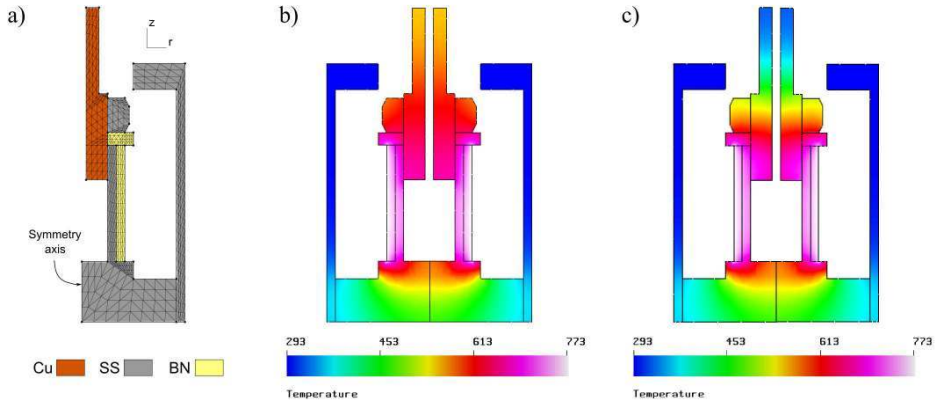

Figure 2.23: Triangular mesh created with the Gmsh program (a) and oven's simulated thermal distribution at 773 K heating temperature, with copper (b) and stainless steel (c) tips.

Its clear that using a stainless steel tip can lead to clogging of the oven's orifice over timer, due to condensation of the gaseous sample in the colder region of the nozzle. The use of a copper tip minimizes the risk of clogging, in virtue of its higher thermal conductivity.

2.1.3.5 High-temperature pyrolysis system

The studies on the pyrolysis of benzylazide and 2-, 3-, and 4-methyl-benzylazide were performed in the PES group, School of Chemistry of the University of Southampton, under the supervision of John Dyke, with the precious collaboration of Grant Copeland.

The necessity of performing the experience abroad was due to the experimental limitations of our resistively heated pyrolysis system: although its redesign effectively increased the maximum working temperature to ca. 1000 K, higher temperatures were needed to reach benzylazides' complete pyrolysis. The PES group in Southampton, working for many years in the subject of photoelectron spectroscopy of transient species and high temperature vapours, provided the means to accomplish this task.

When aiming at high temperatures ($\geq$1500-2800 K), heating with a resistance stands as an herculean task, due to the high thermal losses in conductivity and radiation. Therefore, a number of schemes have been developed to surpass the difficulties in achieving sufficient vapour from very compact solid samples[94] or complete pyrolysis of some gases. Among them, induction heating using a high-power radio-frequency (RF) source prevails as the only method capable of generating temperatures in excess of 2500 K, only limited by the intrinsic thermal characteristics of the crucible materials.

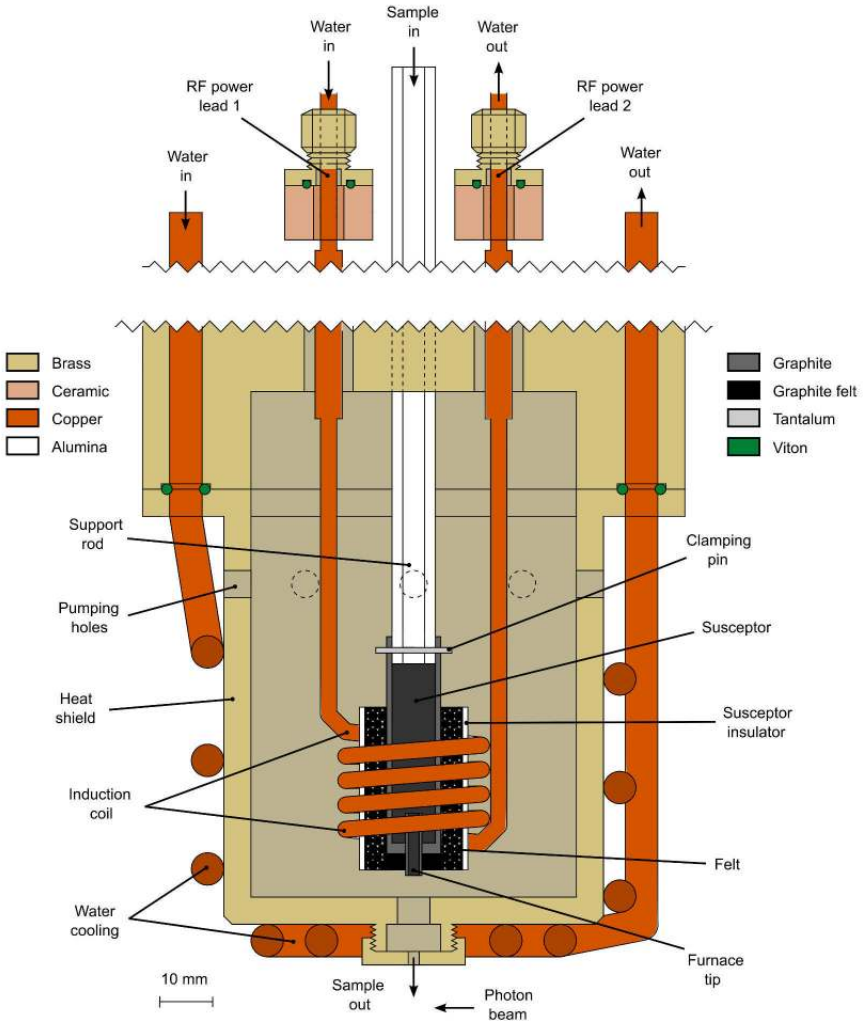

Figure 2.24: Schematic diagram of the inductively heated pyrolysis system, used in Southampton's photoelectron spectrometer.

The high-temperature furnace is mounted in a UV photoelectron spectrometer similar to the one located Lisbon, whose description was given in previous chapters. However, some differences are worth noticing: **(1)** the main body of the reaction cell is smaller but with wider entrance and exit holes; **(2)** calibrators are injected opposite to the propagation vector of the photon beam; **(3)** scanning of the analyser voltages is performed incrementally by an analogical voltage ramp generator, and a computer program records the spectra. All the pressure values, both in the lamp and interaction and analyser/detector chambers, are similar to the ones reported for the Lisbon spectrometer.

Details regarding the design and construction of the high-temperature heating furnace can be found in Refs.[126,127]. Only concise information will be given here.

The high-temperature induction heating furnace is fixed to the top flange of the ionization chamber, above the interaction region. It consists in an induction copper coil (40 mm long, 25 mm wide, 5/6 turns, tube o.d. = 3 mm) wound around an alumina insulated graphite susceptor. The hollow coil is water-cooled from inside and carbon felt is used between the alumina cylinder sheath and the graphite crucible. The crucible is held by a tantalum pin to a long alumina tube which extends outside vacuum and from where the sample gas is admitted. The whole assembly is surrounded by a brass heat shield, brazed to water-cooled copper tubing. At the base of this heat shield, beneath the susceptor, there is an adjustable circular aperture, which serves the purpose of further collimating the gas beam. The escaping hole for the sample gas is located approximately 5 mm above the photon beam axis, in front of the analyser entrance. Fig. 2.24 grossly illustrates the whole furnace assembly.

The RF power supply operates at a frequency of 1 MHz and has a maximum output power of 3 kW. The interference effect of the RF pulse is avoided by gating the RF pulse and acquiring the spectra during the off-time window. The gatting frequency is settle at 50 Hz by a gating box, which cuts the detector signal during the on-time of the RF power supply.

Temperature calibration is first achieved by using a type K thermoucouple (for $T \leq 1600$ K), placed inside the susceptor, and then by using a optical pyrometer ($T \geq 1600$ K), pointed from outside the spectrometer directly into the furnace. The curve of temperature as a function of the applied voltage is used for assessing the real temperature value in all subsequent experiments.

2.2 X-ray photoelectron spectroscopy

In the same period as Turner invested in his early experiments with the UVPES technique, Kai Siegbahn's group, from Uppsala's University, Sweden, developed the electron spectroscopy for chemical analysis (ESCA), which is nowadays known as X-ray photoelectron spectroscopy or XPS.

In 1969, one year before Turner's book regarding UV photoelectron spectroscopy came out, Siegbahn and co-workers published the book *ESCA Applied to Free Molecules*[128] in which the application of XPS to the chemical study of atomic and molecular species in gas-phase was described. This monograph extended the range of applicability of the ESCA technique, which was first considered in 1967 for the purpose of studying atoms and molecules in solid samples[129].

The use of ionizing radiation of higher energy allows the probing of the core molecular electronic levels, which usually do not coalesce with neighbouring orbitals and therefore are non-bonding orbitals in nature. Among several factors, the energy of the ejected photoelectron depends on which atoms are on the vicinity of the ejecting atom i.e. the energy of an X-ray photoelectron is correlated with the electrostatic field created by the surrounding atomic species. This allows for chemical determination of the molecular structure of the sample, and is viewed as one of the main advantages of the the XPS technique.

A complete description of the molecular electronic states of a given gas can be extracted using both UVPES and XPS techniques, by probing the outer-valence (4-20 eV), the inner-valence (20-100 ev) and the core-level electronic states (100-1500 eV). In a lab scale environment, 1487 and 1254 eV X-rays are usually produced via high-energy electron bombardment of Al or Mg targets, respectively. Nowadays, however, the use of synchrotron radiation from the UV to the soft X-ray range (50-1500 eV), readily available in specialized facilities, eases the process of determining all the molecular electronic states available from a given sample in just one experimental run.

In the next sections, a brief description of the XPS technique will be given when applied to the study of gas-phase samples. Furthermore, characteristics and advantages of the use of synchrotron radiation as radiation source in XPS analysis will also be exploited.

2.2.1 Principles

The same physical process underlying photoelectron spectroscopy with ionizing UV radiation assists the photoelectron spectroscopy with X-ray photons. Moreover, Eq. 2.1 also applies to XPS.

However, in most XPS textbooks (specially those concerned with surface science), an additional term[128,130] is added to the general expression of Eq. 2.1:

$$h\nu = BE_i + T_e + T_{ion} + \phi \tag{2.22}$$

where $h\nu$ is the X-ray photon energy, BE_i is the binding (ionization) energy of an electron in core-orbital i, T_e is the photoelectron kinetic energy, and T_{ion} is the recoil energy of the ion created upon ionization (which can be neglected). The constant ϕ is the spectrometer *work function*, a correction term related to space and surface charges and contact potentials. It assumes different values for different gases and it also depends on the gas pressure[128].

As with UV photoelectron spectroscopy, a spectrum can be constructed by irradiating a sample with X-ray photons of constant energy and recording the photoelectron current as a function of the photoelectron's kinetic energy T_e.

2.2.1.1 Decay of core-holes: Auger effect and X-ray fluorescence

The process of direct photoionisation is also on the basis of photoelectron spectroscopy with X-ray photons. In fact, the physical meaning underlying Eq. 2.2 also holds true for XPS: a neutral atomic or molecular species interacts with a photon of sufficient energy to take the core-electron beyond its ionization limit. A vacant orbital seat for an electron is thus created, often called *core-hole*.

The hole is promptly occupied by an electron of a sub-shell of lower binding energy, in a process which has the effect of lowering the overall energy of the system. What the system does with the excess energy defines the physical process taking place after the ejection of the core photoelectron.

If accompanying the electron decay to the core-hole state an X-ray photon is emitted, then we witness the radiative process of *X-ray fluorescence*:

$$M^{*+} \rightarrow M^{+} + h\nu \qquad . \tag{2.23}$$

Here, the superscript asterisk "*" marks the availability of excess energy and not necessarily a specific excited state of the core-hole cation.

On the other hand, if the system deals with the excess energy by transferring it to an outer-shell electron, causing it to be ejected, and leaving a double ionized species behind, then we are on the presence of a non-radiative process termed *Auger effect*.

$$M^{*+} \rightarrow M^{2+} + e^{-} \qquad . \tag{2.24}$$

The Auger effect portrays some similarity with the *autoionization* process described in Sec. 2.1.1.1. In fact, in both processes the molecular system acts upon the excess energy by imparting an electron with additional kinetic energy which takes it beyond its ionization limit.

The processes expressed by Eqs. 2.23 and 2.24 are on the basis of two complementary techniques to XPS, namely X-ray emission spectroscopy (XES) and Auger electron spectroscopy (AES). Auger structure can sometimes be found within XPS spectra, in the form of less prominent Auger electron signals. Usually, the experimentalist has to be sure where to look for them, before taking the Auger effect into account in the assignment of XPS spectra i.e. in order to assign Auger peaks in a XPS spectrum, the experimentalist needs to make sure a priori that a given Auger process is likely to occur at a specific binding energy, usually on the basis of theoretical calculations.

2.2.1.2 Chemical shifts

The core-electron binding energies vary measurably with change of the chemical environment, as noted for the first time by Siegbahn[129], in a routine study of sodium thiosulphate. This variation with chemical environment is called *chemical shift* and its mainly due to direct electrostatic interaction.

A relation between chemical binding energies in a molecule and the observed chemical shifts in XPS can be explained assuming a pure ionic bonding in a diatomic molecule[128].

Consider first two atoms, A and B, where no chemical bond is established. Now consider that an electron is taken from atom A and transferred to atom B, forming a pair of ions, A^+ and B^-. With this operation and according to classical electrostatic theory, the ionization energy of the core-electrons for species A^+ and B^- changes by $1/r_A$ and -$1/r_B$, respectively, where r_A and r_B are the valence shell radii of atoms A and B. The energy required to form the pair A^+B^- is just the difference between the ionization energy of atom A and the electron affinity of atom B i.e. IE_A-EA_B. The

ions attract each other on the basis of pure electrostatic forces, approaching to form the diatomic molecule at the equilibrium internuclear distance R.

The energy associated with the chemical bond is the sum of the terms mentioned above, plus a repulsive term E_{rep} related to the overlap of the ionic wave functions,

$$\Delta E_{\text{bond}} = -(IE_A - EA_B) + 1/R - E_{rep} \quad . \tag{2.25}$$

In this expression, the energy required to form the ion pair is subtracted from the initial available energy (hence, the minus sign).

The core electrons of the cation A^+ experience the repulsion from the negative charge on B, which corresponds to a change in potential energy of $1/R$ for the core electrons in A^+. The electrons in B^- feel an attractive force from A^+ of the same order of magnitude. In effect, the chemical shift for the binding energies of the core electrons in atom A is evaluated as

$$\Delta E_{\text{core,A}} = 1/r_A - 1/R \quad , \tag{2.26}$$

and the shift for the binding energies of the core electrons in atom B is $-(1/r_B - 1/R)$. From a gross point-of-view, each core electron in a neutral molecule screens off the valence electron by one positive charge in the nucleus.

The natural chemical binding picture and its relation to the chemical shifts is somewhat lost when the balance between electron-electron repulsion and electron-nucleus attraction is heavily disturbed upon removal of a core-electron. The core vacancy usually leads to the rearrangement of the molecular electronic distribution, in particular valence electrons tend to reorganize and lower the overall energy of the system. The correct estimation of the core-electron binding energies and the preservation of the quantum mechanical rigour in the description of the one-electron picture of ionization can only be achieved by *ab initio* calculations, which allow for orbital relaxation and electron correlation. This subject will be analysed to greater detail in Chapter 3.

2.2.2 Experimental details

The XPS studies presented in this work were all performed in the Gas Phase beamline of Elettra, the synchrotron facility in Trieste, Italy. A multitechnique spectrometer is permanently coupled to the main branch of the beamline, sharing its beamtime with other equipments from different research teams.

The spectrometer is capable of performing UVPES, XPS, AES and near-edge X-ray absorption fine structure (NEXAFS) analysis on gas samples. Solid samples can be easily evaporated and analysed using a homemade resistively heated oven. The schematic disposition of the main components of the XPS spectrometer, which also follows the general layout in Fig. 2.1, is shown in Fig. 2.25.

In the following sections, some information covering the main components of the Gas-Phase spectrometer will be given, with special emphasis to the radiation source – the Elettra synchrotron ring, and the XPS and UVPES part of the apparatus.

2.2.2.1 Synchrotron radiation source – A

The main advantage of using the spectrometer at the Gas Phase station is, as one would expect, the possibility of using a high-quality, low-dispersion and high-power radiation source – the synchrotron light (see Fig. 2.26).

Several textbooks cover the main aspects of synchrotron facilities, and applications and properties of synchrotron radiation. The books from Margaritondo[131] and from Wiedemann[132] can be consulted if one seeks a more introductory textbook or a more

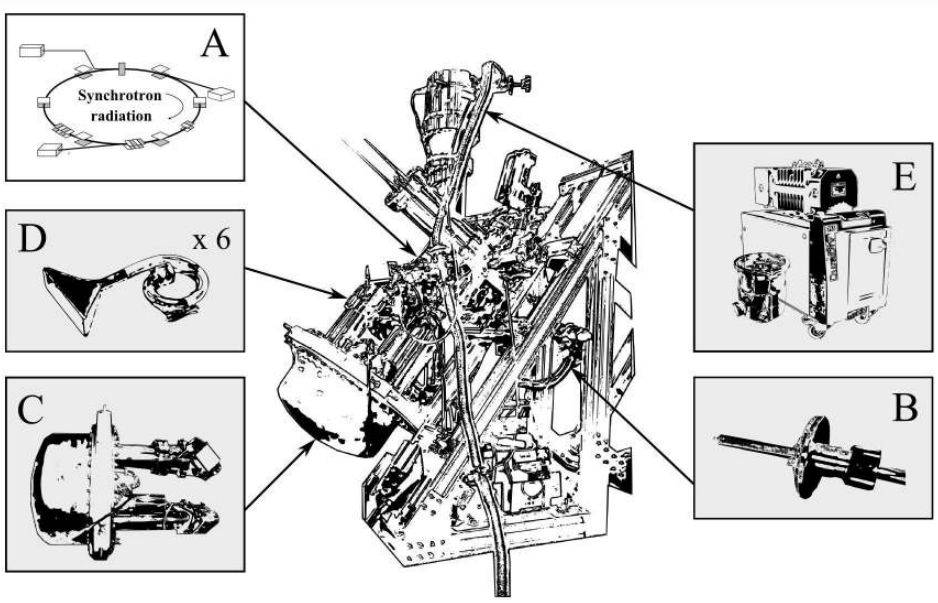

Figure 2.25: Illustration of the main components of the XPS spectrometer, located in the Gas Phase beamline, Elettra. A - synchrotron light, B - sample introduction system, C - energy analyser and lens system, D - electron detector, and E - vacuum system.

detailed theoretical analysis of the physical phenomena underlying the generation of synchrotron radiation, respectively. Only a concise description regarding this subject will be given below.

Huge facilities are used to generate the powerful synchrotron light. A closed-loop tube called *storage ring*, where electrons circulate, is maintained at ultra-high vacuum (UHV) conditions. From time to time, new electrons are injected in the storage ring, being previously accelerated by a linear accelerator apparatus (LINAC).

Inside the storage ring, the electrons are forced to have its trajectories bent by powerful magnets called *bending magnets* (BM), and perform a circular movement at high speed for hours. When forced to bend its linear trajectory, the electrons travelling in the ring will emit radiation covering a wide range of wavelengths ($1 - 10^{-5}$ Å) of the electromagnetic spectrum; this is the radiation called *synchrotron radiation*.

Following each bending magnet, straight tubes destined to collect and channel the synchrotron radiation to the several experimental stations (ES) are placed tangentially to the circulating ring – these are called *beamlines* (BL).

The bending magnets are not the only devices used to change the velocity direction of the electrons, thus leading to the emission of radiation. *Undulators* and *wigglers* are also used for this purpose. The former is a periodic array of magnets which induces small undulations in the electron's trajectory, transversal to the linear direction of propagation. The high-frequency of the transversal oscillation motion leads to the emission of electromagnetic waves of very low wavelengths, with the electron behaving like an oscillating charge, just like in a emitting antenna. Wigglers are physically similar to undulators – a series of magnets in a straight line, affecting the electrons' trajectory – but work with magnetic fields of higher intensity.

A photon detector placed in front of the emitting beam after the effect of a bending magnet, an undulator or a wiggler would output the signals (a), (b) and (c), respectively, presented in Fig. 2.27.

In the case of Elettra's Gas Phase BL, an undulator feeds the line with light ranging

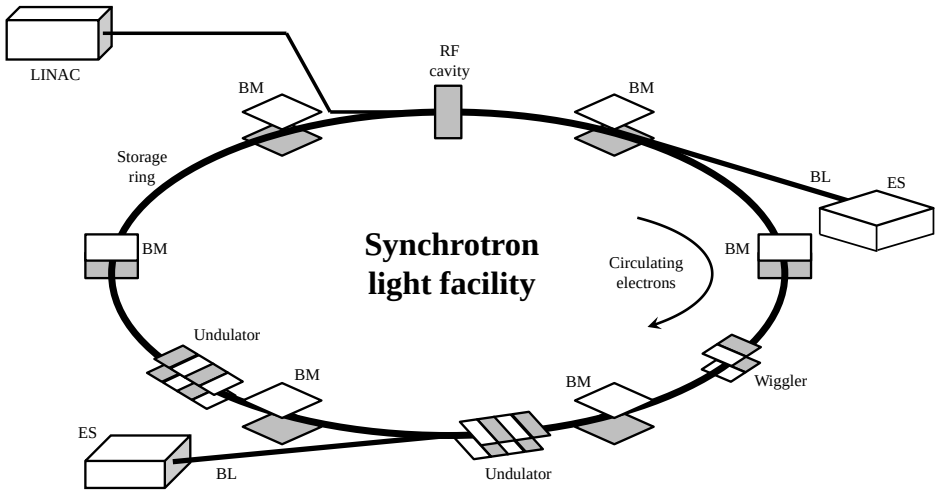

Figure 2.26: The overall structure of a synchrotron facility. BM - bending magnets; LINAC - linear accelerator; BL - beamline; ES - experimental station.

from 14 to 1000 eV, which follows a pattern similar to the one shown in Fig. 2.27 (b).

As the emitted waves are produced at each change of velocity direction, the electrons lose energy. Therefore, some mechanism has to be used to restore the energy to pre-emission values. This is accomplished by devices called *radiofrequency cavities*. The RF device impinges a burst of energy in each retarded electron passing through the cavity, and acts as a pass-by filter for electrons which did not lose any energy. The pulsed actuation of the cavity (ON for retarded electrons and OFF for lossless electrons) leads to the agglomeration of electrons in separated bunches. Thus, the synchrotron source runs effectively in pulsed mode during operation time.

Another important characteristic of synchrotron's light is *polarization* i.e. light's oscillating motion with respect to its direction of propagation. In plane waves, the latter follows the same direction as the so-called Poynting vector S ($= \mathrm{E} \times \mathrm{H}$) which defines the direction of the electromagnetic flux. Polarization occurs when the oscillating electromagnetic features of the propagating wave (the electric and magnetic vectors) assume a fixed direction with respect to the wave motion.

In the case of most UV radiation lab sources, such as the one described in Sec. 2.1.2.1, the light does not go through any polarization filter after being produced. Thus, the light employed in the ionization of gas samples is non-polarized i.e. no preferential direction for the photon's transverse motion exists.

On the other hand, polarization of light produced in the storage ring depends on the specific features of the magnetic devices employed to induce radiation emission (bending magnets, undulators) and the relative position of the detection elements or the interaction region. The light used in the Gas Phase beamline is *linearly polarized*, as is the radiation used in the XPS studies presented in this work.

Given the wide range of photon energies produced in synchrotron sources, further limitation of the radiation wavelength around a narrow energy band or controlled scanning of the wavelength necessary. Therefore, filtering devices known as *monochromators* eliminate light of undesired wavelength prior its entrance into the interaction region. As X-rays pass through the majority of solid materials, most monochromators used in synchrotron facilities are of the reflection type, as opposed to the transmission type monochromators used for visible light (which employ crystals). The former are based in the constructive/destructive overlap of reflected waves by means of *diffraction gratings*

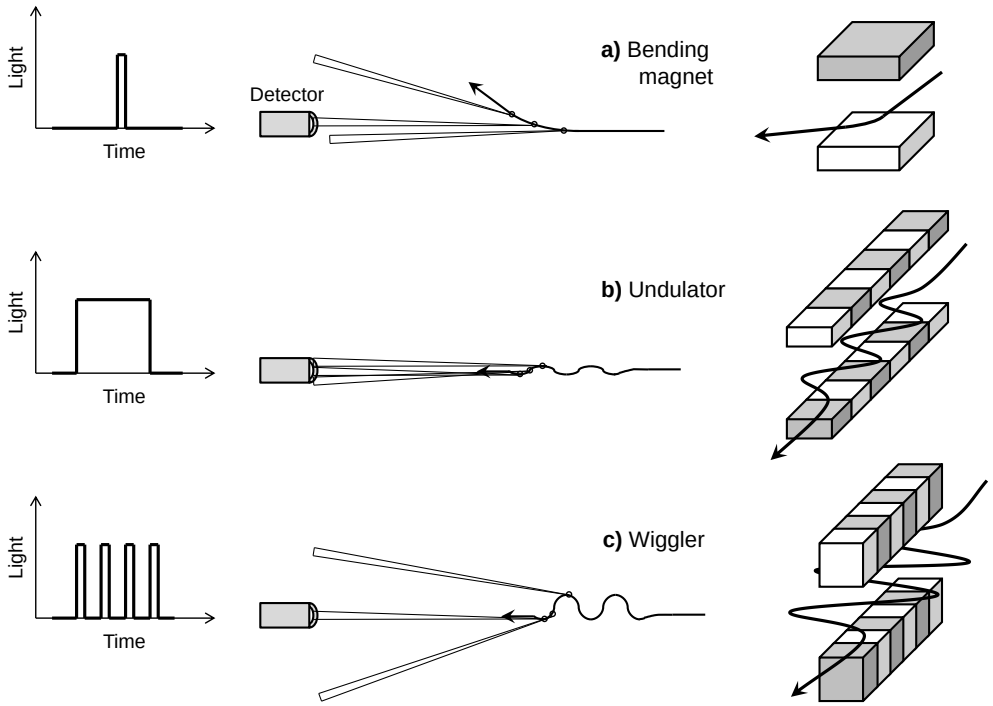

Figure 2.27: Light intensity over time, radiating from an electron passing through three different insertion devices: a bending magnet (a), an undulator (b) and a wiggler (c).

of adjustable spacing between grating lines[133].

Fig. 2.28 shows the optical layout of the Gas-Phase beamline, at Elettra. The monochromator consists of a plane mirror and five spherical gratings, being configured as a variable angle spherical grating monochromator or VASGM. Geometrical parameters of the five spherical gratings are given in Table 2.3, and flux and resolution figures at different photon energies and 10 μm entrance slit are presented in Table 2.4. Information regarding the Gas-Phase beamline and properties of the light fed to the experimental chambers can be found in more detail elsewhere[134,135].

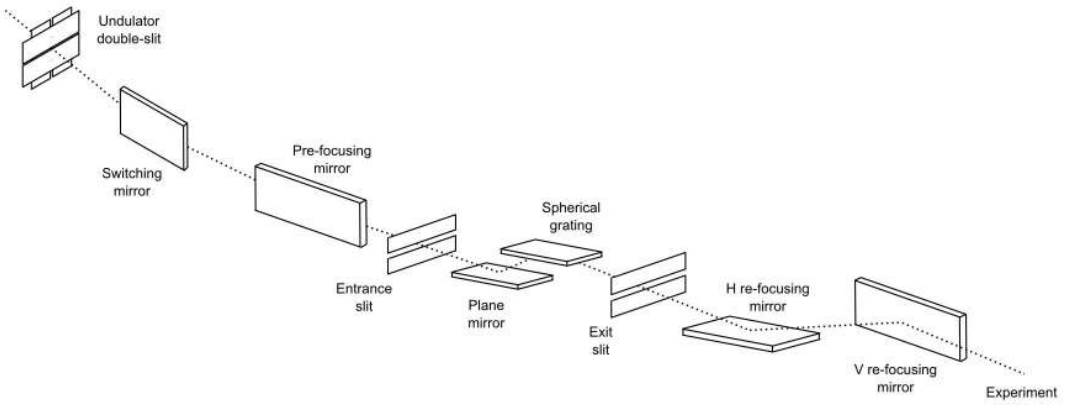

Figure 2.28: Schematic illustration of the optical devices installed in the Gas-Phase beamline, at Elettra.

Table 2.3: Geometrical parameters of the five spherical gratings of the Gas-Phase beamline, at Elettra.

Grating no.	Line spacing mm	Spherical radius cm	Energy range eV
1 (1^{st} order)	400	1700	14-50
1 (2^{nd} order)	400	1700	40-90
3	1200	1700	8-180
4	1200	3200	160-430
5	1200	4600	360-1200
6	140	1700	1420

Table 2.4: Flux and resolving power at different photon energies

Energy eV	Resolving power	Flux photons/s @100 mA
45	>25000	6.3×10^{10}
65	>28000	2.2×10^{11}
86	>10000	1.5×10^{11}
245	12200	1.5×10^{10}
401	>12000	1.1×10^{10}
540	10000	2.0×10^{10}
680	10000	3.0×10^{9}

2.2.2.2 Oven for solid samples – B

A resistively heated oven is used to evaporate the solid samples into the ionization region. A cylindrical crucible made of stainless steel and approximately 100 mm long is non-inductively wound by a Thermocoax® heating element, and placed below the beam of ionizing radiation. The oven is placed inside a stainless steel vessel acting as heat shield, and is held in place by a spring system. The whole assembly is mounted on top of a flange coupled with a X-Y manipulator, which allows for on-the-fly adjustment of the directionality of the evaporating beam.

Several end-caps are available, with holes of different diameters, aimed to adjust and control the escaping rate of samples of different vapour pressures and thermal stability characteristics. A type K thermoucouple, placed in direct contact with the crucible, provides temperature readings from the system.

The heating system is powered by a DC power supply and is capable of achieving a maximum temperature of ca. 900 K at 1 A. There is no feedback control of the heating system, although the temperatures appear to remain stable to at least one decimal figure (±0.1 K), during the whole course of the experiments (one-two days per sample).

Trapping of the evaporating charge after passing through the ionization region is accomplished by condensation of the sample vapour on a surface parallel to the exit plane of the oven, placed after the reaction chamber. This surface is part of a aluminium vessel which can be either filled with liquid nitrogen or cooled with compressed air.

2.2.2.3 Energy analyser and lens system – C

The photoelectron energy analysis is performed by a 150 mm mean radius hemispherical electrostatic analyser, coupled to a four-element electrostatic lens system of cylindrical symmetry. The analyser is a slightly modified version of part of a commercial electron spectrometer, the ESCALab 220i-XL from VG, capable of working in fixed analyser transmission (FAT) mode.

In the FAT mode, the user sets a constant pass energy for the analyser (see Section 2.1.2.3), and the process of energy selection is transferred to the lens system. The voltage of the last electrode of the lens is varied in order to accelerate/decelerate the electrons to the correct pass energy, whereas the voltages of the third and second electrodes are adjusted to maintain the physical characteristics (angular and spatial dispersion) of the photoelectron beam constant, prior its entrance in the analyser. The first lens element is usually maintained at ground potential, with respect to the reaction cell.

As stated before, the analyser transmission is dependent on the analyser's pass energy and the dispersion of the analysed beam. Hence, working in the FAT mode ensures a constant transmission throughout a wide range of photoelectron energies. This brings up the obvious advantage of allowing for direct comparison of the heights and areas of peaks at different energies (which are proportional to the photoionisation cross-sections).

Another advantage of the analyser system is that it is insensitive to the β asymmetry parameter of photoionisation. The system evident rotation portrayed in Fig. 2.25 is not by chance. In fact, the electron analyser is mounted with its axis at a forward scattering angle of 54.7° with respect to the electric vector of the linearly polarized light, and in the same plane as the beam propagation direction. This value is known as the (pseudo) magic angle, because if inserted in the expression for the angular dependence of the photoionisation intensity (for polarized light) of an ejected electron,

$$I(\theta) \propto \frac{\sigma}{4\pi}\left[1+\frac{3\beta}{2}\left(cos^2\theta-\frac{1}{3}\right)\right] \quad , \tag{2.27}$$

it eliminates the need of knowing a priori the value for the β term. The photoionisation peaks appearing in a spectrum based on the signal from photoelectrons collected at this angle can be directly compared, in terms of its relative areas and heights. Relative cross-sections can then be extracted directly from the results.

2.2.2.4 Detector system – D

Six-channel electron multipliers are used in conjunction as detectors. The detectors are placed in such a way that the solid angle for collection is maximized. The symmetric way in which they are held around the analyser's exit, ensures that no preferential angular collection is maintained; therefore, the signal from the six detectors can be summed over to generate higher counts.

These electron multipliers are also configured in pulse-counting mode and polarized at positive high-voltage (ca. 2250 V), similarly to what was already described in Sec. 2.1.2.8.

2.2.2.5 Vacuum system – E

Several differential pumping schemes make up the vacuum environment supporting the main photoelectron spectrometer of the Gas-Phase beamline. The reason for this is to maintain each part of the spectrometer properly isolated (in terms of their local vacuum conditions) from each other and from the beamline insertion point at the storage ring. The pressure inside the ring has to be maintained at UHV conditions at all time i.e. at pressure values below 10^{-7} Pa. Therefore, even if the experiments are to be run in the high vacuum region (10^{-3}–10^{-6} Pa), increased pumping of the interface zone between the interaction region and the photon beam entrance has to be performed.

In addition, all pumps are oil-free (drag, turbomolecular and sublimation pumps) in order to prevent hydrocarbon contamination of the ionization chamber and, in the

possibility of nefarious occurrences, to prevent vacuum contamination of other branches in the beamline or even the storage ring.

The security issues regarding vacuum conditions in the beamline are of extreme importance. A set of actuator valves located after the undulator can only be opened when the low pressure conditions inside the end experimental chamber are met. If pressure suddenly rises inside the experimental chamber, the actuator valves close immediately, maintaining the pressure conditions ahead of the undulator slits stable.

2.3 Complementary techniques

As pointed out before, photoelectron spectroscopy performed on gas-phase samples likely enjoys the company of other standard analytical techniques, such as mass spectrometry or IR spectroscopy. When coupled *in situ* with UVPES these techniques can confirm the integrity of the sample whose electronic structure is being analysed (MS) or provide complete vibrational characterization of the molecules under study (IR spectroscopy).

If the sample is subjected to controlled variations of the thermodynamic conditions prior to its analysis, as is the case of pyrolysis, then both MS and IR spectroscopy can help clarify the existence of unknown decomposition products, either by mass analysis of the residual gas or by identification of the vibrational fingerprint belonging to the decomposition products.

During the course of this work, complementary mass spectrometry information on the benzyl azides (BA and 2-,3- and 4-MBA) was acquired in collaboration with the group of Environmental and Biological Mass Spectrometry from the Chemistry and Biochemistry Center (CQB) of the University of Lisbon (UL), specifically with M. T. Fernandez and M. Filomena Duarte. Furthermore, valuable information was extracted from matrix-isolation IR spectroscopy, performed on the methyl azidopropionate compounds by A. A. Dias, within the PES group of the University of Southampton, in collaboration with J. S. Ogden and J. M. Dyke.

In the next sections, very brief information regarding the instrumentation and principles of mass spectrometry and matrix-isolation IR spectroscopy will be given, in view of the work performed in collaboration with the groups referenced above.

2.3.1 Mass spectrometry

The most general physical phenomena underlying the electron ionization mass spectrometry (EIMS) technique is the production of gas-phase ions by an electron beam of pre-defined energy[136]:

$$\mathrm{M} + e^- \rightarrow \mathrm{M}^{\bullet +} + 2e^- \quad . \tag{2.28}$$

The molecular radical cation formed in this way ($\mathrm{M}^{\bullet +}$=$(\mathrm{AB})^{\bullet +}$) can undergo further fragmentations, leading to the production of either a cation and a neutral radical (A^++$\mathrm{B}^{\bullet}$) or a radical cation and a neutral molecule ($\mathrm{A}^{\bullet +}$+B), always obeying mass and charge conservation. The fragmentation can be due to a number of factors, but it almost always associated with the excess energy imparted by the electron to the interacting molecule.

In a mass spectrometer, all the ions are separated according to their mass-to-charge ratio (m/z) and detected in proportion to their abundance, culminating in the creation of a mass spectrum. A mass spectrometer follows the same general scheme showed in Fig. 2.2, but the radiation source and interaction region are renamed to *ion source*, and the energy analyser is replaced by a *mass analyser*. In fact, a photoelectron spectrometer can be transformed into a mass spectrometer by simply changing the energy

analyser to a mass analyser device. This technique is called photoionisation mass spectrometry (PIMS) but usually requires a very high output photon source in order to produce enough ions to render detection possible.

The most common and readily available ion source is of the *electron ionization* type, in which electrons are liberated from a hot filament and accelerated through an anode, interacting with the gaseous samples in an ion source. The electron energy can be varied, but 70 eV is found as a standard value. Mass analysers differ in geometry, configuration and mass scanning operation but can be divided essentially in: *sector* analysers, *time-of-flight* (TOF) analysers and *quadrupole* filters (in which *ion traps* are included). A detailed description of the physical principles associated with the operation of the different types of mass analysers can be found in several textbooks, more technical-oriented, such as the reference work by Hoffmann and Stroobant[136] or other introductory textbooks[137,138].

The electron ionization mass spectrometry studies on BA, and 2-, 3- and 4-MBA were achieved on a AEI spectrometer, model MS9, updated by VG Analytical Instruments. The spectrometer features a Nier-Jonhson design[139,140] – a 90° spherical sector electrostatic analyser followed by a 60° magnetic sector analyser – with the possibility of performing electron ionization and ionization by fast atom bombardment. In addition, the equipment provides the user with the option of performing mass scans at constant magnetic to electric field ratio i.e. linked scans at constant B/E, which allows for all the fragment ions of a specific precursor ion to be detected. Only electron ionization was used, at nominal electron energies of 70 eV and 200 mA trap current, with source housing pressure of ca. 1×10^{-4} Pa and analyser pressure of about 2×10^{-5} Pa.

2.3.2 Matrix-isolation IR spectroscopy

The matrix-isolation technique for trapping unstable volatile species was first considered by Pimentel and co-workers[28] in 1954. Nowadays, it is a well established technique, which allows for the preservation of very reactive or short-lived species (guest) at low temperatures in a solid medium (host).

The review works by Perutz[141,142] and Barnes[143] in the 1980's soon captured the enormous potential shown by this technique as an analytical tool for photochemical reactions and all different types of isomeric transformations, such as conformerism and tautomerism. Several aspects of the chemistry and physics underlying the behaviour of matrix-isolated species were further treated in the compendium by Andrews and Moskovits[144]. Extensive theoretical and technical information regarding low-temperature molecular spectroscopy employing matrix-isolation techniques can be found in recent literature works by Fausto[145] and Dunkin[146].

The equipment employed in the study of M2AP is build upon the basic configuration of a typical matrix-isolation IR spectrometer, the only difference being the resistively heated inlet system used to pyrolyse the samples prior to their deposition in the host.

Briefly, the system is based in a conventional closed-cycle cryostat (Air Products, model CSW-202) and an IR grating spectrophotometer (Perkin Elmer, model 983G), together with a caesium iodide (CsI) deposition window, maintained at ca. 12 K. The high-vacuum conditions inside the system (ca. 3×10^{-4} Pa) are maintained through a liquid nitrogen trap and a Edwards Diffstak oil-diffusion pump backed by a Edwards rotary pump. The samples vapor, pre-cooled in a liquid nitrogen bath, is admitted to the system through a PTFE valve. Prior its deposition in N_2 matrix, the sample vapor travels through a 150 mm silica furnace (with 5 mm i.d.) which can be resistively heated up to ca. 900 K and whose temperature is measured through a type K thermocouple. A schematic view of the apparatus[123] can be seen in Fig. 2.29.

Matrix ratios are estimated to be in excess of 1000:1 (inert gas:sample) and the

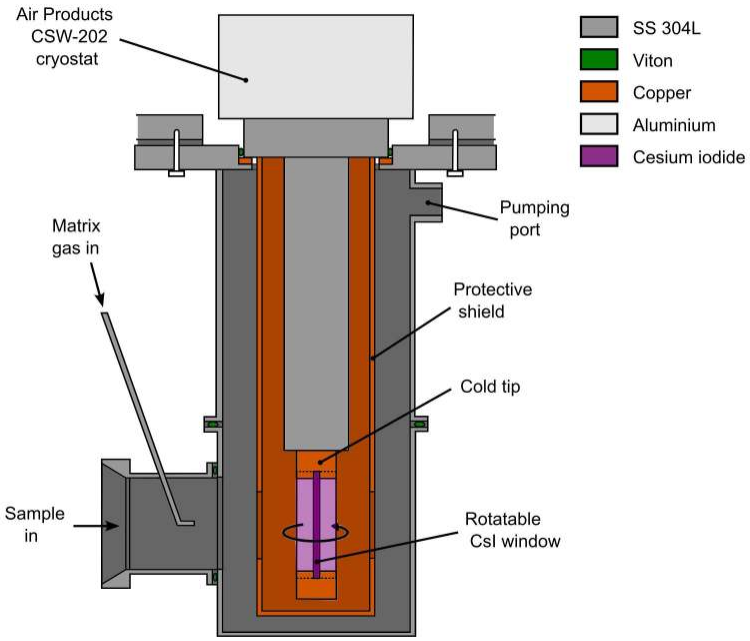

Figure 2.29: Schematic diagram of the matrix-isolation apparatus for analysis of gas-phase samples with IR spectroscopy, maintained by the PES group of the University of Southampton.

sample is deposited during a time period ranging from 30 to 60 minutes. The high matrix ratio minimizes the existence of neighbouring molecules deposited in the matrix, therefore minimizing the formation of dimers. During deposition of the sample onto the matrix, all the thermodynamic conditions inside the system are held constant i.e. the temperature of the furnace, the temperature of the matrix and the partial pressures are constant over time.

When performed together with UVPES, specially if the goal is to study gas-phase thermal decomposition of organic samples, matrix-isolation IR is extremely helpful in detecting unstable species formed upon pyrolysis. The matrix acts as a layer of finite potential wells, where the molecules are trapped and frozen to a degree where rotational motion is suppressed. This represents an obvious an advantage when compared to standard gas-phase IR spectroscopy, because in the latter the rovibrational modes of the molecule are also active and can be populated upon excitation, complicating the interpretation of spectra.

In general, reactions which imply activation energies higher than 5 kJ/mol can only be stimulated by irradiation of the trapped sample with UV or IR light of appropriate wavelength, inducing conformational/tautomeric isomerisation or even excitation of selected vibrational modes.

Chapter 3

Theoretical Framework and Methods

3.1 Electronic structure calculations in a nutshell

Even if some experimental findings are self-evident *per se* and clearly indicate the physical process underlying the phenomena under study, a great deal of information is gained in rationalizing the results at the light of theory.

The general theory behind the photoionisation of molecules and hence of gas-phase photoelectron spectroscopy is that of *molecular quantum mechanics*[147]. Due to the matrix formulation of several mathematical key-aspects of quantum mechanics (QM), code implementation of recursive solutions in standard end-user workstations has become nowadays both so trivial and accurate that it gave rise to a subfield in theoretical chemistry, called *computational chemistry*[148]. Usually, it is the development of new algorithms to treat specific questions in quantum chemistry that brings together the theoretical background of physicists and the more prosaic view of the experienced chemist – *physical-chemistry* works at the blurred interface between the knowledge necessary to treat a system microscopically and the information necessary to relate it to its macroscopic properties and behaviour[149].

The next sections include the necessary mathematical background behind QM computational methods used in this thesis, with the aim of providing an overview of the advantages and limitations of the different approximations to the calculation of the electronic structure of polyatomic molecules.

Finer details regarding mathematical formulation and specificities of its computational implementation will be deprecated in favour of a more succinct analysis, emphasizing general concepts. This will allow for deconstruction of the "black box"'enclosing many software implementations, without rendering the subject too complex.

3.1.1 The many-electron conundrum in Schrödinger's equation

The Hamiltonian $\hat{H}$ $(\hat{T}+\hat{V})$ for a system composed of N-electrons and M-nuclei can be written as[150]

$$\hat{H} = \sum_{i=1}^{N}\sum_{j>i}^{N}\frac{1}{r_{ij}} + \sum_{A=1}^{M}\sum_{B>A}^{M}\frac{Z_A Z_B}{R_{AB}} - \sum_{i=1}^{N}\frac{1}{2}\nabla_i^2 - \sum_{A=1}^{M}\frac{1}{2M_A}\nabla_A^2 - \sum_{i=1}^{N}\sum_{A=1}^{M}\frac{Z_A}{r_{iA}} \quad , \quad (3.1)$$

where M_A is the ratio of the mass of nucleus A to the mass of an electron, Z_A is the atomic number of nucleus A. The distance between the ith electron and Ath nucleus is

$r_{iA} = |\mathbf{r}_i - \mathbf{R}_A|$; the distance between the ith electron and jth electron is $r_{ij} = |\mathbf{r}_i - \mathbf{r}_j|$, and the distance between the Ath nucleus and Bth nucleus is $R_{AB} = |\mathbf{R}_A - \mathbf{R}_B|$ (see Fig. 3.1).

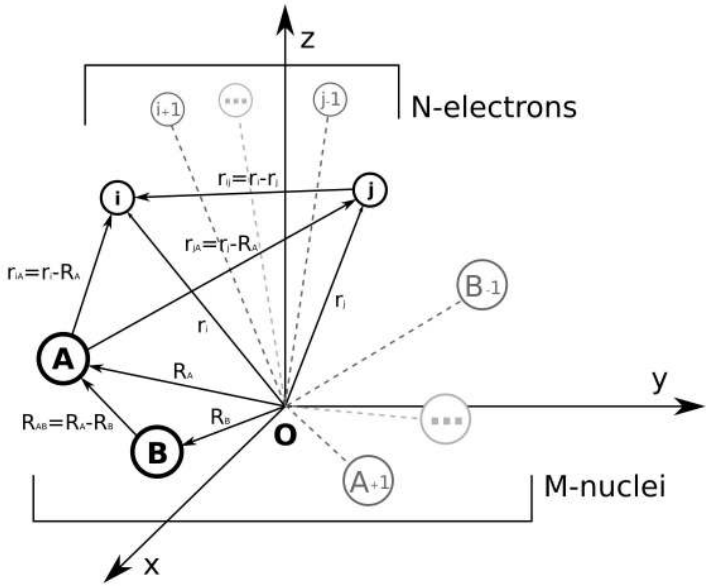

Figure 3.1: General coordinate system for a molecule with N-electrons and M-nuclei.

In Eq. 3.1, the first and second terms represent the electrostatic repulsion between electrons and between nuclei, respectively. The third and fourth terms are the operators for the kinetic energy of the electrons and for the kinetic energy of the nuclei, respectively. The last term represents the Coulomb attraction between electron and nuclei.

Eq. 3.1 is written using *atomic units*, which allow us to play with the molecular Hamiltonian in its dimensionless form: the atomic unit of energy is the *Hartree* (E_H) and the atomic unit of length is the *Bohr radius* (a_0), which are equivalent to 4.360×10^{-18} J and 5.292×10^{-11} m, respectively. In atomic units, the electron mass m_e, the electron charge e, the atomic momentum $\hbar$, the vacuum permittivity $4\pi\epsilon_0$, a_0 and E_H are all equal to unity.

The central subject around which molecular QM revolves is solving the time-independent non-relativistic *Schrödinger equation*[151]

$$\hat{H}\Psi = E\Psi \qquad , \tag{3.2}$$

for a molecular wave function Ψ, using the Hamiltonian of Eq. 3.1. The Schrödinger equation is a second-order partial differential equation, which can be formulated as an eigenvalue equation, as shown above, with Ψ as eigenvector and E as eigenvalue. It cannot be solved analytically for any system with $n > 1$ (as is the case of our molecular Hamiltonian); the problem is only solved numerically and by making some approximations.

3.1.2 The Born-Oppenheimer approximation

By far, the most important approximation is the one introduced by Born and Oppenheimer[152] (BO), in 1927. Since nuclei are much heavier than electrons, they move very slowly in comparison with electrons. Hence, to a good approximation the electrons in a molecule can be thought as moving in a field of fixed nuclei. It is logical then to

separate the two motions, both in the Hamiltonian of Eq. 3.1 and in the molecular wave function Ψ.

Owing to this approximation, the nucleus-nucleus repulsion term and the nuclei kinetic energy operator term can be momentarily neglected, leaving Eq. 3.1 with only three terms which form the electronic Hamiltonian $\hat{H}_e$:

$$\hat{H}_e = \sum_{i=1}^{N}\sum_{j>i}^{N}\frac{1}{r_{ij}} - \sum_{i=1}^{N}\frac{1}{2}\nabla_i^2 - \sum_{i=1}^{N}\sum_{A=1}^{M}\frac{Z_A}{r_{iA}} \quad . \tag{3.3}$$

Defining the Schrödinger equation with the above Hamiltonian, and setting the eigenvector as an electronic wave function Ψ_e which depends parametrically on the nuclear coordinates $\mathbf{R}_A$ and explicitly on the electron coordinates $\mathbf{r}_i$, we get

$$\left[\sum_{i=1}^{N}\sum_{j>i}^{N}\frac{1}{r_{ij}} - \sum_{i=1}^{N}\frac{1}{2}\nabla_i^2 - \sum_{i=1}^{N}\sum_{A=1}^{M}\frac{Z_A}{r_{iA}}\right]\psi_e\left(\mathbf{r}_i,\mathbf{R}_A\right) = E_e\psi_e\left(\mathbf{r}_i,\mathbf{R}_A\right) \quad . \tag{3.4}$$

Its worth noting that every calculation aimed at obtaining the electronic wave function ψ_e is dependent on the nuclear coordinates and ψ_e is a particular eigenfunction with specific eigenvalues; hence a "universal" molecular wave function for a given system does not exist.

The total energy of the system E is computed by adding the constant nuclear repulsion contribution to E_e:

$$E = E_e + \sum_{A=1}^{M}\sum_{B>A}^{M}\frac{Z_A Z_B}{R_{AB}} \quad . \tag{3.5}$$

By solving the electronic problem, in obtaining E, one can write the nuclear Hamiltonian $\hat{H}_n$, which describes the rotation, vibration and translation of the molecular system. The total energy defines the potential for nuclear motion, leading to the formulation of the Scrödinger equation using $\hat{H}_n$ in the BO approximation:

$$\hat{H}_n = E - \sum_{A=1}^{M}\frac{1}{2M_A}\nabla_A^2 \quad , \tag{3.6}$$

and

$$\hat{H}_n\psi_n(\mathbf{R}_A) = E_n\psi_n(\mathbf{R}_A) \quad . \tag{3.7}$$

In the BO approximation, the total wave function used in Eq. 3.2 can be expressed as a product of the nuclear and electronic wave functions:

$$\Psi = \psi_n(\mathbf{R}_A)\psi_e\left(\mathbf{r}_i,\mathbf{R}_A\right) \quad . \tag{3.8}$$

In summary, via the BO approximation: **(1)** the Hamiltonian for a M-nuclei N-electron molecular system can be separated into a nuclear, $\hat{H}_n$, and an electronic part, $\hat{H}_e$, the same occurring for the total wave function; **(2)** separation of variables allows one to obtain two independent Schrödinger equations – one electronic and one containing only nuclear coordinates; **(3)** solution of the electronic Schrödinger equation results in a potential energy term which can be used to solve the nuclear counterpart; **(4)** solutions of the later describe the vibrational, rotational and translational behaviour of the molecule.

The term *adiabatic* is often used to coin the concepts behind Born-Oppenheimer approximation and the potential curves arising from it, because of the formulation of the *adiabatic theorem* by Born and Fock[153]:

> *A physical system remains in its instantaneous eigenstate if a given perturbation is acting on it slowly enough and if there is a gap between the eigenvalue and the rest of the Hamiltonian's spectrum.*

The concept here is similar to that of a quasi-static process in thermodynamics: if a parameter/perturbation of the system varies/acts slowly, the system is allowed to relax its characteristic functional form i.e. it adapts the thermodynamic state function $f(P;V;T)$ or the quantum wave function Ψ. Simply put, in an adiabatic potential curve, the initial wave function Ψ_i is eigenfunction of an initial Hamiltonian $\hat{H}_i$, and the final wave function Ψ_f is an eigenfunction of a final Hamiltonian $\hat{H}_f$.

Although powerful, the BO approximation lives not without caveats. One example occurs when ground and excited electronic surfaces (see Section 2.1.1.2) get very close i.e. when the energy states are almost degenerate and the nuclear and electronic description cannot be decoupled. Bond stretching in the Li^+F^- molecule[148] exhibits such an effect: at the equilibrium distance, the molecule is strongly polarized an can be described as an ionic wave function, Li^+F^-, whereas at long distance the molecule dissociates and the wave function becomes of the covalent type, $Li^{\bullet}F^{\bullet}$. Therefore, at some specific bond length value, the potential curves would cross...however, this does not happen because the curves have the same symmetry. The wave function goes through a region of *avoided crossing* and it changes from being mainly ionic to covalent, breaking the BO approximation.

The formulation of a molecular Hamiltonian disregarding the BO approximation is very complex and will not be analysed in detail here. Extensive information can be found in the review *Diabolical Conical Intersections* by Yarkony[154], and in textbooks by Cederbaum[155] and by Baer[156].

3.1.3 Molecular wave function requirements

Having set our problem mathematically, we now need to define the form of its solution i.e. the requirements for a well-behaved and physically meaningful wave function.

What are the physical requirements the molecular wave function must meet? The wave function describes an electron and, as all elementary particles, the electron also possesses an intrinsic characteristic, known as *spin*[147]. This property can be accounted for by simply adding an extra parameter to the spatial coordinates needed to describe the motion of the electron, defining its spin-state (up or down, +1/2 or -1/2).

Taking the electronic part of Eq. 3.8, dropping the nuclear dependence notation and the "e" subscript for convenience, and adding the spin part, leads to the construction of the *spin orbital* ψ

$$\psi_e(\mathbf{r}_i, \mathbf{R}_A) \rightarrow \psi(\mathbf{r}_i)\chi_{\pm}(s_i) \qquad . \tag{3.9}$$

where the spin function $\chi_{\pm}(s_i)$ is defined by two orthonormal functions $\chi_+(s_i) = \alpha(s)$ and $\chi_-(s_i) = \beta(s)$, for spin-up ($\uparrow$) and spin-down ($\downarrow$) states, respectively, and s being an unspecified spin variable.

In a molecular system, electrons must obey the *antisymmetry principle* which is equivalent to one of the postulates of quantum mechanics – the *Pauli exclusion principle*. One of the many ways to enunciate this principle is[157]

> *In a system of electrons, the measurement of four quantities that are typical of the electron can have a well-defined value for one electron only at any one moment.*

This four quantities are typically defined by appropriate quantum numbers – n, l, m_l and m_s (principal, azimuthal, magnetic and spin projection quantum numbers), but

can be also defined by the three coordinates used to describe the position of the electron and its spin component ($\mathbf{r}_i$ and s).

What are the implications of the Pauli principle to the molecular wave function? Let us consider a system of N non-interacting electrons i.e. a system for which the Hamiltonian is defined as the sum of Hamiltonians like the one of Eq. 3.3 but lacking the electrostatic repulsion term between electrons (these are called *one-electron Hamiltonians*, $\hat{H}_1^i$). If we use the one-electron Hamiltonian summation to set the Schrödinger equation, an adequate wave function Φ can be set as the product of one-electron spin-orbitals:

$$\Phi(\Psi_1, \ldots, \Psi_N) = \Psi_1 \cdots \Psi_N = \psi(\mathbf{r}_1)\chi_{\pm}(s_1) \cdots \psi(\mathbf{r}_N)\chi_{\pm}(s_N) \quad , \tag{3.10}$$

for which

$$\sum \hat{H}_1^i \Phi(\Psi_1, \ldots, \Psi_N) = (E_1 + \ldots + E_N)\Phi(\Psi_1, \ldots, \Psi_N) \quad . \tag{3.11}$$

where $\hat{H}_1^i$ operates only on specific electron i. The eigenvalue summation $E_1 + \ldots + E_N$ is equivalent to the total energy E, which does not alter even if electrons exchange orbitals. In fact, there are $N!$ combinations of single-particle wave functions that give the same energy value E, in what is called *exchange degeneracy* [157].

In order to lift this degeneracy we need to make the wave function antisymmetric (for fermions) on exchange of particles i.e. the wave function has to change sign if electrons change position without however changing their probability density (and energy), hence

$$\Phi(\Psi_1, \ldots, \Psi_N) = -\Phi(\Psi_N, \ldots, \Psi_1) \quad , \tag{3.12}$$

maintaining also

$$|\Phi(\Psi_1, \ldots, \Psi_N)|^2 = |\Phi(\Psi_N, \ldots, \Psi_1)|^2 \quad . \tag{3.13}$$

The antisymmetric wave function can be constructed as a linear combination of spin-orbital products. In a system with two electrons, for instance, the two asymmetric products

$$\Psi(\Psi_1, \Psi_2) = \psi_1(\mathbf{r}_1)\chi_{\pm}(s_1)\psi_2(\mathbf{r}_2)\chi_{\pm}(s_2) \tag{3.14}$$

$$\Psi'(\Psi_1, \Psi_2) = \psi_1(\mathbf{r}_2)\chi_{\pm}(s_2)\psi_2(\mathbf{r}_1)\chi_{\pm}(s_1) \tag{3.15}$$

can be combined to form

$$\Phi(\Psi_1, \Psi_2) = \frac{1}{\sqrt{N!}}(\Psi - \Psi') \tag{3.16}$$

where $1/\sqrt{N!}$ is a normalization factor and N equals the number of electrons (in this case $N = 2$).

The generalization of Eq. 3.16 for N-electrons is achieved by means of a determinant, called *Slater determinant*:

$$\Phi(\Psi_1, \ldots, \Psi_N) = \frac{1}{\sqrt{N!}} \begin{vmatrix} \Psi_{11} & \Psi_{12} & \cdots & \Psi_{1N} \\ \Psi_{21} & \Psi_{22} & \cdots & \Psi_{2N} \\ \vdots & & & \vdots \\ \Psi_{N1} & \Psi_{N2} & \cdots & \Psi_{NN} \end{vmatrix} \tag{3.17}$$

where the row index defines the electron and the column index defines the spin-orbital. As we can see, all electrons cycle through all N available spin-orbitals, making them indistinguishable; the matrix element Ψ_{22}, for example, defines "electron 2" in spin-orbital 2, whereas Ψ_{12} defines "electron 1" in spin-orbital 2. A convenient notation for the determinant elements would be

$$\Psi_{ij} = \Psi(\mathbf{r}_i, s_i, j) = \psi_j(\mathbf{r}_i)\chi_{\pm}(s_i) \equiv \Psi_j(\mathbf{x}_i) \quad , \tag{3.18}$$

where the spatial coordinates $\mathbf{r}_i$ and the spin component s_i have been condensed in the four-element vector $\mathbf{x}_i$.

The Slater determinant accounts for the antisymmetry of the complete N-electron wave function in a very efficient way: by interchanging rows, we interchange electron coordinates and the determinant changes sign, effectively obeying the condition of Eq. 3.12.

Another advantage of the Slater determinant is that it fulfils the Pauli exclusion principle also in a very elegant manner: if two columns were equal, we would have two electrons in the same spin-orbital, and the determinant would then be zero – no two electrons can share the same quantum numbers.

3.1.4 The Hartree-Fock method

Having set the equation central to the many-electron problem – the eigenvalue problem (Eq. 3.4), and an adequate trial solution – the single Slater determinant (Eq. 3.18), we must couple the two and find the best solution (the one which minimizes the ground-state energy of the system).

It is possible to split the Hamilatonian of Eq. 3.4 into three operators, distinguishable by the extent of their dependence: $\hat{H}_0$ if independent of electron coordinates, $\hat{H}_1$ if dependent of one-electron coordinates only, and $\hat{H}_2$ if dependent on the coordinates of two electrons. Zero-, one- and two-electron operators can then be defined as follows:

$$\hat{H}_0 = \sum_{A=1}^{M} \sum_{B>A}^{M} \frac{Z_A Z_B}{R_{AB}} \tag{3.19}$$

$$\hat{H}_1 = -\sum_{i=1}^{N} \frac{1}{2} \nabla_i^2 - \sum_{i=1}^{N} \sum_{A=1}^{M} \frac{Z_A}{r_{iA}} \tag{3.20}$$

$$\hat{H}_2 = \sum_{i=1}^{N} \sum_{j>i}^{N} \frac{1}{r_{ij}} \tag{3.21}$$

At this point, it is also useful to introduce the *bra-ket* or *Dirac notation*, which compresses the notation of lengthy integral expressions often found in QM:

$$\int_{-\infty}^{\infty} \Psi^* \Psi d\tau = \langle \Psi | \Psi \rangle \tag{3.22}$$

$$\int_{-\infty}^{\infty} \Psi^* \hat{H} \Psi d\tau = \langle \Psi | \hat{H} | \Psi \rangle \tag{3.23}$$

where the integral is evaluated over the entire volume τ.

Bras $\langle \dots |$ and kets $| \dots \rangle$ are linear and associative functionals that ease the notation over conjugate-transpose (Hermitian) operators, such as the Hamiltonian used here (any linear $\hat{A}$ operator expressed in its matrix form that follows $A = A^\dagger = \overline{A^T}$ is Hermitian). The conjugate-transpose of a *bra* is the corresponding *ket* and vice-versa i.e. $\langle \psi_1 | \psi_2 \rangle^\dagger = \langle \psi_2 | \psi_1 \rangle$.

We now use another QM postulate which defines a proper way for calculating the expectation value of the observable E, in the many-electron system. Already employing brackets, using the definition for *mean value*

$$\langle E \rangle = \langle \Psi | \hat{H} | \Psi \rangle \qquad , \tag{3.24}$$

on the segmented Hamiltonian of Eq. 3.4, we get

$$\langle E\rangle = \langle\Phi|\hat{H}_0|\Phi\rangle + \langle\Phi|\hat{H}_1|\Phi\rangle + \langle\Phi|\hat{H}_2|\Phi\rangle \qquad , \tag{3.25}$$

where Φ is a single Slater determinant and $\hat{H}_0$, $\hat{H}_1$ and $\hat{H}_2$ are the zero-, one- and two-electron operators as defined above.

After a tedious derivation involving expansion of the Slater determinant and use of the spin-orbitals orthogonality condition, the energy of a single determinant can be written as

$$\begin{aligned} E = E_0 \;+\; & \sum_{i=1}^{N}\int \Psi_i^*(\mathbf{x}_1)\hat{H}_1(\mathbf{x}_1)\Psi_i(\mathbf{x}_1)\,\mathrm{d}\mathbf{x}_1 \\ + \; & \frac{1}{2}\sum_{i=1}^{N}\sum_{j=1}^{N}\iint \Big[\Psi_i^*(\mathbf{x}_1)\Psi_i(\mathbf{x}_1)\hat{H}_2\Psi_j^*(\mathbf{x}_2)\Psi_j(\mathbf{x}_2) \\ & -\Psi_i^*(\mathbf{x}_1)\Psi_j(\mathbf{x}_1)\hat{H}_2\Psi_j^*(\mathbf{x}_2)\Psi_i(\mathbf{x}_2)\Big]\,\mathrm{d}\mathbf{x}_1\mathrm{d}\mathbf{x}_2\,, \end{aligned} \tag{3.26}$$

or in bracket notation

$$\begin{aligned} E = E_0 \;+\; & \sum_{i=1}^{N}\langle\Psi_i(\mathbf{x}_1)|\hat{H}_1(\mathbf{x}_1)|\Psi_i(\mathbf{x}_1)\rangle \\ + \; & \frac{1}{2}\sum_{i=1}^{N}\sum_{j=1}^{N}\Big[\langle\Psi_i(\mathbf{x}_1)\Psi_j(\mathbf{x}_2)|\hat{H}_2|\Psi_i(\mathbf{x}_1)\Psi_j(\mathbf{x}_2)\rangle \\ & -\langle\Psi_i(\mathbf{x}_1)\Psi_j(\mathbf{x}_2)|\hat{H}_2|\Psi_i(\mathbf{x}_2)\Psi_j(\mathbf{x}_1)\rangle\Big]\,. \end{aligned} \tag{3.27}$$

The use of the transposition operator $\hat{P}_{12}$, that commutes with the Hamiltonian and whose only effect is the exchange of coordinates between electron 1 and electron 2, can be used to further abbreviate expression 3.27:

$$\begin{aligned} E = E_0 \;+\; & \sum_{i=1}^{N}\langle\Psi_i(\mathbf{x}_1)|\hat{H}_1(\mathbf{x}_1)|\Psi_i(\mathbf{x}_1)\rangle \\ + \; & \frac{1}{2}\sum_{i,j=1}^{N}\langle\Psi_i(\mathbf{x}_1)\Psi_j(\mathbf{x}_2)|\hat{H}_2(1-\hat{P}_{12})|\Psi_i(\mathbf{x}_1)\Psi_j(\mathbf{x}_2)\rangle \;\equiv\; E[\Psi_i] \end{aligned} \tag{3.28}$$

In Eq. 3.28, $E[\Psi_i]$ is a *functional* – a transformation which maps a field vector into the field itself i.e. a function which transforms a function into a scalar – that can be manipulated in order to find its minimum. In fact, it's the minimization of the energy functional $E[\Psi_i]$, subject to the constraint of orthonormality of the spin-orbitals $\langle\Psi_i|\Psi_j\rangle = \delta_{ij}$, that leads to the canonical *Hartree-Fock equations*.

The procedure used to find the energy minimum is based on Lagrange's *method of undetermined multipliers*. Briefly, in order to optimize a function $f(\mathbf{x}_1,\ldots,\mathbf{x}_N)$ subject to constraints defined by $g(\mathbf{x}_1,\ldots,\mathbf{x}_N)$, one formulates the *Lagrange function* $L(\mathbf{x}_1,\ldots,\mathbf{x}_N,\lambda)$ and then sets its variation to zero:

$$L(\mathbf{x}_1,\ldots,\mathbf{x}_N,\lambda) = f(\mathbf{x}_1,\ldots,\mathbf{x}_N) - \lambda g(\mathbf{x}_1,\ldots,\mathbf{x}_N) \;\wedge\; \delta L = 0 \qquad . \tag{3.29}$$

Applying this method to the problem at hand results in the following expressions:

$$L[\Psi_i,\epsilon_{ij}] = E[\Psi_i] - \sum_{i,j=1}^{N}\epsilon_{ij}(\langle\Psi_i|\Psi_j\rangle - \delta_{ij}) \qquad , \tag{3.30}$$

and

$$\delta L[\Psi_i, \epsilon_{ij}] = \delta E[\Psi_i] - \sum_{i,j=1}^{N} \epsilon_{ij}(\langle \delta\Psi_i|\Psi_j\rangle - \langle \Psi_i|\delta\Psi_j\rangle) = 0 \qquad , \tag{3.31}$$

where ϵ_{ij} takes the place of the variational multiplier λ, and the explicit dependence of the spin-orbital Ψ_i on electron coordinates $\mathbf{x}_i$ is omitted.

After expansion and some manipulation, and considering *c.c.* the complex conjugate, Eq. 3.31 transforms into

$$\begin{aligned} \delta L = \sum_{i=1}^{N} \langle \delta\Psi_i|\hat{H}_1|\Psi_i\rangle \quad &+ \quad \sum_{i,j=1}^{N} \langle \delta\Psi_i\Psi_j|\hat{H}_2|\Psi_i\Psi_j\rangle - \langle \delta\Psi_i\Psi_j|\hat{H}_2|\Psi_j\Psi_i\rangle + c.c. \\ &- \quad \sum_{i,j=1}^{N} \epsilon_{ij}\langle \delta\Psi_i|\Psi_j\rangle + c.c. = 0 \qquad . \end{aligned} \tag{3.32}$$

Making use again of $\hat{P}_{12}$ and highlighting $\langle \delta\Psi_i|$, one obtains

$$\sum_{i=1}^{N} \langle \delta\Psi_i| \left(\hat{H}_1|\Psi_i\rangle + \sum_{j=1}^{N} \langle \Psi_j|\hat{H}_2(1-\hat{P}_{12})|\Psi_i\Psi_j\rangle - \epsilon_{ij}|\Psi_j\rangle + c.c. \right) = 0 \qquad . \tag{3.33}$$

Since the variation in $\langle \delta\Psi_i|$ can take an arbitrary value, its coefficient (the second term of the product) has to be zero, for the above equality to be valid; thus, the following holds true

$$\hat{H}_1|\Psi_i\rangle + \sum_{j=1}^{N} \langle \Psi_j|\hat{H}_2(1-\hat{P}_{12})|\Psi_i\Psi_j\rangle - \epsilon_{ij}|\Psi_j\rangle = 0 \qquad . \tag{3.34}$$

which is equivalent to the expression:

$$\left[\hat{H}_1 + \sum_{j=1}^{N} \langle \Psi_j|\hat{H}_2(1-\hat{P}_{12})|\Psi_j\rangle \right] |\Psi_i\rangle = \sum_{j=1}^{N} \epsilon_{ij}|\Psi_j\rangle \qquad . \tag{3.35}$$

It is common to encounter the above equation expressed in terms of two orbital-dependent operators – the *direct* or *Coulomb operator* $\hat{J}_j$ and the *exchange operator* $\hat{K}_j$, which are defined by their effect on a generic spin-orbital as follows:

$$\begin{aligned} \hat{J}_j\Psi_i(\mathbf{x}_1) &= \left(\int_{-\infty}^{\infty} \Psi_j^*(\mathbf{x}_2)\frac{1}{r_{12}}\Psi_j(\mathbf{x}_2)\mathrm{d}\mathbf{x}_2 \right) \Psi_i(\mathbf{x}_1) \\ &= \left(\langle \Psi_j|\hat{H}_2|\Psi_j\rangle\right) |\Psi_i\rangle = \hat{J}_j|\Psi_i\rangle \qquad , \end{aligned} \tag{3.36}$$

$$\begin{aligned} \hat{K}_j\Psi_i(\mathbf{x}_1) &= \left(\int_{-\infty}^{\infty} \Psi_j^*(\mathbf{x}_2)\frac{1}{r_{12}}\Psi_i(\mathbf{x}_2)\mathrm{d}\mathbf{x}_2 \right) \Psi_j(\mathbf{x}_1) \\ &= \left(\langle \Psi_j|\hat{H}_2\hat{P}_{12}|\Psi_j\rangle\right) |\Psi_i\rangle = \hat{K}_j|\Psi_i\rangle \qquad . \end{aligned} \tag{3.37}$$

Using $\hat{J}_j$ and $\hat{K}_j$, Eq. 3.35 is expressed as

$$\left[\hat{H}_1 + \sum_{j=1}^{N} \hat{J}_j - \hat{K}_j \right] |\Psi_i\rangle = \sum_{j=1}^{N} \epsilon_{ij}|\Psi_j\rangle \qquad . \tag{3.38}$$

The operations inside square brackets define the *Fock operator* $\hat{F}$. Therefore, the above relationship can be written as

$$\hat{F}_i|\Psi_i\rangle = \sum_{j=1}^{N} \epsilon_{ij}|\Psi_j\rangle \qquad , \tag{3.39}$$

representing a set of N equations known collectively as *Hartree-Fock* (HF) *equations*.

By comparison with a typical eigenvalue problem such as the one in Eq. 3.2, it is clear that the above HF equations are not set properly. The set of spin orbitals $\{\Psi_i\}$ composing the single determinant function $|\Phi\rangle$ can be mixed among themselves without changing the expectation value $E = \langle\Phi|\hat{H}|\Phi\rangle$.

In order to write the HF equations in the standard (*canonical*) form of an eigenvalue problem, one has to remove the second summation index in ϵ_{ij}, by diagonalizing the square matrix of eigenvalues. From linear algebra, a square matrix A is diagonalizable if there exists an invertible matrix P such that $A' = P^{-1}AP$. It happens that if P is an Hermitian matrix ($P = P^{\dagger}$) then the diagonalizing transformation is also a unitary transformation i.e. a transformation which maintains unaltered the inner product.

It can be shown that the single determinant wave function Φ is invariant under a unitary transformation and, at most, it differs form a transformed Φ' wave function only by a phase factor θ. It is also demonstrable that the Fock operator is invariant under unitary transformations on the spin-orbitals[150]. Therefore, it is always possible to find an Hermitian matrix P such that

$$\epsilon'_{ij}\delta_{ij} = P^{\dagger}\epsilon_{ij}P \tag{3.40}$$

diagonalizes ϵ_{ij}. There must exist, then, a set of spin-orbitals $|\Psi'_i\rangle$ which are eigenfunctions of the Lagrange multipliers $\epsilon'_{ij}\delta_{ij}$, obtained by unitary transformations for which Eq. 3.39 can be rewritten as a pure eigenvalue problem:

$$\hat{F}_i|\Psi_i\rangle = \epsilon_i|\Psi_i\rangle \ , \ i = 1, \ldots, N \qquad . \tag{3.41}$$

In the above *canonical Hartree-Fock equations*, the primes were dropped and the summation over j was eliminated due to diagonalization of the eigenvalue matrix ϵ_{ij}.

In summary, we have derived a set of N integro-differential equations which describe approximately our N-electron system and that can be solved numerically. The way the N-body problem was tackled was simply to consider the interactions between electron i and the average electrostatic field created by the N-1 electrons. This is why the Hartree-Fock approximation with a single Slater determinant is also known as the *mean field approximation*. The solution to the HF equations is only achieved when this mean field is *self-consistent*...

However, before talking about the method of resolution of the HF equations, which is disseminated among all computational codes, we must further define our spin-orbitals in order to understand how they can represent molecular species before photoionisation – a *neutral molecule*, and after photoionisation – a *cation*.

3.1.4.1 Restricted and unrestricted spin-orbitals

The HF equations have been derived for a single Slater determinant without any restrictions on the spin-orbitals: each Ψ_i spin-orbital composing the determinant is a product of a spatial part and a spin component, the spin component being either $\alpha(s)$ ($\uparrow$) or $\beta(s)$ ($\downarrow$).

However, some modifications over the HF equations occur depending on the number of unpaired electrons and the spin multiplicity of the system. A system with an

even number of electrons, with all electrons paired in doubly occupied orbitals, portrays a *closed-shell* ground-state molecule. A system with an odd number of electrons or a system in an excited state with singly occupied orbitals portrays an *open-shell* configuration.

Both tetrazoles under study, 5MTZ and 5ATZ, have an even number of electrons (44), and are thus examples of closed-shell systems (in their ground-state). BA and MBAs are closed-shell systems (70 and 78 electrons respectively), in their ground-state; methyl azidopropionate likewise (68 electrons).

If we restrict the spatial part of two spin-orbitals of different spin to be equal i.e.

$$\Psi_i = \psi_k \alpha(s_i) \wedge \Psi_j = \psi_k \beta(s_j) \tag{3.42}$$

and consider a closed-shell system with an even number of N electrons, paired at each orbital, then Eq. 3.38 will change accordingly:

$$\hat{F}_{RHF}|\Psi_i\rangle = \epsilon_i|\Psi_i\rangle \ , \ i = 1, \ldots, N/2 \qquad , \tag{3.43}$$

with $\hat{F}_{RHF}$ (RHF means *restricted Hartree-Fock*) defined as

$$\hat{F}_{RHF} = \hat{H}_1 + \sum_{j=1}^{N/2} 2\hat{J}_j - \hat{K}_j \qquad . \tag{3.44}$$

In the closed-shell canonical RHF approach, the expected energy of the ith orbital can be obtained by multiplying both sides of Eq. 3.40 to the left by $\langle\Psi_i|$:

$$\epsilon_i = \langle\Psi_i|\hat{H}_1|\Psi_i\rangle + \sum_{j=1}^{N/2}\langle\Psi_i|2\hat{J}_j - \hat{K}_j)|\Psi_i\rangle \qquad . \tag{3.45}$$

Therefore, the total energy of the system, E_{RHF} is expressed as

$$E_{RHF} = E_0 + \sum_{i=1}^{N/2} \epsilon_i + \langle\Psi_i|\hat{H}_1|\Psi_i\rangle \qquad . \tag{3.46}$$

Now lets focus our attention on the open-shell systems, related to almost all cases of ionized molecular species or neutral molecules of non-zero total spin. In that case, the spatial flexibility of the spin-orbital set is maximized i.e. each spin-orbital is different from the rest. Thus, we can define two sets of orbitals (α and β) as basis of our Slater determinant

$$\Phi = \{\Psi_i^\alpha, \Psi_j^\beta, \ldots, \Psi_k^\alpha, \Psi_l^\beta\} \qquad . \tag{3.47}$$

or equivalently

$$\Phi = \{\{\Psi_1^\alpha, \ldots, \Psi_{N^\alpha}^\alpha\}, \{\Psi_{N^\alpha+1}^\beta, \ldots, \Psi_N^\beta\}\} \qquad . \tag{3.48}$$

where $N = N^\alpha + N^\beta$, and the i and j are implicit as any two indexes of the set.

The Fock operator will now be split into two parts, depending weather both $\hat{J}$ and $\hat{K}$ act on spin-orbitals of $\alpha(s)$ spin component or spin-orbitals of $\beta(s)$ spin component: $\hat{F}_{UHF}^\alpha$ and $\hat{F}_{UHF}^\beta$, respectively (UHF means *unrestricted Hartree-Fock*). These two operators can be derived through spin-integration and some algebraic manipulation from Eq. 3.38, and expressed as

$$\hat{F}_{UHF}^\alpha = \hat{H}_1 + \sum_{j=1}^{N^\alpha} \hat{J}_j^\alpha - \hat{K}_j^\alpha + \sum_{j=1}^{N^\beta} \hat{J}_j^\beta \qquad , \tag{3.49}$$

$$\hat{F}^{\beta}_{UHF} = \hat{H}_1 + \sum_{j=1}^{N^{\beta}} \hat{J}^{\beta}_j - \hat{K}^{\beta}_j + \sum_{j=1}^{N^{\alpha}} \hat{J}^{\alpha}_j \qquad , \tag{3.50}$$

The spin-dependent Fock operators include Coulomb and exchange interactions of the ith electron with all electrons of similar spin, plus a Coulomb interaction with all the electrons of different spin. For the sake of clarity, we must define again the Coulomb and exchange operators, this time within the UHF framework; hence,

$$\begin{aligned} \hat{J}^{\alpha}_j \Psi^{\alpha,\beta}_i(\mathbf{x}_1) &= \left(\int_{-\infty}^{\infty} \Psi^{\alpha *}_j(\mathbf{x}_2) \frac{1}{r_{12}} \Psi^{\alpha}_j(\mathbf{x}_2) \mathrm{d}\mathbf{x}_2 \right) \Psi^{\alpha,\beta}_i(\mathbf{x}_1) \\ &= \left(\langle \Psi^{\alpha}_j | \hat{H}_2 | \Psi^{\alpha}_j \rangle \right) | \Psi^{\alpha,\beta}_i \rangle = \hat{J}_j | \Psi^{\alpha,\beta}_i \rangle \end{aligned} \tag{3.51}$$

$$\begin{aligned} \hat{K}^{\alpha}_j \Psi^{\alpha}_i(\mathbf{x}_1) &= \left(\int_{-\infty}^{\infty} \Psi^{\alpha *}_j(\mathbf{x}_2) \frac{1}{r_{12}} \Psi^{\alpha}_i(\mathbf{x}_2) \mathrm{d}\mathbf{x}_2 \right) \Psi^{\alpha}_j(\mathbf{x}_1) \\ &= \left(\langle \Psi^{\alpha}_j | \hat{H}_2 \hat{P}_{12} | \Psi^{\alpha}_j \rangle \right) | \Psi^{\alpha}_i \rangle = \hat{K}_j | \Psi^{\alpha}_i \rangle \end{aligned} \tag{3.52}$$

In the open-shell UHF approach, the energy of the ith α orbital can be obtained in a similar way as with Eq. 3.42, as

$$\epsilon^{\alpha}_i = \langle \Psi^{\alpha}_i | \hat{H}_1 | \Psi^{\alpha}_i \rangle + \sum_{j=1}^{N^{\alpha}} \langle \Psi^{\alpha}_i | \hat{J}^{\alpha}_j - \hat{K}^{\alpha}_j | \Psi^{\alpha}_i \rangle + \sum_{j=1}^{N^{\beta}} \langle \Psi^{\alpha}_i | \hat{J}^{\beta}_j | \Psi^{\alpha}_i \rangle \qquad , \tag{3.53}$$

whereas the energy expression of the ith β orbital is analogous to the above with inversion of the α and β indices.

The final daunting expression for the total unrestricted HF energy, E_{UHF}, can be written as

$$\begin{aligned} E_{UHF} &= \sum_{i=1}^{N^{\alpha}} \langle \Psi^{\alpha}_i | \hat{H}_1 | \Psi^{\alpha}_i \rangle + \sum_{i=1}^{N^{\beta}} \langle \Psi^{\beta}_i | \hat{H}_1 | \Psi^{\beta}_i \rangle \\ &+ \frac{1}{2} \sum_{i=1}^{N^{\alpha}} \sum_{j=1}^{N^{\alpha}} \langle \Psi^{\alpha}_i | \hat{J}^{\alpha}_j - \hat{K}^{\alpha}_j) | \Psi^{\alpha}_i \rangle \\ &+ \frac{1}{2} \sum_{i=1}^{N^{\beta}} \sum_{j=1}^{N^{\beta}} \langle \Psi^{\beta}_i | \hat{J}^{\beta}_j - \hat{K}^{\beta}_j) | \Psi^{\beta}_i \rangle \\ &+ \sum_{i=1}^{N^{\alpha}} \sum_{j=1}^{N^{\beta}} \langle \Psi^{\alpha}_i | \hat{J}^{\beta}_j | \Psi^{\alpha}_i \rangle + \sum_{i=1}^{N^{\beta}} \sum_{j=1}^{N^{\alpha}} \langle \Psi^{\beta}_i | \hat{J}^{\alpha}_j | \Psi^{\beta}_i \rangle \qquad . \end{aligned} \tag{3.54}$$

These expressions can give the total energy of a neutral or ionic system, whose difference can be used to approximate the first vertical or adiabatic ionization energy (depending on weather we account or not geometry relaxation), associated with the first band in a photoionisation spectra. But how can we implement the HF equations in a computationally feasible way?

3.1.4.2 Roothaan-Hall and Pople-Nesbet equations

The restricted and unrestricted HF equations can be solved numerically for polyatomic molecules, using a set of grid points, and integrating over space using adequate methods[158,159].

However, the numerical approach is only practical for simple systems; usually, one casts the equations in matrix form and uses an expansion of known functions. The form of these functions (exponential, polynomial, gaussian, plane wave) must be chosen on the basis of suitability to the physical problem and ease of solution of the required integrals.

The matrix formulation of the restricted closed-shell HF equations was achieved by C. C. J. Roothaan[160] and independently by G. G. Hall[161], in 1951. Let's introduce a set of m known functions $\{\phi_\mu\}$, formally called *basis set*, and expand the orbital functions as

$$\Psi_i = \sum_{\mu=1}^{m} c_{i\mu}\phi_\mu \tag{3.55}$$

where $c_{i\mu}$ is a matrix of real coefficients. The advantage is obvious: we have introduced variational parameters that do not depend on the functional form of the spatial orbitals, and that can be easily adjusted to yield the best overall solution.

One should notice that we are in fact dealing with *spatial orbitals*, since we already integrated the spin part in the RHF approach. For the sake of clarity, Eq. 3.55 should be written explicitly as

$$\Psi_i \equiv \Psi_i(\mathbf{r}_i) = \sum_{\mu=1}^{m} c_{i\mu}\phi_\mu(\mathbf{r}_i) \qquad . \tag{3.56}$$

Inserting the new orbital definition in the canonical HF equations results in

$$\hat{F}_i|\sum_{\mu=1}^{m} c_{i\mu}\phi_\mu\rangle = \epsilon_i|\sum_{\mu=1}^{m} c_{i\mu}\phi_\mu\rangle \qquad , \tag{3.57}$$

which in turn transforms into

$$\sum_{\mu=1}^{m} c_{i\mu}\langle\phi_\nu|\hat{F}_i|\phi_\mu\rangle = \epsilon_i \sum_{\mu=1}^{m}\langle\phi_\nu|\phi_\mu\rangle c_{i\mu} \qquad , \tag{3.58}$$

if we form the necessary scalar products by multiplying on the left by a specific orbital ϕ_ν^*. Considering an *overlap matrix* $S_{\nu\mu}$ and a *Fock matrix* $F_{\nu\mu}$, with matrix elements $\langle\phi_\nu|\phi_\mu\rangle$ and $\langle\phi_\nu|\hat{F}_i|\phi_\mu\rangle$, respectively, then

$$\sum_{\mu=1}^{m} F_{\nu\mu}c_{i\mu} = \epsilon_i \sum_{\mu=1}^{m} S_{\nu\mu}c_{i\mu} \qquad i = 1, \ldots, n \ , \tag{3.59}$$

or, in pure matrix form,

$$\mathrm{F}\mathrm{c}_i = \epsilon_i \mathrm{S}\mathrm{c}_i \qquad , \tag{3.60}$$

where F and S are $m \times m$ dimensional, and c_i is a column matrix with m elements. If we group the c_i vectors in a $m \times n$ matrix, C, then the above equation transforms into a single matrix equation:

$$\mathrm{FC} = \epsilon\mathrm{SC} \qquad , \tag{3.61}$$

where ϵ is a $n \times n$ diagonal matrix with orbital energies ϵ_i as matrix elements. The above equations are known collectively as the *Roothaan-Hall equations*.

The overlap matrix, also called *metric matrix*, has diagonal elements equal to unity and off-diagonal elements less than one in magnitude, and represents the overlap extent between the non-orthogonal functions which compose the basis set $\{\phi_\mu\}$. It is an Hermitian matrix and thus is invariant under unitary transformations – more interestingly, it can be diagonalized by the transformation 3.40.

Diagonalization of the overlap matrix, $S_{\nu\mu}$, is essential in transforming the Roothaan single matrix equation into a proper eigenvalue equation of the form $\mathrm{A}\mathbf{x}=\lambda\mathbf{x}$. A typical procedure is that of *symmetrical orthogonalization*. By multiplying from the left by $\mathrm{S}^{-1/2}$ and inserting a unit matrix written in the form $\mathrm{S}^{-1/2}\mathrm{S}^{1/2}$, Eq. 3.60 can be rewritten as[148]

$$\begin{aligned}(\mathrm{S}^{-1/2}\mathrm{F}\mathrm{S}^{-1/2})(\mathrm{S}^{1/2}\mathrm{C}) &= \epsilon(\mathrm{S}^{-1/2}\mathrm{S}^{1/2})(\mathrm{S}^{1/2}\mathrm{C}) \\ \mathrm{F}'\mathrm{C}' &= \epsilon\mathrm{C}' \end{aligned} \tag{3.62}$$

where $\mathrm{S}=\mathrm{S}^{1/2}\mathrm{S}^{1/2}$ was used. The initial basis set can be made orthogonal by multiplying on the left by $\mathrm{S}^{-1/2}$,

$$\phi'_\mu = \mathrm{S}^{-1/2}\phi_\mu \qquad , \tag{3.63}$$

and the coefficient eigenvectors collected in C can be expressed in the original coordinate system by

$$\mathrm{C} = \mathrm{S}^{-1/2}\mathrm{C}' \qquad . \tag{3.64}$$

The set of equations comprised by the matrix eigenvalue problem of Eq. 3.62 are the transformed Roothaan-Hall equations, which can be solved for C' by diagonalizing F'. We then can evaluate C by using Eq. 3.63, and consequently use matrix C to solve the Roothaan-Hall equations 3.61.

What if we are dealing with unrestricted functions? A procedure analogous to the Roothaan-Hall derivation can also be performed. In 1954, J. A. Pople and R. K. Nesbet[162] generalized Roothaan's approximation to the case of unrestricted spin-orbitals, and ended up with a pair of coupled matrix equations in all similar to the restricted case, but specific to electrons of α or β spin,

$$\mathrm{F}^\alpha\mathrm{C}^\alpha = \epsilon^\alpha\mathrm{S}\mathrm{C}^\alpha \tag{3.65}$$

$$\mathrm{F}^\beta\mathrm{C}^\beta = \epsilon^\beta\mathrm{S}\mathrm{C}^\beta \tag{3.66}$$

which are known as the *Pople-Nesbet equations*.

The Pople-Nesbet equations can be solved exactly like the Roothaan-Hall equations, but in simultaneous. The coupling occurs in the formation of the Fock matrices albeit the fact that each equation can be solved independently.

3.1.4.3 The self-consistent-field procedure

The resolution of the HF Roothaan-Hall and Pople-Nesbet equations implies an iterative procedure due to the mean-field framework in which we formulated the multi-electronic problem. The Fock equations are non-linear equations i.e.

$$\mathrm{F} = \mathrm{F}(\mathrm{C}) \rightarrow \mathrm{F}(\mathrm{C})\mathrm{C} = \epsilon\mathrm{S}\mathrm{C}$$

and thus the formation of the Fock matrix depends on its solution.

The method employed in solving this eigenvalue problem is called *self-consistent-field* or SCF procedure. Its input values are the molecular (i) nuclear coordinates $\{\mathbf{R}_A\}$, (ii) atomic numbers $\{Z_A\}$, (iii) number of electrons N, and (iv) a basis set $\{\phi_\mu\}$. The SCF algorithm can be synthesized as follows[150]:

1. Calculate all the one- and two-electron integrals.
2. Calculate the matrix elements of the overlap matrix S.
3. Diagonalize the S matrix.
4. Calculate $\mathrm{S}^{-1/2}$.
5. Construct the matrix of initial orbital coefficients C, with e.g. $c_{ij} = 0$.

6. Construct the matrix F.
7. Make the transformation $\mathrm{F}'=\mathrm{S}^{-1/2}\ \mathrm{F}\ \mathrm{S}^{-1/2}$.
8. Diagonalize the F' matrix, in order to obtain C' and ϵ.
9. Obtain the C matrix by $\mathrm{C} = \mathrm{S}^{-1/2}\mathrm{C}'$.
10. Calculate the energy and compare it with the previously calculated value. If the difference is below a predefined threshold value, convergence is met. If not, use the newly obtained set of coefficients to construct the Fock matrix (step 6). Repeat until convergence is met.

Very often the criterion used for checking convergence is based on the *density matrix* P, defined by

$$\mathrm{P} = P_{\mu\nu} = 2\sum_{i=1}^{N/2} c_{i\mu}c_{i\nu}^{*} \qquad , \tag{3.67}$$

in the case of RHF calculations. Instead of checking the energy directly, one can form the density matrix and check if the difference between successive iterations is below some predefined value.

Convergence in a SCF procedure is not always possible. Depending on the initial guess functions (and coefficients), and the system under study, the outcome can diverge. Sometimes, it oscillates around a mean energy value (perhaps the least problematic behaviour); however, it can simply digress from a stable locus. Therefore, some methods are used to help convergence, such as Pulay's *direct inversion in the iterative subspace* (DIIS)[163] or the *quadratically convergent SCF* (QCSCF)[164]. More information regarding this subject (which is outside the scope of this thesis) can be found in the textbook by Jensen[148] and in the book chapter/review by Schlegel[165].

In this work, DIIS was always adopted as the default method in the initial approach. In the few cases of SCF convergence failure, QCSCF was employed (always with success). The importance of obtaining a stable, optimal wave function is crucial because it acts as reference and starting point in further refinements of the molecular description, like the inclusion of electron correlation.

3.1.5 Koopmans' theorem: making ends meet

After laying the first set of theoretical foundations supporting the molecular problem, it's imperative to ask: how can the experimentalist make a liaison between what he observes in the photoelectron spectrum and the results from a HF calculation?

As we stated before, the difference in total energy between the neutral and cationic ground-states of a specific molecule, obtained from RHF and UHF calculations, respectively, using the same basis set and the same geometry, yields the energy necessary to the removal of one electron i.e. the first VIE. However, with this information and based on what we have deduced so far, we can only rationalize the energy value of the first band seen in that molecule's photoelectron spectrum...

What about the rest of the spectrum? In 1934, T. Koopmans published an important theorem[166] which can be stated as follows[150]:

> *Given an N-electron HF single determinant $|^{N}\Phi_0\rangle$ with occupied and virtual spin orbital energies ϵ_a and ϵ_b, then the ionization potential to produce an $(N-1)$-electron single determinant $|^{N-1}\Phi_a\rangle$ with identical spin-orbitals, obtained by removing an electron from spin-orbital Ψ_a, and the electron affinity to produce an $(N+1)$-electron single determinant $|^{N+1}\Phi_b\rangle$ with identical spin-orbitals, obtained by adding an electron to spin-orbital Ψ_b, are just $-\epsilon_a$ and $-\epsilon_b$, respectively.*

Simply put, the ionization potentials IE_i and electron affinities EA_j can be associated with the negative energies ϵ_i^{occ} and ϵ_j^{vir} of occupied and virtual orbitals, respectively, i.e. tentative assignment of all bands in a photoelectron spectrum can be performed on the basis of the results from a RHF calculation on the neutral molecule:

$$IE_i = -\epsilon_i^{occ} \tag{3.68}$$
$$EA_j = -\epsilon_j^{vir} \tag{3.69}$$

The relative accuracy of Koopmans' theorem in predicting VIEs does not go without flaws. Two inaccuracies are on the basis of its success. One is neglect of orbital relaxation and the other is neglect of electron correlation. These two terms have different signs and similar magnitude, so they ultimately cancel each other: if non-optimization of the new set of orbital coefficients associated with the ionic system raises the ionization energy, neglect of electron correlation lowers it.

3.1.6 Electron correlation and post-Hartree-Fock methods

If we could use an infinite basis set, associated with an infinite number of coefficients, on the resolution of the HF equations via the SCF procedure, we would reach the so-called *Hartree-Fock limit*. However, even the energy at the HF limit would be different from the experimental value, due to intrinsic limitations of the mean-field approximation and use of a single Slater determinant wave function.

Using a sufficiently large basis set, the HF wave function can account for ≈99% of the energy, the remainder being attributed to electron correlation. Therefore, in the context of this thesis, *electron correlation* is assumed as the energy difference E_{corr} between the HF limit (E_{HF}) and the exact non-relativistic solution of the Schrödinger equation E_{exact}:

$$E_{corr} = E_{exact} - E_{HF} \tag{3.70}$$

The contribution from electron correlation is less important for properties of single electronic-states (molecular geometry, dipole moments, or electron density), but plays an important role in predicting properties which arise as energy differences (ionization, dissociation, bond energies, or the positions of bands in a spectrum)[167]. Most methods developed after the HF approximation deal exactly with the subject of electron correlation and ways of including it in the one-electron theoretical framework. They are commonly known as *post-Hartree-Fock methods*.

In this section, we will briefly review the post-HF methods used in the assignment of the photoelectron spectra and in the rationalization of the gas-phase thermal decomposition results. Mathematical completeness will be deprecated in favour of a more conceptual viewpoint, without however losing the formalism necessary to overcome possible caveats in their application to real physical problems.

3.1.6.1 Configuration interaction method

Electron correlation is partially accounted for within the HF method, by using the Slater determinant and respecting the Pauli exclusion principle: electrons of equal spin cannot share the same orbital, so *exchange repulsion* (or *Fermi correlation*) is supported. However, the motion of electrons of opposite spin, termed *Coulomb repulsion*, is not accounted for.

Conceptually, *configuration interaction* (CI) is the simplest way of retrieving electron correlation in the many-electron formulation. It does so by modifying the molecular wave function, extending the latter beyond the single Slater determinant. Consider

the following expansion of Slater determinants

$$\Phi = \sum_{i=1}^{\infty} C_i \Phi_i \qquad , \tag{3.71}$$

where C_i is the variational weight coefficient associated with specific Slater determinant Φ_i. If the above sum is taken to infinity, it represents a *complete CI wave function*, whereas if we truncate the summation at the limit of a finite size basis set, the approximation is called *full CI*. The latter approach remains the most complete calculation of correlation energy using a finite sized basis set, and its results are often used as benchmarks tools for other theoretical methods. However, it is only feasible for very small systems and minimal sets.

Construction of Slater determinants other than the initial configuration (see Section 3.1.3), is based on a simple procedure and takes advantage of the fact that one uses a basis set with more available spin-orbitals than the number of electrons.

By promoting an electron from an occupied orbital to a vacant (virtual) orbital, one is modelling a *singly excited state*. If two promotions of that kind occur, then we face a *doubly excited state*. If three, a *triply excited state* and so forth. In picking electrons from occupied states and taking all their possible promotions to vacant orbitals, one gets a summation over different excited Slater determinants, which are preferentially grouped by excitation type (single, double, triple, quadruple, quintuple, ..., n-tuple excitations).

The number (cardinality) of possible n-tuple excited Slater determinants (SD) is defined as:

$$|\mathrm{SD}|(N,K,n) = \binom{N}{n}\binom{2K-N}{n} \qquad , \tag{3.72}$$

where $2K$ is the number of spin-orbitals composing the set and N is the number of occupied orbitals (electrons). Imagine you want to write a CI wave function for 5MTZ (44 electrons), including single excitations only, from a finite basis set of 88 spin-orbitals. The number of singly excited SDs would be $\binom{44}{1} \times \binom{88-44}{1}$ plus the initial reference determinant, amounting to 1937 different determinants. Additional inclusion of double excitations, would raise this number to an astonishing value: 896 853, almost one million determinants!

The mathematical form of the full CI expansion can be written explicitly as:

$$|\Phi\rangle = C_0|\Phi_0\rangle + \left(\frac{1}{1!}\right)^2 \sum_{a,r} C_a^r|\Phi_a^r\rangle + \left(\frac{1}{2!}\right)^2 \sum_{\substack{a,b \\ r,s}} C_{ab}^{rs}|\Phi_{ab}^{rs}\rangle + \left(\frac{1}{3!}\right)^2 \sum_{\substack{a,b,c \\ r,s,t}} C_{abc}^{rst}|\Phi_{abc}^{rst}\rangle + \ldots, \tag{3.73}$$

or symbolical as

$$|\Phi\rangle = C_0|\Phi_0\rangle + C_S|\Phi_S\rangle + C_D|\Phi_D\rangle + C_T|\Phi_T\rangle + \ldots \ . \tag{3.74}$$

where S, D and T label single, double and triple excitations. $|\Phi_0\rangle$ is the reference HF-SCF optimized wave function, upon which the excited determinants are constructed. A determinant in which a electron that was occupying spin-orbital Ψ_a (in the HF reference function) is promoted to an unoccupied spin-orbital Ψ_r is denoted by Φ_a^r. The same reasoning applies to higher excited determinants: pair excitation is described by a Φ_{ab}^{rs} wave function, trio excitation by Φ_{abc}^{rst}, etc.

Similar to the derivation of HF equations, the CI approach is also an optimization problem, under the constraint that the total CI wave function is normalized i.e.

$\langle\Phi_i|\Phi_j\rangle = \delta_{ij}$. Therefore, using again the method of undetermined multipliers, one gets the Lagrange function for the system described by the CI wave function[148],

$$L = \sum_{i=1} C_i E_i + \sum_{i=1}\sum_{j\neq i} C_i C_j \langle\Phi_i|\hat{H}|\Phi_j\rangle - \lambda\left(\sum_{i=1} C_i^2 - 1\right) \tag{3.75}$$

which, upon employing the variational procedure (setting the derivative with respect to the expansion coefficients C_i to zero), transforms into

$$\delta L = \sum_{i=1} \delta C_i (E_i - \lambda) + \sum_{j\neq i} C_j \langle\Phi_i|\hat{H}|\Phi_j\rangle = 0 \tag{3.76}$$

This minimization leads to a set of i expressions which form the *CI secular matrix equation*

$$HC = EC \tag{3.77}$$

which is equivalent to writing:

$$\begin{bmatrix} H_{11}-E & H_{12}-E & \cdots & H_{1j}-E \\ H_{21}-E & H_{22}-E & \cdots & H_{2j}-E \\ \vdots & & & \vdots \\ H_{i1}-E & H_{i2}-E & \cdots & H_{ij}-E \end{bmatrix} \begin{bmatrix} C_1 \\ C_2 \\ \vdots \\ C_i \end{bmatrix} = \begin{bmatrix} 0 \\ 0 \\ \vdots \\ 0 \end{bmatrix} \tag{3.78}$$

where the matrix elements H_{ij} are defined as $\langle\Phi_i|H|\Phi_j\rangle$. The above matrix equation can be solved by diagonalization of the CI matrix: one gets a set of polynomial equations in E, whose roots are the CI energies of the ground-state, of the 1^{st} excited state, of the 2^{nd} excited state, and so on.

In layman terms, we construct a set of excited determinants and mix them for the overall CI energy; by finding the optimal mixture values, we get the best solution i.e. the one which minimizes the CI energy. It is worth noting that, in this procedure, we are not varying the spin-orbital coefficients c_{ij} as we did before, but simply varying the weight C_{ij} of the different determinants.

But how can one evaluate the matrix elements $\langle\Phi_i|\hat{H}|\Phi_j\rangle$ between different determinants? A set of rules can be derived to simplify calculation of some elements, decreasing the computational cost. The most important is perhaps the *Brillouin theorem*, which states that the matrix elements between the reference HF wave function Φ_0 and any single excited determinant Φ_S is essentially zero, thus $\langle\Phi_S|\hat{H}|\Phi_0\rangle = 0$. Moreover, because one-and two-electron integrals of Hartree products which differ by more than two orbitals are zero, the matrix elements between triple or higher-order excited determinants and the reference Φ_0 are excluded. However, the single excited determinants affect *indirectly* the CI energy because they can mix with double excited determinants, and the latter have non-zero matrix elements with the reference HF determinant.

Using the already familiar notation for one- and two-electron integrals and laying these integrals for the CI wave function, we can arrive at the following expressions, known as *Slater-Condon rules*[168,169],

$$\langle\Phi_1|\hat{H}|\Phi_1\rangle = \sum_{i}^{N}\langle\Psi_i|\hat{H}_1|\Psi_i\rangle + \sum_{i>j}^{N}\langle\Psi_i\Psi_j|\hat{H}_2(1-\hat{P}_{12})|\Psi_i\Psi_j\rangle \tag{3.79}$$

$$\langle\Phi_1|\hat{H}|\Phi_2\rangle = \langle\Psi_k|\hat{H}_1|\Psi_i\rangle + \sum_{j}^{N}\langle\Psi_i\Psi_j|\hat{H}_2(1-\hat{P}_{12})|\Psi_k\Psi_j\rangle \tag{3.80}$$

$$\langle\Phi_1|\hat{H}|\Phi_3\rangle = \langle\Psi_i\Psi_j|\hat{H}_2(1-\hat{P}_{12})|\Psi_k\Psi_l\rangle \tag{3.81}$$

which explicitly tell us how to evaluate the matrix elements between Slater determinants. In the above expression, i, j, k and l indexes identify different spin-orbitals composing the determinants; also, Φ_1 and Φ_2 differ by only one orbital, and Φ_3 by only two. As was stated before, matrix elements between determinants which differ by more than two spin-orbitals are null i.e. $\langle\Phi_T|\hat{H}|\Phi_0\rangle$=0, $\langle\Phi_Q|\hat{H}|\Phi_S\rangle$=0, etc.

In most medium-sized systems (like our tetrazoles), the above integrals are only evaluated through single and double excitations, in what is known as the *configuration interaction singles and doubles* (CISD) method. Triple excitations can be included as an *ad-hoc* correction and are not explicitly computed – the method is termed CISD(T). CI methods which account only for finite sets of excited determinants are called *truncated CI* methods – CIS, CID, CISD, CISDT and CISDTQ – and are often used in systems where the reference HF solution is inadequate to express the ground-state function, or in the study of excited states.

Regarding the work presented here, the CI approximation was used at two moments: as part of a composite method for determining relative energies with high accuracy, and as a crutch to obtain specific Slater determinants describing core-ionized states of 5ATZ and 5MTZ. Further information on the subject of configuration interaction can be found, for example, in the textbook of Szabo and Ostlund[150], in the reference article by Pople and co-workers[170] and in the extensive review of Sherrill and Schaefer[171].

3.1.6.2 Møller-Plesset perturbation theory

If CI approximation is the easiest electron correlation method to understand, then Møller-Plesset perturbation theory (MPPT) is perhaps the easiest to implement. This method is due to C. Møller and M. S. Plessett[172] and results from a specific formalism of the more general theory of perturbation, originally developed by Schrödinger[173], based on the work of Lord Rayleigh.

The essential idea behind perturbation theory is the division of the Hamiltonian into two parts: one for which the mathematical form and solutions are known, and another which stems from a small perturbation acting on the system. If we take the unperturbed part as the reference HF eigenvectors and eigenvalues, then the perturbation will be associated with the correlation energy whose contribution to the overall solution we are so eager to estimate. MPPT is commonly referred to as MPn, where n defines the order to which the perturbation expansion is considered.

Aside from the ease of implementation, the MPn methods are known to be *size-consistent*. Size-consistency is a desirable property in studies which involve fragmentation of molecular species, like analysis of the thermal decomposition pathways of tetrazoles and azides. Consider a dimer AB which fragments into monomers A+B; if a method is size-consistent, then the equality $E(AB) = E(A) + E(B)$ holds true. This is particularly important if one is trying to estimate which multi-step dissociation pathway is energetically more advantageous.

How about the mathematical form of the MPn equations? The Hamiltonian is partitioned as[150]:

$$\hat{H} = \hat{H}_0 + \hat{V} \quad , \tag{3.82}$$

where

$$\hat{H}_0 = \sum_i^N \hat{F}_i = \sum_i^N \left[\hat{H}_i + \sum_{j=1}^N \hat{J}_j - \hat{K}_j \right] \tag{3.83}$$

$$\hat{V} = \sum_{i<j} r_{ij}^{-1} - \sum_{i=1}^N \sum_{j=1}^N \hat{J}_j - \hat{K}_j \tag{3.84}$$

Introducing the notation $E^{(n)}$, where n represents the order of the correction, it can be showed that the zeroth-, 1st- and 2nd-order perturbation energies of the system are expressed as

$$E^{(0)} = \sum_{i=1}^{N} \epsilon_i \quad , \tag{3.85}$$

$$E^{(1)} = \langle \Psi_0 | \hat{V} | \Phi_0 \rangle = -\frac{1}{2} \sum_{i,j} \langle \Phi_i | \hat{J}_j - \hat{K}_j | \Phi_i \rangle \quad \text{and} \tag{3.86}$$

$$E^{(2)} = \sum_{i<j}^{occ} \sum_{k<l}^{vir} \frac{|\langle \Phi_0 | \hat{V} | \Phi_{ij}^{kl} \rangle|^2}{\epsilon_i + \epsilon_j - \epsilon_k - \epsilon_l} \quad . \tag{3.87}$$

In the last equation, we employed the notation used prior in the CI discussion to represent doubly excited determinants. The HF energy, E_{HF} is equivalent to the sum $E^{(0)} + E^{(1)}$, therefore electron correlation is only considered within 2nd-order correction and beyond. The MP2 energy is the sum of the perturbation energies until 2nd-order:

$$\begin{aligned} E_{MP2} &= E^{(0)} + E^{(1)} + E^{(2)} \\ &= E_{HF} + \sum_{i<j}^{occ} \sum_{k<l}^{vir} \frac{|\langle \Psi_i \Psi_j | \hat{J}_j - \hat{K}_j | \Psi_k \Psi_l \rangle|^2}{\epsilon_i + \epsilon_j - \epsilon_k - \epsilon_l} \quad . \end{aligned} \tag{3.88}$$

Within the MP2 scheme we are in fact evaluating the energy difference between two Slater determinants, one representing the reference HF wave function and the other a doubly excited determinant; furthermore, we are approximating this by the difference between initial (occupied) and final (virtual) orbital energies, $\epsilon_{i,j} - \epsilon_{k,l}$. Computationally, we only need the two-electron integrals between pairs of orbitals to be evaluated and therefore a MP2 calculation draws as much time to complete as the corresponding HF calculation.

Higher-order perturbation MPn formulas can be derived, which include until triple, quadruple, quintuple or n-tuple excited determinants. MP2 is approximately equivalent to CISD and recovers 80%-90% of the total correlation energy[150]. On the downside, as MPn methods are not derived from a variational procedure, there is no guarantee that the resulting energy is an upper bound to the exact (full CI) energy.

Over the course of this work, the MP2 flavour was used as a method for determining ionization energies (through Koopmans' theorem) of tetrazole and azido compounds, as well as total energies. For high-accuracy relative energies, MP4 was also used as part of composite methods. Explicit derivation of the MPn expressions can be found in Szabo's *Modern Quantum Chemistry* textbook. An insightful and extensive comparison between MP5 and other electron correlation methods, carried out by Pople and coworkers, can also be found in the literature[174].

3.1.6.3 Electron propagator theory: OVGF and P3 methods

Until now, we have talked about two approaches for addressing electron correlation in molecular systems: CI and MPn methods. The first is variational and tries to modify the trial wave function in order to find the optimum mixture of Slater determinants; the latter is not variational and treats correlation as a perturbation to the reference HF Hamiltonian.

This section now turns headlights into a method which reaches electron correlation through a somewhat different formalism. Moreover, the ionization energies are predicted directly from an extension of the Koopmans' theorem encrusted in the theory.

The framework in which *outer-valence Green's function* (OVGF) method[175,176] and *partial third-order* (P3) quasi-particle approximation[177] are developed is called one-particle *many-body Green's function* (MBGF) or *electron propagator theory* (EPT)[150,178].

The complete formalism is given in several textbooks and review articles, and will not be considered here. However, it is worth mentioning Linderberg and Öhrn[178] textbook– *Propagators in Quantum Chemistry* – as one of the few references focusing on propagators and their applications, without disregarding the dense mathematical thread. The textbook by Ostlund and Szabo[150], frequently referred throughout this thesis, is also an excellent choice for understanding the basis of one-elecron Green's function (GF) theory applied to the computation of molecular properties. For an introductory text, the recent review by Danovich[179] serves the purpose of presenting the essential theory, emphasizing the concepts and utility of GF in predicting chemical properties.

The basic idea behind GF applied to the many-electron conundrum: to calculate system properties with extended accuracy one does not need to know exactly how *all particles* behave, but rather how *one* or *two particles* relevant to the desired property behave.

Green's function is a synonymous of *propagator*, and arises from the time evolution of a given quantity. There are several types of propagators (electron, polarization), but we are only interested in *electron propagators* i.e. the Green's function corresponding to the addition or removal of an electron.

In the next explanation, we will follow the textbook of Szabo[150] in order to introduce some key aspects of GF theory, namely the concepts of *pole* and *self-energy*. Then we will briefly interface these concepts with the actual OVGF and P3 methods. Please be aware though, that we are always envisioning the practical aspects of theory and therefore any additional algebra will be kept to a minimum. In fact, we'll try to avoid quantum field formalism as much as possible, by tackling, for example, the introduction of annihilation and creation operators.

Let's assume we want to solve the following matrix equation for a:

$$(E\mathbb{I} - H_0)a = b \qquad , \tag{3.89}$$

where E is a parameter, $\mathbb{I}$ is the identity matrix, H_0 is a N square Hermitian matrix and a and b are column matrices. A solution can be found if we compute the matrix $G_0(E)$ defined as:

$$G_0(E) = (E\mathbb{I} - H_0)^{-1} \qquad . \tag{3.90}$$

which leads to

$$a = G_0(E)b \quad \rightarrow \quad a_i = \sum_j [G_0(E)]_{ij} b_j \qquad . \tag{3.91}$$

If the eigenvalues E_0^α and eigenvectors c^α of H_0 are known, such as $H_0 c^\alpha = E_0^\alpha c^\alpha$ then

$$[G_0(E)]_{ij} = \sum_\alpha \frac{c_i^\alpha (c_j^\alpha)^*}{E - E_0^\alpha} \qquad \alpha = 1, \ldots, N \tag{3.92}$$

In pure mathematical language, this means that one can solve a set of inhomogeneous differential equations if solutions to the homogeneous equivalent are known and also a set of particular solutions (proportional to the degree and number of equations).

Regarding Eq. 3.92, it is important to define right away the meaning of *poles*, which are ubiquitous in complex analysis: *poles* are the values of E which render the denominator null i.e. the values for which the matrix elements show singularities.

We can write the continuous form of the above matrix formulation, for a generic inhomogeneous differential equation as

$$(E - \hat{H}_0)a(x) = b(x) \qquad , \tag{3.93}$$

with solution

$$a(x) = \int G_0(x, x', E)b(x')dx' \qquad , \tag{3.94}$$

and with

$$G_0(x, x', E) = \sum_{\alpha} \frac{\Psi_x^{\alpha}(\Psi_{x'}^{\alpha})^*}{E - E_0^{\alpha}} \qquad \alpha = 1, \ldots, N \qquad , \tag{3.95}$$

where we explicitly denoted the dependence of G_0 on the coordinates (x, x') and the parameter E, and conveniently associated x and x' variables with the usual wave function symbol Ψ. Recall that these wave functions are eigenvectors of the homogeneous equation ($b(x) = 0$), and that we used them to express both $a(x)$ and $b(x)$ on the inhomogeneous equation.

If we add a perturbation $\hat{V}_x$ to the operator $\hat{H}_0$, to what expressions will we arrive to? Considering $\hat{H} = \hat{H}_0 + \hat{V}_x$ and $b(x) = \delta_{xx'}$, we can derive a set of equations similar to the above. To the differential inhomogeneous equation

$$(E - \hat{H}_0)G(x, x', E) = \delta_{xx'} + \hat{V}_x G(x, x', E) \qquad , \tag{3.96}$$

where

$$\begin{aligned} a(x) &\equiv G(x, x', E) \\ b(x) &\equiv \delta_{xx'} + \hat{V}_x G(x, x', E) \qquad , \end{aligned}$$

corresponds a Green's function of the form

$$G(x, x', E) = G_0(x, x', E) + \int G_0(x, x'', E)\hat{V}_{x''}G(x'', x', E)dx'' \tag{3.97}$$

where x'' was introduced to indicate integration over a distinct variable. This last expression is equivalent to the matrix equation

$$G(E) = G_0(E) + G_0(E)VG(E) \tag{3.98}$$

Let's now take a conceptual leap which sits on the basis of the one-particle GF methods. Recalling $\hat{H}_0$ as a summation of one-particle Fock operators over the N spin orbitals composing the basis set (see Eq. 3.83), we reformulate Eq. 3.95 as the *Hartree-Fock Green's function* (HFGF):

$$G_0(\mathbf{x}, \mathbf{x'}, E) = \sum_i \frac{\Psi_i(\mathbf{x})\Psi_i^*(\mathbf{x'})}{E - \epsilon_i} \tag{3.99}$$

The matrix elements of HFGF are defined as:

$$[G_0(E)]_{ij} = \frac{\delta_{ij}}{E - \epsilon_i} \tag{3.100}$$

where ϵ_i are the HF orbital energies which form the diagonal matrix ϵ (see Eq. 3.61). It is evident from the above expression that the poles of the HFGF are simply the HF orbital energies; so we have managed to formulate the HF equations in a rather different approach.

Second conceptual step to be overcome: if $G_0(E)$ gives identical results to the HF method and if the HF method rendered only *approximate* solutions to the orbital energies, how can we improve on that and reach an *exact* value within the GF framework? In other words, in the same way as there is a GFHF method with poles at the eigenvalues of the HF Hamiltonian, there should be a *many-body* GF (MBGF) with poles at the exact differences between eigenvalues.

F. Dyson answered this question by introducing the concept of *self-energy*[180], an effective potential $\Sigma(E)$ which is energy dependent. The *Dyson equation*,

$$G(E) = G_0(E) + G_0(E)\Sigma(E)G(E) \tag{3.101}$$

identical to the GF equation plus the perturbation term (Eq. 3.98), forms an integral expression which defines the MBGF in the basis of HF orbitals. Similarly to the MPn methods, the self-energy can be expanded in higher-order terms:

$$\Sigma(E) = \Sigma^{(2)}(E) + \Sigma^{(3)}(E) + \ldots + \Sigma^{(n)}(E) \tag{3.102}$$

Moreover, the self-energy potential includes all relaxation and correlation corrections, improving the Koopmans' theorem VIEs.

To obtain the VIEs of an N-electron system, one has to solve Dyson's equation for $G(E)$ and find the values of the poles of the $G(E)$ matrix elements. Multiplying by $G_0(E)^{-1}$ on the left and by $G(E)^{-1}$ on the right from both sides of Eq. 3.101 and using Eq. 3.100 one gets:

$$\begin{aligned} & G_0(E)^{-1} = G(E)^{-1} + \Sigma(E) \\ & \Leftrightarrow G(E) = [G_0(E)^{-1} - \Sigma(E)]^{-1} \\ & \Leftrightarrow G(E) = [E\mathbb{I} - \epsilon - \Sigma(E)]^{-1} \end{aligned} \tag{3.103}$$

Notice that $G(E)$ does not exist when E takes specific pole values; this means that, at specific pole values, $G(E)$ is non-invertible. In matrix algebra, a non-invertible square matrix is called *degenerate*; moreover, it is degenerate if and only if its determinant is zero. Therefore, improvement of Koopmans' VIEs can be accomplished within the GF formalism by solving the matrix equation

$$|E\mathbb{I} - \epsilon - \Sigma(E)| = 0 \tag{3.104}$$

Truncation of the expansion 3.102 regulates the degree of accuracy one is willing to have in the correction of the orbital energies. Basically, it is the expression of matrix $\Sigma(E)$ which distinguishes the different flavours of one-electron GF methods encountered in the literature.

The OVGF method, developed by L. S. Cederbaum and co-workers[175,176], is built on the shear fact that usually one only needs the value of few VIEs (the ones from outer-valence orbitals) to characterize molecules in terms of their chemical bonding properties[179]. The method uses a finite expansion of the self-energy, through 3^{rd}-order, and estimates the contribution from higher-orders by a renormalization procedure. The explicit form of $\Sigma(E)$ in the OVGF approach is:

$$\Sigma(E)_{OVGF} = \Sigma^{(2)}(E) + (1 + A)^{-1}\Sigma^{(3)}(E) \quad , \tag{3.105}$$

where A is a constant. Three versions of the OVGF method were originally created by Cederbaum's team – A, B and C, which differ by the number of terms included in the diagonal elements of $\Sigma^{(3)}(E)$. A very useful algorithm was sought by J. V. Ortiz for choosing among the three approximations[181]. Regarding tetrazole and azido

compounds studied herein, with VIEs of interest between ca. 9-15 eV, version B is the most adequate choice.

The P3 method, developed by Ortiz[177], tries to further simplify the OVGF procedure by eliminating the renormalization constant A and some additional terms from $\Sigma^{(3)}(E)$. The P3 method is known to be as accurate as the OVGF procedure, but at decreased computational cost. Regarding the VIEs of a small set of closed-shell molecules, the P3 procedure yields a mean absolute deviation (MAD) of 0.19 eV, whereas OVGF yields a MAD of 0.25 eV[177].

3.1.6.4 Density functional theory

In this section, we shall present an alternative formulation of the many-electron problem which shares no conceptual resemblance with the previous methods, aside from some mathematical tools required for its resolution. The framework is called *density functional theory* or DFT. Due to the fact that DFT was used sparsely during this thesis, we will focus only on its essential concepts. Further reading can be found in the seminal textbook by Parr and Yang, *Density-Functional Theory of Atoms and Molecules*[182], and in many review articles[183–186].

DFT draws its origins in the proof by Hohenberg and Kohn[187] that the ground-state electronic energy is determined completely by the electron density ρ i.e. that there is a direct correspondence between the electron density of a system and the energy.

How to connect *electron density* – a function of wave functions, and *energy* – a real value? Through a *functional*, a transformation upon functions, which returns a number (remember the Lagrange function?). The goal of DFT methods is to design functionals $A[\rho]$ which connect the electron density ρ with the energy E[148]. The accuracy of the method can only be evaluated by comparison between experimental results and the outcome of a given functional.

Contrary to the HF perspective of electrons in a central field of positive nuclei (the MO theory), the DFT approach considers nuclei immersed in an electron cloud. The effect of the nuclei is envisioned like an external potential to the electron cloud. The energy functional $E[\rho]$ for a system of N-electrons can be written as the sum of the *Hohenberg-Kohn* functional, $F[\rho]$, and the external potential from the nuclei, $V_{ne}[\rho]$, as

$$E[\rho] = F[\rho] + V_{ne}[\rho] = F[\rho] + \int \rho(r)v(r)dr \tag{3.106}$$

with

$$F[\rho] = T[\rho] + V_{ee}[\rho] \tag{3.107}$$

where the contribution from the nuclear-nuclear repulsion was ignored and $v(r)$ represents the external potential felt by the electrons.

The Hohenberg-Kohn functional is the same for different molecules because it is only dependent on the number of electrons and not on an external potential. It is composed by the kinetic energy functional $T[\rho]$, and the electron repulsion functional $V_{ee}[\rho]$.

The minimum of the energy functional $E[\rho]$ can be obtained by the variational principle (also proved by Hohenberg and Kohn) using Lagrange's method of undetermined multipliers (which is omnipresent throughout QM):

$$\delta\left[E[\rho] - \mu\left(\int \rho(r)v(r)dr - n\right)\right] = 0 \tag{3.108}$$

where the coinstrain is $\int \rho(r)v(r)dr = n$ i.e. the electron density ρ evaluated throughout all space dr must be equal to the number of electrons n, and μ is the Lagrange multiplier.

The above leads to the expression

$$\frac{\delta F[\rho]}{\delta \rho(r)} + v(r) = \mu \qquad . \tag{3.109}$$

So the problem is now to know the exact form or a very accurate approximation to the functional $F[\rho]$. This issued was treated by Kohn and Sham[188] (KS), in 1965, by establishing a liaison between the well-known Hartree-Fock formalism and that of Hohenberg-Kohn. The following approximation to $F[\rho]$ was made:

$$T[\rho] \equiv T_s[\rho] + E_{xc}[\rho] \tag{3.110}$$

where $T_s[\rho]$ is the exact kinetic energy of a system of non-interacting electrons and $E_{xc}[\rho]$ is the exchange ($_x$) and correlation ($_c$) energy of an interacting system with the same electron density as the non-interacting one. Eq. 3.107 can be rewritten as

$$F[\rho] = T_s[\rho] + J[\rho] + E_{xc}[\rho] \tag{3.111}$$

where $J[\rho]$ is the classical electron-electron repulsion term. As a consequence, the variational equation is redefined as

$$\frac{\delta T_s[\rho]}{\delta \rho(r)} + v_{\text{eff}}(r) = \mu \qquad , \tag{3.112}$$

where

$$v_{\text{eff}}(r) = v(r) + \frac{\delta J[\rho]}{\delta \rho(r)} + \frac{\delta E_{xc}[\rho]}{\delta \rho(r)} \qquad . \tag{3.113}$$

and

$$J[\rho] = \frac{1}{2} \int \frac{\rho(r)\rho(r')}{|r - r'|}\, dr\, dr' \qquad . \tag{3.114}$$

Since $v_{\text{eff}}(r)$ is a one-electron function, it follows that we can reach something similar to the HF equations 3.41:

$$\left[\hat{H}_1 + v_{\text{eff}}(r)\right] |\Psi_i\rangle = \epsilon_i |\Psi_i\rangle \ , \ i = 1, \ldots, N \qquad . \tag{3.115}$$

The above set of equations are known as the *canonical Kohn-Sham equations*, and although they resemble the HF counterpart, their are conceptually different.

The *Kohn-Sham molecular orbitals* do not have any physical meaning and so the Koopmans' theorem cannot be applied to estimate the ionization energies; this is an obvious drawback when we are interested in using electronic structure calculations to effectively assign photoelectron spectra. In fact, only the negative of the energy of the *highest occupied molecular orbital* (HOMO) can be assigned to the first ionization energy.

We still have to define the mathematical expression for the exchange-correlation functional E_{xc}. The plethora of available options[186], with their own particular advantages and caveats, would take us a whole chapter to discuss, and so only the one single functional used in this thesis will be described.

Becke's three-parameter functional[189] (B3) coupled to the Lee-Yang-Parr functional (LYP)[190], termed B3LYP[191,192], uses a mixture of HF exchange and DFT exchange-correlation functionals, with adjustable parameters optimized to fit a set of properties (atomization energies, ionization energies and proton affinities) extracted from *empirical* data. The use of this functional detracts the DFT method from the ways of a pure *ab initio* approach. The expression for E_{xc}^{B3LYP} is[191,192]:

$$E_{xc}^{\text{B3LYP}} = (1 - a_0)E_x^{\text{LSDA}} + a_0(E_x^{\text{HF}}) + a_x \Delta E_x^{\text{B88}} + a_c E_c^{\text{LYP}} + (1 - a_c)E_c^{\text{VWN}} \tag{3.116}$$

where $a_0 = 0.2$, $a_x = 0.72$ and $a_x = 0.81$. Explicit definitions for the local-spin density approximation functional (E_x^{LSDA})[182,193], exact exchange functional (E_x^{HF})[182], Becke's gradient correction to the exchange functional ($\Delta E_x^{\mathrm{B88}}$)[194], and the local correlation functional of Vosko, Wilk and Nusair[193] can be found in the literature.

Finally, the DFT KS equations can be solved iteratively, just like in the HF equations, using the SCF approach. The advantage is that with virtually the same computationally effort DFT results account for electron correlation, whereas HF don't.

3.1.7 Basis sets

Molecular orbitals (MO) can be thought as functions which are projected onto the finite dimension of a basis set. Therefore, the choice of functions comprising the basis set is of vital importance in the degree of accuracy achieved. In other words, MOs will be as close to its exact description as the functions in the basis set allow.

As we have seen before, the Slater determinant can be expanded as a linear combination of one-electron functions. The convention *linear-combination of atomic orbitals* (LCAO) is often used to designate MOs, explicitly stating how the molecular wave function is formed. However, these functions are usually not solutions to the atomic Schrödinger equation.

Two types of functions are commonly disseminated: the *Slater type orbitals* (STO)[195] and the *Gaussian type orbitals* (GTO)[196]. STOs have the general form

$$\Psi_{\mathrm{STO}} = NY_{l,m}(\theta,\psi)r^{n-1}e^{-\zeta r} \quad , \tag{3.117}$$

where N is a normalization constant, $Y_{l,m}$ the hydrogen spherical harmonic, (n,l,m) the quantum numbers and ζ a parameter. GTOs have the general form

$$\Psi_{\mathrm{GTO}} = NY_{l,m}(\theta,\psi)r^{2n-2-l}e^{-\zeta r^2} \qquad \text{(spherical)} \tag{3.118}$$

$$\Psi_{\mathrm{GTO}} = Nx^{l_x}y^{l_y}z^{l_z}e^{-\zeta r^2} \qquad \text{(cartesian)} \tag{3.119}$$

where the sum $l_x + l_y + l_z$ defines the type or orbital, and ζ is again a parameter for adjusting the radial size.

GTOs were introduced as they speed up the evaluation of two-electron integrals by 4-5 times, when compared with STOs. Moreover, calculation of three- and four-centre two-electron integrals cannot be performed analytically when using STOs. The product of two Gaussian functions is also a Gaussian function, a fact that eases the evaluation of integrals with AOs centred at different nuclei. On the downside, GTOs have zero slope at the nucleus, in contrast with STOs which behave correctly by having a discontinuous derivative at $r = 0$ (known as the "cusp" behaviour).

A *minimum basis set* ascribes the system with only enough functions to contain all electrons. For describing hydrogen, we would only need a $1s$ function; for the first-row of the periodic table, we would need two s-functions ($1s$ and $2s$) and one set of p-functions ($2p_x$, $2p_y$ and $2p_z$); for the second-row elements, three s-functions ($1s$, 2s and 3s) and two sets of p-functions ($2p$ and $3p$).

A *double-ζ* basis set doubles all the functions from the minimum basis set, whereas *triple-ζ* has three times the number of minimum functions. If only the number of valence orbitals is doubled or tripled, then the basis set is also called *split-valence* or just *valence*.

Before particularizing which basis sets were used throughout this work, some additional concepts need to be presented. First, GTOs are frequently, if not always, *centred at the nuclei position*. Second, GTOs are either used directly in their original form, or

form linear combinations with coefficients optimized to fit a well-adjusted STO. Consequently, the orbitals are either called *primitive Gaussian-type orbitals* (PGTOs) or *contracted Gaussian-type orbitals* (CGTOs).

Contraction schemes are important in describing core-electron orbitals, specifically in mimicking the cusp condition absent from the GTOs. In practice, more functions are needed to model the correct behaviour near the nucleus. If the interest is only in obtaining valence ionization energies, there is no need for equal variational freedom in adjusting the 1s inner orbitals. More functions can be used to correctly describe the cusp condition and fix the variational coefficients of these AOs, letting only two or three more functions to be optimized in the SCF procedure.

Contrary to inner-core contraction, spatial augmentation of the "tails" of orbitals describing valence electrons leads to the so-called *diffuse functions*. These are often denoted by the prefix *aug−* or by adding "+" or "++" to the basis set notation. If one aims at modelling anions with loosely bound electrons or highly-excited Rydberg states, the use of diffuse functions is imperative. With "+" only heavy atoms have their range extended, whereas "++" gives all atoms longer "tails".

Finally, *polarization* is also a very important characteristic of a basis set. In order to extend the spatial flexibility of the MO, and correctly describe the electron distribution in the interatomic space, the atoms need AOs of angular momentum higher than that of the minimum basis set. These are called *polarization functions*: p-functions which polarize s-functions and f-functions for polarizing d-functions, for example. To indicate polarization, the basis set notation includes the letter "p" or "P", one or two asterisks ,"*" or "**", or explicitly state how the functions are polarized i.e. "(2d,2p)" in the basis set indicates two-sets of d-functions on the heavy atoms and two-sets of p-functions on the hydrogens.

3.1.7.1 Pople basis sets

The basis sets designed by Pople and co-workers follow the notation[148] *a-bcd*, where *a* indicates how many PGTOs are used for representing the core-orbitals, and *bcd* gives the number of PGTOs in the double-valence (*bc*) or triple-valence (*bcd*) variants. *G* only means that we are using GTOs.

The use of diffuse functions is denoted by placing "+" or "++" *before* "*G*"; use of polarization functions is denoted by one/two asterisks or the explicit polarization functions *after* "*G*" .

In this thesis, we have used almost all variants of Pople's valence double- and triple-ζ basis set. For the record: 6-31G(d), 6-31G(d,p), 6-31++G(d,p) and 6-311++G(d,p). Most information regarding these sets can be found in the literature[197–201] and will not be given here.

3.1.7.2 Dunning's correlation consistent basis sets

Dunning and co-workers developed basis sets which use a *generalized contraction scheme* i.e. where *all* the functions to be contracted enter in the optimization procedure albeit with different coefficients. Moreover, the basis are designed so that functions which contribute similar amounts of correlation energy are included at the same stage, independently of the function type[148]. This leads to well-balanced basis sets, for which increasing the number of functions (double-, triple-, quadruple-, quintuple-ζ, etc.) effectively leads to the *complete basis set limit* (CBS) i.e. we can reach by extrapolation a energy value similar to that of the full CI approach.

These basis sets are known as *correlation-consistent* (*cc*) basis sets, and they are presented as cc-pVXZ , where "p" denotes polarization, "V" is for valence and "Z"

stands for zeta. X can be D, T, Q, 5 and 6 and denotes how many contracted functions are used for the H atom (D – 2 functions, T – 3 functions, and so on). Diffuse functions can also be added to the basis sets, being represented by the prefix *aug-*.

In our work, we have used the cc-pVDZ and cc-pVTZ basis sets, and their augmented versions with diffuse functions, aug-cc-pVDZ and aug-cc-pVTZ. Explicit information regarding these sets for the H, C, N and O atoms can be found in the literature[202,203].

3.1.7.3 Ahlrichs basis sets

As an intermediate quality set between Pople's and Dunning's proposals, we have Ahlrichs' pVXZ basis sets, where the "p" denotes polarization and X can assume the letters D, T and Q (with the same meaning as before). The contraction scheme is segmented, but the polarization exponents are taken from the cc-pVXZ basis sets. The article by Ahlrichs and co-workers describes the basis sets in detail[204].

3.1.8 Computational resources

Methods discussed in the previous sections are nowadays widely disseminated in every other program dedicated at computing the electronic structure of molecules. In addition, it is also possible to run very demanding calculations in a simple end-user workstation, fairly equipped with a recent processor and a large amount of storage space.

We had the opportunity to use the computer cluster at Centro de Física Atómica, which is composed of one AMD Opteron 275 at 2.2 GHz as the master node and nine Intel Core2 Quad Q6600 at 2.4 GHz as computing nodes. The advantage of running several different jobs at once and being able to process the output of several approaches as a whole, in hours time, is priceless. Mainly because the experimentalist is always craving for more time around the apparatus, but also because more quality time is spent comparing between experimental and theoretical results and finding answers.

All the methods presented in this thesis are implemented either in the Gaussian 03/09[205,206] software package or in the Dalton 2005[207] program for electronic structure calculations. Most computations however were done with Gaussian. These include geometry optimizations, single-point energies and vibrational analysis jobs based on HF, MPn, OVGF, P3 or B3LYP methods, as well as on several composite procedures. Use of Dalton 2005 was necessary due to its ability to model core-hole states, using a modified SCF procedure; it was Dalton that rendered possible the assignment of the XPS spectra of 5ATZ and 5MTZ.

3.2 Application techniques

In the next sections, we will briefly describe how the electronic structure methods were put to work to fulfil our needs. There will be abundant computational chemistry jargon, and most auxiliary methods will not be described in detail. In sum, we will explain how we simulated photoelectron spectra, and how we tried to model the results for the gas-phase thermal decomposition studies. For detailed information regarding some auxiliary methods, it is advisable to consult the original articles or one of the many available textbooks focusing theoretical and computational chemistry, such as Jack Simons' *An Introduction to Theoretical Chemistry*[208] or Frank Jensen's *Introduction to Computational Chemistry*[148].

In the following, the *level of theory* at which a specific result was computed is given as *method/basis*; if no other information is given, this notation means that the

molecule's geometry was optimized and its energy evaluated at the same level of theory i.e. the same method and basis set were used to optimize the molecule and to compute its single point energy. If the geometry of the molecule was optimized at a different level of theory then the notation is $method_{sp}/basis_{sp}//method_{opt}/basis_{opt}$.

3.2.1 Outer-valence photoelectron spectra

The He(I) photoelectron spectra of all compounds presented herein, with the exception of the benzyl azides, were simulated using results from electron propagator methods, more precisely, from the VIEs obtained with OVGF and P3 methods. The procedure employed is as follows.

First, the optimized structures of all lowest energy conformers/tautomers were found, using HF, MP2 and B3LYP and the 6-311++G(d,p) basis set. The optimization procedure is readily available in Gaussian and is based on the Berny geometry optimization algorithm[209]. The minimum nature of the optimized structures was confirmed by vibrational analysis at the same level of theory, rendering no imaginary frequencies.

The MP2/6-311++G(d,p) optimized structures were used as initial guess structures for the so-called *composite* or *chemical accuracy* methods. More information regarding composite methods can be found below and in their original articles. From these methods, relative Gibbs energies (ΔG) between conformers/tautomers were computed, and used with the Boltzmann distribution formula

$$n_i = \frac{e^{-(G_i - G_0)/k_B T}}{\sum_n e^{-(G_n - G_0)/k_B T}} \tag{3.120}$$

where n_i is the population ($\in [0, 1]$) of the ith tautomer, G_i is the Gibbs energy of the ith tautomer, G_0 the Gibbs energy of the most stable tautomer and T the desired temperature. The resulting populations are called Boltzmann population ratios (BPRs).

The MP2/6-311++G(d,p) optimized structures were also used as input for the EPT methods, using the same basis set. Thus, VIEs for M2AP, 5ATZ and 5MTZ were effectively obtained at the OVGF/6-311++G(d,p)//MP2/6-311++G(d,p) level of theory. This was done for every conformer/tautomer found in the initial conformational analysis.

The spectra were constructed from pole values whose strength (see Section 3.1.6.3) was above 0.85, the limit for breakdown of the one-electron picture of ionization. Each line was convoluted with a Lorentzian function of FWHM = 0.4 eV. This value was found to yield the best fit to the experimental results; moreover, it accounts for the broadening of unresolved vibrational envelopes due to experimental conditions.

The set of convoluted VIEs of each conformer/tautomer was then summed over to generate the corresponding simulated spectrum. The final spectrum, which results from contributions of all conformers/tautomers, comes from the sum of every conformer/tautomer individual spectrum, scaled by its specific BPR.

Molecular orbital contours were created using the open-source program Molekel[210], based on results obtained at the MP2/6-311++G(d,p) level of theory. Given that OVGF, P3 and MP2 methods are based on the one-electron picture of ionization set by the HF theory, the assignment of the spectra derives from Koopmans' approach on orbital energies and ordering of the bands.

3.2.2 Core photoelectron spectra

In order to calculate the core-electron binding energies (CEBEs), the delta-self-consistent-field (ΔSCF) approach was used[211]. In this approximation, the energy required for

removal of a core-electron is calculated as the difference in energy between the neutral and the core-ionized ground-states of the molecule.

The readjustment of the electrons around the core-hole leads to a significant reduction of the binding energy. Thus, it is important to allow for relaxation of the other orbitals, maintaining the core-hole state. The relaxation energy $E_{\text{relax}}(i)$ can be defined as the difference between a Koopmans' theorem binding energy, $E_{\text{KT}}(i)$, and the binding energy $E_{\Delta\text{SCF}}(i)$ obtained by an exact SCF approach using an Hartree-Fock total energy calculation for both the initial and final states:

$$E_{\text{relax}}(i) = E_{\text{KT}}(i) - E_{\Delta\text{SCF}}(i) \tag{3.121}$$

Aiming at preventing the collapse of the core-hole during the SCF procedure, some constraints are usually adopted: forcing single occupancy of the core-orbital, making use of an intermediate optimization step (where the core-hole orbital is kept frozen) or restring orbital rotation. The ΔSCF procedure, including orbital relaxation, was implemented using the Dalton program package. The procedure implies an initial SCF calculation for the neutral ground-state of the molecule and several separate SCF calculations for each core-hole ground-state of the cation.

All calculations regarding computation of the CEBEs by means of the ΔSCF approach, as well as geometry optimizations of the neutral tautomers, were performed with the Hartree-Fock (HF) method. The stationary nature of the geometries was confirmed by vibrational analysis (no imaginary frequencies). Several basis sets of increasing quality were experimented, ranging from standard 6-31G(d) to large correlation consistent polarized triple-valence basis set (cc-pVTZ). However, only results with 6-311++G(d,p), Ahlrichs pVDZ and cc-pVTZ basis sets will be presented.

Simulated spectra include contributions from both 1H- and 2H-tautomers (of 5MTZ and 5ATZ) and result from the convolution of CEBEs with Gaussian profiles (FWHM = 0.5 eV). Each profile was scaled according with the BPRs of the tautomers, based on relative Gibbs energies computed from composite methods.

3.2.3 Thermal decomposition reactions

By far, the most involved computations are the ones which try to mimic the thermal decomposition reactions, because they require several jobs and several trials which most of the time render useless. The studies presented herein regarding thermal dissociation are based on the pictorial view of *transition state theory*. However, no rate constants were calculated (simply because no experimental data is available to compare them with), either by the Eyring equation or the Arrhenius expression[149].

A brief introduction is necessary before proceeding onto the details, so the textbook from Jensen[148] will be followed almost *ipsis verbis*. Transition state theory (TST) assumes that a reaction proceeds from one energy minimum to another via an intermediate maximum[212]. *Transition state* is the configuration which divides the reactant and product parts of the surface, while the geometrical configuration at the energy maximum is denoted as *transition structure* (TS).

The reaction proceeds via a *reaction coordinate*, usually taken to be negative at the reactant, zero at the TS and positive for the product. The reaction coordinate leads from the reactant to product along a path where the energy is as low as possible, usually called *minimum-energy path* or MEP. In a multidimensional case (see Sections 2.1.1.2 and 3.1.2), the transition state is a *first-order saddle point* on the potential energy surface, a maximum in the reaction coordinate direction and a minimum along all other coordinates.

How was the outcome of pyrolysis and thermal decomposition processes rationalized? First, a quick qualitatively analysis of the experimental decomposition spectrum

allows identification of some (if not all) products. Second, by looking at the structure of the reactant (the parent molecule), it is possible to imagine some bond ruptures and angle bending options, possibly with the aid of results from vibrational analysis. In this way, probable molecular motions leading to dissociation and formation of the decomposition products are registered.

Only after pre-screening of possible dissociative motions, the calculations start. The following 4-step prescription was applied: **(i)** a relaxed potential energy surface scan along the bond or motion of interest, in order to detect a possible TS; **(ii)** full optimization and validation of the candidate TS (vibrational analysis with one imaginary frequency); **(iii)** an intrinsic reaction coordinate (IRC) calculation starting from this TS, connecting reactant, TS and products; and finally, **(iv)** the full optimization of the final products.

Steps **(i)** and **(iii)** were calculated at the MP2(Full)/6-31G(d) or B3LYP/6-31G(d) level of theory, and steps **(ii)** and **(iv)** were calculated with an high-accuracy composite method. For each intermediate stage product which underwent further decomposition, the same prescription was applied, until the final products were reached. For each decomposition pathway, only *unimolecular* reactions were considered. The final results were arranged in a graphical manner, as reaction schematics or *potential energy diagrams*, giving an overview of all thermal decomposition pathways.

All computations were performed with the Gaussian software. Details regarding IRC calculations can be found in Gaussian's reference textbook *Exploring Chemistry with Electronic Structure Methods*[213] and references therein. The original work was developed by Fukui[214], but Gaussian 09 uses a recent algorithm introduced by Hratchian and Schlegel[215,216].

3.2.4 Composite methods

Throughout this work, several methods were used which rely on successive calculations of increasing sophistication. These *composite methods* are aimed at obtaining energies values of chemical-accuracy i.e. to an error of ≈ 1 kcal mol^{-1}. They use extrapolation techniques for reaching the CBS limit, based on fits to large sets of empirical data (atomization energies, ionization energies, electron affinities and proton affinities); therefore, they cannot be considered full *ab initio* procedures.

The most known composite methods are the Gaussian-n procedures (Gn, with $n = 1, 2, 3, 4$)[217–221]. All of them were used (with the exception of G4) for calculating relative energies of several molecular species, including transition states and ionized species.

The G1 procedure involves the following steps[217]:

1. HF/6-31G(d) geometry optimization.
2. HF/6-31G(d) vibrational frequencies, scaled by 0.839 to produce ZPEs.
3. MP2(Full)/6-31G(d) geometry optimization starting from previous geometry. The resulting structure is used in all subsequent calculations.
4. MP4/6-311G(d,p) single-point energy.
5. MP4/6-311+G(d,p) single-point energy.
6. MP4/6-311G(2df,p) single-point energy.
7. QCISD(T)/6-311G(d,p) single-point energy.

The contribution from diffuse functions is evaluated from the difference between energies obtained at points 4 and 5. The contribution from higher polarization on non-hydrogen atoms is evaluated at points 4 and 6. Correlation effects beyond quadruple excitations is evaluated as the difference between energies obtained at points 4 and 7. An additional correction, termed *higher-level correction* (HLC), which depends on the

number of electrons of α and β spin, is added for accounting correlation effects beyond QCISD(T).

The G2[218] procedure uses an additional correction and a modified HLC version, but only requires an additional computation at the MP2/6-311++G(3df,2p) level of theory. It outperforms the G1 results, by decreasing the MADs between the empirical set of data and the computed results.

An alternative, less costly version of G2 is termed G2(MP2)[219], where the steps performed at MP4 are substituted by equivalent MP2 approaches.

The more recent G3 method[220] is very similar to the G2 procedure:

1. HF/6-31G(d) geometry optimization.
2. HF/6-31G(d) vibrational frequencies, scaled by 0.839 to produce ZPEs.
3. MP2(Full)/6-31G(d) geometry optimization starting from previous geometry. The resulting structure is used in all subsequent calculations.
4. MP4/6-31G(d) single-point energy.
5. MP4/6-31+G(d) single-point energy.
6. MP4/6-31G(2df,p) single-point energy.
7. QCISD(T)/6-31G(d) single-point energy.
8. MP2(Full)/G3Large single-point energy.

The contributions from higher polarization and diffuse functions are evaluated as in the G1 and G2 procedures, but using a smaller basis set. The last step uses a non-standard basis function, G3Large, and assumes full correlation on all electrons in the variational procedure ("Full"). In addition to the HLC correction, a *spin-orbit* (SO) correction is also added to the final energy.

Another standard set of multi-level procedures was developed by Petersson and co-workers: the *complete basis set* (CBS) methods. As the name suggests, these composite methods try to reach the complete basis set limit in the framework of finite basis sets. In this thesis, only the CBS-4M[222] and CBS-Q[223] models were used (in the XPS studies, for evaluating tautomeric populations between tetrazoles), mainly because CBS methods are the only reference composite methods other than the well-established Gn procedures.

The CBS-Q procedure is detailed as follows:

1. HF/6-31G(d†) geometry optimization
2. HF/6-31G(d†) vibrational frequencies, scaled by 0.918 to produce ZPEs.
3. MP2/6-31G(d†) geometry optimization starting from previous geometry. The resulting structure is used in all subsequent calculations.
4. MP2/6-311+G(2df,2p) single-point energy. This result is extrapolated to the CBS limit by the pair-orbital method.
5. MP4(SDQ)/6-31+G(d(f),d,p) single-point energy.
6. QCISD(T)/6-31G(d†) single-point energy.

Also in the CBS methods, empirical corrections are used for accounting correlation and spin-orbit effects. Relatively to the CBS-Q method, the (faster) CBS-4M procedure relaxes on the size of the basis-set and introduces a correction for size-consistency in the extrapolation procedure. Further information can be found in the articles by Petersson[222,223].

Part II
Case Studies

Chapter 4

Methyl 2-Azidopropionate: UVPES and Matrix-Isolation IR

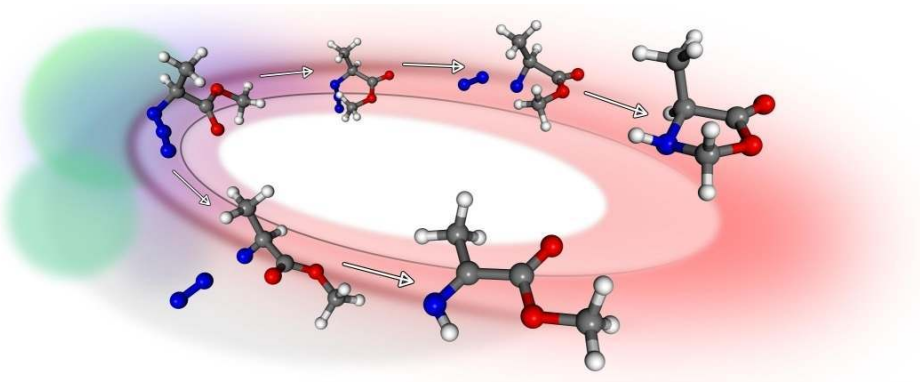

4.1 Introduction

The gas-phase thermal decomposition of azides ($R-N_3$) has long been an exciting and interesting research subject[1], mainly due to the fact that these molecules release nitrogen very easily, together with an high amount of energy, when heated. Therefore, most practical applications of azides are based on this property, whether being adopted as building blocks in organic chemistry synthesis[2], or being used as energetic additives for solid propellants[13]. Their uses span a wide range of areas, from industrial to pharmaceutical and biological applications.

An important element in the study of the thermal decomposition of azides is the potential for detecting reactive, often unstable, intermediate compounds. Some successful examples are the cases of methanimine[23,224] ($H_2C{=}NH$), 2-iminoacetamide[32] ($H_2NCOCHNH$), iminodimethyl acetamide[33] and 2-oxazolidone[33] ($C_3H_5NO_2$).

The extensive studies undertaken by Dyke and co-workers on the thermal decomposition of organic azides[32,33], using the UV photoelectron spectroscopy (UVPES) and the matrix isolation IR technique, have lead to the establishment of two main decomposition mechanisms.

[†]Reproduced with permission from *J. Phys. Chem. A* **2011**, *115*, 8447-8457.

The Type 1 mechanism (see Fig. 4.1), originally proposed by Bock[23], involves the loss of N_2 and formation of the imine associated with the parent azide. Within a Type 1 mechanism, a 1,2-H shift always occurs, the question being if it starts after or before the N_2 loss. In the first case, a singlet nitrene is left from the N_2 elimination, and then it converts into a more stable imine, through a 1,2-H shift. In the second case, the 1,2-H shift itself promotes the dissociation of N_2 and leads to the formation of the imine, in a synchronous way. The Type 1 mechanism was successfully proposed to explain the thermal decomposition of 2-azidoethanol[31] ($N_3CH_2CH_2OH$), 2-azidoacetamide[32] ($N_3CH_2CONH_2$) and 2-azido-*N,N*-dimethylacetamide[33] ($N_3CH_2CONMe_2$).

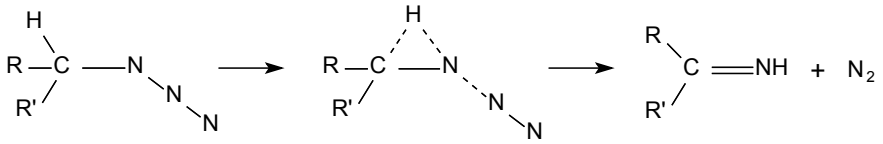

Figure 4.1: Example of Type 1 mechanism

The second mechanism, Type 2, proposed for the first time by Dyke and co-workers, involves the formation of a cyclic transition state or stable intermediate, which originates from the transfer of a H-atom or an alkyl group from a remote site of the molecule to the electron deficient N atom (see Fig. 4.2). The pyrolyses of ethyl azidoacetate[31] (N_3CH_2COOEt), and methyl (N_3COOMe) and ethyl azidoformate[33] (N_3COOEt) were explained on the basis of this mechanism.

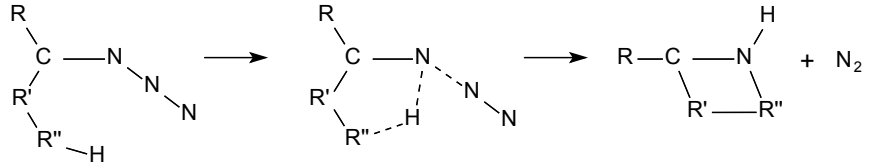

Figure 4.2: Example of Type 2 mechanism

In a more recent study, O'Keeffe[37] revisited the thermal decomposition of 2-azidoacetone, previously investigated by Dyke[30], using flash pyrolysis in combination with molecular beam mass spectrometry. Low residence times (20-30 μs) in the pyrolysis zone and internal cooling of the nascent thermal decomposition fragments due to supersonic jet expansion, allowed the authors to find experimental evidence for the occurrence of both Type 1 and Type 2 mechanisms, at different stages of the thermal decomposition process.

The present work describes the study of the electronic structure and thermal decomposition of methyl 2-azidopropionate (M2AP, $N_3CH_3CHCOOCH_3$), using UVPES and matrix isolation IR spectroscopy. These combined techniques have already proven to be excellent tools in the analysis of the gas-phase thermal decomposition of several azides and investigating their decomposition mechanisms[29–33]. Moreover, the molecular properties of M2AP have already been investigated by us, in a previous theoretical study[225].

The experimental results presented in this study will be supported and rationalized through computational analysis on (i) the electronic structure and relative populations of the conformers of the parent azide (see Fig. 4.3), and (ii) on the possible decomposition pathways and the associated energy barriers for their activation, calculated with high-accuracy *ab initio* methods.

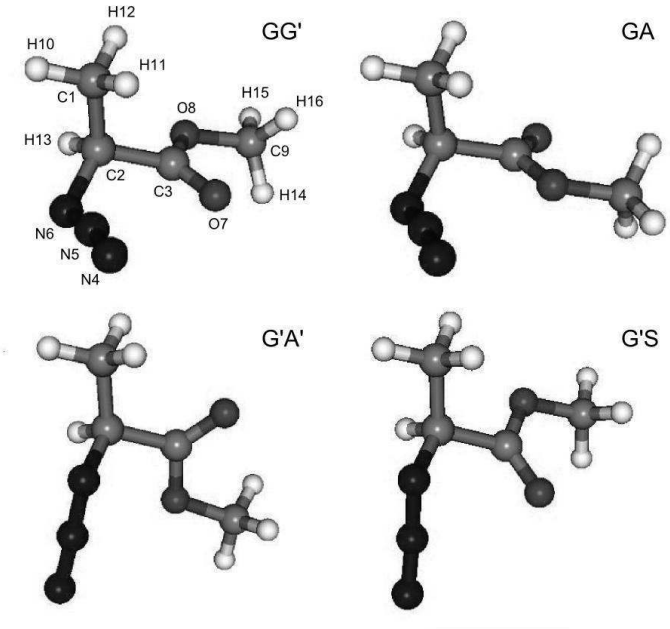

Figure 4.3: The four lowest energy conformations of M2AP: GG' (*gauche-gauche*), GA (*gauche-anticlinal*), G'A' and G'S (*gauche-synperiplanar*).

4.2 Experimental and computational methods

4.2.1 Sample preparation and characterization

Methyl 2-azidopropionate was prepared from the reaction of sodium azide (NaN_3) and methyl 2-bromopropionate ($BrCH_3CHCOOCH_3$). A mixture of $BrCH_3CHCOOCH_3$ and saturated aqueous NaN_3 was stirred continuously, at 60 °C, for 48 h. The product, $N_3CH_3CHCOOCH_3$, was then extracted with dichloromethane (CH_2Cl) and dried over anhydrous Na_2SO_4. Finally, the product was distilled under vacuum, in a Kugelrohr, at 80 °C. The high purity (>99%) of methyl 2-azidopropionate was confirmed in the liquid phase by IR and ^{1}H NMR spectroscopies and in the gas-phase by electron impact (EI) mass spectrometry.

The IR spectrum of M2AP exhibited the most intense absorption at 2107 cm^{-1}, assigned to a vibration of the N_3 group. Several prominent bands were also present: 2958 cm^{-1} (C-H stretching), 1747 cm^{-1} (C-O stretching), 1454 cm^{-1}, 1257 cm^{-1} and 1208 cm^{-1}. The 400 MHz ^{1}H NMR spectrum of M2AP in deuterated chloroform ($CDCl_3$) solution revealed three signals: δ=3.927 (1H, q, J=7.2 Hz, R_3CH), 3.759 (3H, s, $ROCH_3$) and 1.443 (3H, d, J=7.2 Hz, RCH_3) ppm. The 100 MHz ^{13}C NMR spectrum of M2AP in deuterated chloroform ($CDCl_3$) solution revealed four signals: δ=171.38 (C=O), 57.23 (R_3CH), 52.56 ($ROCH_3$) and 16.68 (RCH_3) ppm. The 70 eV EI mass spectrum of M2AP showed the parent ion peak at 129 *m/z* (5%), together with the following fragments: 42 (100%, $C_2H_4N^+$), 28 (45%, N_2^+), 18 (30%, H_2O^+) and 59 (28%, $C_2H_3O_2^+$) *m/z*.

Azides are potentially explosive and therefore must be handled with all due precautions. Care was taken to avoid possible explosions at all stages in the preparation and handling of the azide samples. In practice, no explosions were experienced during this work.

4.2.2 UV photoelectron spectroscopy

The UV photoelectron spectrometer used in Lisbon to record the spectra is very similar to the one described elsewhere[99]. An illustrated view of the apparatus is given in Fig. 4.4. It operates under high vacuum conditions and it consists of a large 150° spherical sector electrostatic analyser (mean radius = 200 mm) and a DC discharge lamp, capable of producing He(I) (21.22 eV) radiation. Typical working resolution is 30 meV full width at half maximum (FWHM) as measured for the $(3p)^{-1}\ ^2P_{3/2}$ Ar^+ photoelectron line. In a typical experiment, a sample of liquid M2AP is admitted through a PTFE valve, from a glass vial outside the spectrometer reaction chamber, and the vapour passes into the ionization region. The sample was degassed with repeated freeze-pump-thaw cycles prior to its injection into the system.

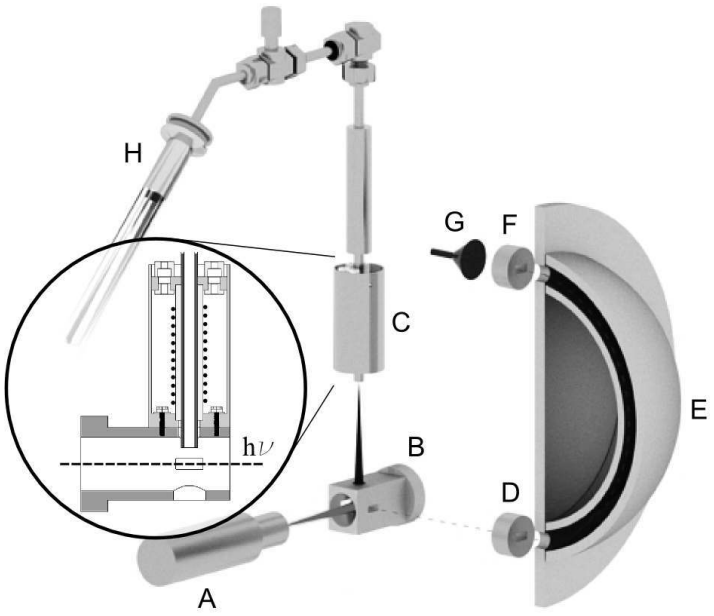

Figure 4.4: Schematics of the experimental setup, with an expanded view of the resistively heated furnace: A - UV source, B - reaction cell, C - furnace, D - entrance slits, E - energy analyser, F - exit slits, G - electron detector and H - liquid sample.

Before it reaches the ionization region, the M2AP vapour flows through a 45 mm resistively heated stainless-steel furnace (with 4 mm i.d.), where the pyrolysis process takes place (Fig. 4.4, C). The heating resistance is powered by an AC variable transformer which is coupled to a solid state relay (SSR) and a PID controller. The feedback signal is the temperature read at the end of the tube, with a type K (Ni-Cr/Ni-Al) thermocouple. A LabView program drives the PID and sets the oven temperature, which remains stable to within ±1 °C around the desired value. A maximum temperature of ca. 725 °C can be achieved.

The photoelectron spectra of M2AP recorded at room temperature were calibrated by the admission of a small amount of methyl iodide (CH_3I) and argon (Ar) into the reaction chamber[116]. During the thermal decomposition studies, the ionization energy scale calibration was achieved by using the known ionization bands of the major pyrolysis products, such as N_2 and CO, as well as traces of H_2O present in the system[116].

4.2.3 Matrix isolation IR spectroscopy

The experimental setup for the matrix isolation IR studies, in Southampton, is identical to the one described previously[29]. Briefly, it is based on a conventional closed-cycle cryostat (Air Products, model CSW-202) and an IR grating spectrophotometer (Perkin Elmer, model 983G), together with a CsI deposition window, maintained at ca. 12 K. The M2AP vapor, pre-cooled in a liquid nitrogen bath, is admitted to the system through a PTFE valve. Prior its deposition in a N_2 matrix, the M2AP vapour travels through a 150 mm silica furnace (with 5 mm i.d.) which can be resistively heated to 800 °C.

Matrix ratios were estimated to be in excess of 1000:1 (inert gas:sample). Typical deposition times were 40 minutes at a specific furnace temperature, and the matrix IR spectra were recorded over the 4000-500 cm^{-1} wavenumber range. Similarly to the UVPES experiments, an initial matrix IR spectrum of M2AP was recorded with the heater switched off, in order to obtain consistent spectra for the parent compound, prior to its thermal decomposition.

4.2.4 Computational methods

The optimized geometries of all four lowest energy conformers of M2AP were taken from our previous work on its molecular properties[225], obtained with the second-order Møller-Plesset (MP2) perturbation theory[172] and with density-functional theory (DFT)[182], using the B3LYP functional. The 6-311++G(d,p) Pople basis set[200] was used in conjunction with the aforementioned methods.

The framework of our computational studies on the valence ionization region is based on the one-electron propagator description[175] (EPT) of the molecular system, implemented at the level of outer-valence Green's function (OVGF) and partial third-order (P3) schemes[176,177]. These methods have already proven to be an invaluable tool in the study of photoelectron spectra of several molecules[226–228], provided one-electron ionization is valid.

Relative energies of all four M2AP conformers (GG', GA, G'A' and GS') were calculated with the hybrid G3 method[220]. The G3 method provides a computationally economic way of obtaining very accurate relative energies, which include allowance for thermal enthalpy and the zero-point energy (ZPE) corrections. However, the error arising from basis-set superposition (BSSE) is not considered. Estimates for the relative populations of the conformers, at room temperature, were obtained using the Boltzmann distribution formula:

$$n_i = \frac{e^{-G_i/kT}}{\sum_n e^{-G_n/kT}} \tag{4.1}$$

where n_i is the population of the ith conformer, G_i is the Gibbs energy of the ith conformer and T the desired temperature. The resulting populations are designated by Boltzmann population ratios (BPRs).

For each conformer, the computed VIEs obtained from the EPT methods were convoluted with Lorentzian functions of 0.4 eV FWHM[229] and summed over to generate the corresponding simulated photoelectron spectrum. This value was chosen in order to accommodate the broadening due to the vibrational envelope associated with each transition and due to the experimental resolution of the apparatus. The final simulated photoelectron spectrum of M2AP resulted from the sum of each conformer's photoelectron spectrum, weighted by its specific BPR. The same approach was used to produce the simulated IR spectrum of M2AP, which also includes the contribution of all four conformers. The wavenumbers were scaled[230] by 0.9679 and the vibrational lines were

convoluted with Lorentzian functions of 10 cm^{-1} FWHM (which was found to give a good fit to the experimental data).

Regarding thermal decomposition pathways, we have carried out several calculations, based on a simple 4-step procedure: (i) a relaxed potential energy surface scan along the bond of interest, in order to detect a possible TS; (ii) full optimization and validation of the candidate TS; (iii) a IRC calculation starting from this TS, connecting reactant, TS and products; and finally, (iv) the full optimization of the final products. Steps (i) and (iii) were calculated at the B3LYP/6-31+G(d) level, and steps (ii) and (iv) were carried out with the G3 method. All calculations presented in this work were carried out using the Gaussian 09 software[206].

4.3 Results and discussion

4.3.1 Electronic structure and vibrational analysis of M2AP

The electronic structure of M2AP was investigated using UVPES and molecular orbital (MO) calculations. None of the M2AP conformations (see Fig. 4.3) studied in this work are of higher symmetry than C_1.

The highest occupied molecular orbital (HOMO) and the next five highest HOMOs (33a-29a) of the most stable conformer, GG', are shown in Fig. 4.5. The first four MOs are almost exclusively comprised of -N_3 and -$COOCH_3$ contributions. The HOMO is a $\pi^*_{N_3}$ MO almost entirely localized in the azido group, whereas MO 33a is a $\sigma^*_{N_3}$ from the N_3 moiety, together with a very small contribution from the O7 oxygen lone-pair (n_O). Regarding MO 33a, we have used the same σ notation as employed by Bock[23], even though this MO is composed of a rotated p_z orbital between N4-N5 and a rotated antibonding π orbital from N6, relatively to the quasi-linear N_3 chain.

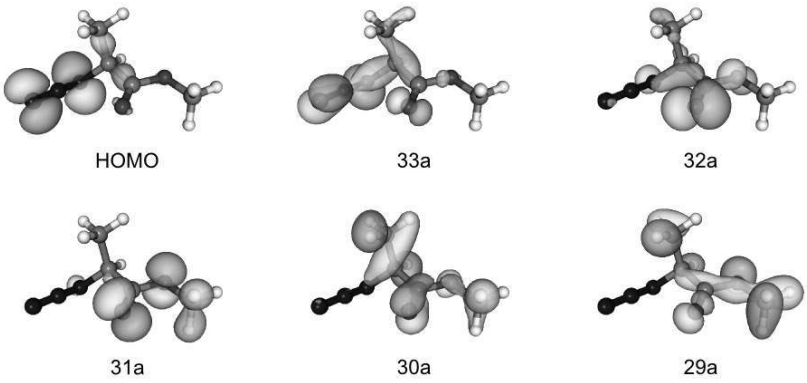

Figure 4.5: Molecular orbitals contours (isovalue = 0.05) of the GG' conformer of M2AP, from MP2/6-311++G(d,p) results.

The next MO (32a) is localized on the carbonyl lone pair (n_O), in-plane with the -$COOCH_3$ group. MO 31a is a bonding π_{CO} with a considerable amount of antibonding character from the p lone pair (LP) localized on the O8 oxygen. The last MOs appearing in Fig. 4.5, 30a and 29a, result from a combination of different amounts of σ and π orbitals on the -CH_3(CH)$COOCH_3$ moiety: 30a draws its character mainly from a bonding π_{CO} and 29a features a C-C-O-C σ bonding orbital.

The valence electronic structure of M2AP can be described as a combination of the two outermost occupied orbitals of methyl azide (CH_3N_3) and the two outermost orbitals of methyl formate (MF, $C_2H_4O_2$). The HOMO and MO 33a of M2AP resemble

the 3a″ and 12a′ MOs of CH_3N_3, respectively[23]. Analysis of recent work on the occupied MOs of MF[231], clearly shows the similarity between MOs 32a and 31a of M2AP and the MOs 13a′ and 3a″ of MF.

The vertical ionization energies (VIEs) of all four conformers, obtained from OVGF/6-311++G(d,p) calculations are collected in Table 4.1. Pole strengths associated with all the VIEs calculated with the EPT methods fall between 0.85 and 0.91. The relative populations of the conformers, from G3 results, are estimated at room temperature to be ca. 34, 25, 25 and 16% of GG', G'A', GA and G'S, respectively (see Table 4.2).

Table 4.1: Calculated vertical ionization energies (VIEs, in eV) of the GG', G'A', G'S and GA conformers of M2AP, obtained with the OVGF B method and the 6-311++G(d,p) basis, on optimized MP2/6-311++G(d,p) geometries.

MO	GG'	G'A'	G'S	GA
HOMO	9.20	9.30	9.30	9.25
33a	10.67	10.95	10.78	10.75
32a	11.42	11.64	11.28	11.56
31a	11.70	11.52	11.74	11.62
30a	13.42	13.39	13.31	13.46
29a	13.51	13.55	13.37	13.51
28a	14.03	13.82	14.11	13.95
27a	14.59	14.09	14.26	14.65
26a	14.72	14.26	14.56	14.83
25a	15.34	15.46	15.33	15.29
24a	15.53	16.26	15.92	15.58
23a	16.01	16.17	15.67	16.25
22a	16.56	15.78	16.49	16.45
21a	16.64	16.55	16.61	16.40

Table 4.2: Relative energies (ΔG, kJ/mol) calculated with the G3 method (see text for details) and Boltzmann population ratios (BPR, %) of the GG', G'A', GA and G'S confomers of M2AP.

Conformer	ΔG	BPR
GG'	0	34.2
G'A'	0.77	25.0
GA	0.81	24.6
G'S	1.86	16.2

A typical photoelectron spectrum of M2AP, obtained at room temperature, is presented in Fig. 4.6, panel (a), where the bands are labelled A-G. The simulated outer-valence photoelectron spectrum presented in panel (b) of Fig. 4.6, results from the sum of each conformer contribution to the 8-19 eV IE (ionization energy) region of M2AP. The experimental VIEs (vertical ionization energies) of bands A-G, the respective energy uncertainties and the OVGF B orbital energies (GG' conformer) of M2AP are collected in Table 4.3, together with the main character of the MO from which ionization occurs for each band.

Although the simulated spectrum of the GG' conformer alone (the lowest energy conformer) could be fitted to the experimental spectrum, there are some features that

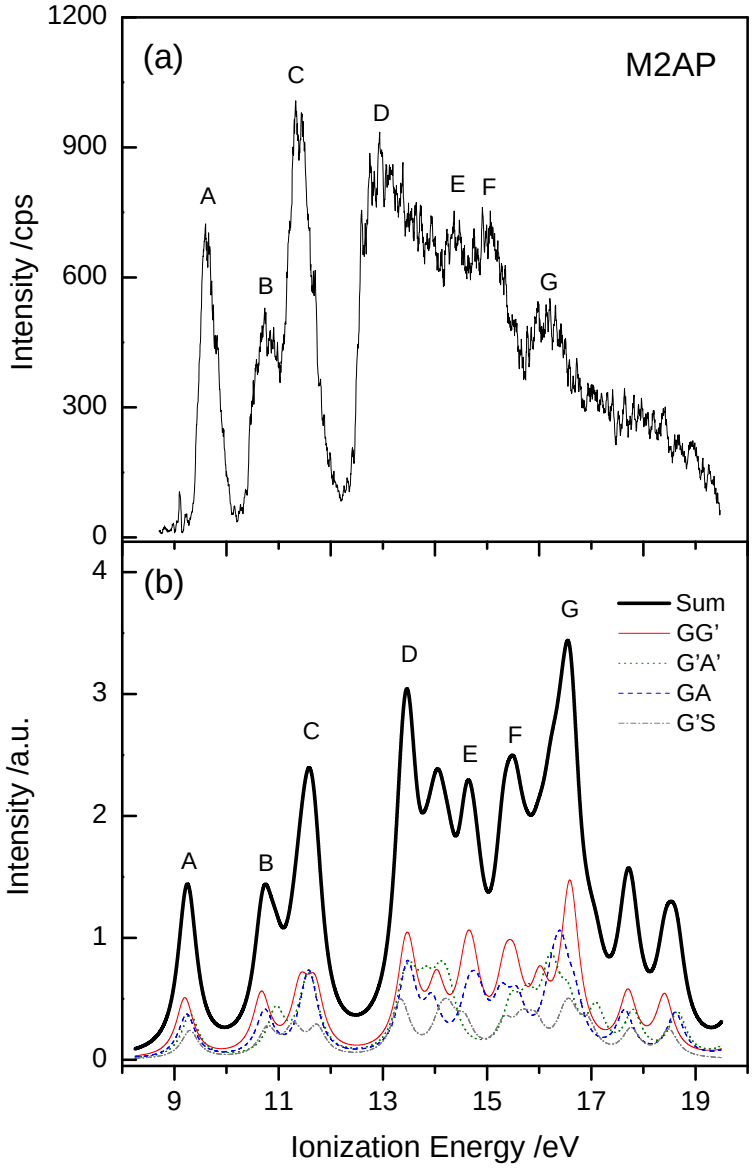

Figure 4.6: He(I) photoelectron spectrum of M2AP, recorded at room temperature (a), and simulated outer-valence photoelectron spectrum, based on OVGF/6-311++G(d,p) results (b).

Table 4.3: Experimental and calculated vertical ionization energies (VIEs, eV) for M2AP. MO stands for molecular orbital.

Band	MO	VIE	Calc.[a]	Character
A	HOMO	9.60±0.03	9.20	$\pi^*_{N_3}$
B	33a	10.74±0.03	10.67	$\sigma^*_{N_3}$
C	32a	11.41±0.04	11.42	n_O
	31a		11.70	π_{CO}
D	30a	12.97±0.06	13.42	π_{CO}
	29a		13.51	σ
-	28a		14.03	π_{CO}
E	27a	14.30±0.07	14.59	π_{CO}
	26a		14.72	π_{NN}
F	25a	15.05±0.06	15.34	σ
	24a		15.53	n_N
-	23a		16.01	n_N
G	22a	16.16±0.09	16.56	π_{N_3}
	21a		16.57	π
	20a		16.64	π

[a]From OVGF B results on the GG' confomer of M2AP.

are only explained by the inclusion of the contributions of the other conformers: the right shoulder of peak A, the asymmetric shape of peak B and the broadening of peak C. The other two most abundant conformers, GA and G'A', which are almost degenerate (ΔG_{G3} = 0.04 kJ/mol), have similar spectral patterns, but only the GA conformer seems to fit more extensively the experimental spectral band shape, specially the correct profile of bands E and F. The rich 13-17 eV IE region presents several bands, which overlap to form the intricate profile shown in the experimental photoelectron spectrum; the less accurate computational description in this region is mainly due to the fact that, within the OVGF and P3 approximations, "hot bands" and shake-up states are completely neglected. Also, experimentally there is a loss of transmission of the analyser at low electron kinetic energies (<4 eV) which will reduce the relative intensity of band G and further bands.

However, there is a good agreement between the experimental and the predicted spectra: comparison between the experimental and the predicted VIEs in Table 4.2 and Table 4.3 (considering only bands A-D and the GG' conformer of M2AP), leads to mean absolute differences (MADs) of 0.23 and 0.22 eV, from OVGF B and P3 calculations, respectively. For the HF/6-311++G(d,p) orbital energies (scaled by a 0.92 factor) from our previous computational work[225], the corresponding MAD increases slightly, up to 0.27 eV. On the other hand, unscaled HF orbital energies lead to a very high MAD of 1.25 eV, indicating that the EPT framework is the approximation of choice in terms of predicting VIEs and spectral band profiles.

Fig. 4.7 shows the IR spectrum of M2AP (panel (a)) isolated in the N_2 matrix (12 K), together with the calculated IR spectrum of M2AP (panel (b)), which includes the contributions from the four conformers. Selected vibrational modes are displayed in Fig. 4.4, together with their descriptions and the calculated (from B3LYP/6-311++G(d,p) scaled wavenumbers of the GG' conformer) and observed wavenumbers. The easily identifiable modes are useful to monitor the thermal decomposition evolution of M2AP,

in the matrix IR studies.

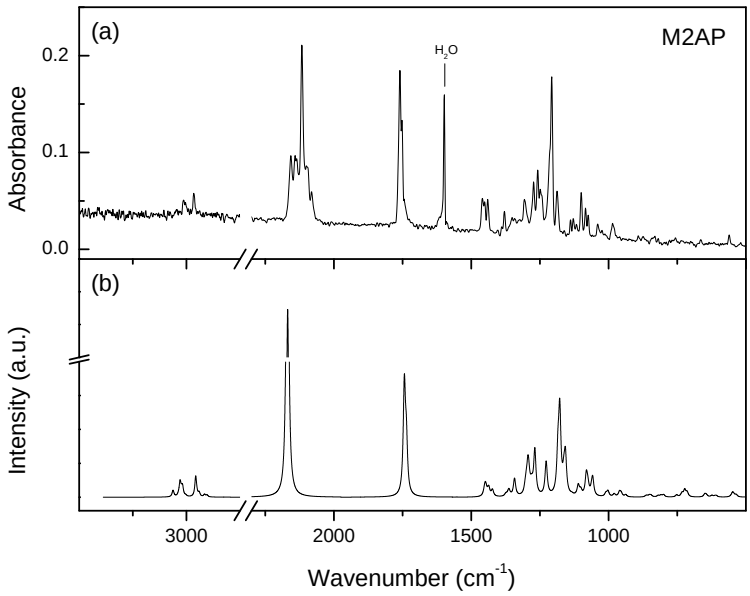

Figure 4.7: N_2 matrix IR spectrum (3500-500 cm^{-1} spectral range) of M2AP (a), and simulated IR spectrum, based on scaled B3LYP/6-311++G(d,p) results (b).

Table 4.4: Observed IR bands of M2AP isolated in a N_2 matrix (12 K), and corresponding calculated wavenumbers (cm^{-1}) and intensities (km mol^{-1}).

Mode	Assign.	Calc.[a] wavenumber	Observed wavenumber	Calc.[a] intensity
v_{35}	$\nu(N_3)$as	2168	2117	511
v_{34}	ν(C=O)	1743	1760/1752	177
v_{24}	w(CH_3)	1177	1207	222
v_{23}	w(CH_3)	1157	1187	159

ν, stretching. w, wagging. δ, bending. as, asymmetric.
[a]Scaled B3LYP/6-311++G(d,p) calculations on the GG' conformer (see text for details).

In Fig. 4.8, the region between 1500-900 cm^{-1} is presented in more detail, with the denoted contributions of each conformer. Apart from a slightly shifted main peak (w(CH_3), 1207 cm^{-1} obs., 1177 cm^{-1} calc.), towards the low wavenumbers region, the computed spectrum shows a very good agreement with the experimental matrix IR results. The marked presence of the other conformers, confirmed by the three consecutive peaks, immediately at the left hand side of the most intense peak, is quite interesting. The absorption line at 1249 cm^{-1} (w(CH_3), 1227 cm^{-1} calc.) is only due to the GA conformer, whereas the band at 1273 cm^{-1} (δ(N−C−H), 1293 cm^{-1} calc.) comes essentially from the G'A' conformer.

4.3.2 Thermal decomposition of M2AP - UVPES studies

Several spectra were obtained at different stages of the pyrolysis process, from room temperature to approximately 650 °C. A typical full thermal decomposition spectrum of M2AP, taken at 650 °C, is shown in Fig. 4.9, where clear signals of nitrogen (N_2,

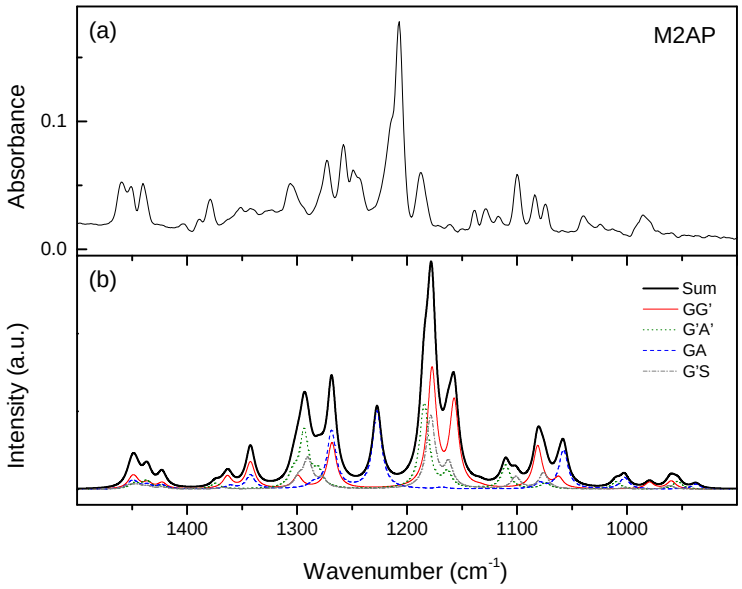

Figure 4.8: N_2 matrix IR spectrum (1500-900 cm^{-1} spectral range) of M2AP (a), and simulated IR spectrum, based on scaled B3LYP/6-311++G(d,p) results (b).

VIE = 15.60 eV), acetonitrile (CH_3CN, VIE = 12.21 eV), methanol (CH_3OH, VIE = 10.95 eV), carbon monoxide (CO, VIE = 14.01 eV) and dioxide (CO_2, VIE = 13.78 eV) can be identified. Methyl formate (MF, $HCOOCH_3$) is also detectable as a broad shoulder at the right side of the first band of methanol. The first and second bands of MF, at 10.99 and 11.54 eV (VIEs), respectively, are thus overlapped with the first band of CH_3OH, which hinders its clear identification in the spectrum.

The thermal decomposition of M2AP starts at ca. 400 °C, when the intensity of band A of the parent azide (at 9.60 eV) diminishes and the valley between bands B and C disappears. This is accompanied by the elimination of N_2, almost simultaneous to the appearance of CO and CO_2 in the spectrum. The transformation occurring in the IE range of bands B/C of M2AP is due to the formation of methanol, with an intense first band centred at 10.95 eV. Subtraction of a properly normalized room temperature spectrum of M2AP from the pyrolysis spectra obtained at the early stages of decomposition (400-500 °C), revealed the clear presence of CH_3OH and also the contribution of MF, overlapped in the 10.0-12.5 eV IE range. CH_3CN is also formed in this first stage of decomposition, with the increase of its three very distinctive bands (12.21, 12.47 and 13.16 eV) in the 12.0-13.5 eV IE region. The individual contributions of each thermal decomposition product to the overall spectral band shape (at 650 °C) can best be seen in Fig. 4.10.

From 500 to 650°C, there were no observed changes in the pyrolysis process, with an expected increase in the intensity of all the decomposition products with increased temperature. At 650 °C, the first band of M2AP has completely disappeared, indicating full decomposition of this molecule.

4.3.3 Thermal decomposition of M2AP - Matrix isolation IR studies

After obtaining the matrix IR spectrum of M2AP at room temperature, the heater was switched on and the temperature slowly increased, until almost full decomposition was observed. At each step, the matrix IR spectra were obtained after 40 min of deposition, during which the temperature was held constant. The results are shown in Fig. 4.11, where the spectral evolution at different stages of the thermal decomposition can be

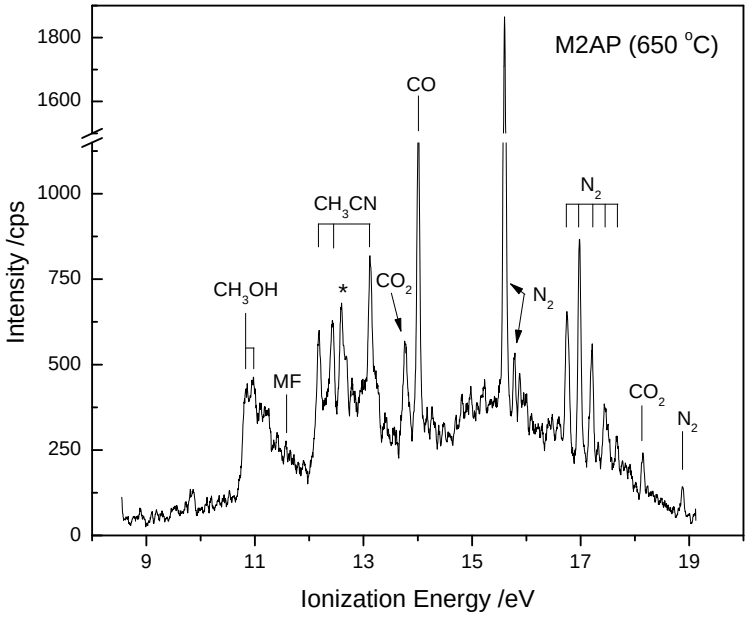

Figure 4.9: He(I) photoelectron spectrum of the thermal decomposition of M2AP, taken at 650 °C. The asterisk marks the characteristic ionization line of H_2O.

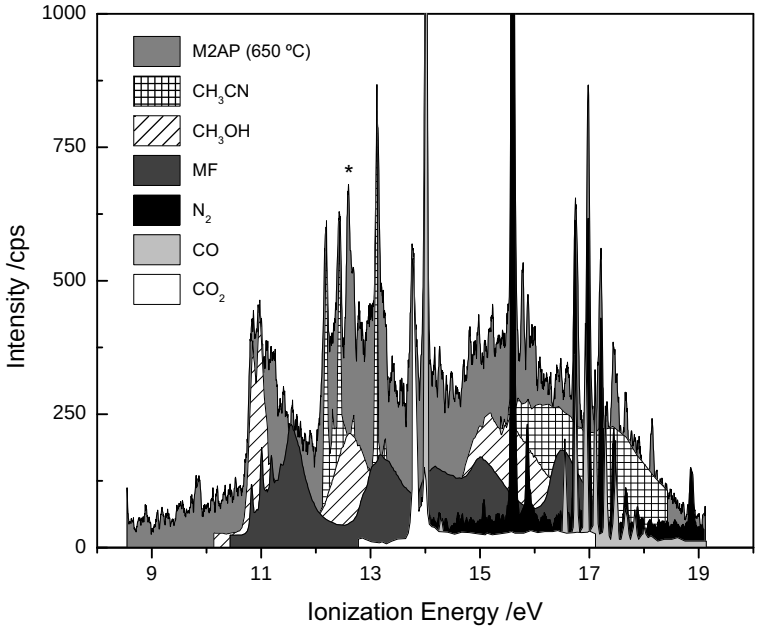

Figure 4.10: Detail of the He(I) photoelectron spectrum of the thermal decomposition of M2AP (gray), taken at 650 °C, with estimated contributions from the decomposition species CH_3CN (cross-hatched), CH_3OH (hatched), MF (dark gray), N_2 (black), CO (light gray) and CO_2 (white). The asterisk marks the characteristic ionization line of H_2O.

seen. It should be noted that the temperatures at which partial and full decomposition were observed are lower than the corresponding temperatures in the UVPES study as the pressures and pumping speeds were different from those used in the UVPES study.

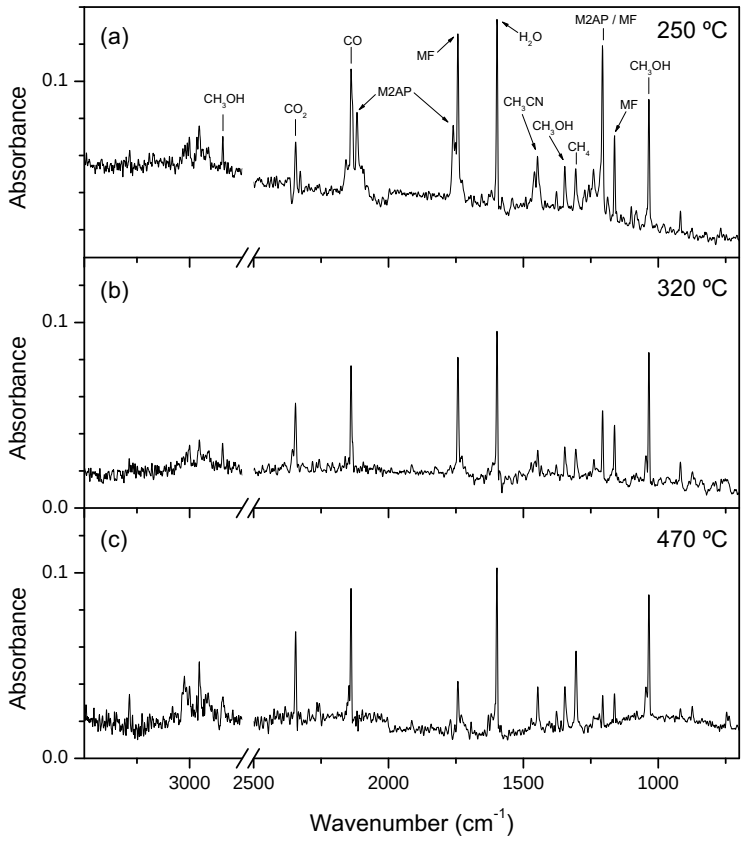

Figure 4.11: N_2 matrix IR spectrum (3500-700 cm^{-1} spectral range) of M2AP after partial pyrolysis at 250 °C (a), 320 °C (b), and after complete pyrolysis at 470 °C (c).

The IR studies reveal that the M2AP molecule starts to decompose around 250 °C, with the simultaneous appearance of the characteristic absorption peaks of CO (2139 cm^{-1}), CO_2 (2347 cm^{-1}), CH_3OH (1034, 1347, 2842 cm^{-1}), CH_3CN (1447, 1378 cm^{-1}) and methyl formate (MF, at 1743, 1207, 1162, 918 cm^{-1}). Methane (CH_4), clearly identifiable by the 1306 cm^{-1} band, also appears as a product, in the early stages of the thermal decomposition. This represents extra information from the matrix studies compared to those obtained from the UVPES results, because the photoelectron band of CH_4 is very broad and has a very low cross-section, in the He(I) IE range of the photoelectron spectra.

Careful comparison between the IR spectra obtained at 320 and 470 °C reveals an interesting feature: in this temperature range, the absorption bands assigned to MF decrease significantly, whereas the bands from the other products remain at approximately the same height. MF can indeed decompose into CH_4 and CO_2, but that pathway is not the lowest energy pathway: MF decomposition yields predominantly methanol and CO[232]. This suggests that two channels, at least, are leading to the formation of methanol, and that the one involving methyl formate and its decomposition is not the most favourable pathway.

4.3.4 Mechanism of gas-phase thermal decomposition of M2AP

The thermal decomposition studies with both the matrix IR and the UVPES techniques show that N_2, CO, CH_3CN, CH_3OH, MF, CO_2 and CH_4 are being formed from the pyrolysis of M2AP. However, only in the matrix IR spectra is CH_4 clearly identifiable. In addition, the UVPES spectra suggest that N_2 appears almost simultaneously with the other decomposition products, namely CO, CH_3OH and CH_3CN, pointing to the occurrence of a multi-fragmentation mechanism.

Although no clear evidence for the formation of an imine or an unknown intermediate has been detected experimentally, our computational studies on the thermal decomposition of M2AP have focused primarily on the two known mechanisms: a Type 1 mechanism, associated with the imine formation, and a Type 2 mechanism, associated with the formation of a cyclic TS/intermediate. These results are summarized in the potential energy diagram for the thermal decomposition of M2AP, presented in Fig. 4.12. All the transition structures are depicted in Fig. 4.13.

4.3.4.1 Imine formation through a 1,2-H shift synchronous with N_2 elimination (a Type 1 mechanism)

Studies concerning the Type 1 mechanism i.e. imine (R'RC=NH) formation with N_2 elimination, revealed the formation of methyl 2-iminopropionate (M2IP) from the GG' conformer of M2AP, through a 160.8 kJ/mol energy barrier (ΔE_{G3}). Elimination of N_2 from the azide chain is assisted by the H-atom transfer (H13) to the nitrogen atom (N6), in a synchronous process, through the formation of TS1 (Fig. 4.12, left side).

The M2IP molecule can adopt a number of conformations, which are essentially distinguished by the values of three dihedral angles: C1-C2-N6-H, C1-C2-C3-O8 and C9-O8-C3-O7 (where the atom labelling is the same as that used in Fig. 4.3). The first angle sets the position of the imine H-atom relative to the central CH_3 group, the second angle sets the position of the $HN{=}C{-}CH_3$ fragment relative to the MF group and, finally, the third angle distinguishes between the $\mathbb{E}$ and $\mathbb{Z}$ geometries of the $COOCH_3$ group. The M2IP structure shown in Fig. 4.12 is thus denoted as *trans-trans-cis* (*ttc*). All other conformers of M2IP are named according to the above scheme.

Calculations on the *ttc* conformer of M2IP show that it can dissociate into CO, CH_3OH and CH_3CN, by a simple H-atom transfer (H13) to the oxygen atom (O8). The activation barrier involved in this process is calculated at 260.2 kJ/mol, obtained from the difference between the G3 energies of M2IP *ttc* and the transition structure TS2. One of the conformers of M2IP has the CH_3 groups in opposite directions and the MF moiety in a *trans* ($\mathbb{E}$) configuration. This M2IP *ttt* conformer is 40.4 kJ/mol above the *ttc* conformer and can break into CH_4, CO_2 and CH_3CN, with an activation energy of 272.0 kJ/mol, through the transition structure TS3.

It is appropriate to investigate if MF can be formed also from M2IP *ttc*, in a fragmentation process which gives rise to CH_3CN + MF. Energy-wise, the lowest energy path for this to be accomplished is by letting the H13 hydrogen move to the vicinity of the carbon atom (see Fig. 4.13, TS4). The high energy barrier ($\Delta E_{G3} = 446.1$ kJ/mol) clearly indicates that this process is very unlikely to compete with the former routes, although it accounts for MF formation.

The decomposition of MF was recently analysed in a study by Metcalfe[233], in which the author concluded that MF's decomposition was dominated by a single channel producing CH_3OH + CO, and that the other two decomposition channels yielding CH_2O + CH_2O and CH_4 + CO_2, respectively, could be removed from the kinetic mechanism describing the pyrolysis of MF. The G3 energy differences between MF and the transitions structures leading to CH_3OH + CO and CH_4 + CO_2, calculated by

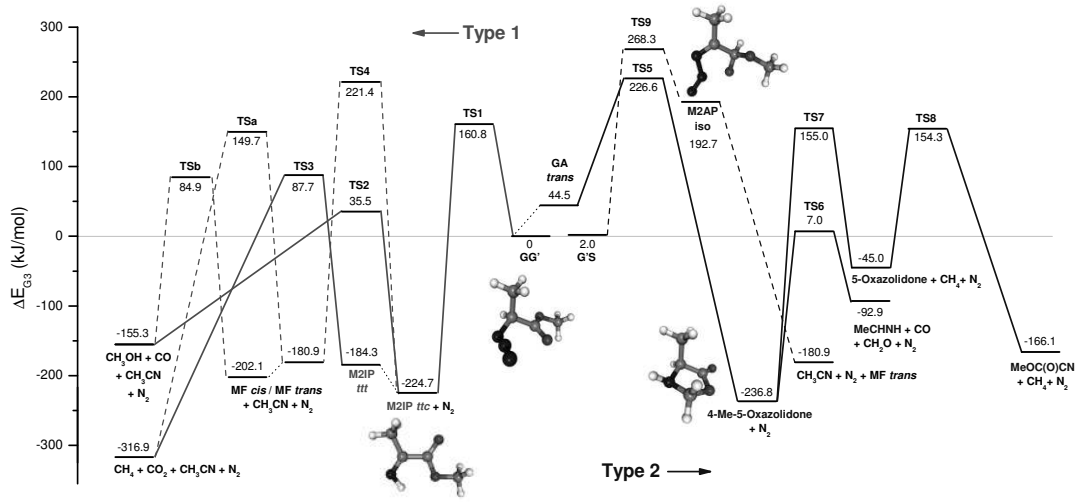

Figure 4.12: Potential energy diagram (in kJ/mol) for the thermal decomposition of M2AP, calculated with the G3 method. Pathways derived from a Type 1 mechanism are shown at the left hand side and pathways derived from a Type 2 mechanism are shown at the right hand side of the diagram. The G3 energy barriers associated with the decomposition of MF (left side) were taken from the work of Metcalfe[233]. All other results are from these study.

Metcalfe[233] with the G3 method, are included in Fig. 4.12, for comparison.

Overall, the Type 1 mechanism can be applied to the thermal decomposition of M2AP, effectively leading to the formation of N_2 and an imine (M2IP *ttc*), from which CH_3OH, CO and CH_3NH can be formed, through accessible energy barriers. MF formation from this imine requires a large amount of energy to occur and, even then, CH_4 and CO_2 do not originate from the most probable decomposition route of MF[232,233]. On the other hand, the M2IP imine can alternatively adopt a *ttt* conformation and decompose to give $CH_4 + CO_2 + CH_3CN$, through a lower barrier (272.0 kJ/mol) than the one required for MF to decompose into $CH_4 + CO_2$ (330.6 kJ/mol). These results can be summarized as follows:

$$N_3CH(CH_3)CO_2CH_3 \xrightarrow{TS1} HN{=}C(CH_3)CO_2CH_3 + N_2 \tag{4.2}$$

$$HN{=}C(CH_3)CO_2CH_3 \xrightarrow{TS2} CO + CH_3OH + CH_3CN \tag{4.3}$$

$$HN{=}C(CH_3)CO_2CH_3 \xrightarrow{TS3} CO_2 + CH_4 + CH_3CN \tag{4.4}$$

$$HN{=}C(CH_3)CO_2CH_3 \xrightarrow{TS4} HC(O)OCH_3 + CH_3CN \tag{4.5}$$

$$HC(O)OCH_3 \xrightarrow{TSa} CO_2 + CH_4 \tag{4.6}$$

$$HC(O)OCH_3 \xrightarrow{TSb} CO + CH_3OH \tag{4.7}$$

4.3.4.2 Heterocyclic formation synchronous with N_2 elimination (a Type 2 mechanism)

If the 1,2-R rearrangement (R being an hydrogen or alkyl group) is initiated from a remote site of the molecule, a cyclic intermediate may be formed, either as a 5-membered TS or as a more stable ring structure. Likely donors in this process are the

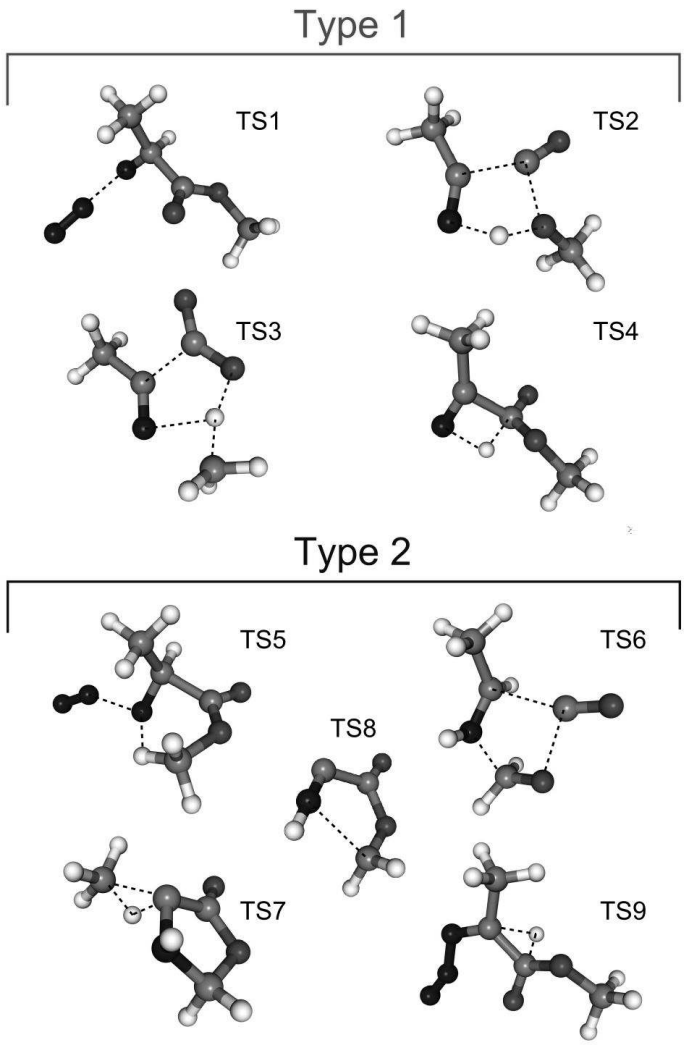

Figure 4.13: Geometry of all the transition structures, calculated with the G3 method, involved in the thermal decomposition of M2AP, originated by either a Type 1 or a Type 2 mechanism.

methyl hydrogens closest to the electron deficient N in M2AP. However, in the case of the CH_3 group associated with the MF moiety, this implies some prior conformational rearrangement in M2AP into a more favourable geometry, one in which the -$COOCH_3$ group assumes a *trans* configuration. Hence, the optimized structures of a set of M2AP conformers, lying 35-45 kJ/mol above the GG' conformation, were computed with the G3 method, and possible hydrogen transfers from remote alkyl sites were considered.

From the *trans* configuration of M2AP G'A', a 5-membered heterocyclic compound – 4-methyl-1,3-oxazolidine-5-one – was found to be formed through migration of the methyl hydrogen onto the nitrogen atom, simultaneous to the N_2 elimination (TS5, Fig. 4.12), with an activation energy of 182.1 kJ/mol (relatively to M2AP G'A' *trans*). The non-methylated form of this 5-membered intermediate has been already identified in a previous study by[33], of the pyrolysis of ethyl azidoformate ($N_3COO(CH_2)CH_3$). At that time, it was proposed on the basis of results of *ab initio* calculations that the oxazolidone could further decompose into CO_2 and Me(CH)NH (ethanimine). Applying the same reasoning to the decomposition of 4-Me-5-oxazolidone, a transition structure (TS6) leading to the production of ethanimine was found to be formed from three

interdependent steps: breaking of the C-C bound, release of CO and formation of formaldehyde (CH_2O). The proposed computed reaction, shown in the lower right side of Fig. 4.12, has a activation energy of 243.8 kJ/mol and gives MeCHNH, CO and CH_2O from 4-Me-5-oxazolidone.

Although CO is observed as a decomposition product, the easily identifiable CH_2O is not. Ethanimine is the resulting imine from the pyrolysis of ethyl azide[23] and it can decompose *via* two competitive[234] routes: CH_4 + HNC and H_2 + CH_3CN. Again, although CH_3CN is found within the thermal decomposition products detected spectroscopically, no evidence of HNC or HCN was found. Therefore, in spite of being energetically feasible, no support for the decomposition route involving formation of ethanimine from 5-oxazolidone was obtained experimentally.

Another way for the 4-Me-5-oxazolidone to decompose is through a 1,2-H shift onto the methyl substituent, which implies an high activation energy of 391.8 kJ/mol (TS7) and leaves behind CH_4 + 5-oxazolidone as products. The 5-oxazolidone can then undergo ring opening and isomerise into methyl cyanoformate (MeOC(O)CN), through a 199.3 kJ/mol energy barrier (TS8). Previous work on the pyrolysis of cyanoformates by Sheppard[235], showed that MeOC(O)CN loses CO_2 and forms CH_3CN (at 700 °C), two of the decomposition products detected in our UVPES results.

An alternative, simple mechanism, which fits the Type 2 format because it does not imply a nitrene or an imine, leads to the formation of an M2AP isomer, is shown in the upper right side of Fig. 4.12. This isomer is easily formed from the GS' conformer of M2AP, through a 1,2-H shift of the H13 atom onto the C3 atom, which needs 266.3 kJ/mol to be activated. This isomer then dissociates with no barrier into CH_3CN, N_2 and MF. The former route represents the only Type 2 based explanation for the formation of MF, and is energetically more favourable (ΔE_{G3}=266.3 kJ/mol) than the equivalent Type 1 reaction (M2AP GG' → M2IP *ttc* → MF, max. ΔE_{G3}=446.1 kJ/mol).

A Type 2 mechanism could in fact be used to explain the presence of the products in the experimental spectra. However, the 5-oxazolidone intermediate or its methylated form were not detected experimentally, whereas in related studies on ethyl azidoformate, formation of the oxazolidone intermediate was spectroscopically verified by UVPES and matrix isolation IR[33]. If the formation of the M2AP isomer is included in the Type 2 description, then it fulfils the need for explaining the presence of MF, something which we were not able to model (computationally) from the decomposition of the oxazolidone. These two compounds, 4-Me-5-oxazolidone and the M2AP isomer, are thus needed if one wishes to explain the complete thermal decomposition of M2AP, without the formation of an imine or nitrene. The proposed routes involving 4-Me-5-oxazolidone and M2AP are summarized as follows:

$$N_3CH(CH_3)CO_2CH_3 \xrightarrow{TS5} \text{4-Me-5-oxazolidone} + N_2 \tag{4.8}$$

$$\text{4-Me-5-oxazolidone} \xrightarrow{TS6} CH_3(CH)NH + CO + CH_2O \tag{4.9}$$

$$CH_3(CH)NH \rightarrow CH_4 + HNC \tag{4.10}$$

$$CH_3(CH)NH \rightarrow H_2 + CH_3CN \tag{4.11}$$

$$\text{4-Me-5-oxazolidone} \xrightarrow{TS7} \text{5-oxazolidone} + CH_4 \tag{4.12}$$

$$\text{5-oxazolidone} \xrightarrow{TS8} CH_3OC(O)CN \tag{4.13}$$

$$CH_3OC(O)CN \rightarrow CO_2 + CH_3CN \tag{4.14}$$

$$N_3CH(CH_3)CO_2CH_3 \xrightarrow{TS9} \text{M2AP isomer} \tag{4.15}$$

$$\text{M2AP isomer} \rightarrow HC(O)OCH_3 + CH_3CN + N_2 \tag{4.16}$$

Overall, considering the analysis just in terms of the activation barriers, the thermal decomposition of M2AP is clearly dominated by the Type 1 mechanism. Relative to the most abundant conformer, M2AP GG', the initial formation of the imine is 65.8 kJ/mol less expensive than the formation of 4-Me-5-oxazolidone, and requires 107.5 kJ/mol less energy to activate than the route leading to the M2AP isomer. The Type 2 mechanism can only be considered energetically more advantageous over Type 1 in a latter stage of the pyrolysis, in which the MF formation from the M2AP isomer clearly requires less energy than the one needed in the dissociation of M2IP into MF and CH_3CN. Also, the experimental evidence from UVPES and IR matrix isolation spectroscopy favors a Type 1 mechanism as the dominant mechanism.

4.4 Conclusion

Methyl 2-azidopropionate (M2AP) has been synthesized and characterized by means of ^{1}H NMR and IR spectroscopies, mass spectrometry and photoelectron spectroscopy. Results from IR absorption and UVPES were interpreted with the aid of molecular orbital calculations. The valence photoelectron spectrum of M2AP encompasses contributions from the four lowest energy conformations (GG', GA, G'A' and G'S) and consists of seven bands in the 8.0-17.0 eV IE region. Its HOMO VIE is 9.60±0.03 eV, which corresponds to the ionization of a π^* MO located in the azide chain. The next two uppermost MOs are essentially nonbonding orbitals. A $(\sigma^*_{N_3})^{-1}$ ionization occurs at 10.74±0.03 eV and an oxygen 2p lone-pair $(n_O)^{-1}$ ionization occurs at 11.41±0.04 eV. Comparison between the experimental matrix IR spectrum of M2AP and the simulated spectrum based on DFT calculations, at room temperature, also points to the coexistence of all four lowest energy conformers.

The thermal decomposition of M2AP in the gas-phase was also studied by UVPES and matrix isolation IR spectroscopy. For this purpose, a new and more stable heating system was developed and successfully coupled to a photoelectron spectrometer. The experimental studies revealed N_2, CH_3OH, CH_3CN, CH_4, CO, CO_2 and methyl formate (MF) as the final decomposition products. Unfortunately, no intermediate species were detected spectroscopically.

Two already established mechanisms of decomposition, Type 1 (imine/nitrene formation) and Type 2 (heterocyclic formation), were used to understand the pyrolysis process of M2AP. Computational studies of two mechanisms, based on results from the G3 hybrid method, revealed the predominance of the Type 1 option over Type 2.

The proposed Type 1 pathways imply the formation of methyl 2-iminopropionate (M2IP) synchronous with the N_2 elimination, through a 160.8 kJ/mol barrier, and further decomposition of M2IP *via* two competitive routes: one accounting for CO, CH_3OH and CH_3CN (ΔE_{G3}=260.2 kJ/mol), and another leading to CO_2, CH_4 and CH_3CN (ΔE_{G3}=268.6 kJ/mol). Type 2 pathways involve the formation of a cyclic intermediate – 4-Me-5-oxazolidone, together with the N_2 elimination (ΔE_{G3}=182.1 kJ/mol), which could compete with the imine formation. On the other hand, some easily detectable products which follow from the decomposition of oxazolidone (CH_2O and HCN from the decomposition of ethanimine) were not observed experimentally. Also, we were unable to propose a plausible reaction which accounted for the formation of CH_3OH, a major pyrolysis product, from the oxazolidone intermediate. The former two arguments are sufficient to disfavour a Type 2 mechanism over a Type 1 mechanism.

Finally, an isomer of M2AP was found to be formed from a 1,2-H shift to a central carbon atom (ΔE_{G3}=268.3 kJ/mol), which dissociates without any barrier to form CH_3CN, N_2 and MF. As MF can decompose into CH_3OH + CO and CH_4 + CO_2, through 287.0 and 330.6 kJ/mol energy barriers, respectively, then this "Type 3" mechanism also accounts for all the detected decomposition products. Although not capable of competing with the Type 1 and 2 mechanisms, in terms of overall activation energy, further experimental and computational work is needed to clarify its existence.

In summary, a Type 1 mechanism accounts for the observed pyrolysis behaviour and all the observed products, and is the dominant decomposition mechanism of M2AP.

Chapter 5

BA and 2-, 3-, 4-MBA: Computational Study on VIEs

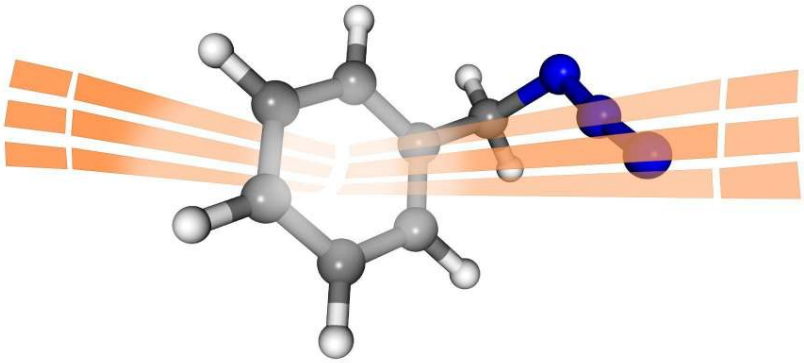

5.1 Introduction

During the past three decades, several compounds containing the azido group (-N_3) have drawn a considerable attention mainly because of their role as primary agents in explosive reactions. If subjected to a sudden increase in temperature or a strong mechanical stimulus, they react violently, releasing a large amount of energy through the elimination of N_2 from the azide chain[1,236,237].

Furthermore, organic azides' applications cover a wide range of other areas[13], going from reactants in the preparation of superconducting materials[238] to biochemical applications as non-protonated inhibitors in human carbonic anhydrase[239,240]. More recently, the application of aryl-azides as photoaffinity labelling agents for proteins[241] or in phototherapy[242] of tumours and other lesions has enforced the general interest in these compounds.

The characterization of the electronic structure and the conformational analysis of the azides is thus of extreme importance to these subjects; the geometry of the molecules affects the nature of the valence orbitals, which in turn dictates the chemical properties of the compound. This is specially relevant if one wishes to study the

[†]Reproduced with permission from *J. Mol. Struct. (THEOCHEM)* **2010**, *948*, 15-20.

activation of certain photochemical properties with changes in geometry[243] or the most stable conformers that favour a specific thermal decomposition pathway[244].

Although much has already been done in studying several azides systems, the aromatic ones, such as the benzyl azide (BA), lack the full theoretical and experimental characterization that already covered other simpler systems.

In this work, we analyse the character and energies of the outermost orbitals of benzyl azide (BA, $\Delta_f H^0_{gas}$=416 kJ mol^{-1}[245]) 2–, 3– and 4–methyl benzyl azide (2–, 3– and 4–MBA), based on theoretical results derived from quantum mechanical methods with different basis sets. The results will support the experimental work on these molecules, obtained with ultraviolet photoelectron spectroscopy (UVPES), namely by render possible the correct assignment of the bands. Additionally and in spite of the absence of experimental results on 1–methyl benzyl azide (1–MBA) with UVPES, calculations on this molecule are also presented, in order to complete the theoretical study of the different isomers of the methylated benzyl azides.

As there are some known discrepancies between theoretical and experimental ionization values in aromatic systems[246], care should be taken on the direct, non-scaled, use of Koopmans' theorem; therefore, at least two *ab initio* methods and several basis sets combinations are used in order to assess the accuracy of the calculated results.

The structure of this paper is as follows: Section 2 details the nature and the methodology employed in the computations, Section 3 presents and discusses the results and Section 4 presents the most relevant concluding remarks.

5.2 Computational details

The Koopmans' theorem[166] was applied to the SCF orbital energies and the search for the optimum combination of method and basis was exclusively restrained to *ab initio* methods.

The Hartree-Fock (HF) and Møller-Plesset (MP2) methods[247–249] were employed with seven different basis sets – 6-31G(d,p), 6-31++G(d,p), 6-311++G(d,p), cc-pVXZ and aug-cc-pVXZ, where X=D,T . The first three are part of the commonly used Pople basis sets[200] which usually provide good results. The last four are referred as Dunning (correlation-consistent) basis set[202,250], and can include diffuse functions, emphasized by the prefix "aug". As shown further in this work, adding diffuse functions to the hydrogen atoms, and thus extending the spatial range of these atomic orbitals, changes the expected optimal geometry of the BA derivatives, specially if the N_3 chain is closer to the methyl group, like in 2–MBA.

The most complete and computational demanding basis set used in this work is the correlation-consistent, valence triple ζ , augmented by diffuse functions in the s, p and d atomic functions (aug-cc-pVTZ), constituted of 713 basis functions, which is expected to produce the best results, as it is the one that best approximates the complete-basis-set (CBS) limit.

Structure optimization of all parameters was accomplished through the standard optimization procedures in the Gaussian code, namely the Berny optimization procedure and the following threshold values for the maximum remaining force on an atom in the system, the average (RMS) force on all atoms, the maximum structural change of one coordinate (maximum displacement), and the average (RMS) change over all structural parameters in the last two iterations, respectively: 0.45×10^{-3}, 0.3×10^{-3}, 1.8×10^{-3}, 1.2×10^{-3}. The starting geometries to these optimizations correspond already to the lowest energy conformations and were taken from our previous studies[251].

All calculations were performed on our cluster, composed of one AMD Opteron 275 at 2.2 GHz as the master node and nine Intel Core2 Quad Q6600 at 2.4 GHz as

computing nodes, running the Gaussian 03[205] program in a Linux environment. The orbital pictures were created using the Molekel[210] program (isosurface value of 0.07).

5.3 Results and discussion

5.3.1 Molecular structures

The molecular structures of BA and its methyl derivatives are depicted in Fig. 5.1. As stated earlier, the starting geometries for all optimizations were the ones obtained in a previous study; therefore only minor changes arose from the new optimizations with the different methods/basis set combinations.

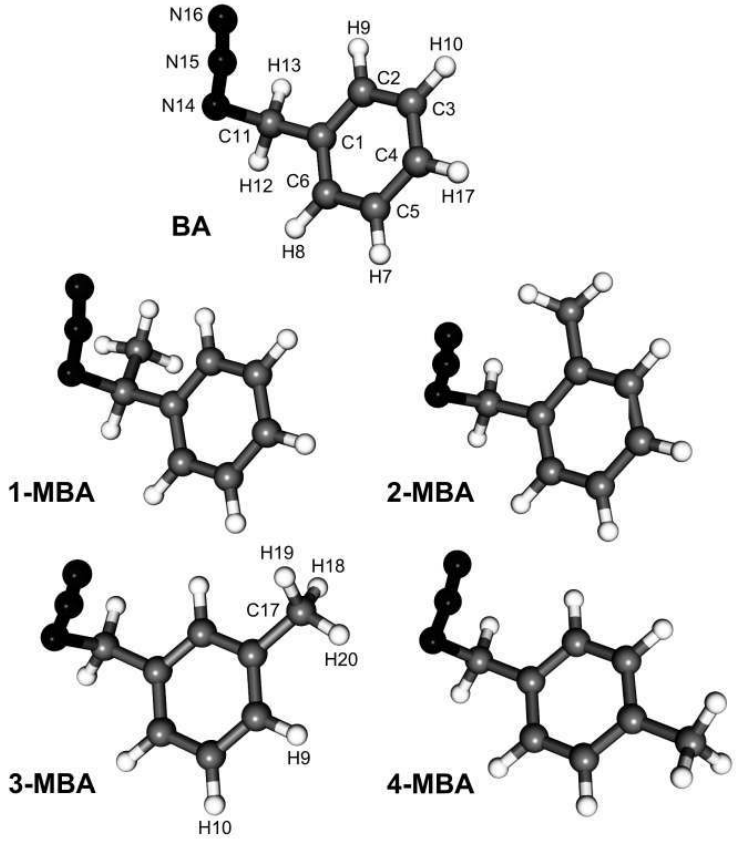

Figure 5.1: Molecular structure of benzyl azide and 1–, 2–, 3– and 4–methyl benzyl azide. 3–MBA has the same labelling/numbering as BA, except for the atoms that are explicitly labelled differently on the figure. 1–, 2– and 4–MBA share the same labelling/numbering as the 3– isomer.

The geometries correspond to the lowest energy conformers, where the benzene ring and the carbon atoms from the CH_2 and methyl groups reside in the same plane. The dihedral angle N_{15}–N_{14}–C_{11}–C_1 is always between 55° and 60°, except in the case of 2–MBA, in which its value goes down to approximately 35°, due to interactions between the nitrogen atoms and the methyl group. In 1–MBA, both azide and methyl groups step off the plane formed by the benzene ring, in opposite directions.

No symmetry group other than the trivial C_1 can be attributed to the molecules in study, at least in the lowest energy conformations; belonging to the C_S group could only occur with BA and 4–MBA, and only if the dihedral N_{15}–N_{14}–C_{11}–C_1 was 0° or 180° (and thus positioning the azide chain in a possible mirror plane that would cut

Table 5.1: Selected optimized parameters of BA and 1–, 2–, 3– and 4–MBA.

	MP2/aug-cc-pVTZ				
	BA	1–MBA	2–MBA	3–MBA	4–MBA
Bond length (Å)					
$r_{(N16-N15)}$	1.151	1.152	1.152	1.152	1.151
$r_{(N15-N14)}$	1.234	1.234	1.234	1.235	1.235
$r_{(N14-C11)}$	1.494	1.502	1.498	1.495	1.495
$r_{(C11-C1)}$	1.497	1.504	1.497	1.497	1.496
$r_{(C1-C2)}$	1.398	1.399	1.406	1.397	1.397
$r_{(C2-C3)}$	1.394	1.394	1.398	1.398	1.394
$r_{(C3-C4)}$	1.393	1.393	1.393	1.397	1.396
$r_{(C4-C5)}$	1.396	1.395	1.394	1.395	1.400
$r_{(C5-C6)}$	1.392	1.392	1.391	1.391	1.391
$r_{(C6-C1)}$	1.398	1.398	1.398	1.398	1.398
$r_{(C-CH_3)}$	–	1.520	1.505	1.503	1.503
$r_{(C-H)}$	≈1.08	≈1.08	≈1.08	≈1.08	≈1.08
Valence angles (°)					
$\angle_{(N16-N15-N14)}$	174.3	174.5	173.9	174.4	174.3
$\angle_{(N15-N14-C11)}$	113.1	113.3	114.7	113.1	113.1
$\angle_{(N14-C11-C1)}$	111.4	110.0	112.2	111.4	111.6
Torsion angles (°)					
$\angle_{(N15-N14-C11-C1)}$	54.9	57.25	34.7	53.9	54.5

the benzene ring through C_1, C_4 and C_{11}).

Table 5.1 presents a set of selected geometric parameters, obtained from the complete structure optimization of BA and its methyl derivatives, at the highest method/basis combination employed in this study – MP2/aug-cc-pVTZ.

5.3.2 Molecular orbitals and ionization energies

The molecular orbitals (MOs) of BA and its methylated compounds can be described in terms of the contributions of the MOs of benzene and azido groups[22,252]. Results arising from calculations with the MP2/6-311++G(d,p) method/basis combination provide a good qualitative description of the MOs shapes and orientations, whose contours are depicted in Fig. 5.2.

The first two MOs of the series (first and second columns of Fig. 5.2) originate mainly from the degenerate $1e_{1g}$ HOMO of benzene, which follows either a π_3 (HOMO of 4–MBA and BA's MO 34) or a π_2 (the remaining orbitals from the first and second columns) pattern.

The third and fourth MOs come from the azido group N_3: the third is comprised almost exclusively from the $\pi^*_{N_3}$ MO established in the nitrogen chain, whereas the fourth MO is a $\sigma^*_{N_3}$ that also features a very small σ_{CN} contribution. Considering the three outermost orbitals – $(11a')(12a')(3a'')$ – from the electronic configuration of methyl azide CH_3N_3, one can undoubtedly assign the third column MOs to the $3a''$ state and the fourth column MOs to the $12a'$ state.

The remaining MOs (fifth to seventh columns) correspond chiefly to several benzene orbitals, with more or less contributions from the nitrogens. MO 31 of BA and MO 34

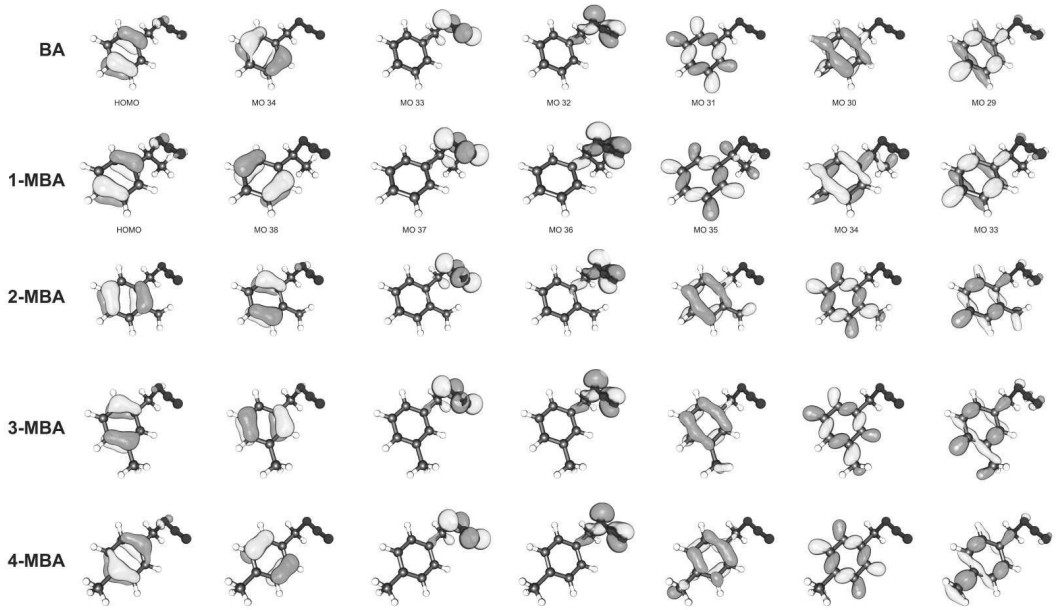

Figure 5.2: Selected molecular orbitals of benzyl azide and 1–, 2–, 3– and 4–methyl benzyl azide. The pictures are based on the MP2/6-311++G(d,p) results.

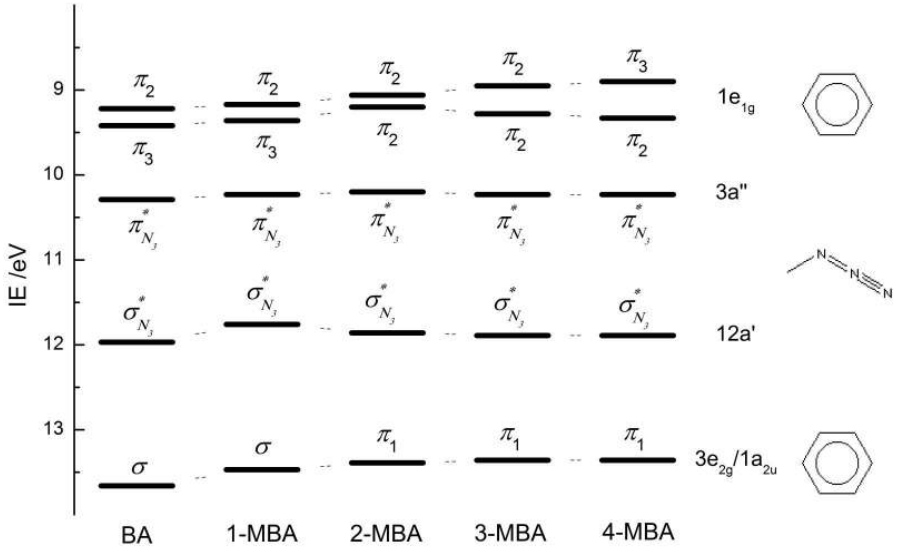

Figure 5.3: Energy diagram of BA and its methyl derivatives, based on MP2/6-311++G(d,p) results. On the right, the states from benzene and methyl azide that resemble the most to the MOs in study.

Table 5.2: Experimental VIEs of BA and its methyl derivatives, taken from Ref.[253], and theoretical results from MP2/aug-cc-pVTZ computations.

BA		1–MBA	2–MBA		3–MBA		4–MBA	
Exp	Calc	Calc	Exp	Calc	Exp	Calc	Exp	Calc
9.28	9.22	9.17	9.03	9.06	9.02	8.95	8.89	8.90
9.63	9.42	9.36	9.47	9.22	9.61	9.28	9.50	9.33
10.96	10.31	10.23	10.88	10.18	10.88	10.23	10.88	10.23
11.88	11.95	11.76	11.84	11.84	11.69	11.89	11.66	11.86
14.13	13.61	13.42	13.36	13.42	13.16	13.39	13.14	13.39

of 2–, 3– and 4–MBA portrait a strong resemblance to the degenerate $3e_{2g}$ orbital (σ) of benzene. Also, MO 30 of BA and MOs 35 of 2–, 3– and 4–MBA are mainly constituted from benzene's $1a_{2u}$ orbital, following a π_1 pattern. The last column (MO 29 of BA and MO 33 in the case of the methyl derivatives) can also be attributed to another pattern of $3e_{2g}$. Finally, the character of 1–MBA orbitals follow the same scheme and ordering as in BA. These interpretations are summarized in the energy diagram of Fig. 5.3.

Table 5.2 accounts for the experimental ionization energies (IEs) of the first 5 bands of each compound. The theoretical IEs obtained from the optimized structures of Table 5.1 (computed with MP2/aug-cc-pVTZ) are also presented, for comparison. The experimental values of the IEs are taken from our recent UVPES study[253] on these molecules (except 1–MBA) and are reliable within an error margin of ± 0.03 eV. Although this energy resolution could allow the study of the vibrational progressions on top of some of the bands, we only assess the vertical ionization energy (VIE) values through the theoretical methods employed; therefore, when referring to the IE's values, we are talking about the vertical values, which implies no geometry changes between the neutral molecule and the ion.

The following results are grouped by the type of *ab initio* method employed and the data is presented as differences from the experimental values, following the relationship $\Delta E_i = \epsilon_i$ - IE_i , where ϵ_i equals the absolute value of the energy of the i^{th} MO (counting upwards from the HOMO to the ground state) and IE_i stands for the experimental energy value obtained for the i^{th} band.

5.3.2.1 HF method

In Fig. 5.4 we notice that the HOMO energy of BA, 6-311++G(d,p) and aug-cc-pVTZ yield the best comparison between experimental and theoretical values. It is also noticeable from Fig. 5.4 that there is a significant approximation to the experimental values by adding diffuse functions to the set, for both Pople and Dunning basis set.

The exception occurs for the MO 32, a $\sigma^*_{N_3}$ orbital, where the inclusion of diffuse functions sets the computed energy farther away from the experimental value. There is also a clear discrepancy between the predicted and experimental energies of the third band (MO 33), that corresponds to the $\pi^*_{N_3}$ of the azide chain, giving rise to the highest differences over all basis sets, followed by major differences in MO 31.

In the case of 2–MBA (see Fig. 5.5), the best approximation to the HOMO energy is achieved with cc-pVTZ and aug-cc-pVDZ. Again, the inclusion of diffuse functions extends the range of interaction between the methyl group and the azide chain, changing the dihedral angle N_{15}–N_{14}–C_{11}–C_1 to lower values. As in BA, the energy of the second orbital assigned to the azide chain (MO 36) is gradually separated from the experimental value, as the basis set involves more and more diffuse functions. The largest differences occurs again in the computation of the energy of the first MO of the azide chain (MO

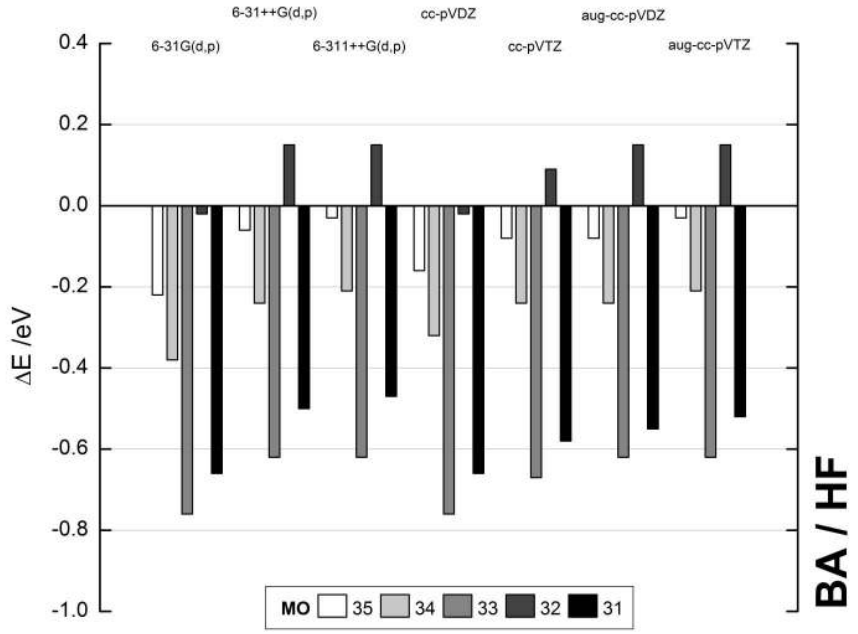

Figure 5.4: IE differences between the theoretical and experimental values, ΔE, for the first 5 bands of BA, calculated with HF and several basis.

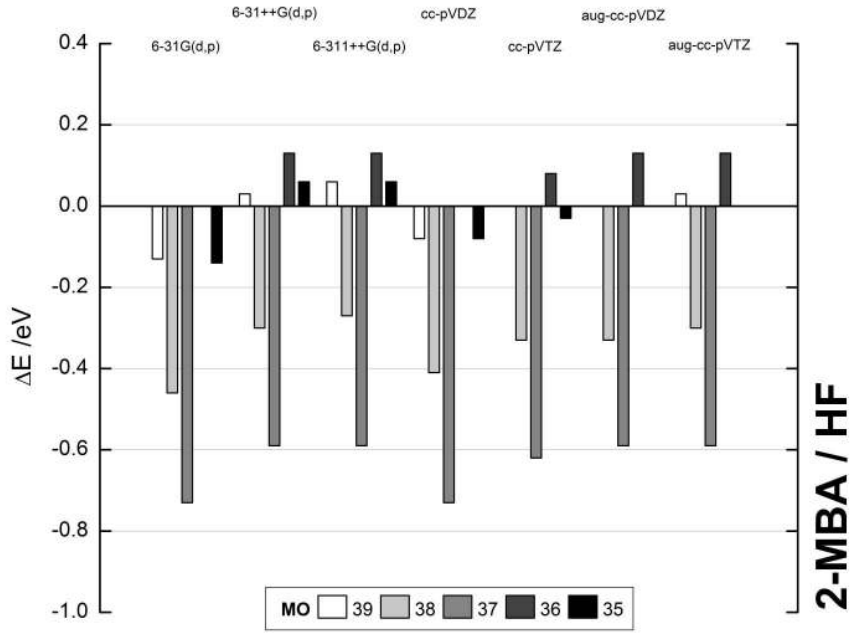

Figure 5.5: IE differences between the theoretical and experimental values, ΔE, for the first 5 bands of 2–MBA, calculated with HF and several basis.

35), by underestimation of the values.

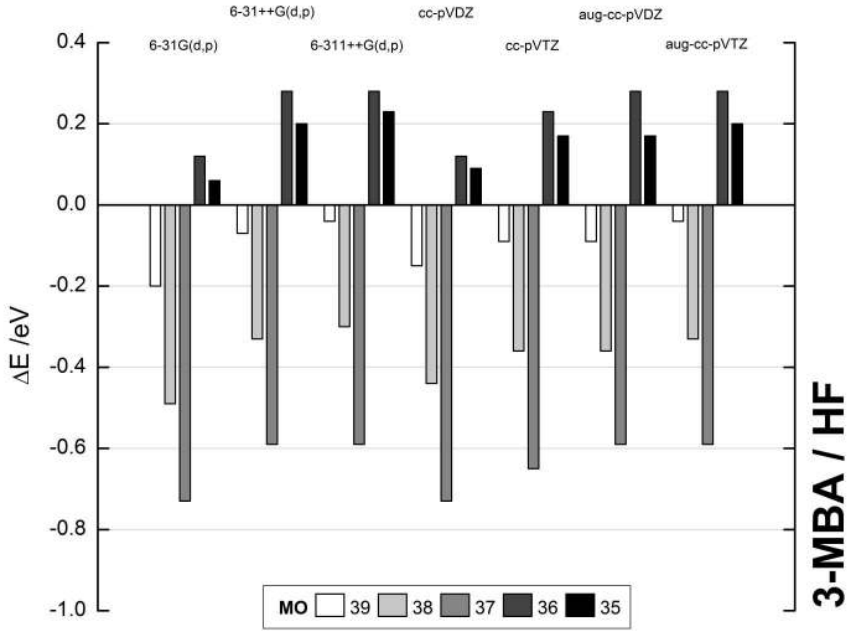

Figure 5.6: IE differences between the theoretical and experimental values, ΔE, for the first 5 bands of 3–MBA, calculated with HF and several basis.

The analysis of Figs. 5.6 and 5.7 reveals that the energies of the 3– and 4–MBA orbitals follow an equivalent pattern: adding diffuse functions to the basis sets lowers the energy difference of the first three MOs (two assigned to the benzene ring and one to the azide chain), but also originates an increase in the energy differences of the two last MOs (one corresponding to the azide chain and the last to the benzene ring). The best approximation to the HOMO energy is achieved with 6-311++G(d,p) and aug-cc-pVTZ, in the case of 3–MBA, and cc-pVTZ and aug-cc-pVDZ, in the case of 4–MBA.

5.3.2.2 MP2 method

From an overall perspective, the MP2 energy characterization of the first three MOs of BA and its methyl derivatives follows the same pattern as in the HF study: adding diffuse functions and enlarging the basis set leads to an approximation to the experimental values (Figs. 5.8 to 5.11).

When comparing the results derived from the two theoretical methods, one can state that the correlation energy correction introduced via MP2 implementation does not constitute that much of an improvement over the previous HF values, for the first three bands in study. Moreover, the effective influence of this correction can only be translated into a slight decrease in the energy differences of the last two bands considered in this study (MOs 32 and 31 of BA and MOs 36 and 35 of the derivatives). The huge discrepancy between the experimental and theoretical energies of the first azide band still does not change within the MP2 framework, with differences ranging from -0.84 eV, in the worst case, and -0.61 eV, at best (the negative value indicating that the IE prediction is underestimated relatively to the experimental value).

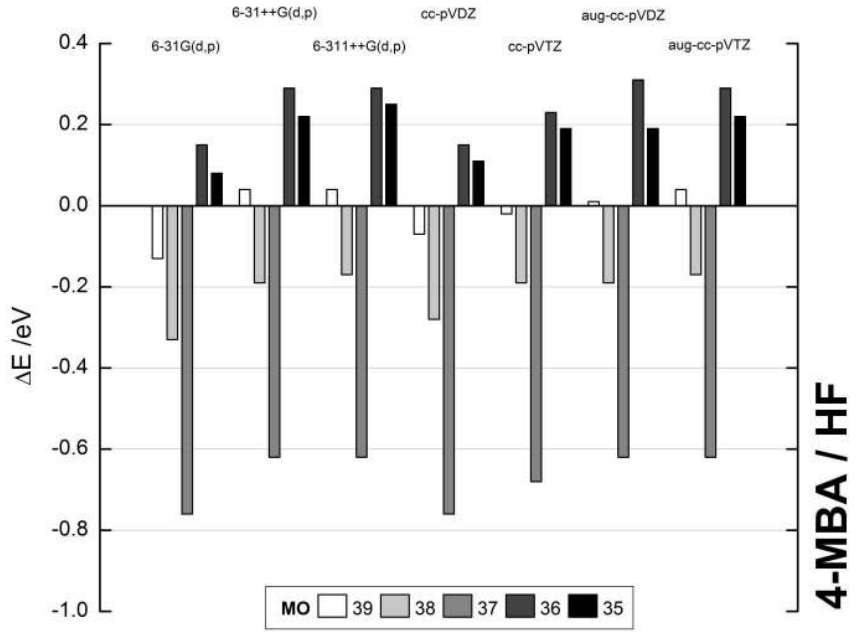

Figure 5.7: IE differences between the theoretical and experimental values, ΔE, for the first 5 bands of 4–MBA, calculated with HF and several basis.

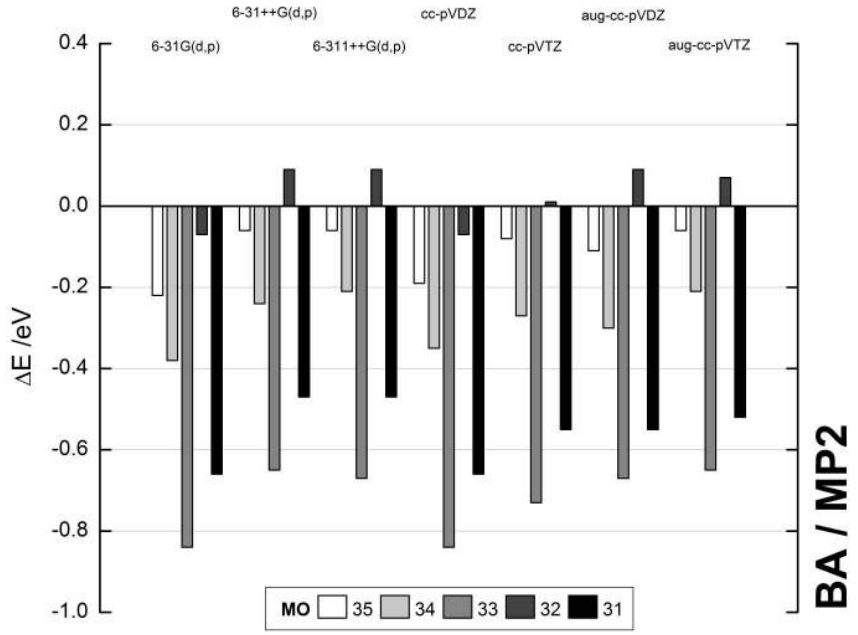

Figure 5.8: IE differences between the theoretical and experimental values, ΔE, for the first 5 bands of BA, calculated with MP2 and several basis.

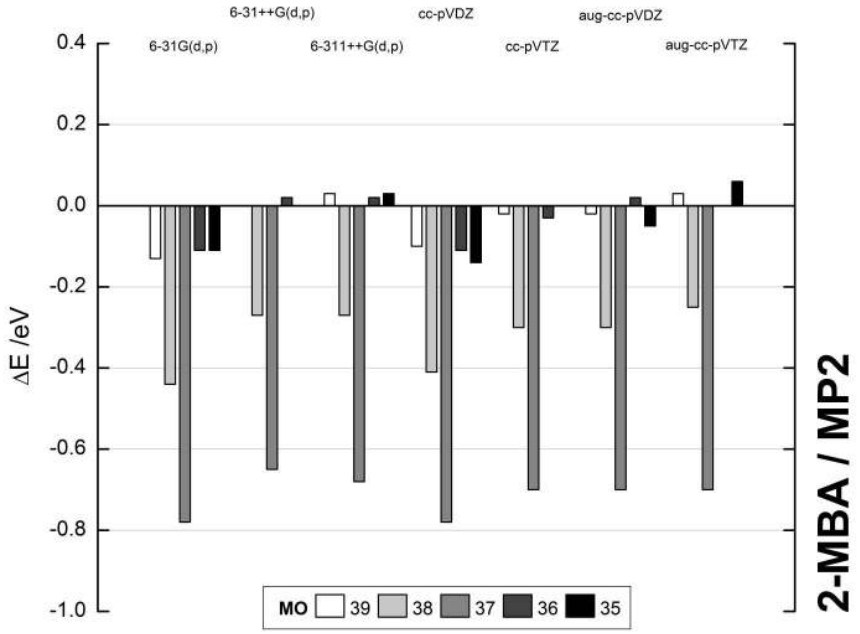

Figure 5.9: IE differences between the theoretical and experimental values, ΔE, for the first 5 bands of 2–MBA, calculated with MP2 and several basis.

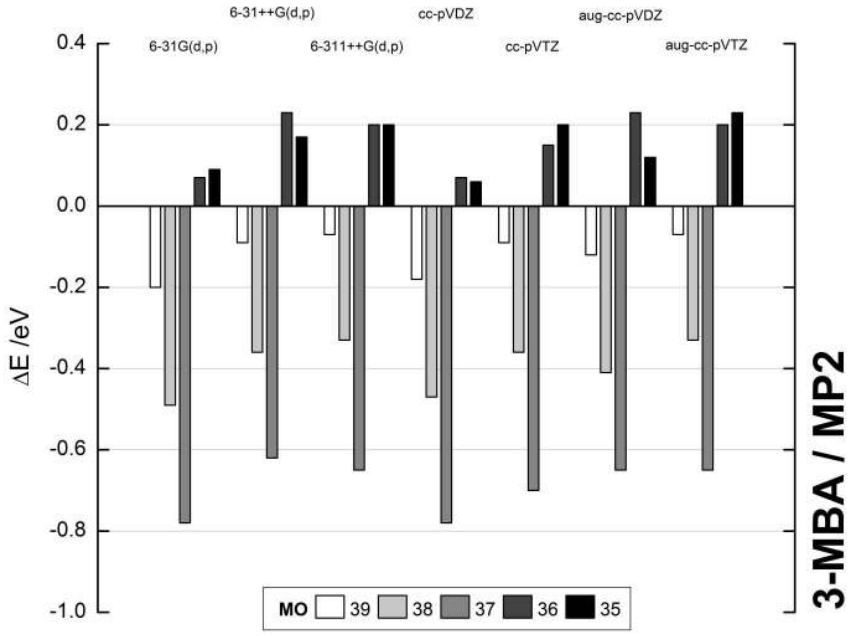

Figure 5.10: IE differences between the theoretical and experimental values, ΔE, for the first 5 bands of 3–MBA, calculated with MP2 and several basis.

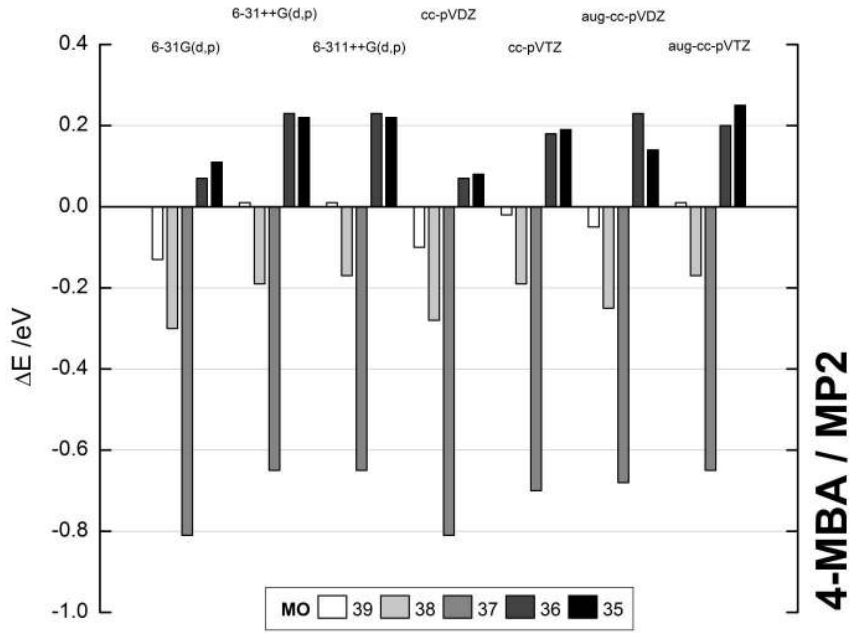

Figure 5.11: IE differences between the theoretical and experimental values, ΔE, for the first 5 bands of 4–MBA, calculated with MP2 and several basis.

5.4 Conclusions

From this study, two evident facts emerge: the need of higher level calculations is crucial in the theoretical study of the molecular structure and IEs of aromatic azides, by means of a large basis set, and the difficulty in predicting the energy of both azide states $\pi^*_{N_3}$ and $\sigma^*_{N_3}$ with the same level of accuracy, with increasing completeness of basis set. Also, the proximity of the CH_3 relatively to the N_3 chain clearly affects the energy separation between the two first ionization energies of the methyl derivatives of BA – the energy gap between MOs 39 and 38 , which are mainly $1e_{1g}$ states of benzene, increases as the methyl group is positioned farther away from the azide chain, into different ring positions. This energy gap should be noticeable in the UVPES spectra of the compounds.

Finally, BA and 1–, 2–, 3– and 4–MBA share the same orbital ordering until the fifth band, where MO 31 of BA is made up almost entirely of one pattern of benzene $3e_{2g}$ state, whereas MO 35 of the methyl derivatives is made up of $1a_{2u}$ state of benzene.

Although the HF and MP2 methods employed in this work provide good results that support the assignment of UVPES spectra, the application of electron propagator theory for predicting the IEs could prove fruitful in future studies.

Chapter 6

BA and 2-, 3-, 4-MBA: UVPES and Mass Spectrometry

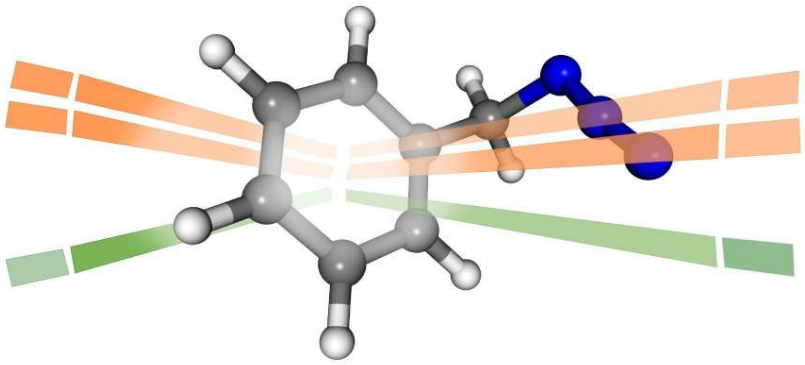

6.1 Introduction

Phenyl azide prepared in the nineteenth century was the first synthetic organic azide[12]. Since then the application of organic azides, in science and technology, has grown dramatically[11–13]. Organic azides have been largely used as precursors for synthesis[11–13], for amines and recently in "click" chemistry[254–257]. This concept has, recently, emerged[254] exploiting rapid, modular reactions developing under a large thermodynamic driving force. The resulting synthetic products have been applied in areas such as supramolecular chemistry[255], biochemistry[256] and in developing compounds relevant for antiviral and anticancer treatment[257]. On the other hand, azidonucleosides showed to be of primordial interest in AIDS treatment[11,258], azido sugars in biological labelling[68] and in tumour-growth inhibition[259]. Moreover, azides are potential high-energy density materials (HEDMs)[69] and are also used in the generation of electrically conducting polymers[70] and in the covalent modification of polymer surfaces[260].

Due to their thermodynamic instability, explosive nature and shock sensitivity[69], their structural characterization is experimentally challenging. However, the physicochemical properties of some aliphatic azides have been investigated spectroscopically

[†]Reproduced with permission from *J. Mol. Struct.* **2010**, *980*, 163-171.

by ultraviolet photoelectron spectroscopy (UVPES) and matrix isolation infrared spectroscopy (MIIS)[29–31]. Electron ionization mass spectrometry (EIMS) has been successfully applied to the study of phenyl azides and its derivatives[261]. Some azides, already studied by UVPES and MIIS were also investigated by EIMS[35,262] and chemical ionization mass spectrometry (CIMS)[36].

Table 6.1: Structures of the studied benzyl azides

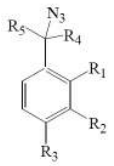

Compound	R_1	R_2	R_3	R_4	R_5
1	H	H	H	H	H
2	H	H	H	D	D
3	CH_3	H	H	H	H
4	H	CH_3	H	H	H
5	H	H	CH_3	H	H

At present very little is known about the fate of organic azides involving an aromatic ring such as benzyl azide. Thus, benzyl azide and three methylated isomers were synthesized and characterized in terms of electronic configuration and ionization energies, using mass spectrometry and UV photoelectron spectroscopy.

The present paper reports a combined experimental study of the following compounds shown in Table 6.1: benzyl azide (BA) (**1**), deuterated benzyl azide (**2**), 2-methylbenzyl azide (2-MBA) (**3**), 3-methylbenzyl azide (3-MBA) (**4**), 4-methylbenzyl azide (4-MBA) (**5**). Experimental results were supported by theoretical calculations.

6.2 Experimental and theoretical methods

6.2.1 General procedure for sample preparation and characterization

The azides are potentially explosive and therefore must be handled with all due precautions. Azides and some decomposition products like HCN may be toxic[71].

Sodium azide (2 equiv.) was added slowly to a solution of the appropriate benzyl halide in dimethyl sulfoxide. The mixture was stirred at room temperature until TLC analysis (hexane:dichlorometane 7:3) indicated completion of the reaction. The mixture was quenched with distilled water, extracted with diethyl ether and the combined organic phases were dried over anhydrous sodium sulphate, filtered and concentrated[263]. After preparative TLC the product obtained (η>90%) was analysed by FTIR (Mattson Satellite-FITR) and by NMR (Bruker ARX400). The deuterated benzyl azide was prepared under argon from benzyl bromide-α, α-d_2 in deuterium oxide.

Care was taken to minimize the effect of possible explosions at all stages in the preparation and handling of the azide samples, but no untoward occurrences were experienced during this work. The products were characterized in the vapour phase by UV photoelectron spectroscopy and mass spectrometry and in the liquid phase by ^{1}H and ^{13}C NMR and by IR spectroscopy.

Benzyl azide (**1**): IR data (neat): ν_{max} 2098 (N_3) cm^{-1}; ^{1}H NMR data (400 MHz, $CDCl_3$): δ 4.35 (s, CH_2), 7.34-7.44 (m, CH arom.) ppm; ^{13}C NMR data (100 MHz, $CDCl_3$): δ 54.7 (CH_2), 128.2-128.8, 135.3 ppm.

Deuterated benzyl azide (**2**): IR data (neat): ν_{max} 2100 (N_3) cm^{-1}; ^{1}H NMR data (400 MHz, $CDCl_3$): δ 7.25-7.41 (m, CH arom.) ppm; ^{13}C NMR data (100 MHz, $CDCl_3$): δ 128.2-128.8, 135.3 ppm.

2-methylbenzyl azide (**3**): IR data (neat): ν_{max} 2096 (N_3) cm-1; ^{1}H NMR data (400 MHz, $CDCl_3$): δ 2.35 (CH_3), 4.32 (s, CH_2), 7.18-7.26 (m, CH arom.) ppm; ^{13}C

NMR data (100 MHz, $CDCl_3$): δ 18.9 (CH_3), 53.0 (CH_2), 126.2, 128.6, 129.3, 130.6, 133.3, 136.7 ppm.

3-methylbenzyl azide (**4**): IR data (neat): ν_{max} 2096 (N_3) cm-1; ^{1}H NMR data (400 MHz, $CDCl_3$): δ 2.39 (CH_3), 4.32 (s, CH_2), 7.13-7.32 (m, CH arom.) ppm; ^{13}C NMR data (100 MHz, $CDCl_3$): δ 21.3 (CH_3), 54.8 (CH_2), 125.2, 128.7, 128.9, 129.0, 135.3, 138.5 ppm.

4-methylbenzyl azide (**5**): IR data (neat): ν_{max} 2098 (N_3) cm^{-1}; ^{1}H NMR data (400 MHz, $CDCl_3$): δ 2.35 (CH_3), 4.27 (s, CH_2), 7.17-7.23 (m, CH arom.) ppm; ^{13}C NMR data (100 MHz, $CDCl_3$): δ 21.1 (CH_3), 54.6 (CH_2), 128.2, 129.5, 132.3, 138.1 ppm.

6.2.2 Mass spectrometry

The electron ionization (EI) mass spectrometry technique was used to undertake all the mass spectra presented herein by using an AEI - MS9 mass spectrometer updated by VG Analytical Instruments. Electron ionization mass spectrometry was performed with nominal electron energies of 70 eV, 200 mA trap current, and a source housing pressure of about 1.33 x10^{-4} Pa and analyser pressure about 2.66 x10^{-5} Pa. The ions were accelerated through 8 kV. Linked scans at constant B/E were also accomplished for all important fragmentation peaks identified in the normal mass spectra. For some of the ions, high resolution accurate mass data, were obtained using a VG70-250SE mass spectrometer with resolution of 10,000 (10% valley) by the peak matching technique with perfluorokerosene (PFK) as a reference compound.

6.2.3 Photoelectron spectroscopy

The photoelectron (PE) spectra obtained for benzyl azide and its methyl derivatives were recorded using the single detector instrument described elsewhere[99]. All the aromatic azides investigated herein were liquid with a relatively sufficient vapour pressure at room temperature to allow PE spectra to be recorded with acceptable signal-to-noise ratio. The spectra were obtained by direct pumping on a liquid sample held in a small flask through a needle valve outside the spectrometer ionization chamber. The operating resolution of the photoelectron spectrometer was typically 30 meV as measured for argon $(3p)^{-1}$ fwhm ionized with He(I)α radiation (21.22 eV).

Calibration of the vertical ionization energies (VIEs) of the parent azides photoelectron bands was achieved using argon and methyl iodide[116] added to the ionization chamber at the same time as the azide vapour samples. PE spectra were obtained for the starting materials used in the preparation of the studied samples. No evidence of bands associated with starting materials was found in PE spectra recorded for purified samples of the azides under study.

6.2.4 Computational details

All theoretical calculations were carried out with the Gaussian 03 program package[205]. Full structure optimization was performed on each molecule, with the Hartree-Fock (HF) method and the 6-311++G(d,p) basis[200], to establish equilibrium geometries, and subsequently to calculate VIEs. The starting geometries for all optimizations were the ones obtained in a previous conformational study and already correspond to lowest energy geometries[251].

For the VIEs, Koopmans' theorem[166] was applied to the SCF orbital energies obtained at HF/6-311++G(d,p) level. The computed molecular orbital (MOs) energies ϵ_i of benzyl azide and its methyl derivatives were assigned to the experimental ionization energies obtained in the spectra, as $IE_i \approx -\epsilon_i$, in a non-scaled form.

In order to support the mass spectrometry studies, the optimized geometries of the radical cations of benzyl azide (BA), 2-, 3- and 4-methylbenzyl azide (2-, 3- and 4-MBA) were obtained at the UHF/6-311++G(d,p) level of theory. Furthermore, in order to support some fragmentation pathways concerning 4-MBA, an initial search for the transition structures (TS) connecting the precursor and the product ions was performed by scanning the length of a particular bond of interest and optimizing the remaining structural parameters. The TS existence was verified by full optimization of its geometry, followed by vibrational analysis (producing only one imaginary frequency), at the UHF/6-311++G(d,p) level of theory. In addition, the minima connected by a given TS were confirmed by intrinsic reaction coordinate (IRC) calculations[264], with the UHF/6-31G(d) method/basis.

6.3 Results and discussion

6.3.1 Mass spectrometry

All the compounds were studied under EI conditions. The mass spectra of the compounds examined are summarized in Table 6.2. The molecular ion of all the compounds were observed, but some of them with very low abundance. The fragmentation sequences were clarified by linked scans at constant B/E[265]. Besides mass spectrometric methods, isotopic labelling of benzyl azide was useful for the understanding of some mechanisms.

A metastable transition study was required in order to distinguish between ions resulting from the ionization of thermal degradation products and ions produced by ionization of samples and their further fragmentation. All the fragmentation pathways proposed have been based on both, fragmentation sequences observed in the linked scan spectra and high resolution mass spectra data. In addition, the full optimized structures of the methylbenzyl azide radical cations (2-MBA$^{+\bullet}$, 3-MBA$^{+\bullet}$ and 4-MBA$^{+\bullet}$) were obtained at the UHF/6-311++G(d,p) level. Fig. 6.1 shows these structures, with special emphasis to changes in the CC-NN dihedral angle, before and after the loss of an electron. In all normal EI spectra intense peaks were detected at *m/z* 18 being, probably, due to water present in the hygroscopic azides.

6.3.1.1 Benzyl azide

Although aliphatic azides such as α-carbonyl azides[35] normally lose N_2, from the molecular ion, this was not observed for benzyl azide. It was found, through linked scans at constant B/E, that N_3 and HN_2 were the preferred losses from the molecular ion of benzyl azide (Table 6.3). The loss of N_3 seems to be the most favoured one (Table 6.2) since ion at *m/z* 91 is the base peak. Similar behaviour is observed in a typical EI mass spectrum obtained for deuterated benzyl azide (Fig. 6.2).

For this azide the peak at *m/z* 28 can be explained by thermal decomposition prior to ionization. From Table 6.3 it can be seen that the molecular ion never loses 28 Da.

The fragmentation mechanisms were established by linked scans at constant B/E and accurate mass measurements (Table 6.3 and Table 6.4). The proposed mechanisms were supported by labelling as presented in Fig. 6.3. According with the parallel mechanisms, in that figure, the ion at *m/z* 91 and its deuterated form at *m/z* 93 must have a tropylium ion structure. In fact, ion at *m/z* 93 displays a loss of C_2H_2 and not C_2D_2 which proves a scrambling of H/D atoms only possible in a $C_7H_7^+$ with a tropylium structure. Furthermore, the other main loss, HN_2, is also clarified by the deuterated benzyl azide. Since the latter benzyl azide loses DN_2 the leaving hydrogen/deuterium is in a neighbouring position relative to the azido group.

Table 6.2: EI (70 eV) mass spectra of compounds 1-5. Relative ionic abundances in %.

	Compound				
m/z	1	2	3	4	5
17	5.0	3.6	5.0	4.0	-
18	24.7	12.9	24.0	19.0	4.2
26	1.0	-	2.0	-	-
27	2.8	2.9	5.0	8.0	1.4
28	34.4	20.0	35.0	31.0	14.8
32	6.3	5.7	5.0	4.0	2.3
37	1.6	2.1	2.0	-	-
38	2.8	2.9	4.0	4.0	-
39	6.9	6.4	18.0	19.0	3.8
40	-	5.0	3.0	4.0	-
41	2.5	2.9	5.0	4.0	1.1
43	1.9	-	2.0	-	-
50	9.4	11.4	7.0	-	1.7
51	16.9	20.7	13.0	8.0	3.0
52	9.1	8.6	5.0	15.0	-
53	-	6.4	4.0	8.0	-
59	-	-	7.0	8.0	-
62	1.6	2.9	5.0	8.0	1.1
63	3.8	4.3	13.0	15.0	2.6
64	1.3	4.3	5.0	8.0	1.0
65	5.9	4.3	22.0	23.0	5.5
66	-	5.7	3.0	4.0	-
67	-	5.7	-	-	-
74	3.1	4.3	2.0	2.0	-
75	2.5	3.6	2.0	2.0	-
76	5.0	5.7	2.0	2.0	-
77	34.4	27.1	13.0	15.0	2.7
78	15.6	8.6	7.0	8.0	1.0
79	1.9	17.1	9.0	8.0	1.8
80	-	4.3	-	-	-
89	1.9	-	13.0	12.0	2.5
90	1.3	2.1	9.0	8.0	1.9
91	100.0	2.9	64.0	77.0	43.6
92	6.3	3.6	15.0	15.0	3.4
93	-	100.0	2.0	-	-
94		9.3			
103	4.1	11.4	8.0	8.0	1.6
104	37.5	8.6	73.0	8.0	1.4
105	5.3	34.3	100.0	100.0	100.0
106	2.5	9.3	9.0	12.0	3.8
107	-	9.3	-	-	-
115	-	-	7.0	-	-
116	-	-	24.0	8.0	2.0
117	-	-	91.0	12.0	3.4
118	-	-	36.0	58.0	59.1
119	-	-	4.0	31.0	17.0
133	$M^{+\bullet}$43.8	-	-	-	-
134	3.8	-	-	-	-
135	-	$M^{+\bullet}$45.7	-	-	-
136	-	5.7	-	-	-
147	-	-	$M^{+\bullet}$15	$M^{+\bullet}$77	$M^{+\bullet}$20.5

Table 6.3: Linked scans data for compounds 1-5.

Compound	Precursor ion (m/z)	Product ions (m/z)
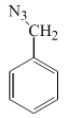	133	104,91
	104	77
	91	65
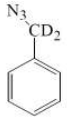	135	105, 93
	105	104, 77
	93	67
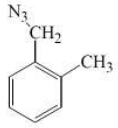	147	120, 119, 118, 105, 104
	118	117, 116, 104, 92, 91, 77
	105	104, 103, 79, 78, 77
	104	103, 102, 78, 77
	91	90, 65, 64
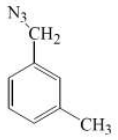	147	119, 118, 117, 105, 91
	118	117, 116, 103, 92, 91, 90, 78, 77
	105	104, 103, 79, 78, 77
	91	90, 65, 64
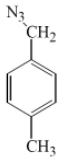	147	119, 118, 105, 91
	118	92, 91, 77
	105	103, 79, 77
	91	65

Table 6.4: Accurate mass data for benzyl azide.

m/z	Elemental composition	Measured value	Calculated value	Diff. (ppm)
133	$C_7H_7N_3$	133.06416	133.06400	-1.2
104	C_7H_6N	104.05079	104.05002	-7.4
91	C_7H_7	91.05380	91.05478	10.7
77	C_6H_5	77.03846	77.03913	8.7
65	C_5H_5	65.03786	65.03913	19.4

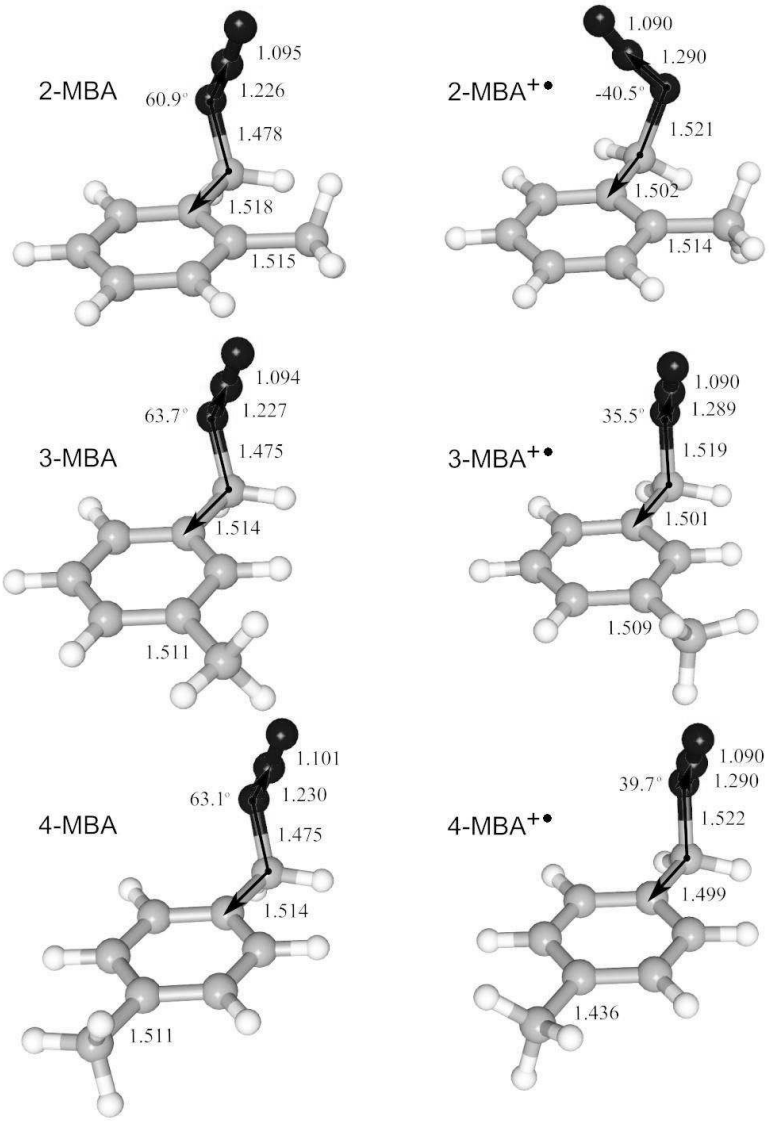

Figure 6.1: Optimized structures of 2-, 3- and 4-MBA and corresponding radical cations, obtained with restricted and unrestricted HF/6-311++G(d,p), respectively. Bond lengths are in angstroms (Å).

6.3.1.2 Methylbenzyl azides

From the mass spectrometry data analysis it can be concluded that all the methylbenzyl azides present common features. All the normal mass spectra showed the molecular ion peak which is most intense in the case of the *meta*-isomer (see Table 6.2). The linked scans study was essential to establish sequential fragmentation patterns of benzylic azides. Based on both, linked scans (Table 6.3) and accurate mass measurements (Table 6.5), a possible general mechanism for *para*-methylbenzyl azide is summarized in Fig. 6.4. In this scheme is observed a forbidden transition, loss of $HN_2^{\bullet}$ from the molecular ion followed by the loss of another radical, $CN^{\bullet}$. Nevertheless, exceptions to the even electron rule, are reported in the literature[266]. However, when the molecular ion loses 29 Da, the sequential loss of N_2 and H cannot be excluded.

Considering benzyl azide as the model compound we found that there should be at least two possible major fragmentation pathways, corresponding to loss of 29 and 42 Da from the molecular ion. These losses must be due to elimination of HN_2 radical

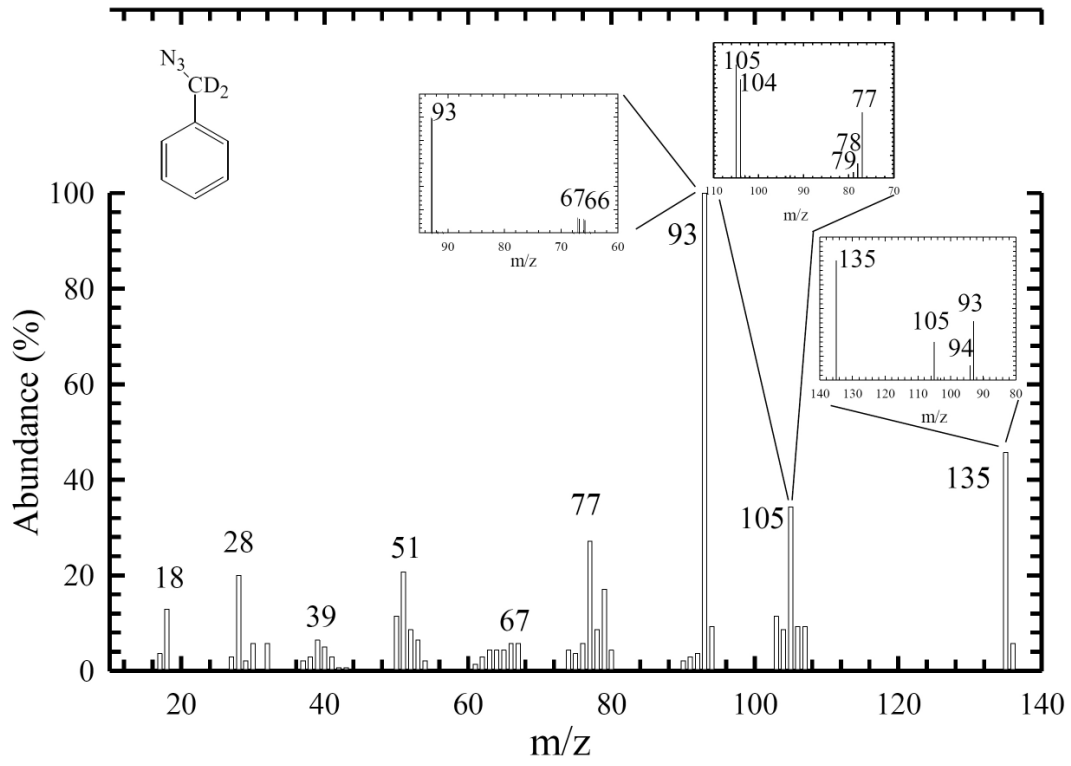

Figure 6.2: Mass spectrum for deuterated benzyl azide and its linked scan at constant B/E for the main peaks.

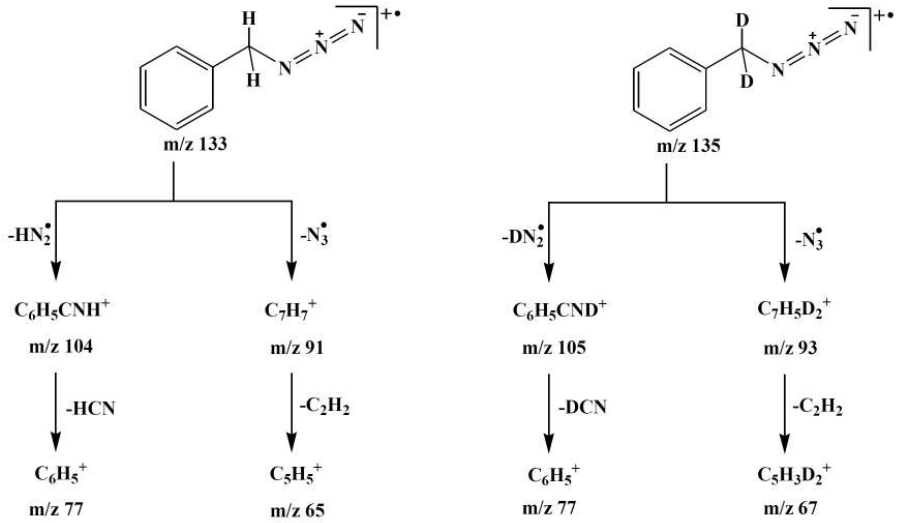

Figure 6.3: Main fragmentation pathways, for benzyl azide and deuterated benzyl azide, based on metastable transitions and accurate mass measurements.

and N_3 radical from the molecular ion. The resulting ions in the case of benzyl azide are at *m/z* 104 and 91, respectively, and in the cases of all methyl isomers are at *m/z* 118 and 105.

Among all methyl isomers the *ortho* can be characterized by a very abundant ion at *m/z* 104. In fact, the presence of a CH_3 group in the *ortho* position must be a determinant factor for the releasing of HN_3 from the molecular ion. This metastable transition is not observed for the other isomers, which explains the insignificant abundance of ion at *m/z* 104 in the other two isomers. On the other hand, while there is a parallel between the mechanism that leads to the formation of ion at *m/z* 118 in methylbenzyl azides and the formation of an ion at *m/z* 104 for benzyl azide, the ion at *m/z* 104 for *ortho*-methylbenzyl azide must be formed through a different mechanism, involving a six member ring intermediate (Fig. 6.5), not observed for the other isomers neither for benzyl azide.

Another interesting difference of the *ortho* isomer towards the *meta* and *para* isomers is the origin of ion at *m/z* 91. This ion has various precursor ions as shown in Table 6.3. For *meta* and *para* isomers this ion can be a product ion of the molecular ion by loss of $CH_2N_3^{\bullet}$ unlike the *ortho* for which this route is not observed. This is consistent with a favoured loss of HN_3 from the molecular ion in the *ortho* case. This is an example of the reported *ortho* effect[267,268] which explains rearrangements involving hydrogen transfer between neighbouring groups on an aromatic ring. A rigid planar arrangement of the interacting groups facilitates the formation of a cyclic transition state. This effect is very useful in the characterization of *ortho*-substituted compounds as the larger spatial separation of interacting groups, in *meta*- and *para*-substituted isomers, makes the same type of interaction weaker or non-existent.

The main difference between *meta* and *para* isomers is that less fragmentation is observed in the normal spectra, for the *para* isomer, which is supported by a smaller number of metastable transitions (Table 6.3). In fact, the substituents in *para* position must introduce resonance stabilization in the resulting ions. Moreover, comparing *meta* and *para* fragmentations, from the linked scans in Table 6.3, it can be seen that besides the fragmentation routes presented in Fig. 6.4 for *para*, some other complementary routes can be observed for *meta*, namely the fragmentation routes for ions at *m/z* 105 and 91. Nevertheless, the *meta* derivative presents the most abundant molecular ion. This must be due to the methyl group in *meta* position not being able to stabilize positive charges of the fragments. In addition, the abundance of ion at *m/z* 91 is higher for *meta* isomer.

Finally, in spite of the strong evidence of its occurrence in the linked scans results,

Table 6.5: Accurate mass data for *para*-methylbenzyl azide.

m/z	Elemental composition	Measured value	Calculated value	Diff. (ppm)
147	$C_8H_9N_3$	147.07938	147.07965	1.8
119	C_8H_9N	119.07274	119.07350	6.4
118	C_8H_8N	118.06627	118.06567	-5.0
105	C_8H_9	105.07055	105.07043	-1.2
103	C_8H_7	103.05347	103.05478	12.6
92	C_7H_8	92.06064	92.06260	21.3
91	C_7H_7	91.05582	91.05478	-11.5
79	C_6H_7	79.05639	79.05478	-20.5
77	C_6H_5	77.04060	77.03913	-19.1
65	C_5H_5	65.03960	65.03913	-7.3

the first two pathways presented in Fig. 6.4 were also confirmed by IRC calculations. The route leading to the formation of *para*-methyl-benzylidene imine cation, through N_2 elimination and concerted migration of the H atom to the neighbouring N, is depicted in Fig. 6.6, where a reaction barrier of approximately 33.9 kJ/mol was computed at the UHF/6-31G(d) level of theory. The TS is formed by a concerted mechanism: simultaneous to the elongation of the N-N_2 bond, the H-C-N angle closes significantly.

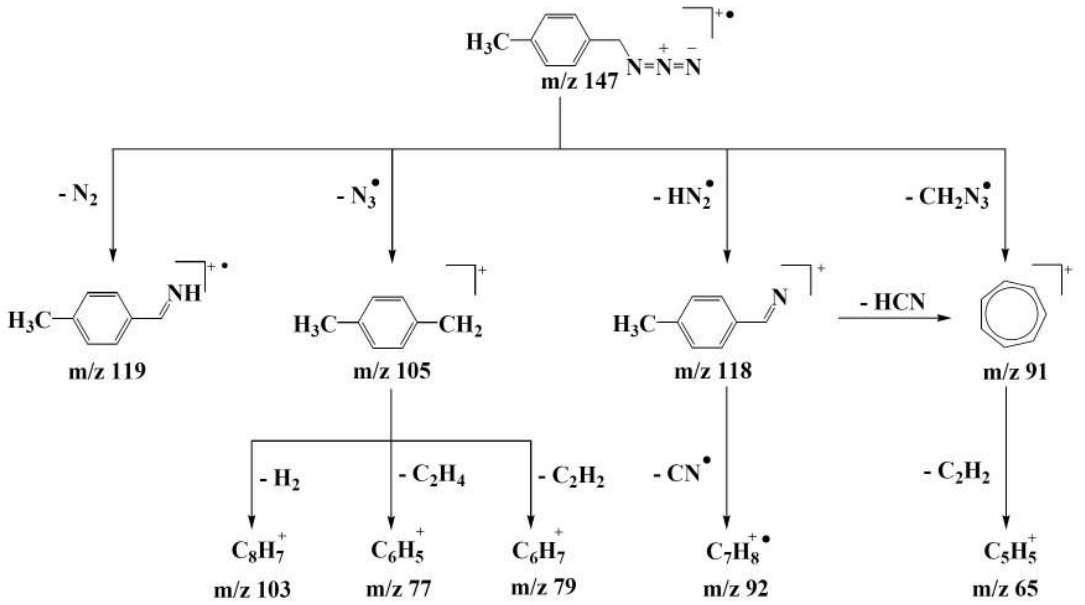

Figure 6.4: Main fragmentation pathways, for *para*-methylbenzyl azide, based on metastable transitions and accurate mass measurements.

The second pathway portrayed in Fig. 6.4, releasing of N_3 from the *para*-isomer, and formation of the N_3 radical plus the *para*-methylbenzyl cation, has also been the subject of theoretical investigation. IRC calculations initiated at the transition structure connecting the precursor ion and product molecules are shown in Fig. 6.7, where a reaction barrier of approximately 19.5 kJ/mol arises. This barrier lower than the one for the N_2 loss explains the *m/z* 105 ion abundance higher than the one for *m/z* 119 ion (Table 6.2). In addition, for benzyl azide, the $N_3^{\bullet}$ elimination must be, also, the most favoured decomposition channel as *m/z* 91 corresponds to the most abundant ion.

Table 6.6 presents the total and relative energies of benzyl azide and methylbenzyl azide radical cations, as well as transition structures and fragmentation products associated with the first two channels depicted in Fig. 6.4, obtained at UHF/6-311 ++G(d,p) level. The fully optimized transition structures TS1 and TS2, also obtained with UHF/6-311++G(d,p), are shown in Fig. 6.8, where some selected geometric pa-

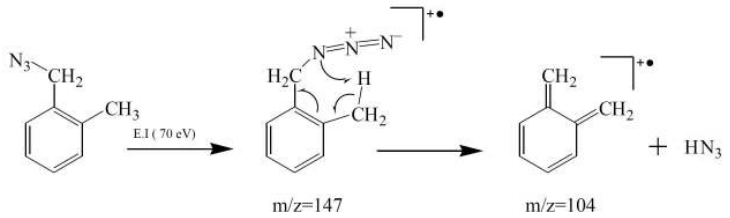

Figure 6.5: Possible mechanism for formation of ions at *m/z* 104 in *ortho*-methylbenzyl azide.

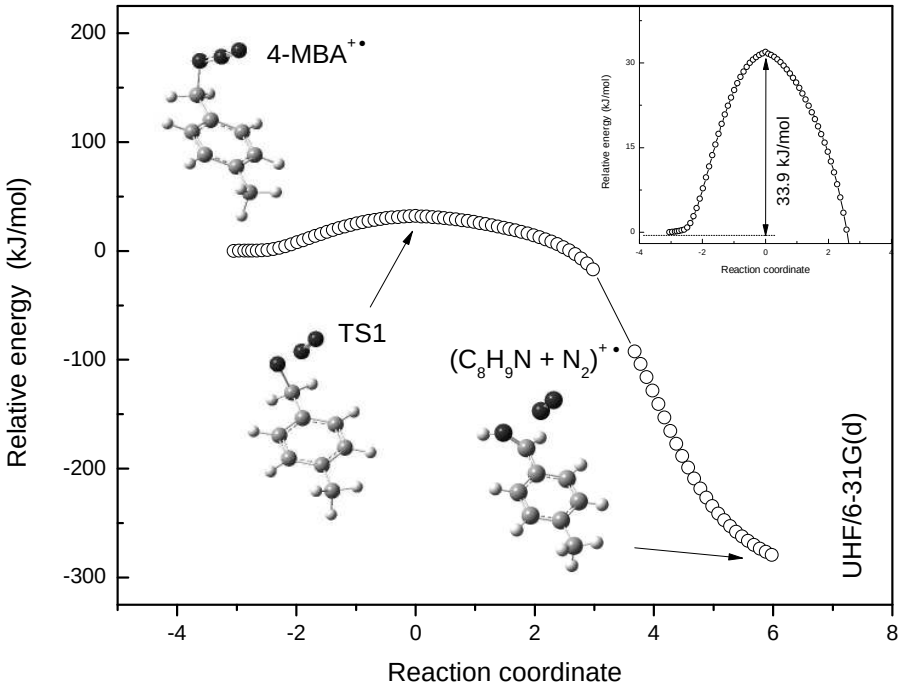

Figure 6.6: IRC calculation results for the fragmentation pathway leading to the formation of *para*-methylbenzylidene imine radical cation + N_2 from 4-MBA$^{+\bullet}$, determined with UHF/6-31G(d).

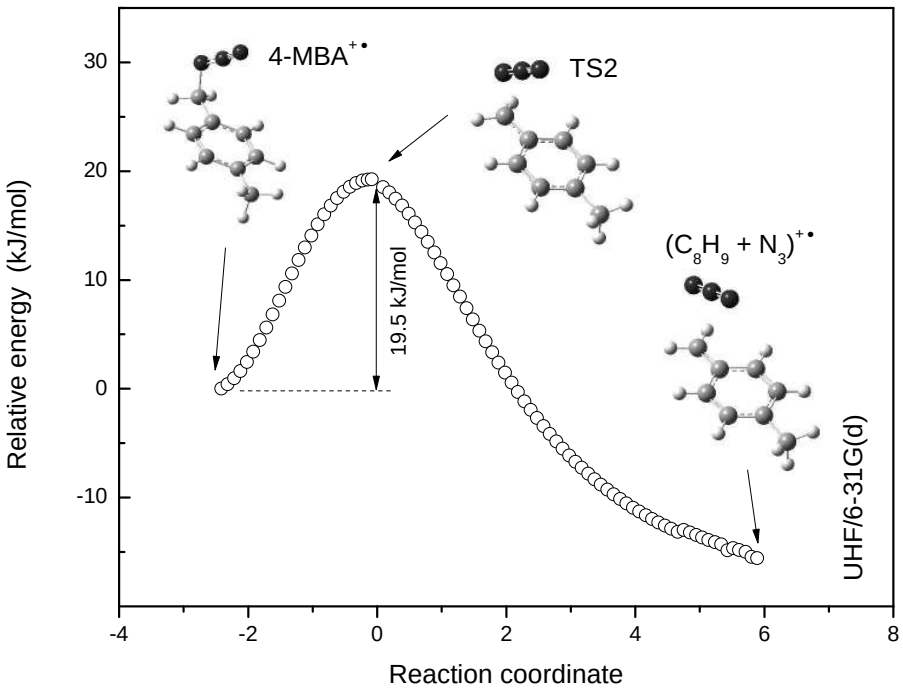

Figure 6.7: IRC calculation results for the fragmentation pathway leading to the formation of *para*-methylbenzyl cation + N_3 radical from 4-MBA$^{+\bullet}$, determined with UHF/6-31G(d).

Table 6.6: Total (hartree) and relative energies (kJ/mol) of benzyl and methylbenzyl azide ions, selected transition structures and corresponding fragmentation products.

	UHF/6-311++G(d,p)	
Cations	Total energy	Relative energy
$BA^{+\bullet}$	-432.233760	-
2-$MBA^{+\bullet}$	-471.279870	-
3-$MBA^{+\bullet}$	-471.282090	-
4-$MBA^{+\bullet}$	-471.283047	0
$TS1^{+}$	-471.272439	27.85
$TS2^{+}$	-471.275500	19.81
$(C_8H_9N+N_2)^{+\bullet}$	-471.293263	-341.97
$(C_8H_9+N_3)^{+\bullet}$	-471.293263	-26.82

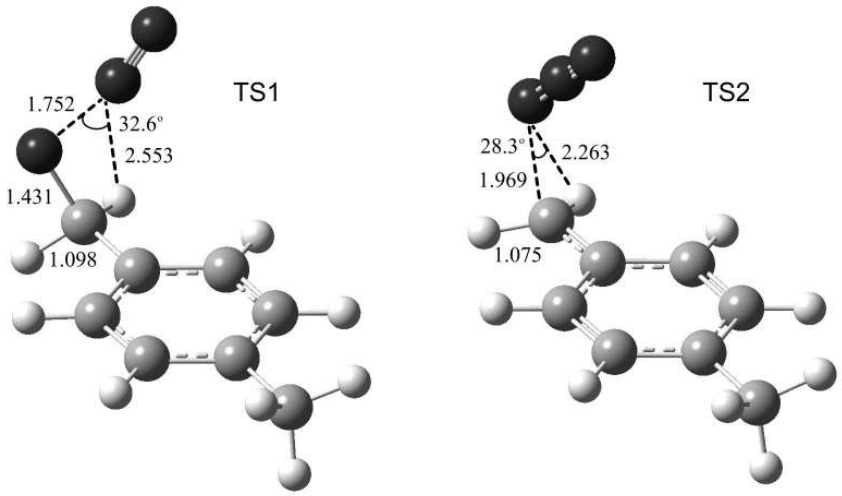

Figure 6.8: Optimized structures of TS1 and TS2, connecting 4-$MBA^{+\bullet}$ and the products from the first two fragmentation channels of Fig. 6.4, obtained with UHF/6-311++G(d,p). Bond lengths and distances are in angstroms (Å).

rameters are emphasized. Resuming the fragmentation routes in Fig. 6.4, two of them were not investigated, by IRC calculations, $CH_2N_3^{\bullet}$ and $HN_2^{\bullet}$ elimination. The former pathway, loss of $CH_2N_3^{\bullet}$, yielded $C_7H_7^{+}$, which must present a tropylium ion structure. For the latter loss, HN_2, it is expected that the experimental evidence obtained for benzyl azide, shown in Fig. 6.3, applies. This means that the release of HN_2 must involve an hydrogen from the -CH_2- group adjacent to the azido group.

6.3.2 Photoelectron spectroscopy

Assignment of He(I) PE spectra of benzyl azide and methylbenzyl azides was made with reference to our recent results on *ab initio* molecular orbital calculations[269]. Results arising from calculations with the HF method and the 6-311++G(d,p) basis provide a good qualitative description of the MOs shapes and orientations. For each azide, the PE spectra were recorded, and experimental vertical ionization energies (VIEs) were obtained by averaging the VIEs of the bands from several different spectra. Typical PE spectra and MOs for theses azides are shown in Figs. 6.9, 6.10 and 6.11 (a), (b)

and (c). Experimental and calculated VIEs are summarized in Tables 6.7 and 6.8.

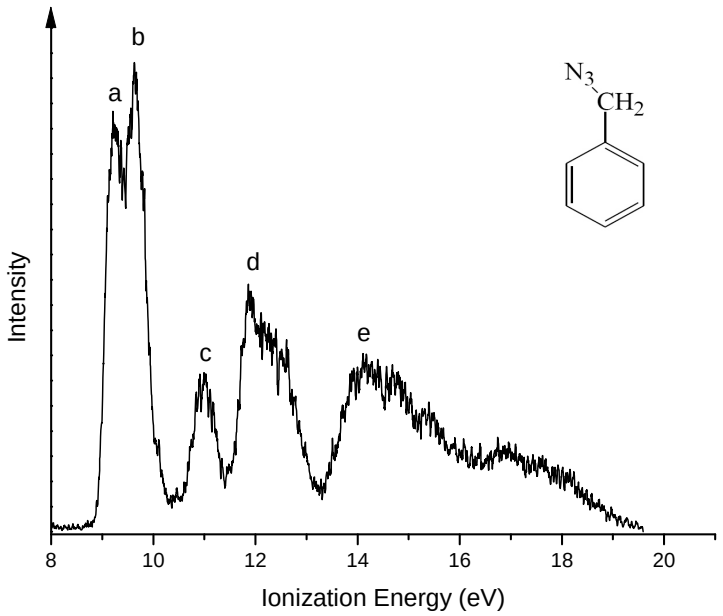

Figure 6.9: He(I) photoelectron spectrum of benzyl azide. The labeled bands are listed in Table 6.7.

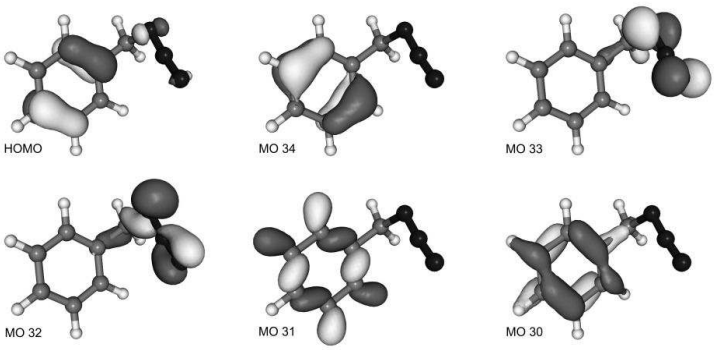

Figure 6.10: Selected molecular orbitals (HOMO-MO 30) from benzyl azide, based on HF/6-311++G(d,p) results.

Table 6.7: Experimental (VIE) and calculated (-ϵ_i) ionization energies (eV) of benzyl azide.

Exp.		Calc.	
Band	VIE	MO	-ϵ_i
a	9.28±0.01	HOMO	9.26
b	9.63±0.01	34	9.44
c	10.96±0.01	33	10.36
d	11.88±0.04	32	12.03
		31	13.67
e	14.13±0.09	30	13.78
		29	14.06

6.3.2.1 Benzyl and methylbenzyl azides

Fig. 6.9 shows a typical PE spectrum, at room temperature, of benzyl azide. Five distinct bands labelled a-e in this figure may be readily identified. The shapes and orientations of the MOs of BA resulting from calculations with the HF method and the 6-311++G(d,p) basis are presented in Fig. 6.10. Experimental and calculated VIEs of the benzyl azide are listed in the Table 6.7, where a quite satisfactory agreement between the calculated values and the experimental data is clearly seen.

The first two intense bands of the BA photoelectron spectrum (see Fig. 6.9, and Table 6.7), at 9.28 and 9.63 eV, respectively, can be assigned to the two highest occupied MOs in the ground state of this molecule, originated mainly from the degenerate $1e_{1g}$ HOMO of benzene[252], which follows either a π_2 (HOMO) or a π_3 (MO 34) pattern. The bands centered at 10.96 and 11.88 eV can be attributed to MOs coming from the azido group N_3: the third (MO 33) is comprised almost exclusively from the $\pi^*_{N_3}$ MO established in the nitrogen chain, whereas the fourth (MO 32) is a $\sigma^*_{N_3}$ that also features a very small σ_{CN} contribution. Considering the three outermost orbitals, (11a')(12a')(3a"), in the electronic configuration of methyl azide, CH_3N_3[22], one can undoubtedly relate the third MO to the 3a" state of CH_3N_3 and the fourth MO to the 12a' state of CH_3N_3.

The broad band e arises from overlap of the remaining MOs and correspond chiefly to several benzene orbitals, with more or less contributions from the nitrogens. MO 31 portraits a strong resemblance to the degenerate $3e_{2g}$ orbital (σ) of benzene. MO 30 is mainly constituted from benzene's $1a_{2u}$ orbital, following a π_1 pattern.

Fig. 6.11 (a), (b) and (c) shows typical PE spectra, at room temperature, of *ortho*-methylbenzyl azide (2-MBA), *metha* -methylbenzyl azide (3-MBA) and *para*-methylbenzyl azide (4-MBA). Seven bands labelled a-g may be identified, respectively, in this figure. The photoelectron spectra also show traces of water (12.62 eV)[116], due to the samples' hygroscopic nature. Experimental and calculated VIEs of 2-, 3- and 4-MBA are listed in Table 6.8, which also shows a satisfactory agreement between the calculated values and the experimental data. Bands a and b in the PE spectra of the

Table 6.8: Experimental (VIE) and calculated ($-\epsilon_i$) ionization energies (eV) of *ortho*-methylbenzyl azide, *metha*-methylbenzyl azide and *para*-methylbenzyl azide.

	2-MBA		3-MBA		4-MBA		
	Exp.	Calc.	Exp.	Calc.	Exp.	Calc.	
Band	VIE	$-\epsilon_i$	VIE	$-\epsilon_i$	VIE	$-\epsilon_i$	MO
a	9.03±0.02	9.09	9.02±0.01	8.99	8.89±0.01	8.95	39
b	9.47±0.04	9.20	9.61±0.01	9.31	9.50±0.01	9.36	38
c	10.88±0.01	10.30	10.88±0.01	10.30	10.88±0.01	10.28	37
d	11.84±0.08	11.98	11.69±0.02	11.98	11.66±0.02	11.96	36
e	13.36±0.03	13.42	13.16±0.02	13.41	13.14±0.03	13.41	35
		13.47		13.45		13.47	34
f	13.72±0.09	13.76	13.87±0.02	13.82	14.08±0.02	13.74	33
g	14.71±0.05	15.04	14.75±0.01	14.83	14.69±0.04	14.79	32

BA methyl derivatives (Fig. 6.11 (a), (b) and (c)) can also be related to two patterns of the degenerate $1e_{1g}$ HOMO of benzene. Bands c and d can be attributed to the third and fourth MOs of 2-, 3- and 4-MBA, that also come from the azido group N_3: a $\pi^*_{N_3}$ MO and a $\sigma^*_{N_3}$ MO, respectively. In a similar way to the BA spectrum, band e in the PE spectrum of the methylbenzyl azides results from the overlap of several benzene orbitals. Finally, band f is associated with another π pattern of $3e_{2g}$ of benzene.

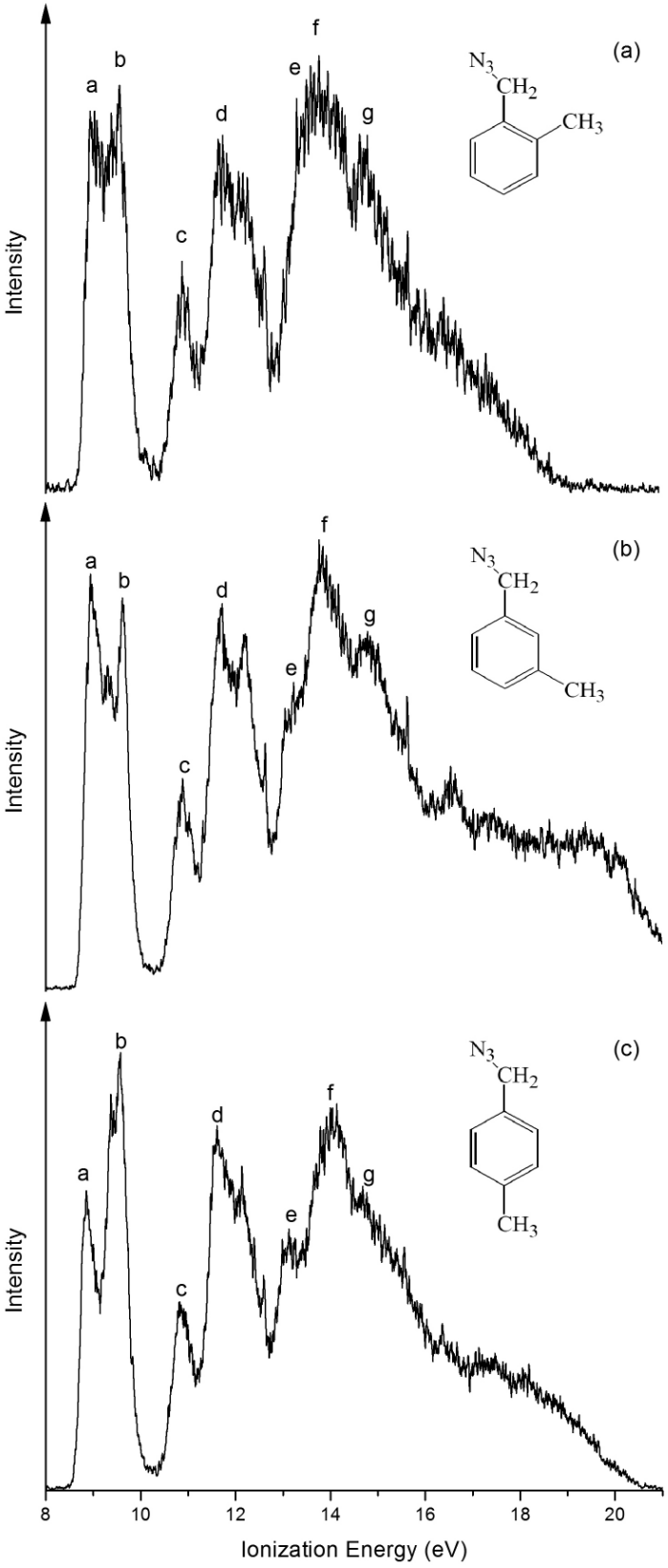

Figure 6.11: He(I) photoelectron spectra obtained for: (a) *ortho*-methylbenzyl azide; (b) *metha*-methylbenzyl azide; and (c) *para*-methylbenzyl azide. The labeled bands are listed in Table 6.8.

6.4 Conclusions

Benzyl azide and its methyl substituted isomers have been synthesized and characterized by mass spectrometry and UV photoelectron spectroscopy.

Mass spectrometry allowed us to examine the fragmentation pathways of benzyl azide and to investigate the effect of different relative positions of methyl group, on the aromatic ring, on the fragmentation of the benzyl azides. The $N_3^\bullet$ loss is favoured in all five compounds. In addition, theoretical calculations showed that in terms of barriers for $N_3^\bullet$ and N_2 elimination channels, the former is more favourable. The loss of C_2H_2 from the fragment *m/z* 105 can be expected via a pericycle reaction involving a 1,2 hydrogen migration, which is helped by the electronic effect of the methyl group. The application of mass spectrometry techniques proved to be effective, in particular, in characterization and differentiation of the *ortho* isomer. In fact, the substituent group in the *ortho* position has a profound influence on the fragmentation pathways and consequently on the ion abundance. The differentiation between *meta* and *para* isomers is not so unequivocally established as for *ortho*. However, some evidence to distinguish them was observed.

The He(I) photoelectron spectra of 2-MBA, 3-MBA and 4-MBA and the He(I) photoelectron spectrum of BA are quite similar within the 8-13 eV ionization energy range. The molecular orbital calculations, concerning the four existing bands in that region, show two bands below 10 eV associated with π benzene ring orbitals, while above that energy, the other two bands are associated with the azide chain orbitals. Moving towards the 13-16 eV ionization energy range, the BA presents a broad band while three bands arise for their methyl derivatives. According to the theoretical calculations, and in contrast with former experimental results on aliphatic azides, the HOMO ionization energy is associated with removal of an electron from a MO located on the benzene ring and not on the azido group.

Chapter 7

BA and 2-, 3-, 4-MBA: Gas-Phase Thermal Decomposition

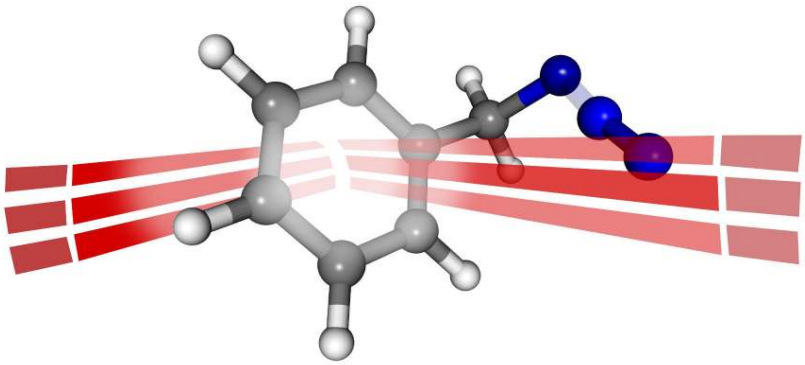

7.1 Introduction

This chapter is based on a brief report concerning the work accomplished in the photoelectron spectroscopy (PES) laboratory, at the School of Chemistry of Southampton University, during the period from 16th June to 6th July, in the year 2009, under the supervision of Prof. John M. Dyke and Ph.D. student Grant Copeland.

The main objective of the work is to study the gas-phase thermal decomposition of benzyl azide, BA, and its methyl derivatives, 2-, 3- and 4-MBA, using the PES technique. It is important to note that, at this level, the thermal decomposition pathways are only evaluated through direct analysis of experimental results, and lack the usual theoretical studies which should accompany these studies. Nevertheless, some simple calculations are included throughout the report in order simulate some non-existent PES data.

The framework for these experiments is well documented by Dyke *et al.*[29,30,82,99], in a vast legion of papers which basically constitute the founding research of transient species in the gas phase. Although a bibliographic review is outside the scope of this report, some recent articles are also well suited for describing the methods employed in the present study[33,270].

[†]Unpublished work.

If no other experimental technique is employed, the starting point is necessarily the photoelectron (PE) spectra of the samples at room temperature. Our prior work (in Lisbon) has produced such results, therefore the spectra and vertical ionization energies (VIEs) at room temperature of the initial compounds constituted valuable information that was used in the initial stage of the decomposition experiments. The molecular structure of BA, 2-MBA, 3-MBA and 4-MBA (Fig. 7.1) and the assignment of the spectra taken at room temperature was also studied[253], prior to the work in Southampton.

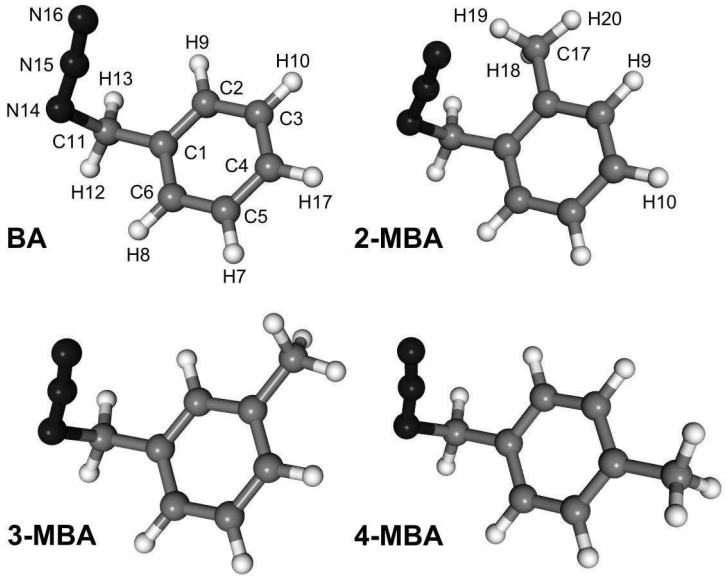

Figure 7.1: Molecular structures of BA, 2-, 3- and 4-MBA

7.2 Experimental details

The He(I) photoelectron spectra of the azides depicted in Fig. 7.1 were recorded in a apparatus similar to the one described elsewhere[127]. Briefly, it consists of a DC discharge lamp, capable of producing He(I) radiation (21.22 eV), a 150° spherical sector electrostatic analyser and a single channel electron detector. Scanning of the analyser voltages is achieved by an analogical ramp generator and spectra are acquired in a computer program, coded in C. The samples are pumped directly from a glass vial outside the ionization chamber, through a teflon valve. Due to the low vapour-pressure of the samples, both glass vial and pumping tubes were pre-heated to approximately 50 °C with an industrial blow-dryer.

The evaporated compound then travels to the ionization cell, passing through an inductively heated furnace, capable of achieving temperatures above 1700 °C. The crucible is made of graphite and wounded by a water-cooled induction coil (copper). An RF power supply (600–1000 kHz) feeds this coil, operating up to 15 kW. As the electromagnetic field produced at this frequency and power interferes with the electron trajectory in the analyser, the power supply is operated in a half-rectified manner and the detection electronics is controlled by a gate circuit.

The internal furnace temperature was measured without any sample admitted in the system, using a type K (Ni-Cr/Ni-Al) thermocouple in contact with the internal wall of the crucible. Above the thermocouple measuring range (>1200 °C), the temperature value was estimated using an extrapolation curve and assuming a linear relationship

between the temperature and the applied voltage on the furnace.

As with most azides, the decomposition onset is marked by the appearance of molecular nitrogen in the spectra; therefore, calibration of the spectra with N_2 lines (15.60 eV, 16.98 eV) and traces of H_2O (12.62), was possible during the whole decomposition process. As other decomposition products appeared, some easily identifiable molecules like HCN (13.60 eV) aided the calibration process. The resolution was approximately 35 meV (FWMH), as measured at the $^2P_{3/2}$ argon peak, and seemed to be unaffected by the heating system, even at very high temperatures.

7.3 Results and discussion

7.3.1 Benzyl azide

The thermal decomposition of BA (see Fig. 7.2) starts with the unequivocal appearance of N_2, through elimination from the azide ($-N_3$) chain, at approximately 300 °C. This process is also accompanied by a decrease in intensity in band C, which is assigned to the azide $\pi^*_{N_3}$ orbital, clearly marking the onset of decomposition. At a slightly higher temperature, 340 °C, we also notice a decrease in intensity and a shift towards the low IE range in bands A and B, which are assigned to π patterns of the benzene ring.

Looking at the full decomposition spectra, recorded at a temperature above 1350 °C, we can clearly identify N_2 and hydrogen cyanide, HCN, as the final products. There is also a persistent peak near the region usually associated with water (12.62 eV), although an objective assignment cannot be made. An initial reaction can thus be written in the form:

$$C_6H_5CH_2N_3 \xrightarrow{Pyrolysis} \text{Intermediates} \longrightarrow HCN + N_2 + \text{products}$$

However, at an early stage of decomposition, we are left with several potential products that could arise directly from the N_2 extrusion:

Pathway 1: $N_2 + Ph{-}N{=}CH_2$ (N-methyleneaniline)

Pathway 2: $N_2 + Ph{-}HC{=}NH$ (N-phenylmethanimine)

Pathway 3: $N_2 + Ph{-}CN + H_2$ (benzonitrile + hydrogen)

Pathway 4: $N_2 + PhH + HCN$ (benzene + hydrogen cyanide)

Pathway 5: $N_2 + Ph^{\bullet} + CH_2N^{\bullet}$ (phenyl radical + methylene amidogen)

In addition, several other products arising from the benzene ring cleavage should also originate other decomposition pathways, in competition with the above reactions. It should be noted that reactions 1 to 4 are more easily identifiable in the PE spectra, as opposing to reaction 5, because the latter pathway involves the formation of transient radicals (which are prone to quickly decompose or isomerise into more stable forms).

The main product from pathway 1, N-methyleneaniline, involves a position exchange between the nitrogen atom and the carbon from the CH_2 group, which in practice would imply the formation of a ring structure (the nitrogen atom would form a 4-point closed structure by bonding to the adjacent carbon atom in the benzene chain), followed by a detachment of the CH_2 group from the benzene ring. Nevertheless, the He(I) PE spectrum of N-methyleneaniline[271] presents a strong and identifiable feature at 10.30 eV, which never appears in the set of decomposition spectra of Fig. 7.2.

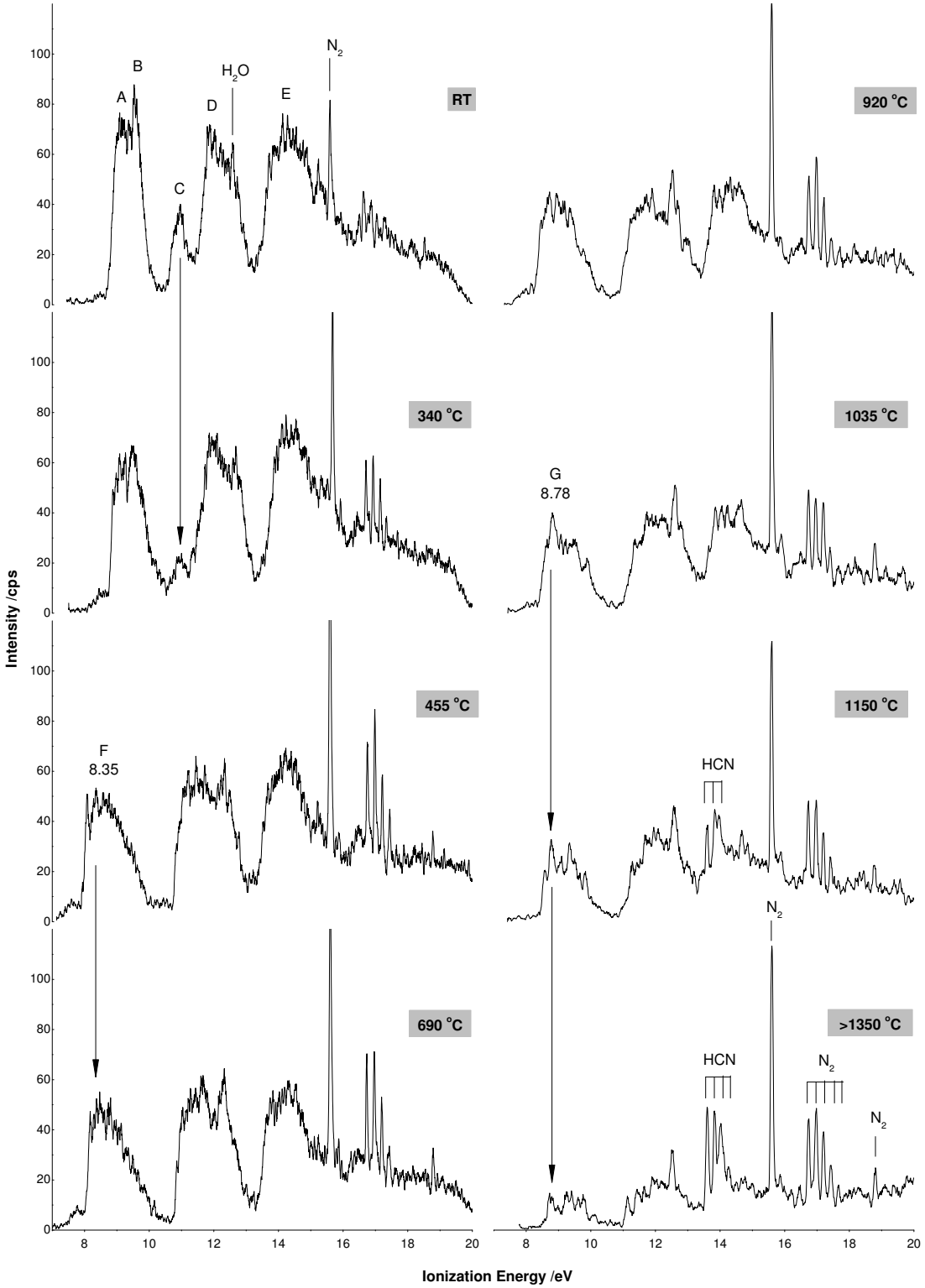

Figure 7.2: Benzyl azide He(I) photoelectron spectra recorded at increasing furnace temperature.

In pathway 2, N-phenylmethanimine, Ph−HC=NH, could be formed after N_2 elimination. Unfortunately, to the best of our knowledge, a PE spectrum of this imine (in our range of interest) has not yet been recorded. Only the ionization energy of the first band is available – 8.72 eV, obtained through flame spectroscopy[272]. In order to obtain a simulated spectra of Ph-HC=NH, we have obtained its optimized structure at the B3LYP/6-31+G(d,p) level and used it to compute the VIEs with outer-valence Greens function methods, namely, OVGF (method B) and partial third-order (P3) (the compound calculation is designated by OVGF/6-311++G(d,p)//B3LYP/6-31+G(d,p) and P3/6-311++G(d,p)//B3LYP/6-31+G(d,p)). These results were then used to obtain a simulated PE spectrum of N-phenylmethanimine, by convolving each VIE with a lorentzian function of 0.4 eV FHMH, in order to accommodate the natural width of the states, the contributions from the vibrational progressions and to better approach the experimental resolution (see Fig. 7.6 and Table 7.2).

In the next reaction – pathway 3, benzonitrile, Ph–CN, could be formed, along with molecular hydrogen, H_2; nevertheless, the first ionization band[273] of Ph–CN, located at 9.71 eV, does not appear at all in the spectra recorded up to 920 °C. At higher temperatures and before the formation of HCN, the band located between 12 and 14 eV could be associated with benzonitrile, which has its most prominent peak at 12.61 eV[274]. Aside from that, if benzonitrile was formed, we would have to detect H_2 in the spectra, with only one vibrational progression centred at 15.98 eV. As we can see in the spectra, there is some additional structure near 16 eV, after the second vibrational peak in the first band of N_2. Thus, pathway 3 is not completely discarded, but it is clearly not the most probable route of decomposition.

Pathway 4 explains the existence of HCN and N_2 in the final spectra, but it relies on the simultaneous formation of benzene (VIEs =9.25, 11.53, 12.38, 13.98 eV). Such traces cannot be assigned throughout the spectra, although they could be part of the first three bands that appear on the spectra taken from 575 to 1035 °C, together with other compounds.

At last, pathway 5 refers to possible radical formations phenyl and methylene amidogen radicals. Only the phenyl radical, $Ph^{\bullet}$, has been detected using the UVPES technique[121] and its formation should occur alongside with that of methylene amidogen, $CH_2N^{\bullet}$. Neither of them has been detected in the present decomposition, thus portraying pathway 5 as a mere speculative reaction.

At this stage, it is important to point out that there is a very high probability that the two first wide bands that appear on the spectra taken at 455 and 690 °C (see Fig. 7.2), with an adiabatic ionization energy (AIE) of approximately 8.05 eV and a vertical maximum of 8.36 eV, could result from the ionization of several alkyl substituted benzenes, being formed in the pyroslysis process. The PES spectra of toluene, o-, m- and p-xylene[275], show great resemblance to the low IE region of our pyrolysis spectra, with VIEs close to our values (8.78, 8.45, 8.50 and 8.37 eV). Further investigation on this subject is fully advised.

At temperatures above 1000 °C, there is a rearrangement (accompanied by a shift towards higher IEs) of the first wide band, with the appearance of additional structures, which could aid the process of assignment. The band starts approximately at 8.40 eV, with a maximum (VIE) at approx. 8.78 eV. The same shift (although less) is recorded for the second large band, located between 11 and 13.40 eV, approximately. Additional structure also appears on top of that band, with increasing temperature.

The information about the thermal decomposition products and pathways is shown in Table 7.1 and Fig. 7.3. In addition, taking the literature spectra of benzene, benzonitrile, N-methyleneaniline and the theoretical spectrum of N-phenylmethanimine, and assuming a simultaneous multi-channel thermal decomposition involving pathways

	Band/Compound	VIE /eV	Reference
Benzyl azide	A	9.28±0.01	Pinto[253]
	B	9.63±0.01	
	C	10.96±0.01	
	D	11.88±0.04	
	E	14.13±0.09	
Pyrolysis products	F (435 °C)	8.35	
	G (1035 °C)	8.78	
	N-methyleneaniline	8.73, 9.38, 10.30	DiStefano[271]
	N-phenylmethanimine	8.72	Tian[272]
	Benzene	9.25, 11.53, 12.38, 13.98	Klasinc[274]
	Benzonitrile	9.72, 10.14, 11.84, 12.11, 12.61	Kobayashi[273]
	Toluene	8.83, 9.36, 11.43, 11.98, 13.70	Maier[50]
	HCN	13.60	Kimura[116]
	N_2	15.60, 16.98, 18.78	Kimura[116]

Table 7.1: Experimental VIEs of BA, detected pyrolysis products and possible thermal decomposition species.

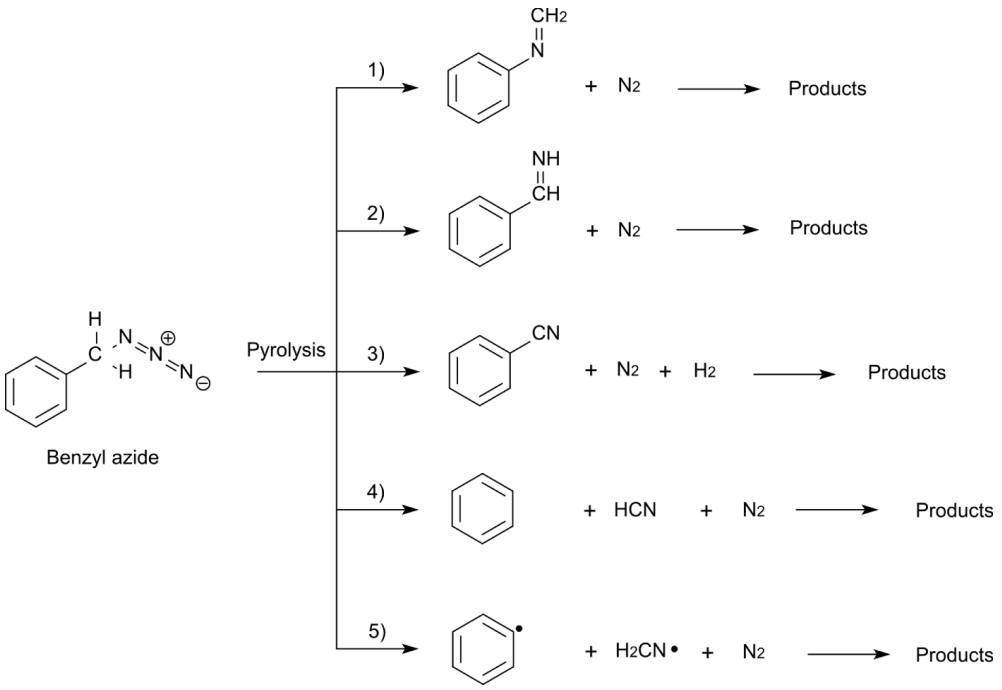

Figure 7.3: Proposed thermal decomposition pathways for benzyl azide, associated with the formation of the main intermediate products N–methyleneaniline (1), N–phenylmethanimine (2), benzonitrile (3), benzene (4) and the phenyl radical (5).

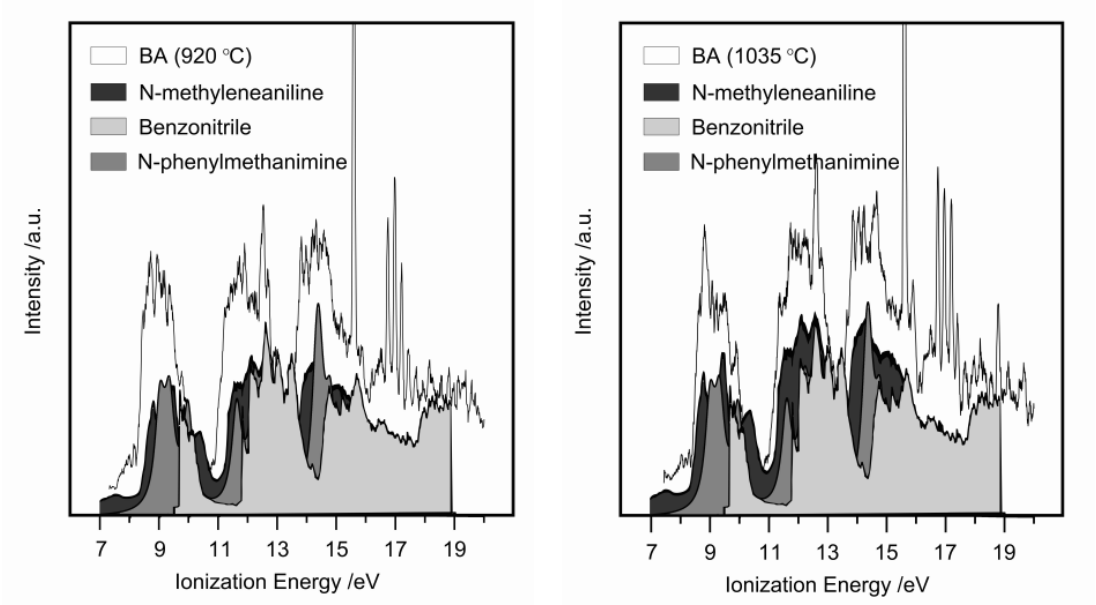

Figure 7.4: He(I) PE spectrum of BA, taken at 920 °C (left) and 1035 °C (right), and superimposed spectra of benzenonitrile (Ref.[273]), N-methyleneaniline (Ref.[271]) and N-phenylmethanimine (simulated spectra, based on P3/6-311++G(d,p)//B3LYP/6-31+G(d,p) results, see text for details). At 1035 °C, the contribution of N-methyleneaniline has been augmented.

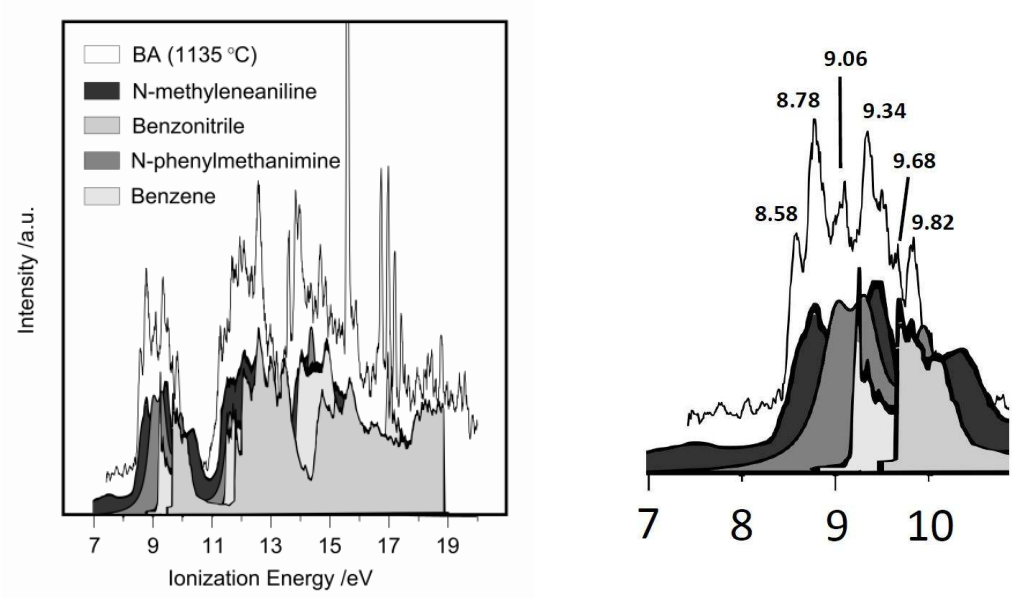

Figure 7.5: He(I) PE spectrum of BA (left), taken at 1150 °C and superimposed spectra of benzene (Ref.[274]), benzenonitrile (Ref.[273]), N-methyleneaniline (Ref.[271]) and N-phenylmethanimine (simulated spectra, based on P3/6-311++G(d,p)//B3LYP/6-31+G(d,p) results, see text for details). At the right, a close-up view of the first band (VIEs in eV). The addition of benzene is explained by the formation of HCN.

1, 2, 3 and 4, we can try to portrait a probable spectrum of BA thermal decomposition, on the onset of HCN formation (920 °C) and at higher temperatures. Figs. 7.4 and 7.5 show these results.

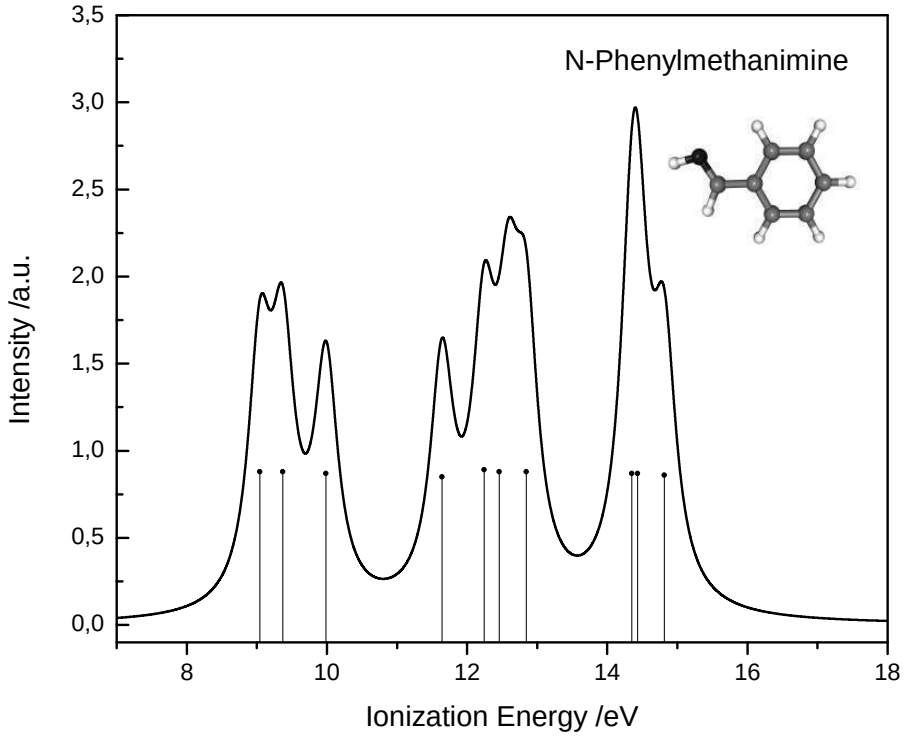

Figure 7.6: Simulated outer-valence PE spectrum of N-phenylmethanimine and associated stick bar graph, based on P3/6-311++G(d,p)//B3LYP/6-31+G(d,p) results.

	VIEs /eV		
MO	HF	OVGF B	P3
28	8.99	8.75	9.04
27	9.35	9.10	9.37
26	11.68	10.10	9.99
25	12.33	11.60	11.64
24	13.62	12.10	12.24
23	13.95	12.30	12.46
22	14.24	12.84	12.84
21	16.12	14.29	14.35
20	16.18	14.42	14.43
19	16.71	14.63	14.81

Table 7.2: Vertical ionization energies (VIEs, in eV) of N-phenylmethanimine, based on P3/6-311++G(d,p) results, calculated at B3LYP/6-31+G(d,p) fully optimized geometry.

7.3.2 2-methyl benzyl azide

The thermal decomposition of 2-MBA (see Fig. 7.7) also starts with the appearance of N_2, through elimination from the azide (–N_3) chain, at approximately 200 °C. As in BA, the process is also accompanied by a decrease in intensity in band C, which is assigned to the azide $\pi^*_{N_3}$ orbital. At this temperature, we also notice a decrease in intensity and a shift towards the low IE range in bands A and B, which are assigned to patterns of the benzene ring. Bands D and E appear to maintain the same structure and relative intensity.

The full decomposition spectra, recorded at a temperature above 1400 °C, clearly shows traces of N_2 and hydrogen cyanide, HCN, as the final products. There is also a sharp peak (12.55 eV) near the region usually associated with water (12.62 eV), although an objective assignment cannot be made. An initial reaction can thus be written in the form:

$$C_6H_5(CH_3)CH_2N \xrightarrow{Pyrolysis} \text{Intermediates} \longrightarrow HCN + N_2 + \text{products}$$

Analyzing now the early stage of decomposition, we are left with several potential products that could arise directly from the N_2 extrusion:

Pathway 6:	N_2 + Ph(CH_3) + HCN	(toluene + hydrogen cyanide)
Pathway 7:	N_2 + PhH + CH_3CN	(benzene + acetonitrile)
Pathway 8:	N_2 + Ph(CH_3)−CN + H_2	(o-tolunitrile + hydrogen)
Pathway 9:	N_2 + Ph−CH=N−CH_3	(N-methylbenzaldimine)
Pathway 10:	N_2 + Ph(CH_3)−HC=NH	(o-methyl benzylidene imine)
Pathway 11a:	N_2 + Ph−(CH_2−NH−CH_2)	(isoindoline, cyclic)
Pathway 11b:	N_2 + Ph−(NH−CH_2−CH_2)	(indoline, cyclic)

The first three reactions, pathways 6 to 8, give rise to the formation of more stable compounds, whereas reactions 11a, 11b yield cyclic products, which are prone to exhibit tautomerism and to undergo isomerisations towards more stable structures. Reactions 9 and 10 are based on the assumption that an imine compound can be formed. Other less obvious ring cleavage products can also be formed, simultaneous to these reactions. In addition, reaction 10 can lead to the cyclic product in 11a.

At first sight, it appears that pathway 6 is the most probable reaction, as it yields directly the two final decomposition products, HCN and N_2, plus toluene, Ph(CH_3). Toluene He(I) spectrum[116] exhibits a wide first band, originated from the overlapping of two peaks at 8.83 and 9.36 eV. These two peaks do not appear distinctively when HCN starts to form (>1200 °C), and there is a chance that Ph(CH_3) could be decomposing into other products[276] looking at the unidentified features near 11 eV, this could be attributed to acetylene, C_2H_2 (11.40 eV) and 2-butanedinitrile, NC(CH=CH)CN (11.15 eV).

Pathway 7 infers the formation of benzene and acetonitrile, CH_3CN, which implies the full detachment of the methyl group in the orto position and subsequent bonding to the CN moiety. However, neither benzene (9.25 eV) nor acetonitrile (12.21 eV) appear distinctively in the spectra, a fact that makes this channel a very improbable one.

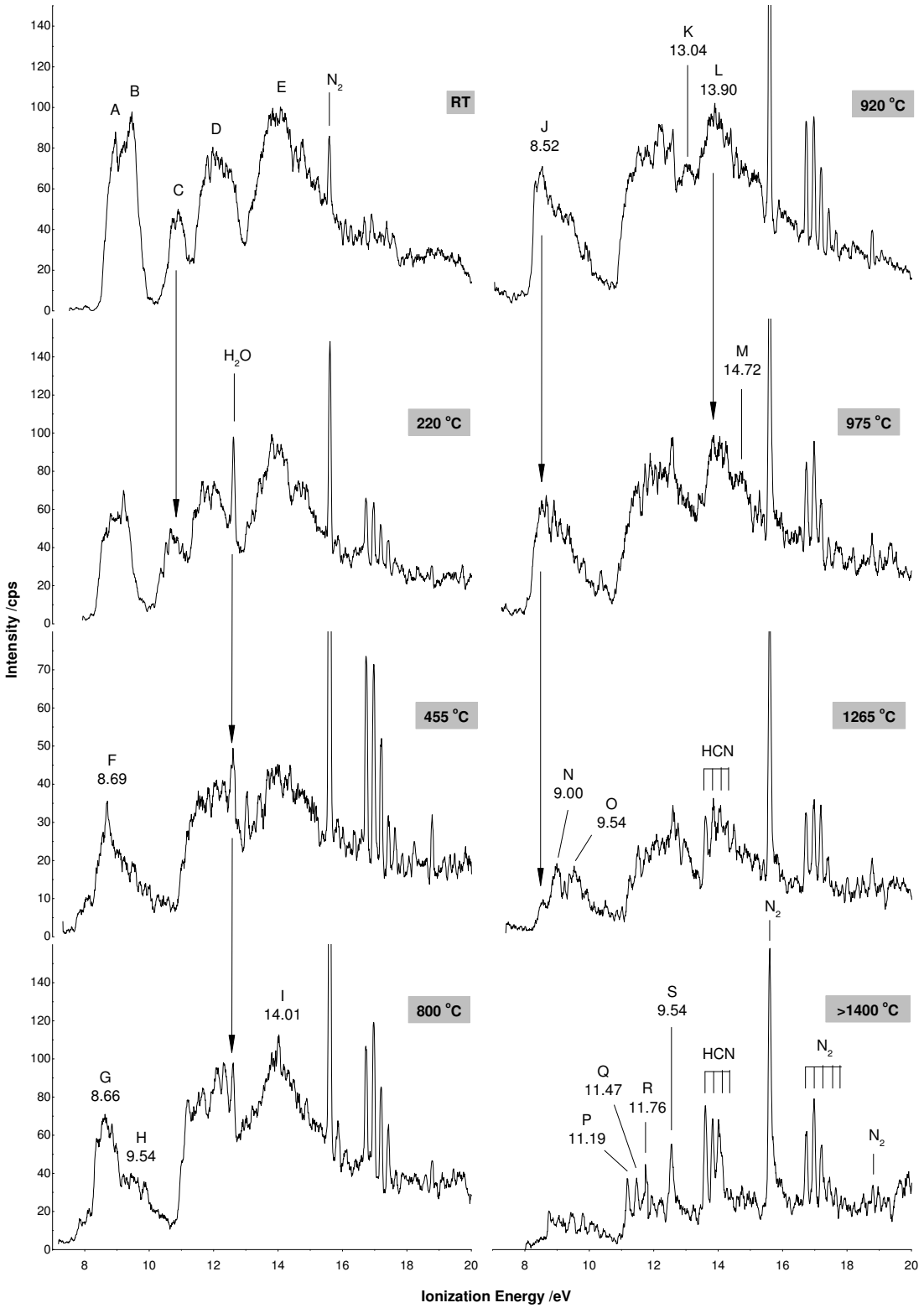

Figure 7.7: 2-Methyl benzyl azide He(I) photoelectron spectra recorded at increasing furnace temperature.

In analogy with the formation of benzonitrile in pathway 3 of BA's thermal decomposition, o-tolunitrile (pathway 8) could also be formed, alongside with hydrogen, in an early stage of the pyrolysis process. Looking at spectrum taken at 920 °C, we can detect a peak near 9.38 eV, another at 9.88 eV, and one at 13.04 (peak K). The first two coincide with the first two VIEs of o-tolunitrile[273], whereas peak K also coincides with the most intense peak of that of o-tolunitrile (approx. 13 eV). Therefore, this channel is clearly taking place on the onset of HCN formation (near 925 °C).

	Band/Compound	VIE /eV	Reference
2-Methyl benzyl azide	A	9.03±0.02	Pinto[253]
	B	9.47±0.04	
	C	10.88±0.01	
	D	11.84±0.08	
	E	13.72±0.09	
Pyrolysis products	F (455 °C)	8.69	
	G (800 °C)	8.66	
	H	9.54	
	I	14.01	
	J (920 °C)	8.52	
	K	13.04	
	L	13.90	
	M (975 °C)	14.72	
	N (1265 °C)	9.00	
	O	9.54	
	P (>1400 °C)	11.19	
	Q	11.47	
	R	11.76	
	S	12.55	
	Toluene	8.83, 9.36, 11.43, 11.98, 13.7	Kimura[116]
	Benzene	9.25, 11.53, 12.38, 13.98	Klasinc[274]
	Acetonitrile	12.21, 13.14	Kimura[116]
	o-tolunitrile	9.38, 9.84, 11.62, 12.01	Kobayashi[273]
	N-methylbenzaldimine	8.77, 9.38, 10.87, 11.71	Bally[277]
	o-methyl benzylidene	9.11	This work
	Isoindoline	8.58	This work
	Indoline	7.67, 8.90, 10.25, 11.3, 11.9	Maier[275]
	Acetylene	11.40	Kimura[116]
	HCN	13.60	Kimura[116]
	N_2	15.60, 16.98, 18.78	Kimura[116]

Table 7.3: Experimental VIEs of 2-MBA, detected pyrolysis products and possible thermal decomposition species.

Pathways 9 and 10 lead to the formation of two imines, N-methylbenzaldimine (8.77 eV) and o-methyl benzylidene imine (no available literature data). The formation of the first imine also implies the detachment of the methyl group from the *ortho* position and bonding to the remaining nitrogen atom. This imine clearly progresses to the formation of acetonitrile and benzene, more stable compounds; therefore, we could state that pathway 9 leads to scheme 7, described above.

The second imine (from pathway 10) is simply the molecule that is formed after the N_2 extrusion, with the only rearrangement being a proton transfer from the CH_2 moiety to the nitrogen atom. This imine should also progress to the more stable form of

isoindoline, bonding to the nearby CH_3 group and thus creating a ring structure. Inspite this fact, its first VIE (9.11 eV) was obtained at the P3/6-311++G(d,p)//B3LYP/6-31+G(d,p) level of theory.

Finally, in pathways 11a and 11b, a cyclic structure is formed called isoindoline. No PES data is available for this molecule. Therefore, we have adopted the same procedure as in N-phenylmethanimine: P3/6-311++G(d,p)//B3LYP/6-31+G(d,p) results on this molecule were used to create a simulated spectra (Fig. 7.11), where each VIE was convoluted by 0.4 FWMH lorentzian function.

The information about the thermal decomposition products and pathways of 2-MBA is shown in Table 7.3 and Fig. 7.8. In addition, taking the literature spectra of toluene, o-tolunitrile and the theoretical spectrum of isoindoline, and assuming a simultaneous multi-channel thermal decomposition involving pathways 6, 7 and 11a, we can try to portrait a probable spectrum of 2-MBA thermal decomposition, on the onset of HCN formation (920 °C). Figs. 7.9 and 7.10 support this analysis.

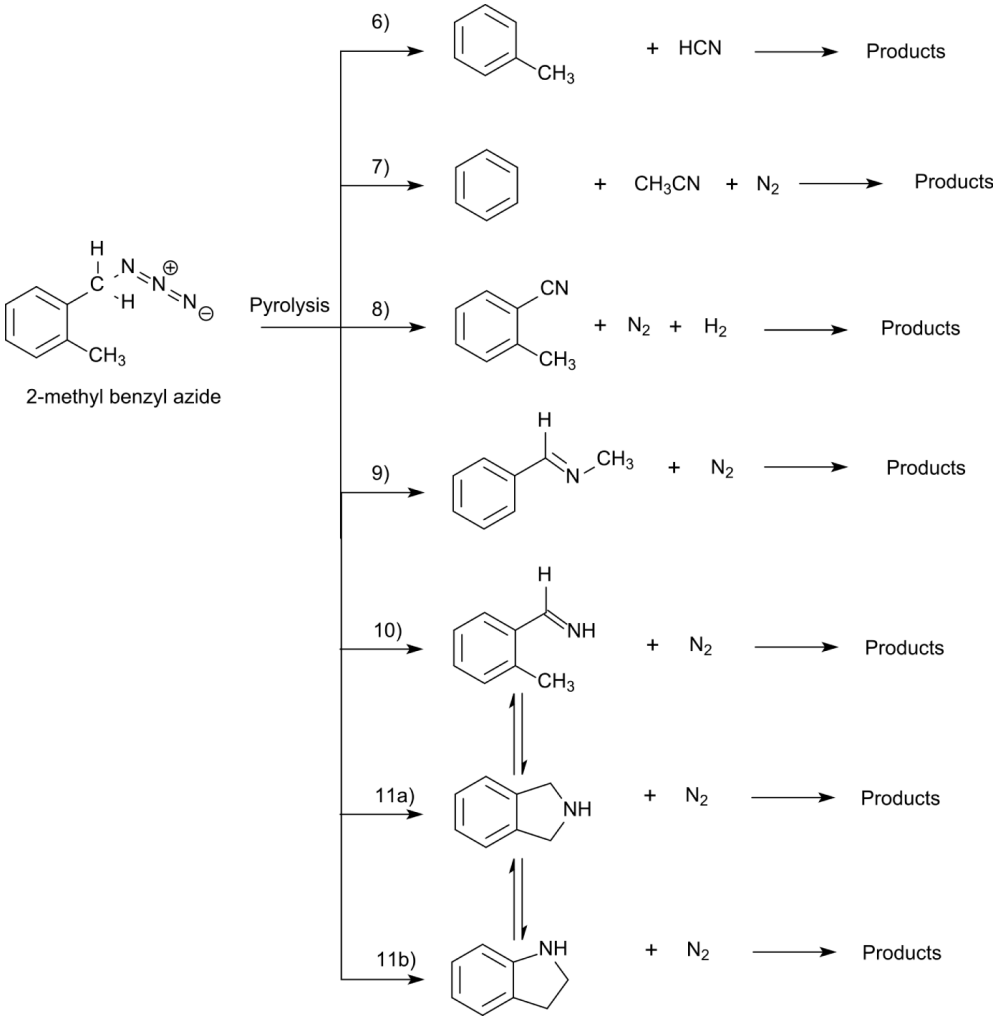

Figure 7.8: Proposed thermal decomposition pathways for 2-methyl benzyl azide, associated with the formation of the main intermediate products toluene (6), benzene (7), o-tolunitrile (8), N-methylbenzaldimine (9), o-methyl benzylidene imine (10), isoindoline (11a) and indoline (11b).

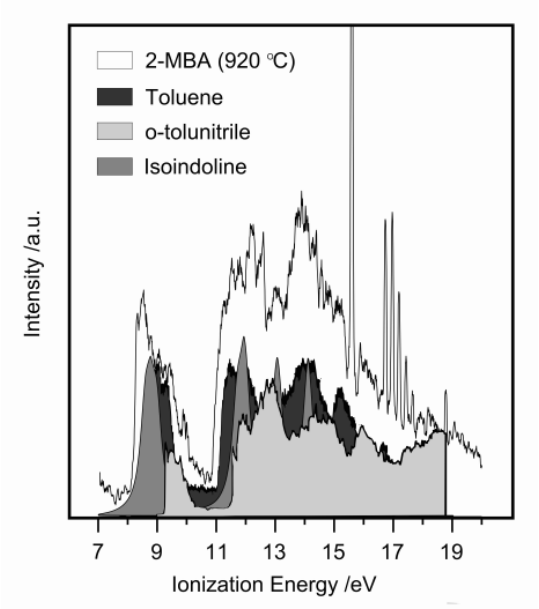

Figure 7.9: He(I) PE spectrum of 2-MBA, taken at 920 °C, and superimposed spectra of toluene (taken from Ref.[275]), o-tolunitrile (Ref.[273]) and isoindoline (simulated spectra, based on P3/6-311++G(d,p)//B3LYP/6-31+G(d,p) results).

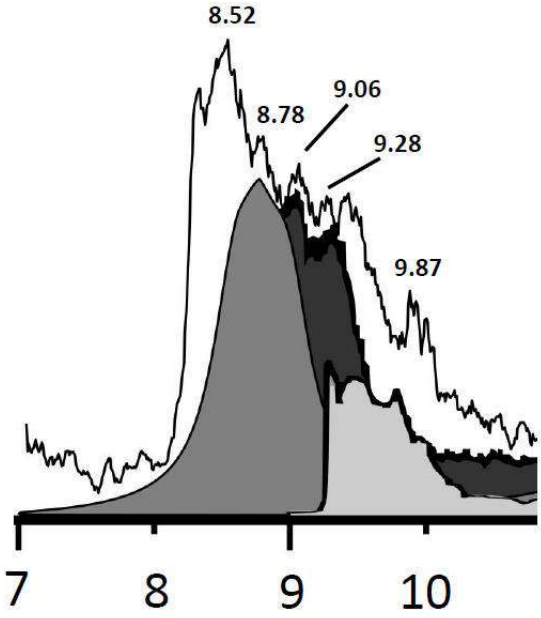

Figure 7.10: Close-up detail of the first band in Fig. 7.9 (VIEs in eV). The contribution of o-tolunitrile (light gray) has been augmented.

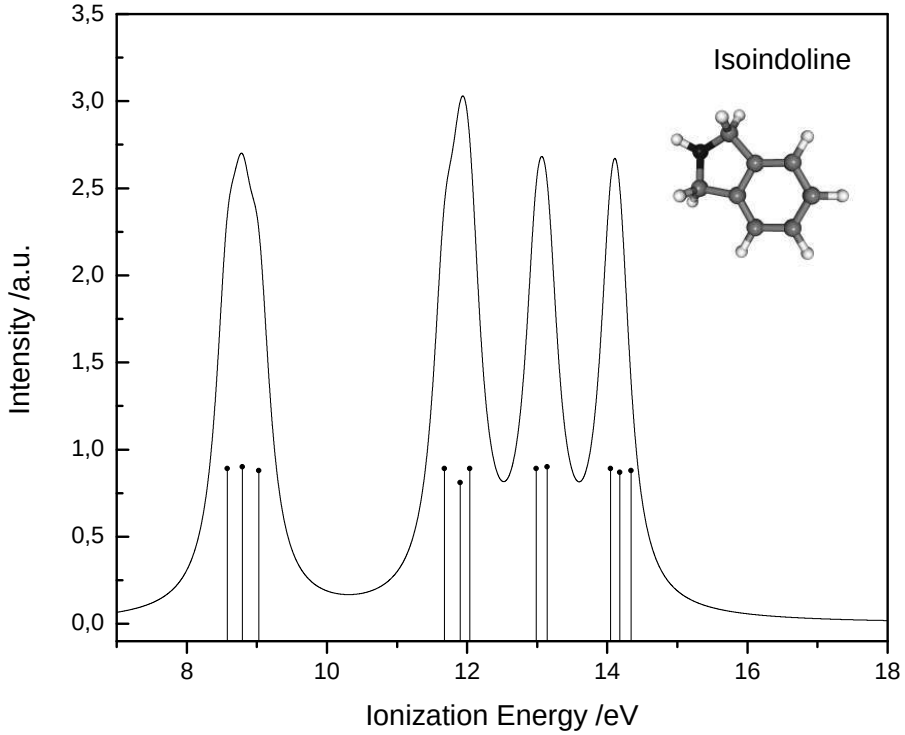

Figure 7.11: Simulated outer-valence PE spectrum of isoindoline and associated stick bar graph, based on P3/6-311++G(d,p)//B3LYP/6-31+G(d,p) results.

	VIEs /eV		
MO	HF	OVGF B	P3
32	8.64	8.37	8.58
31	10.18	8.95	8.79
30	9.06	8.81	9.03
29	12.98	11.55	11.68
28	13.35	11.97	11.90
27	13.43	11.90	12.04
26	14.45	12.99	12.99
25	14.40	13.27	13.15
24	15.50	14.23	14.05
23	15.90	14.15	14.18
22	15.96	14.38	14.34

Table 7.4: Vertical ionization energies (VIEs, in eV) of isoindoline, based on P3/6-311++G(d,p) results, calculated at B3LYP/6-31+G(d,p) fully optimized geometry.

7.3.3 3-methyl benzyl azide

The thermal decomposition of 3-MBA (see Fig. 7.12) starts with the appearance of N_2, through its elimination from the azide ($-N_3$) chain, at approximately 250 °C. The process is also accompanied by a decrease in intensity in band C, which is assigned to the azide $\pi^*_{N_3}$ orbital. At 340 °C, we also notice a decrease in intensity and a shift towards the low IE range in bands A and B, which are assigned to π patterns of the benzene ring. Bands E, F and G appear to maintain the same structure and relative intensity. At higher temperatures, there is a full rearrangement of the bands, due to the formation of unidentified pyrolysis products.

As with the other azides, N_2 and hydrogen cyanide, HCN, are the final products of the decomposition (> 1350 °C). Again, there is a sharp peak (12.60 eV) near the region usually associated with water (12.62 eV), although an objective assignment cannot be made at that temperature, water should not exist in the system. An initial reaction can thus be written in the form:

$$C_6H_5(CH_3)CH_2N \xrightarrow{Pyrolysis} \text{Intermediates} \longrightarrow HCN + N_2 + \text{products}$$

Some possible initial decomposition products that could arise directly from the N_2 extrusion, can be associated with the following reactions:

Pathway 12: $N_2 + Ph(CH_3) + HCN$ (toluene + hydrogen cyanide)

Pathway 13: $N_2 + Ph(CH_3){-}CN + H_2$ (m-tolunitrile + hydrogen)

Pathway 14: $N_2 + Ph(CH_3){-}HC{=}NH$ (m-methyl benzylidene imine)

Pathway 15: $N_2 + PhH + CH_3CN$ (benzene + acetonitrile)

These pathways are similar to the ones described for 2-MBA, although the reactions leading to cyclic structures and/or bonding of the nitrile group to the CH_3 moiety have been excluded. This is due to the fact that the methyl group in 3-MBA is now positioned farther away from the remaining nitrogen atom, which greatly decreases the possibility of bonding between the CH_3 and CN groups. Pathway 14 gives rise to the formation of an imine compound.

Analysing the spectra of Fig. 7.12, we notice that traces of the first two main decomposition products (m-tolunitrile and toluene) are clearly identifiable throughout the decomposition. M-tolunitrile first band (9.40 eV) appears as early as 690 °C, and remains present until approximately 1100 °C, which validates pathway 13. Although this pathway involves the formation of hydrogen, the assignment of H_2 is very difficult due to the high noise conditions and presence of hot bands, near 16 eV.

The formation of acetonitrile (12.21 and 13.14 eV), CH_3CN, via dissociation of the nitrile group plus the H atom and capture of the CH_2 moiety in the meta position of the ring, leads to the formation of benzene. At 690 and 800 °C, these phenomena are clearly happening, with the presence of traces at precisely 9.25 eV (benzene) and 12.31, 12.51 and 13.04 eV (probably associated with acetonitrile).

Toluene (8.83 eV), in pathway 12, should appear at the onset of HCN formation, but its presence is masquerade by the formation of other compounds with VIEs in the same ionization energy range. Similar to what was already concluded in the analysis of 2-MBA thermal decomposition, the formation of an imine (pathway 14) seems to be energetically very advantageous. As there are no reference data on m-methyl benzylidene imine, we use the same theoretical approach as before, to simulate a possible

PE spectrum of this compound in the outer-valence region (Fig. 7.16 and Table 7.6). Finally, Table 7.5 and Figs. 7.13 to 7.15 summarize and present a possible assignment of the decomposition spectra.

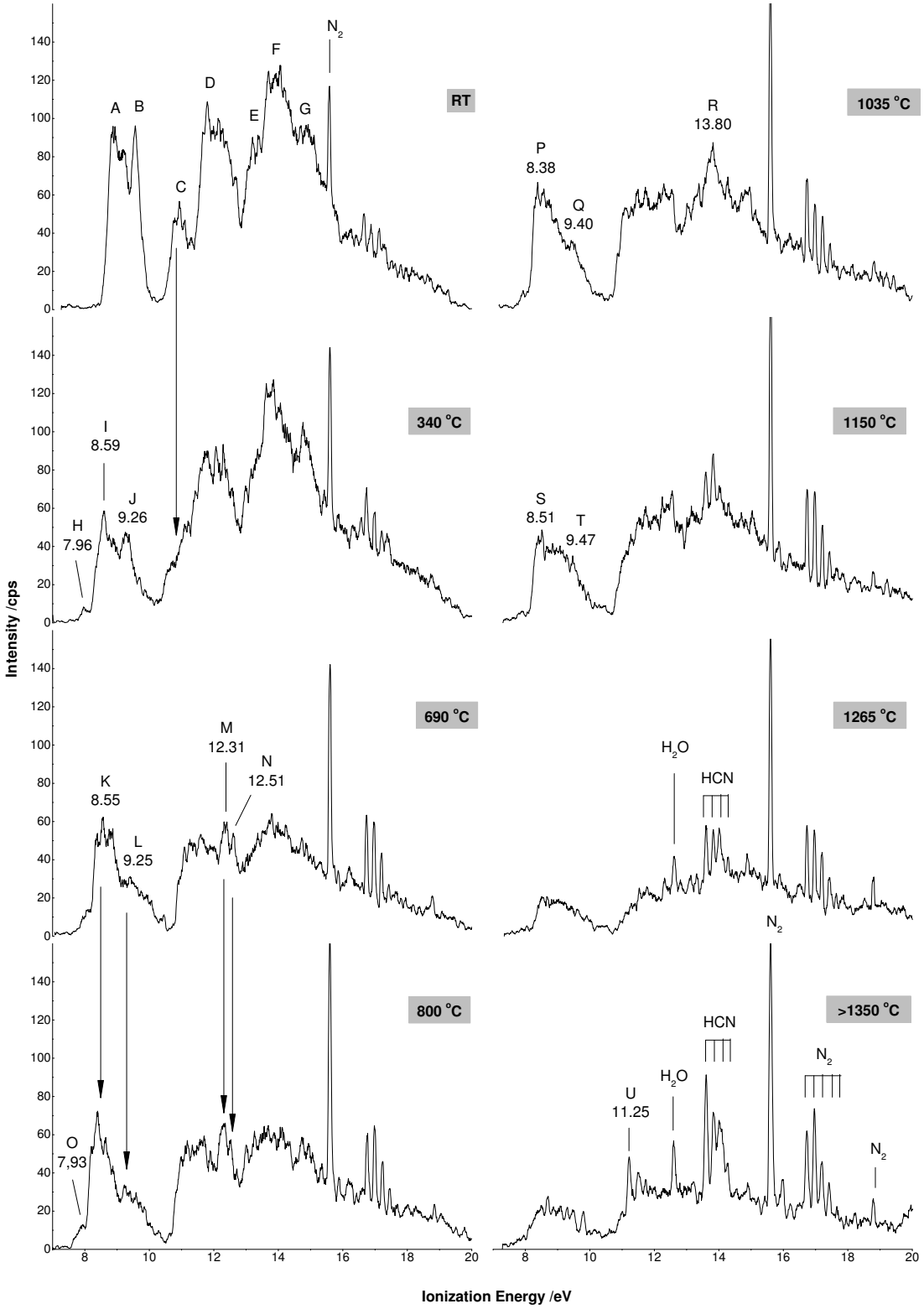

Figure 7.12: 3-Methyl benzyl azide He(I) photoelectron spectra recorded at increasing furnace temperature.

	Band/Compound	VIE /eV	Reference
3-Methyl benzyl azide	A	9.02±0.01	Pinto[253]
	B	9.61±0.01	
	C	10.88±0.01	
	D	11.69±0.02	
	E	13.16±0.02	
	F	13.87±0.02	
	G	14.75±0.01	
Pyrolysis products	H (340 °C)	7.96	
	I	8.59	
	J	9.26	
	K (690 °C)	8.55	
	L	9.25	
	M	12.31	
	N	12.51	
	O (800 °C)	7.93	
	P (1035 °C)	8.38	
	Q	9.40	
	R	13.80	
	S (1150 °C)	8.51	
	T	9.47	
	U (>1350 °C)	12.55	
	Toluene	8.83, 9.36, 11.43, 11.98, 13.7	Kimura[116]
	m-tolunitrile	9.40, 9.83, 11.69, 11.95	Kobayashi[273]
	m-methyl benzylidene	9.08	This work
	HCN	13.60	Kimura[116]
	N_2	15.60, 16.98, 18.78	Kimura[116]

Table 7.5: Experimental VIEs of 3-MBA, detected pyrolysis products and possible thermal decomposition species.

	VIEs /eV		
MO	HF	OVGF B	P3
32	9.07	8.77	9.08
31	9.38	9.07	9.35
30	11.56	9.92	9.84
29	12.21	11.46	11.51
28	13.65	12.08	12.26
27	14.10	12.49	12.62
26	14.12	12.78	12.79
25	14.95	13.65	13.60
24	15.82	14.10	14.16
23	15.97	14.77	14.59
22	16.09	14.46	14.44

Table 7.6: Vertical ionization energies (VIEs, in eV) of m-methyl benzylidene imine, based on P3/6-311++G(d,p) results, calculated at B3LYP/6-31+G(d,p) fully optimized geometry.

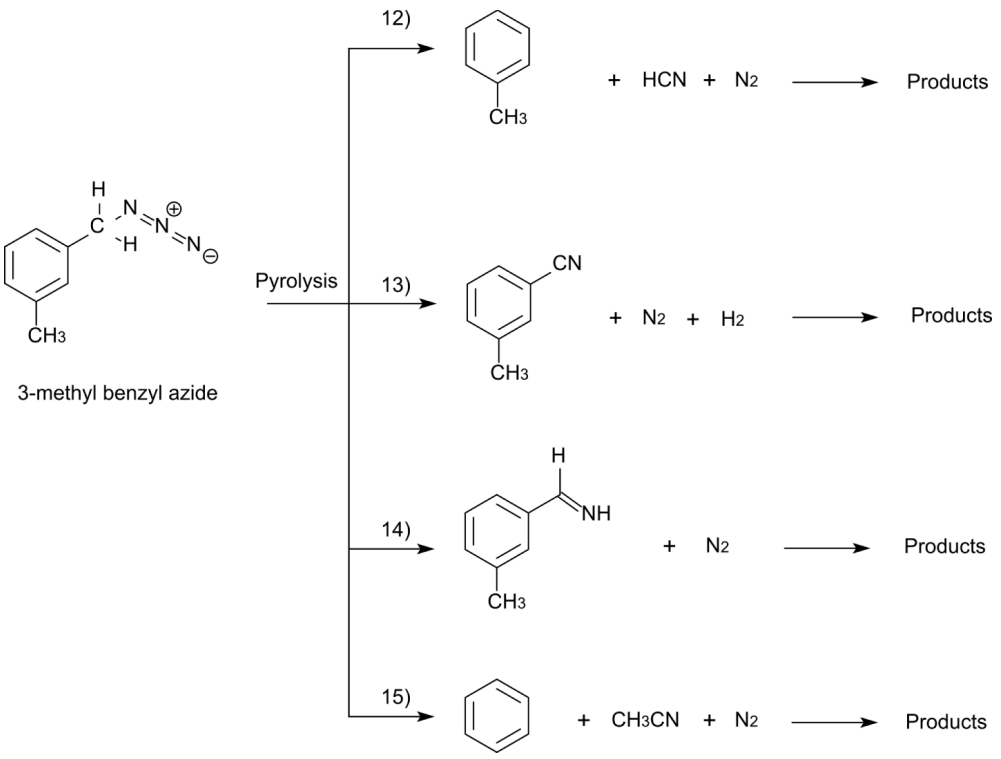

Figure 7.13: Proposed thermal decomposition pathways for 3-methyl benzyl azide, associated with the formation of the main intermediate products toluene (12), m-tolunitrile (13), m-methyl benzylidene imine (14) and benzene (15).

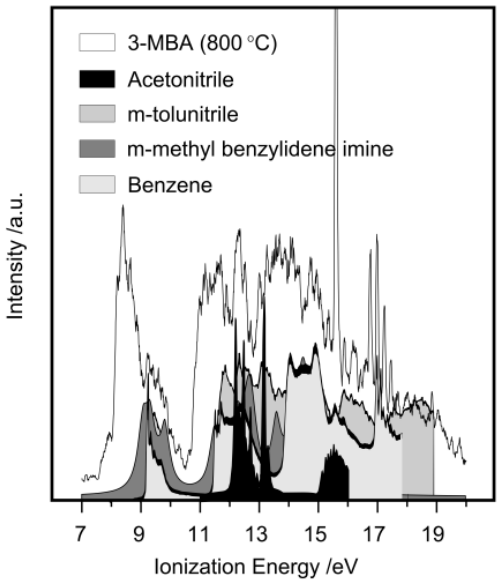

Figure 7.14: He(I) PE spectrum of 3-MBA, taken at 800 °C, and superimposed spectra of acetonitrile (Ref.[116]), benzene (Ref.[274]), m-tolunitrile (Ref.[273]) and m-methyl benzylidene imine (P3/6-311++G(d,p)//B3LYP/6-31+G(d,p) results)

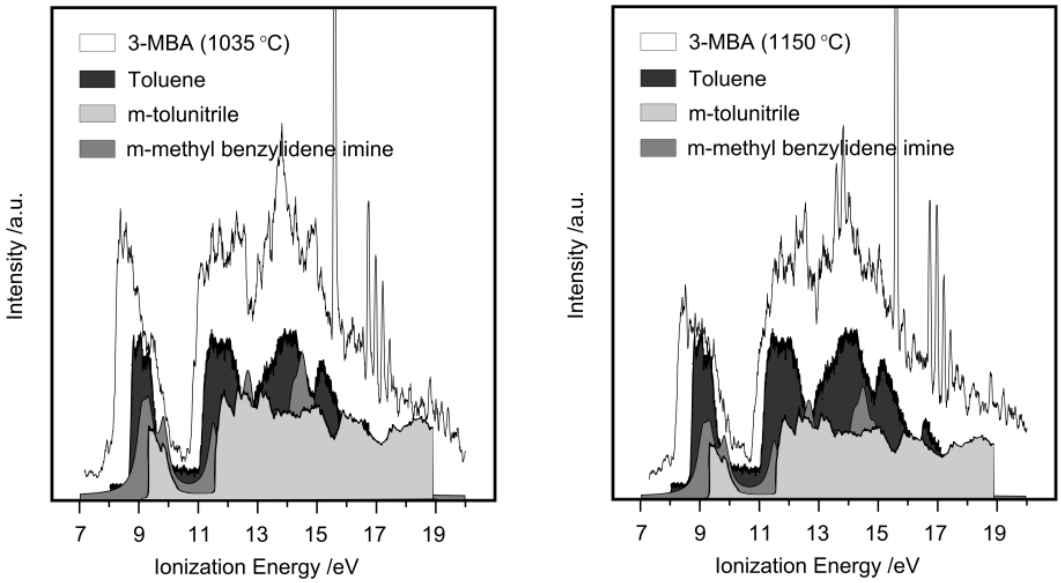

Figure 7.15: He(I) PE spectrum of 3-MBA, taken at 1035 °C (left) and 1150 °C (right), and superimposed spectra of toluene (taken from Ref.[275]), m-tolunitrile (Ref.[273]) and m-methyl benzylidene imine (simulated spectra, based on P3/6-311++G(d,p)//B3LYP/6-31+G(d,p) results). At 1150 °C, the contribution of m-tolunitrile and benzylidene has been decreased.

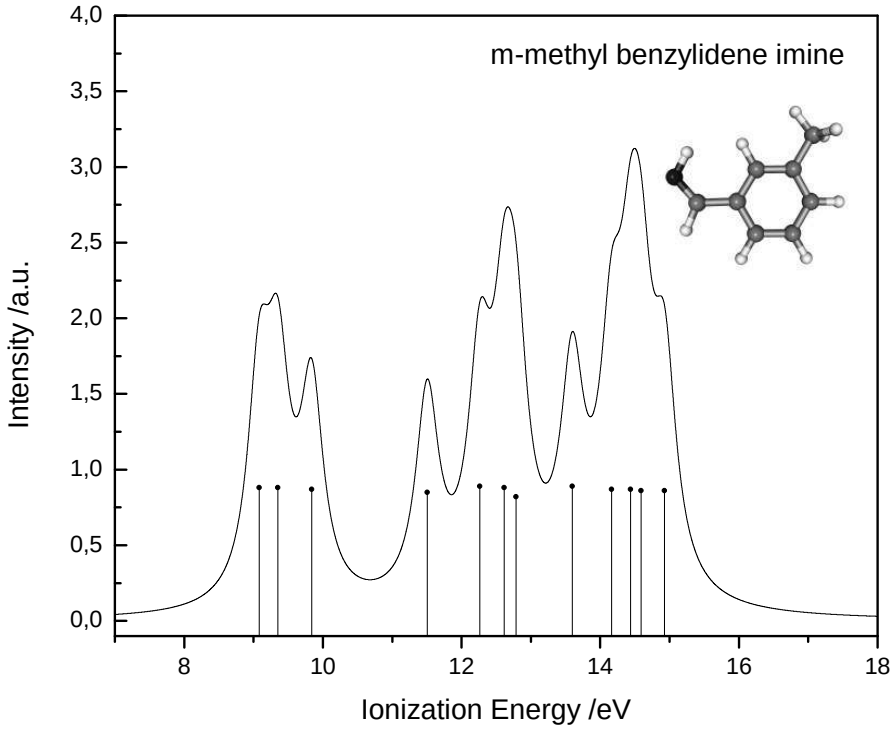

Figure 7.16: Simulated outer-valence PE spectrum of m-benzylidene imine and associated stick bar graph, based on P3/6-311++G(d,p)//B3LYP/6-31+G(d,p) results.

7.3.4 4-methyl benzyl azide

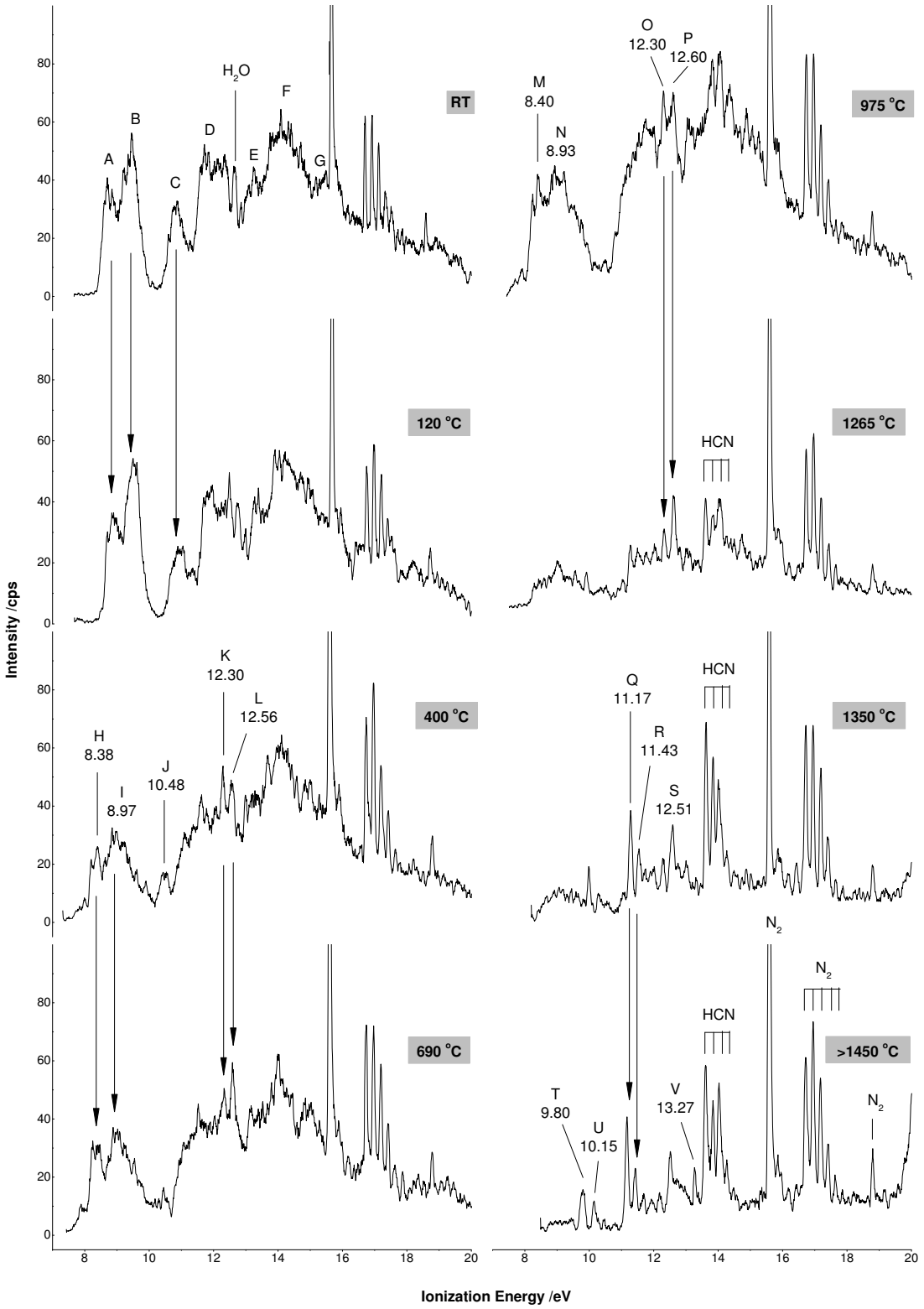

Figure 7.17: 4-Methyl benzyl azide He(I) photoelectron spectra recorded at increasing furnace temperature.

The thermal decomposition of 4-MBA (see Fig. 7.17) starts with the appearance of N_2, through its elimination from the azide ($-N_3$) chain, at approximately 300 °C (please note that N_2 is present from the beginning of the decomposition, even at room

temperature, due to a leak somewhere in the system, that could not be detected in time). As usual, the process is also accompanied by a decrease in intensity in band C, which is assigned to the azide $\pi^*_{N_3}$ orbital. At 400 °C, we notice a decrease in intensity and a shift towards the low IE range in bands A and B, which are assigned to π patterns of the benzene ring. Bands E, F and G appear to maintain the same structure and relative intensity. At higher temperatures, there is a full rearrangement of the bands, due to the formation of unidentified pyrolysis products.

Again, N_2 and HCN are the final products of the decomposition (> 1400 °C). An initial reaction can thus be written in the form:

$$C_6H_5(CH_3)CH_2N \xrightarrow{Pyrolysis} \text{Intermediates} \longrightarrow HCN + N_2 + \text{products}$$

Some possible initial decomposition products that could arise directly from the N_2 extrusion, can be linked to the following reactions:

Pathway 16: $N_2 + Ph(CH_3) + HCN$ (toluene + hydrogen cyanide)

Pathway 17: $N_2 + Ph(CH_3){-}CN + H_2$ (p-tolunitrile + hydrogen)

Pathway 18: $N_2 + Ph(CH_3){-}HC{=}NH$ (p-methyl benzylidene imine)

Pathway 19: $N_2 + PhH + CH_3CN$ (benzene + acetonitrile)

These reactions are essentially the same as in 3-MBA thermal decomposition, except for the position of the methyl group on the benzene ring (position 4, para-). Therefore, the description of these pathways is similar to the ones mentioned before. The decomposition of this molecule occurs within a multi-channel environment (see Fig. 7.18), in which pathways 16 to 19 occur simultaneously.

All the spectra portraying the decomposition products are available in the reference literature, with the exception of the outer-valence PE spectrum of p-methyl benzylidene imine which was calculated on the basis of P3/6-311++G(d,p)//B3LYP/6-31+g(d,p) results (Table 7.8 and Fig. 7.21), following the procedure already described. In a similar way to the previous analysis, these spectra are used in the next sequence of figures (Figs. 7.19 and 7.20) and superimposed in front of the real spectra of 4-MBA, taken at different temperatures.

	Band/Compound	VIE /eV	Reference
4-Methyl benzyl azide	A	8.89±0.01	Pinto[253]
	B	9.50±0.01	
	C	10.88±0.01	
	D	11.66±0.02	
	E	13.14±0.03	
	F	14.08±0.02	
	G	14.69±0.04	
Pyrolysis products	H (400 °C)	8.38	
	I	8.97	
	J	10.48	
	K	12.30	
	L	12.56	
	M (975 °C)	8.40	
	N	8.93	
	O (800 °C)	12.30	
	P	12.60	
	Q (>1350 °C)	11.17	
	R	11.43	
	S	12.51	
	T (>1450 °C)	9.80	
	U	10.15	
	V	13.27	
	Toluene	8.83, 9.36, 11.43, 11.98, 13.7	Kimura[116]
	p-tolunitrile	9.33, 9.97, 11.68, 11.90	Kobayashi[273]
	p-methyl benzylidene	8.72	This work
	HCN	13.60	Kimura[116]
	N_2	15.60, 16.98, 18.78	Kimura[116]

Table 7.7: Experimental VIEs of 4-MBA, detected pyrolysis products and possible thermal decomposition species.

	VIEs /eV		
MO	HF	OVGF B	P3
32	8.69	8.41	8.72
31	9.28	8.98	9.23
30	11.57	10.00	9.87
29	12.09	11.32	11.34
28	13.37	11.87	12.00
27	13.69	12.00	12.21
26	13.96	12.65	12.64
25	14.80	13.56	13.47
24	15.66	13.77	13.88
23	15.80	14.69	14.42
22	16.05	14.30	14.30

Table 7.8: Vertical ionization energies (VIEs, in eV) of p-methyl benzylidene imine, based on P3/6-311++G(d,p) results, calculated at B3LYP/6-31+G(d,p) fully optimized geometry.

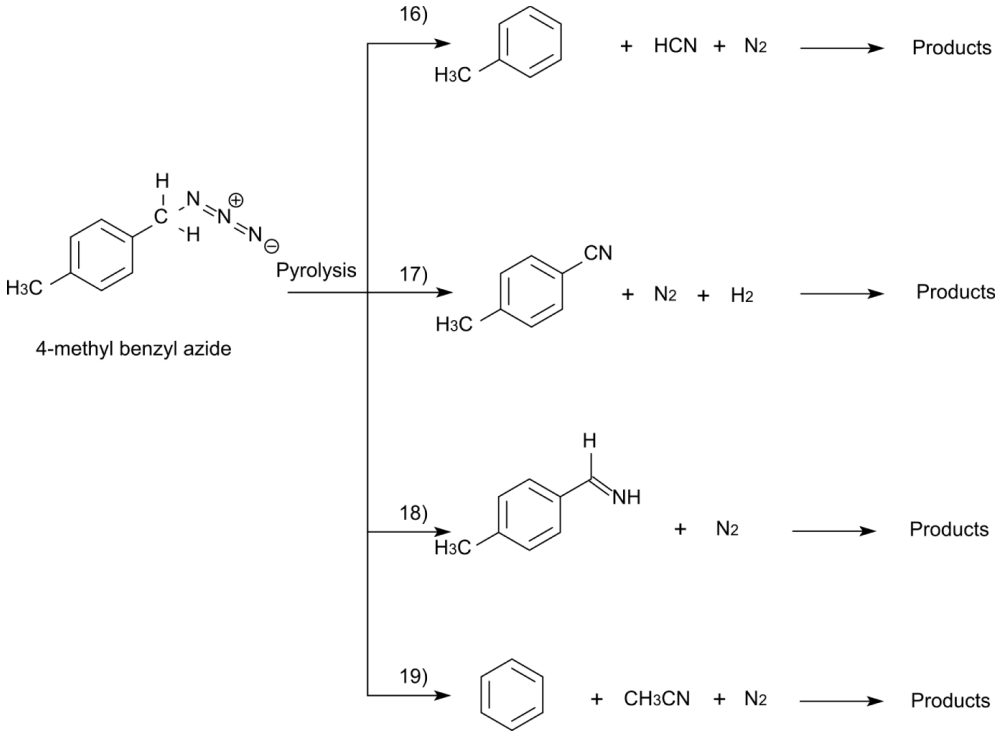

Figure 7.18: Proposed thermal decomposition pathways for 4-methyl benzyl azide, associated with the formation of the main intermediate products toluene (16), p-tolunitrile (17), p-methyl benzylidene imine (18) and benzene (19).

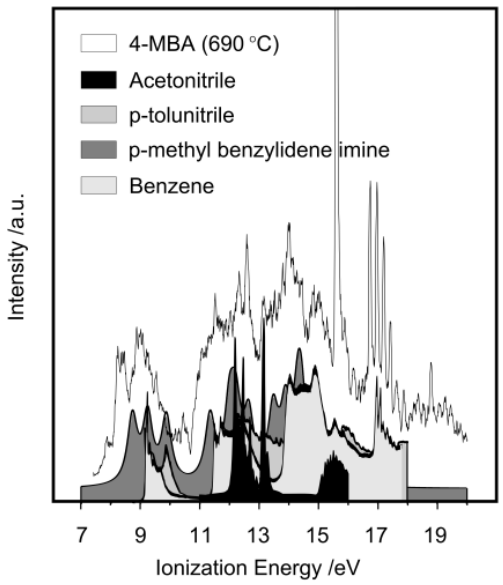

Figure 7.19: He(I) PE spectrum of 4-MBA, taken at 690 °C, and superimposed spectra of acetonitrile (taken from Ref.[116]), benzene (Ref.[274]), p-tolunitrile (Ref.[273]) and p-methyl benzylidene imine (simulated spectra, based on P3/6-311++G(d,p)//B3LYP/6-31+G(d,p) results).

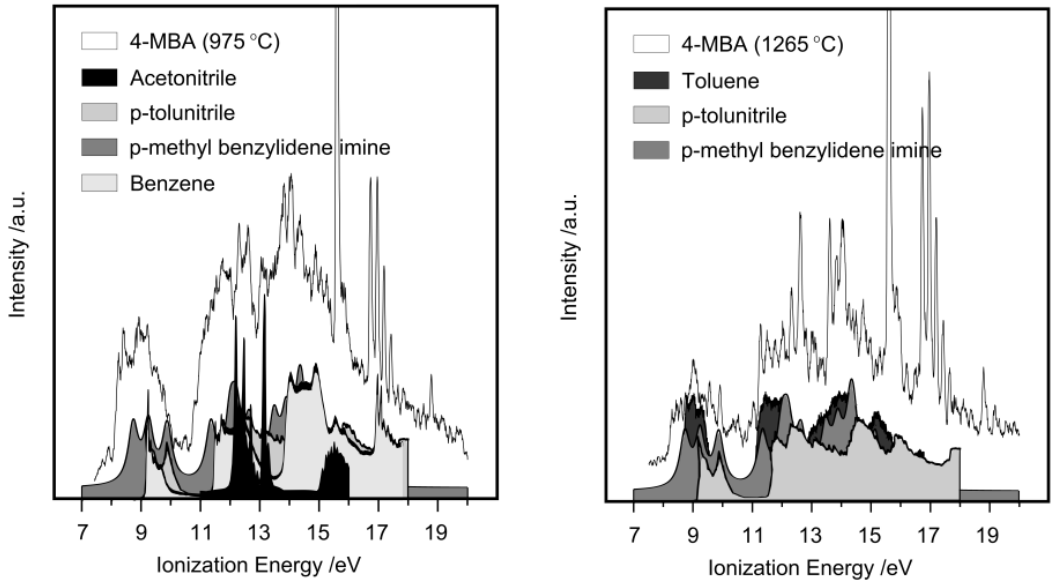

Figure 7.20: He(I) PE spectrum of 4-MBA, taken at 975 °C (left) and 1265 °C (right), and superimposed spectra of toluene (taken from Ref.[275]), p-tolunitrile (Ref.[273]) and p-methyl benzylidene imine (simulated spectra, based on P3/6-311++G(d,p)//B3LYP/6-31+G(d,p) results). At 1265 °C, benzene and acetonitrile contributions were eliminated.

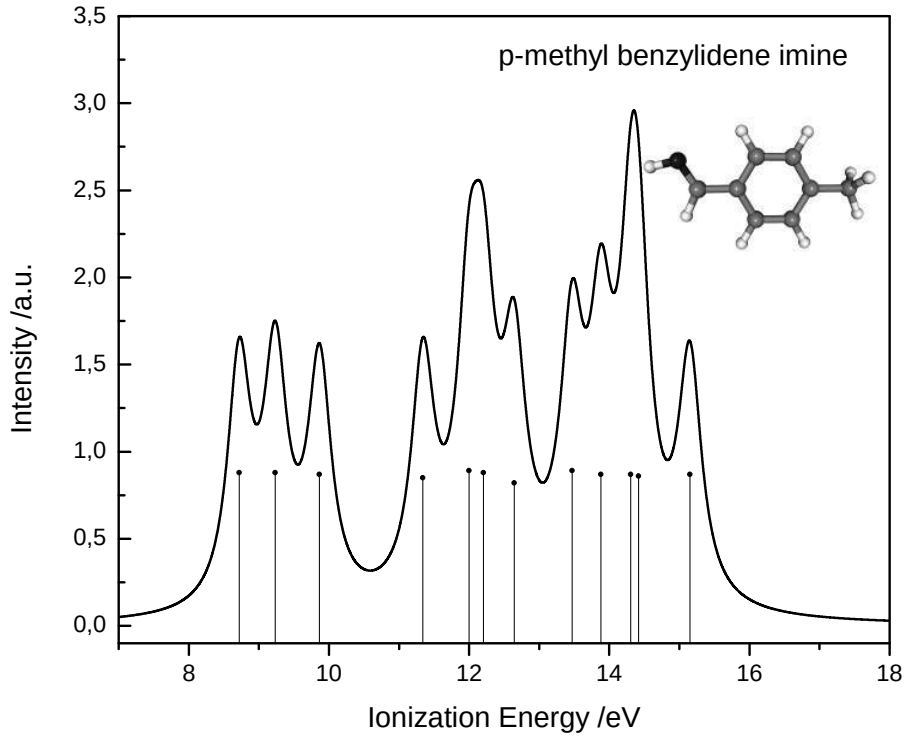

Figure 7.21: Simulated outer-valence PE spectrum of p-methyl benzylidene imine and associated stick bar graph, based on P3/6-311++G(d,p)//B3LYP/6-31+G(d,p) results.

7.4 Conclusions

On the basis of the preceding analysis, some general schemes explaining the thermal decomposition of benzyl azide and its methyl derivatives can be introduced. It is only fair to notice that the following interpretations are exclusively based on the experimental assignment of the pyrolysis spectra and lack the usual theoretical background that support this type of study. A consequent theoretical analysis should include transition structures calculations between reactants and products, as well as estimation of the energy involved in the correspondent reaction barriers and formation energies, using high level procedures (QCISD(T) and Gaussian-n (Gn) methods).

Benzyl azide results show that the thermal decomposition process of this molecule occurs in a multi-channel process that involves the formation of several intermediate products. After N_2 elimination, the remaining nitrogen atom captures the hydrogen from the CH_2 group, thus forming N-phenylmethanimine, which in turn decomposes into benzene and HCN (Scheme 1).

Scheme 1

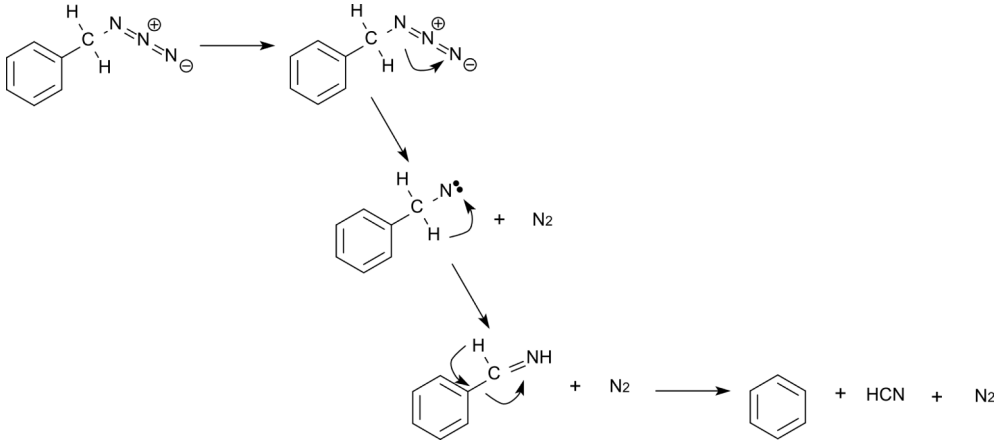

Scheme 2

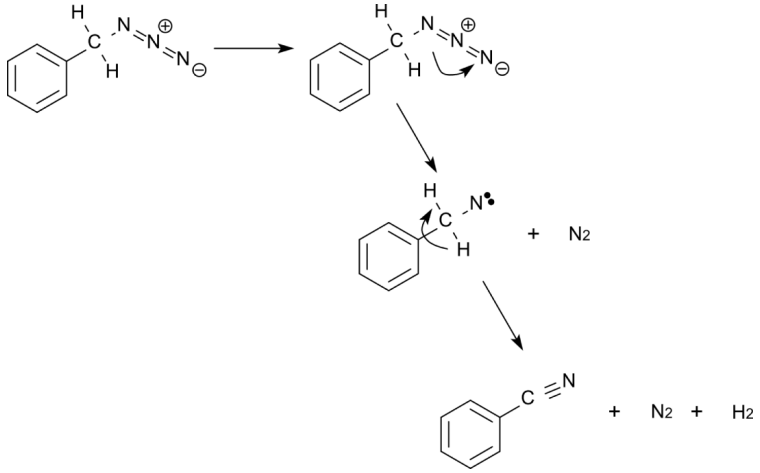

In a simultaneous reaction, the two hydrogen atoms from CH_2 detach from the carbon, forming H_2 and impelling the formation of a triple bond between the nitrogen and the carbon atoms, thus forming the intermediate molecule benzonitrile (Scheme 2).

Eventually, a third intermediate arises after the extrusion of N_2, a cyclic compound that quickly rearranges to N-methyleneaniline (Scheme 3). This molecule was actually

detected in the spectrum of BA, taken at 1135 °C (see Fig. 7.5).

Scheme 3

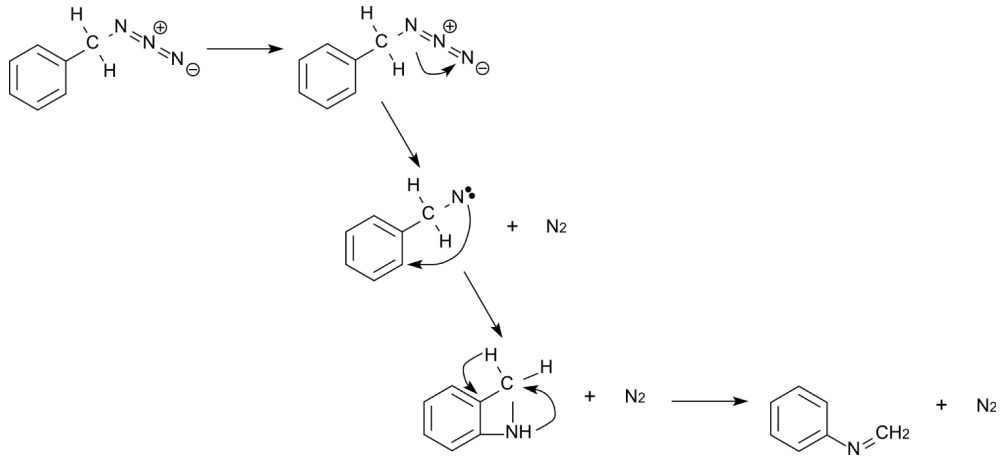

The final decomposition products of BA come from the pyrolysis of theses four intermediates N-phenylmethanimine, N-methyleneaniline, benzene and benzonitrile, and probably result from several consequent ring cleavages.

The results from 2-MBA also show similar mechanisms and similar intermediates arising from the pyrolysis process. In analogy to Scheme 1, an imine is formed, o-methyl benzylidene imine, which in turn decomposes into toluene and HCN (Scheme 4).

Scheme 4

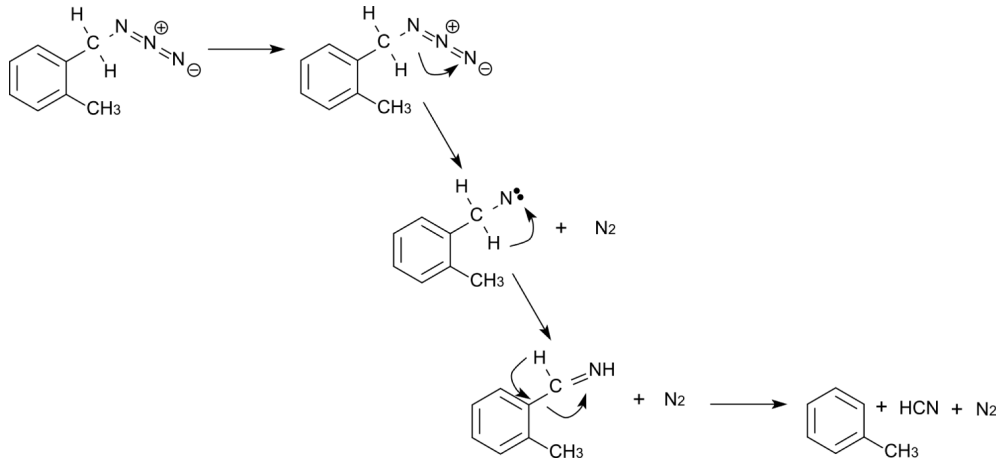

Also simultaneous, a second reaction occurs, similar to the one in Scheme 2, in which o-tolunitrile and molecular hydrogen are formed (Scheme 5). O-tolunitrile was in fact identified in the spectrum of 2-MBA pyrolysis, taken at 920 °C (Fig. 7.9).

Another cyclic intermediate is formed in the thermal decomposition of 2-MBA, entitled isoindoline (Scheme 6). This product is clearly formed during the pyrolysis process, as shown before in Fig. 7.9. Isoindoline arises from o-methyl benzylidene imine, by bonding of the imine moiety (NH) to the nearby methyl group and proton transfer to the CH group.

Consequently, the final decomposition products of 2-MBA must come from the pyrolysis of the aforementioned intermediates o-methyl benzylidene imine, isoindoline, toluene and o-tolunitrile, and result from several ring cleavages of these compounds.

Scheme 5

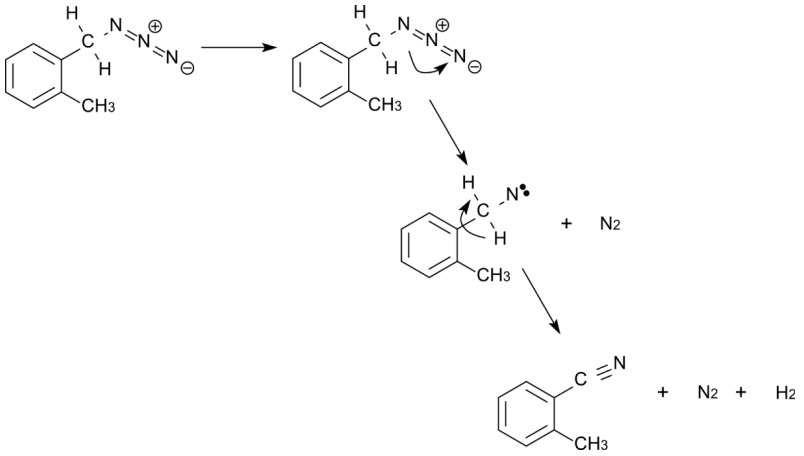

Scheme 6

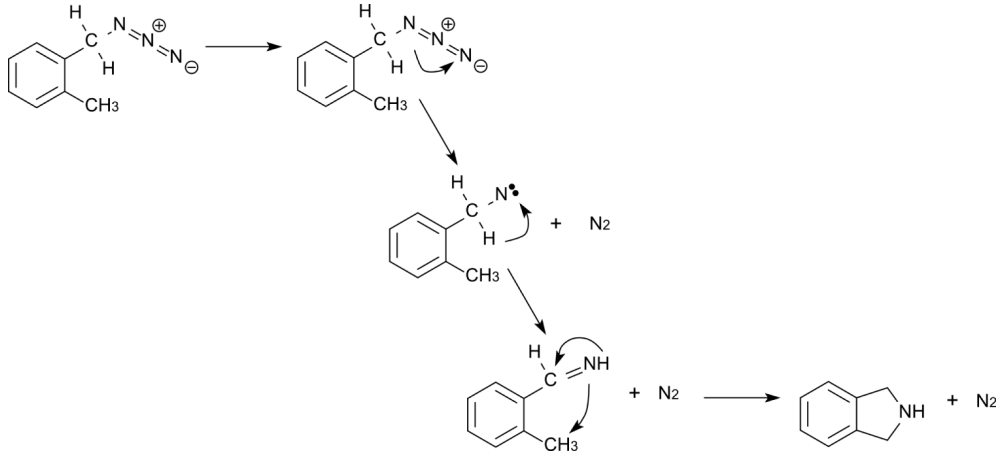

The thermal decomposition of 3- and 4-MBA follow similar mechanisms to the ones portrayed in Schemes 4 and 5, the only difference being the position of the methyl substituent: meta (3-MBA) and para (4-MBA). In addition, in the pyrolysis spectra of both compounds, acetonitrile and benzene appear to be forming, together with the imine and nitrile molecules. One way to explain this is by an increase in proximity between the azide chain and the methyl substituent, upon ionization. In this situation, N_3 is placed above the ring and the detachment of N_2 occurs in the vicinity of CH_3, which leaves the imine moiety very close to the methyl group. It then captures the whole CH_2 group, leaving only the hydrogen to satisfy the carbon in the benzene ring. Another explanation (less probable) is the formation of o-tolunitrile (or p-tolunitrile) and bonding of the nitrile group to CH_3. As the pathway involving tolunitrile also gives rise to H_2, the high presence of hydrogen at that temperature satisfies the electron deficient carbon atoms in the benzene ring.

This study proved to be fruitful at unveiling some mechanisms behind the aromatic azides thermal decomposition, although the variety of reactants coming from possible ring cleavages of the intermediates is vast and difficult to identify. Also, some sharp peaks in 3- and 4-MBA full decomposition spectra lack a more thorough analysis that should be aimed at the area of unsaturated carbons and toluene pyrolysis products. Finally, the use of a complementary technique, such as matrix-isolation IR, should help to clarify the decomposition mechanisms and provide a sturdy support to some of the PES assignments.

Chapter 8

Electronic Structure and Thermal Decomposition of 5ATZ

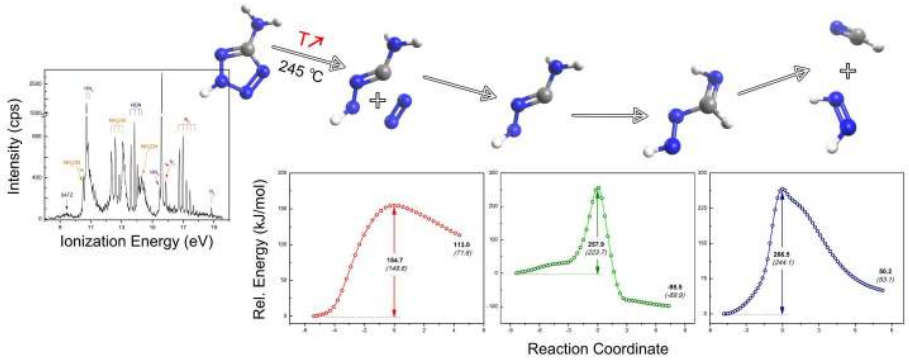

8.1 Introduction

Tetrazoles[278] (CN_4H_2) are exceedingly important compounds due to their practical role in different industrial and medical applications.

In industry, tetrazole derivatives are of common use and newly synthesized compounds[54] offspring from research at a frequent pace. They present appealing tribological functionalities if coupled to some active elements, functioning as an additive to liquid paraffin, in applications where anti-wear and friction reduction oils are needed[279]. In addition, its use as a corrosion inhibitor in copper polishing has also been reported[75]. Also, its thermal stability in conjunction with the high nitrogen content, lead to its use in safer and environment-friendly explosives and pyrotechnics[76,280,281].

In medicine, the tetrazole ring is present in a wide range of drugs[282,283], acting as a powerful isosteric substituent of the carboxylic group, -CO_2H, with the advantage of being metabolically more stable than the latter[72,73].

From a fundamental point-of-view, some tetrazoles are best known for exhibiting annular tautomerism, a characteristic which has been studied both through a myriad of theoretical methods[284–286] and several experiments based on NMR[287,288], IR[50,289,290] and UV photoelectron[56] spectroscopies and mass spectrometry[65,291]. These studies

[†]Reproduced with permission from *Chem. Phys.* **2011**, *381*, 49-58.

suggest that both 1H- and 2H-forms can coexist in the gas-phase, the 2H-tautomer being predominant over the 1H-tautomer, in the vast majority of simple tetrazole based molecules; it is also a matter of overall agreement that the nature of the 5-substituent affects the tautomeric equilibrium of the tetrazole ring.

5-aminotetrazole (5ATZ, NH_2CN_4H, Fig. 8.1) is a perfect example of a tetrazole derivative. It is widely used as an intermediate in the synthesis of tetrazole compounds because of its assorted reactions and ease of preparation. Its nitrogen content is rated above 82.3 wt % and it is considered a high-energetic material[76,280,281].

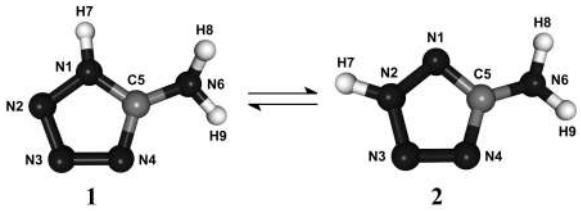

Figure 8.1: 1H-form and 2H-form of 5ATZ (**1** and **2**, respectively).

Fundamental experimental research on 5ATZ is mainly based on thermal decomposition analysis with subsequent tautomeric equilibrium evaluation, through the assessment of the intermediates associated with the different decomposition pathways[62,292–294]. To our knowledge, the only experimental study trying to characterize the outer-valence electronic structure of 5ATZ is the work by Sun *et al.*[295], using ultraviolet photoelectron spectroscopy (UVPES). However, there is no mention to the preferable tautomeric form adopted by this molecule, and an incomplete assignment is done based on calculations on the 1H-tautomer only.

Levchik *et al.*[292], using different spectroscopic methods, analysed the thermal degradation of 5ATZ between 25 and 700 °C. They argued that heating the intact solid sample to a temperature near its melting point (≈201°C) and quenching it to room temperature, or evaporating it under vacuum lead to an increase of the amino form. Interdependent parallel routes for the thermal decomposition of 5ATZ were proposed, which accounted for the formation of hydrogen azide (HN_3) plus cyanamide (NH_2CN), and for the formation of N_2 plus a metastable CH_3N_3 product. Brill and Ramanathan[293] studied the chemical pathways behind 5ATZ thermal decomposition, by using temperature jump/Fourier transform IR (T-Jump/FTIR) spectroscopy and analysing the gaseous final products of the flash pyrolysis of 5ATZ, at 350 °C, 400 °C and 450 °C. The authors have shown that the evaporation of intact 5ATZ resulted in HN_3 and NH_2CN.

Lesnikovich *et al.*[62] used several thermal analysis methods, associated with gas-chromatography mass-spectrometry (GC/MS) and FTIR spectroscopy, to shed light on the kinetics and thermal decomposition mechanisms of aminotetrazoles, including 5ATZ. Originating from the thermal decomposition of 5ATZ, the compounds N_2, HN_3 and NH_3 were identified among the gaseous products, and ammonium azide (NH_4N_3) and melamine were found among the volatile condensed products. Lesnikovich *et al.*[62] also pointed out that the heating or evaporation of 5ATZ resulted in a population increase of the amino form.

Finally, the recent work of Paletsky *et al.*[294] presents results for the kinetics of 5ATZ thermal decomposition, at high heating rates ($50 - 275$ °C/s). In agreement with the results from the above mentioned references, Paletsky *et al.*[294] also identify HN_3, N_2, NH_2CN, HCN, and NH_3 as the products formed upon thermal decomposition of 5ATZ.

The theoretical studies[296–298] on the thermal decomposition of 5-ATZ (and its imino

form, 5ITZ) by Zhang *et al.*[296], Kiselev and Gritsan[297] and Paul *et al.*[298], give a crucial insight on the interpretation of the data arising from thermal decomposition experiments. Zhang *et al.*[296] have studied the kinetics of decomposition of 1H-5ATZ to HN_3 and NH_2CN, presenting intrinsic reaction coordinate (IRC) curves connecting the reactants, the transition structures (TS) and the products.

The work by Kiselev and Gritsan[297] covered the thermal decomposition and isomeric interconversion of 1H-, 2H-5ATZ and 5ITZ, by analysing most of the decomposition pathways for the three isomers. Conclusions show that the imino form is prone to the fast bimolecular conversion to the more thermodynamically preferable 1H-5ATZ tautomer. HN_3, N_2, NH_2CN, carbodiimide, 3-imino-diaziridin, an azide intermediate (NH_2NHCN_3) leading also to a metastable CH_3N_3 compound, and a carbene are pointed out as possible decomposition products from unimolecular reactions.

Paul *et al.*[298] also studied the unimolecular thermal decomposition reactions of 1H-, 2H-5ATZ and 5ITZ by isopotential searching. According to the authors, 5ITZ can decompose through two different routes: formation of HN_3 plus NH_2CN, and formation of N_2 plus 3-imino-diazirin. This study suggested that 3-imino-diazirin readily decomposes into hydrogen isocyanide (HNC) and *trans*-diazene (HNNH). Furthermore, Paul *et al.*[298] also show that the decomposition of 1H-5ATZ and 2H-5ATZ leads to the formation of HN_3, N_2, NH_2CN, HN=C=NH and a metastable CH_3N_3 product, in agreement with Kiselev and Gritsan[297].

In order to study the electronic structure of 5ATZ, we elect the UVPES technique as the primary method of accessing the ionization energy values and band profiles, paying special attention to the tautomerism issue, a matter which can also be evaluated through UVPES[56,226,299]. Contrary to Sun *et al.*[295], both 5ATZ tautomers are studied by theoretical calculations, in order to correctly assign the gas-phase photoelectron spectrum of 5ATZ.

UVPES is also used for studying the thermal decomposition of 5ATZ, by means of a molecular oven, specifically built for this task. The decomposition routes are thoroughly followed by IRC calculations, which further rationalize and clarify the experimental results, definitively unveiling the intricate mechanisms behind the thermal decomposition of this tetrazole based compound.

8.2 Experimental method

The UV photoelectron spectrometer used to record the spectra is very similar to the one described elsewhere[99]. An illustrated view of the apparatus is given in Fig. 8.2. It operates under high vacuum conditions and it consists of a large 150° spherical sector electrostatic analyser (mean radius = 200 mm) and a DC discharge lamp, capable of producing He(I) (21.22 eV) radiation. Typical working resolution is 30 meV full width at half maximum (FWHM) as measured at the $Ar^+\ ^2P_{3/2} \leftarrow Ar\ (^1S_0)\ (3p)^{-1}$ band.

As 5ATZ is a crystalline solid at room temperature, we designed and used a resistively heated oven to evaporate the sample (Fig. 8.2, C). The heating resistance is powered by a DC power supply which is coupled to a solid state relay (SSR) and a PID controller. The feedback signal is the temperature read at the nozzle of the oven, with a type J (Fe/Cu-Ni) thermocouple. A LabView program drives the PID and sets the oven temperature, which remains stable to within 0.2 °C around the desired value. The internal space available for the evaporating charge is 0.35 cm^3 and the oven tip is made of stainless steel, with an internal diameter of 1.0 mm and a length of 20.0 mm.

In order to obtain photoelectron (PE) spectra of 5ATZ (*Aldrich*, 97%, mp = 201°C), with no traces of the thermal decomposition products, the tip with the largest ID was used (3.0 mm), and the heating process was conducted at low heating rates (< 60

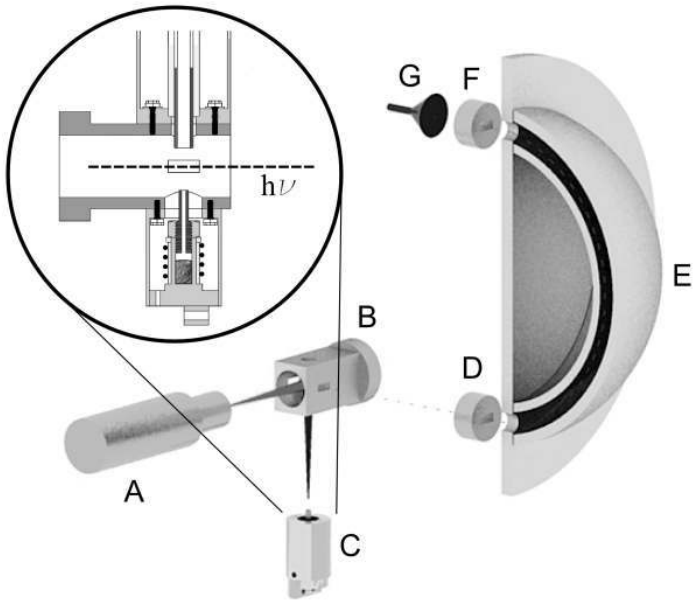

Figure 8.2: Schematics of the experimental setup, with an expanded view of the resistively heated oven: A - UV source, B - reaction cell, C - oven, D - entrance slits, E - energy analyser, F - exit slits and G - electron detector.

°C/min), in 10 °C steps, until a temperature close to the melting temperature was reached. The temperature was then increased in 2 °C steps until a sufficient signal was obtained. Experimental vertical ionization energies (VIEs) were calibrated by addition of a small amount of argon and by traces of water present in the sample[116].

For the thermal decomposition studies, tips with different IDs were experimented in order to maintain the pressure below maxima workable values ($\approx 2 \times 10^{-2}$ Pa), inside the reaction chamber. The heating process was also conducted with caution, by slowly increasing the temperature, in 10 or 5 °C steps, at low heating rates. The thermal decomposition spectra were calibrated using the ionization lines associated with the final decomposition products (N_2, HCN and HN_3).

8.3 Computational details

The framework for our theoretical studies on 5ATZ is based on the one-electron propagator description[175] of the molecular system, implemented at the level of outer-valence Green's function (OVGF) and partial third-order (P3) schemes[176,177]. These methods have already proven to be an invaluable tool in the study of PE spectra of several molecules[226–228], up to the one-electron picture breakdown.

The structures and total energies presented in this work were obtained with the Hartree-Fock (HF) method[160], second-order Møller-Plesset (MP2) perturbation theory[172] and density-functional theory (DFT)[182], together with the split-valence double- and triple-ζ basis sets[200], 6-31+G(d) and 6-311++G(d,p), with added diffuse and polarized functions. DTF results were obtained with Becke's hybrid three parameter exchange functional[189] along with the Lee, Yang and Parr correlation functional[190].

Initial geometry optimization of the isomeric forms of 5ATZ was computed with the modest HF/6-31+G(d) procedure, followed by a more refined optimization at MP2/6-311++G(d,p) and DFT B3LYP/6-311++G(d,p) levels of theory. No symmetry restrictions were imposed in these optimizations. The OVGF/6-311++G(d,p) and P3/6-

311++G(d,p) calculations were performed on the fully optimized geometries obtained with MP2/6-311++G(d,p), within the frozen-core approximation.

The optimized geometries of the cations of 1H- and 2H-5ATZ were calculated with the unrestricted B3LYP method (UB3LYP), maintaining the same basis set used in the computations for the neutral species (6-311++G(d,p)).

The thermochemical data regarding 1H-, 2H-5ATZ and 5ITZ were calculated with the hybrid G2(MP2) method[219]. Estimates of relative populations of tautomers at the evaporation temperature of 1H- and 2H-5ATZ, were based on the Boltzmann distribution formula:

$$n_i = \frac{e^{-(G_i - G_0)/kT}}{\sum_n e^{-(G_n - G_0)/kT}} \tag{8.1}$$

where n_i is the population ($\in [0,1]$) of the ith tautomer, G_i is the Gibbs energy of the ith tautomer, G_0 the Gibbs energy of the most stable tautomer and T the desired temperature. The resulting populations are designated by Boltzmann population ratios (BPR).

Regarding the thermal decomposition pathways, we have carried out several calculations, based on a simple 4-step procedure: **(i)** a relaxed potential energy surface (PES) scan along the bond of interest, in order to detect a possible TS; **(ii)** the full optimization and validation of the candidate TS; **(iii)** a IRC calculation starting from this TS, connecting reactant, TS and products; and finally, **(iv)** the full optimization of the final products. Steps **i** and **iii** were calculated with MP2(Full)/6-31G(d), and steps **ii** and **iv** with the G2(MP2) method.

It should be pointed out that, although the G2(MP2) results presented in this work include zero-point energy (ZPE) and thermal enthalpy corrections, the important and emergent question of basis set superposition error (BSSE)[300–302] is not addressed. Standard Counterpoise (CP) corrections or the use of a local MP2 method could help estimate/minimize the BSSE value. Eventually, for maximum accuracy in relative energy differences, the focal-point analysis (FPA) is the solution of choice[286].

All calculations were carried out using the Gaussian 09 suite of programs[206]. For each tautomer, the computed VIEs obtained at OVGF/6-311++G(d,p)// MP2/6-311++G(d,p) and P3/6-311++G(d,p)//MP2/6-311++G(d,p) levels were convoluted with Lorentzian functions of 0.4 eV FWHM[229] and summed over to generate the corresponding simulated spectrum.

8.4 Results and discussion

8.4.1 Structures and molecular orbitals of 5ATZ

The full optimized structures of the two 5-aminotetrazole tautomers, 1H- and 2H-5ATZ, in the neutral ground state, obtained at the MP2/6-311++G(d,p) and B3LYP/6-311++G(d,p) levels of theory, are shown in Table 8.1.

Both MP2 and B3LYP methods present similar structural parameters, with differences no greater than 0.05 Å for bond lengths and 1.5° for angle values. With the exception of the hydrogen (H8) that is positioned on the same side of the 1-substituent (H7), all the atoms forming 1H-5ATZ neutral reside in same plane. In terms of symmetry, 1H-5ATZ belongs to the trivial C_1 group.

The re-positioning of the hydrogen substituent on the tetrazole ring slightly affects the opening of the cyclic structure. Changing the hydrogen position from 1 to 2, increases the N1-N2-N3 and the N4-C5-N1 angles in 10° and 5°, respectively. In addition, as H7 is placed farther away in the ring, the interaction between it and the amino

Table 8.1: Calculated geometric parameters (Å, deg) for the 1H- and 2H-tautomer of 5ATZ, with two different methods and the 6-311++G(d,p) basis.

	1H-5ATZ		2H-5ATZ	
Parameter	MP2	B3LYP	MP2	B3LYP
r_{N1N2}	1.350	1.368	1.325	1.338
r_{N2N3}	1.313	1.280	1.334	1.317
r_{N3N4}	1.360	1.362	1.329	1.308
r_{N4C5}	1.324	1.319	1.353	1.362
r_{C5N1}	1.352	1.350	1.348	1.330
r_{NH}	1.011	1.010	1.012	1.010
r_{CNH_2}	1.385	1.372	1.381	1.371
α_{N1N2N3}	105.6	105.8	115.8	114.8
α_{N2N3N4}	111.1	111.9	104.8	106.0
α_{N3N4C5}	106.1	105.9	106.3	106.3
α_{N4C5N1}	108.0	108.2	113.0	112.6
α_{N1C5N6}	124.5	125.5	123.4	124.5

group's hydrogen (H8) diminishes, placing the latter closer to the tetrazole containing plane. As with the 1H-tautomer, 2H-5ATZ also belongs to the C_1 symmetry group.

The optimized structures of the 1H- and 2H-5ATZ cations were obtained with the unrestricted B3LYP/6-311++G(d,p) method/basis. The major differences between the cationic and neutral geometric parameters of both tautomers of 5ATZ are displayed in Table 8.2. Based on these results, elongations of bonds N2-N3 and N4-C5 and shortening of the substituent bond (C5-R) should accompany the ionization process. Also, the loss of an electron raises the symmetry of both tautomers to C_s.

Table 8.2: Differences between selected geometric parameters (Å) of the tautomers of 5ATZ in cationic and neutral ground states, obtained with B3LYP/6-311++G(d,p). R = NH_2.

Difference	1H-5ATZ$^+$	2H-5ATZ$^+$
Δr_{N1N2}	-0.045	-0.052
Δr_{N2N3}	0.085	0.080
Δr_{N3N4}	-0.076	-0.043
Δr_{N4C5}	0.061	0.028
Δr_{C5-R}	-0.062	-0.055

Fig. 8.3 depicts the contours of selected MOs (isovalue=0.07) of 1H- and 2H-5ATZ, based on MP2/6-311++G(d,p) results. The highest occupied molecular orbitals (HOMOs) of 1H- and 2H-5ATZ are both very similar π orbitals originating from the atoms that constitute the tetrazole ring (π_{N4-C5} and π_{N2-N3}). MO 21a of the 1H-tautomer is formed by a π lone pair (LP) originated at N1 (π_{LPN1}) and by the two π contributions from the two opposite nitrogens (π_{N3-N4}). In the 2H-tautomer, this π_{LPN1} coalesces with the adjacent π_{N2} orbital, forming a π_{N1-N2} MO. The next orbital in both tautomers, MO 20a, is largely formed from two lone pair orbitals, σ_{LPN3} and σ_{LPN4}, even tough the contribution from the σ_{LPN3} in 2H-5ATZ appears to a lesser extent than in 1H-5ATZ. Orbital 19a of 1H-5ATZ consists of three LPs, coming from

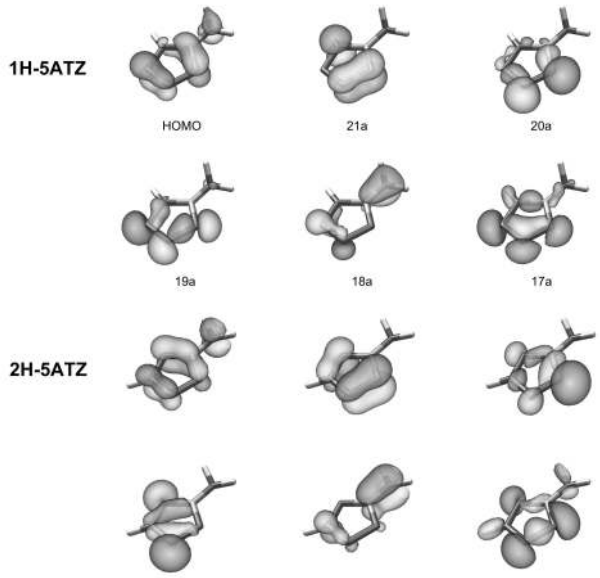

Figure 8.3: Molecular orbitals contours (isovalue = 0.07) of 1H- and 2H-5ATZ, from MP2/6-311++G(d,p) results.

three consecutive atoms in the tetrazole ring (N2, N3 and N4), mixed with σ bondings between N1-N2 and N3-N4. A more symmetric distribution takes place in the 19a MO of the 2H-tautomer, where two opposite LPs (σ_{LPN1}, σ_{LPN3}) compose the MO. In both tautomers, 18a is a π orbital bonding the carbon and the nitrogen from the amino group (π_{C5-N6}). Finally, orbital 17a in both tautomers comes from different patterns of three σ LPs of the tetrazole nitrogens, with small amounts of σ contributions from the remaining atoms.

8.4.2 Total energies and thermochemistry

The total and relative electronic energies of 1H-5ATZ and 2H-5ATZ obtained with different methods and basis are displayed in Table 8.3. In addition to our results, other references are given, for the sake of comparison[62,298,303,304].

Table 8.3: Total (hartree) and relative (kJ/mol) electronic energies of 1H- and 2H-5ATZ, calculated at different levels of theory.

	Total Energy		ΔE_{1H-2H}
Method/basis	1H-5ATZ	2H-5ATZ	kJ/mol
MP2/6-31G(d,p)[a]	-312.759013	-312.766312	19.16
MP2/6-311++G(d,p)	-312.888254	-312.896752	22.31
B3LYP/6-31G(d)[b]	-313.608830	-313.613980	13.52
B3LYP/6-31++G(d,p)[c]	-313.635719	-313.641361	14.81
B3LYP/6-311++G(d,p)	-313.705810	-313.711580	15.15
CCSD(T)/aug-cc-pVTZ			
//B3LYP/6-311++G(3df,3pd)[d]	-313.156788	-313.161212	11.61
G2(MP2)	-313.142366	-313.146959	12.06

[a]Ref.[62], [b]Ref.[303], [c]Ref.[304] and [d]Ref.[298]

Table 8.4: Gibbs free energies ($G_{G2(MP2)}$, a.u.), relative energies (ΔG, kJ/mol) and Boltzmann population ratios (BPR, %) of 1H- and 2H-5ATZ.

	T=298 K			T=460 K		
Tautomer	$G_{G2(MP2)}$	ΔG	BPR	$G_{G2(MP2)}$	ΔG	BPR
2H-5ATZ	-313.179643	0.0	99.0	-313.199190	0.0	94.7
1H-5ATZ	-313.175281	11.5	1.0	-313.194972	11.1	5.3
5ITZ	-313.157839	57.2	-	-313.177829	56.1	-

As expected, 2H-5ATZ lies lower in energy than the 1H-tautomer, within all theory levels. B3LYP/6-311++G(d,p) places the latter tautomer 15.1 kJ/mol above the 2H form, whereas MP2/6-311++G(d,p) raises this difference to 22.3 kJ/mol. The more accurate G2(MP2) method settles this value to 12.1 kJ/mol, approximately. Comparison of the G2(MP2) energy with the single point energy obtained from the high-end coupled cluster method (CCSD(T))[298], upon a fully optimized B3LYP/6-311++G(d,p) structure, shows that G2(MP2) is a very accurate method, with the advantage of being computationally less demanding.

In order to obtain the relative abundance of the 1H- and 2H-tautomers of 5ATZ, at room temperature (T≈298 K) and at the compound approximate melting temperature (T≈460 K), the G2(MP2) Gibbs free energies were used in conjunction with Eq. 8.1. The results are shown in Table 8.4.

The optimized structure and energy of the imino tautomer (5-iminotetrazole, 5ITZ) was also obtained at the G2(MP2) level, to check whether it could really be excluded from comparison with the other two tautomers, in terms of energy and stability. The results place the imino form 56.1 kJ/mol above the lowest energy tautomer (2H-5ATZ), which corresponds to a very low BPR, relatively to the more stable 1H- and 2H-forms. At 460 K, the 2H-tautomer is predominant over the 1H-form, with 94.7% of the 5ATZ population assuming this configuration.

8.4.3 Photoelectron spectrum of 5ATZ

Assignment of the experimental PE spectra of 5ATZ is supported by calculations performed at the OVGF/6-311++G(d,p) and at the P3/6-311++G(d,p) levels over the fully optimized MP2/6-311++G(d,p) 1H- and 2H-tautomer structures. These results are shown in Table 8.5 and Table 8.6, together with the main character of the first six HOMOs and the MP2 energies obtained with the same basis set. The pole strengths associated with all VIEs from P3 and OVGF B calculations fall between 0.85 and 0.91.

The PE spectrum of 5ATZ, taken at 190 °C, is presented in Fig. 8.4, section (a), where the bands are labelled A-E and the asterisk marks the N_2 trace from a controlled leak. Our spectrum follows the same pattern as the only spectrum reported previously in the literature[295], with a broad first peak (A) centred at 9.44 eV, some vibrational structure on top of it and a pronounced shoulder on the right side. This peak corresponds to the ionization of the HOMO, a $\pi_{N4-C5,N2-N3}$ plus the amino π lone pair from N6. P3 results for this first ionization energy (IE) give 9.51 eV, taken from calculations upon the 2H-tautomer, and guarantee a good agreement between experiment and theory.

Next, within the 10-12.5 eV IE range, there is a large asymmetric group, in which only two experimental bands (B and C) can be identified and distinguished. Band B is centred at 10.85 eV and band C lies at 11.57 eV. Considering again the 2H-tautomer as the most abundant 5ATZ form and therefore taking the P3 results on 2H-5ATZ for the

Table 8.5: Calculated vertical ionization energies (VIE, in eV) of 1H-5ATZ

		1H-5ATZ		
		MP2	OVGF[a]	P3[a]
MO	Character	VIE	VIE	VIE
22a	$\pi_{N4-C5,N2-N3}$	10.29	9.75	10.09
21a	$\pi_{N3-N4,LPN1}$	12.41	10.79	11.04
20a	$\sigma_{LPN3,LPN4}$	12.68	11.11	11.36
19a	$\sigma_{LPN2,LPN3,LPN4}$	12.93	11.48	11.73
18a	π_{C5-N6}	14.37	12.91	12.97
17a	$\sigma_{LPN2,LPN3,LPN4}$	15.43	13.27	13.46
16a		18.20	16.36	16.34
15a		18.97	17.31	17.53
14a		19.38	17.95	17.85

[a]Fully optimized MP2/6-311++G(d,p) geometry.

Table 8.6: Calculated vertical ionization energies (VIE, in eV) of 2H-5ATZ

		2H-5ATZ		
		MP2	OVGF[a]	P3[a]
MO	Character	VIE	VIE	VIE
22a	$\pi_{N4-C5,N2-N3}$	9.80	9.23	9.51
21a	$\pi_{N1-N2,N3-N4}$	12.16	11.06	11.34
20a	σ_{LPN4}	13.01	11.35	11.72
19a	$\sigma_{LPN1,LPN3}$	13.69	11.66	11.99
18a	π_{C5-N6}	14.15	12.84	12.86
17a	$\sigma_{LPN1,LPN3,LPN4}$	15.70	13.67	13.99
16a		17.96	16.47	16.39
15a		18.61	16.55	16.59
14a		19.02	17.46	17.39

[a]Fully optimized MP2/6-311++G(d,p) geometry.

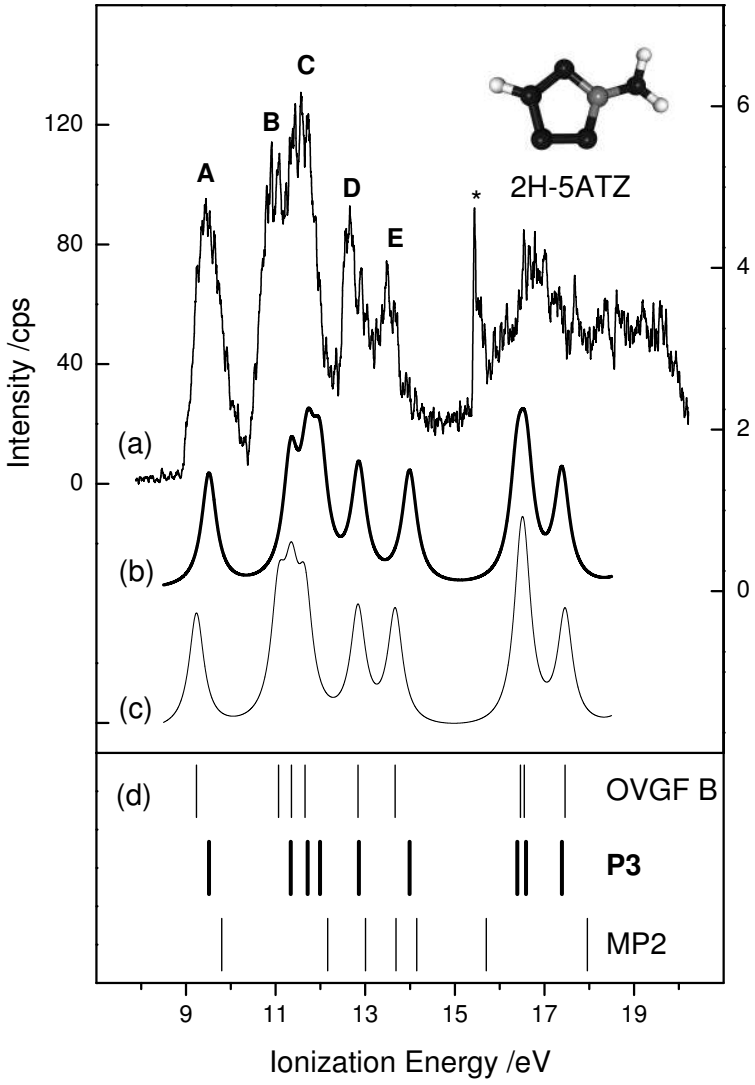

Figure 8.4: He(I) PE spectrum of 5ATZ, taken at 190 °C (a). The asterisk marks the N_2 peak from a controlled leak. Simulated PE spectrum of 2H-5ATZ, based on P3 (b) and OVGF B (c) results. VIEs of tetrazole 2H-5ATZ, using the MP2, P3 and OVGF B methods (d).

assignment, one can state that band B comes from the ionization of MO 21a, comprised of two opposing π orbitals in the tetrazole ring. Band C, however, is formed by the overlap of two σ lone pair orbitals, located in the tetrazole. P3 results give the correct asymmetry disposition (band C higher than band B), whereas OVFG B portrays no asymmetry at all, with the three theoretical ionization lines equally spaced.

The following features appearing in the spectrum (bands D and E), within the 12.5-15 eV IE range, have similar narrow and peak-like shapes, which are known to be associated with ionizations of π type orbitals. In fact, according to our studies on the molecular orbitals contours (see Fig. 8.3), band D (12.66 eV) corresponds to the ionization of MO 18a, a π type orbital between the carbon and the nitrogen from the NH_2 group. The nearby band E (13.58 eV) is related to the ionization of MO 17a, which is comprised of several σ lone pairs on the tetrazole ring. The experimental IEs of bands A-E, the respective energy uncertainties and the P3 orbital energies for 2H-5ATZ are collected in Table 8.7. Comparison between the experimental values and the predicted VIEs on Tables 8.5 and 8.6 (considering only the first six HOMOs), leads to mean absolute differences (MADs) of 1.44, 0.24 and 0.26 eV, for 1H-5ATZ, and 1.41, 0.15 and 0.29 eV, for 2H-5ATZ, from MP2, OVGF and P3 calculations, respectively.

Although the P3 simulation of the 2H-tautomer perfectly describes the experimental spectrum until 15 eV, there are some additional features in this region that can only be explained by the inclusion of the 1H-5ATZ contribution: the shoulder at the right hand side of band A and the small band between peaks D and E.

Table 8.7: Experimental vertical ionization energies (VIE, eV) and theoretical IE values (eV) for 5ATZ. MO stands for molecular orbital and ΔE for energy uncertainty (in eV).

Band	MO	VIE	ΔE	Previous[a]	Calc.[b]
A	22a	9.44	0.04	9.40	9.51
B	21a	10.85	0.07	10.87	11.34
C	20a	11.57	0.06	11.59	11.72
	19a				11.99
D	18a	12.66	0.03	12.81	12.86
E	17a	13.58	0.03	13.44	13.90

[a]Ref.[295]. [b]From P3 results on 2H-5ATZ.

The band patterns originating from the 1H-5ATZ simulation are markedly different from the ones obtained in the experimental spectrum, a fact that supports even more the known predominance of the 2H-tautomer in the gas-phase.

Finally, using the BPRs in Table 8.4, for 5ATZ at T=460 K, a simulated PE spectrum of 5-aminotetrazole, containing the two tautomers, was produced (Fig. 8.5, section (b)), which almost perfectly fits the experimental spectrum.

Further quantitative evaluation of the tautomeric stability from the experimental data implies the adoption of a proper deconvolution scheme which should take into account the spectrometer response function[305,306]. In alternative, the determination of the exact Franck-Condon (FC) profile of the first band, through FC factors calculation, for both tautomers, would lead to almost exact tautomer population values[307]. However, these two approaches are outside the scope of the present work.

8.4.4 Thermal Decomposition of 5ATZ

Several spectra were recorded at increasing oven temperature, in small temperature steps and low heating rates, from an initial temperature near the melting point of

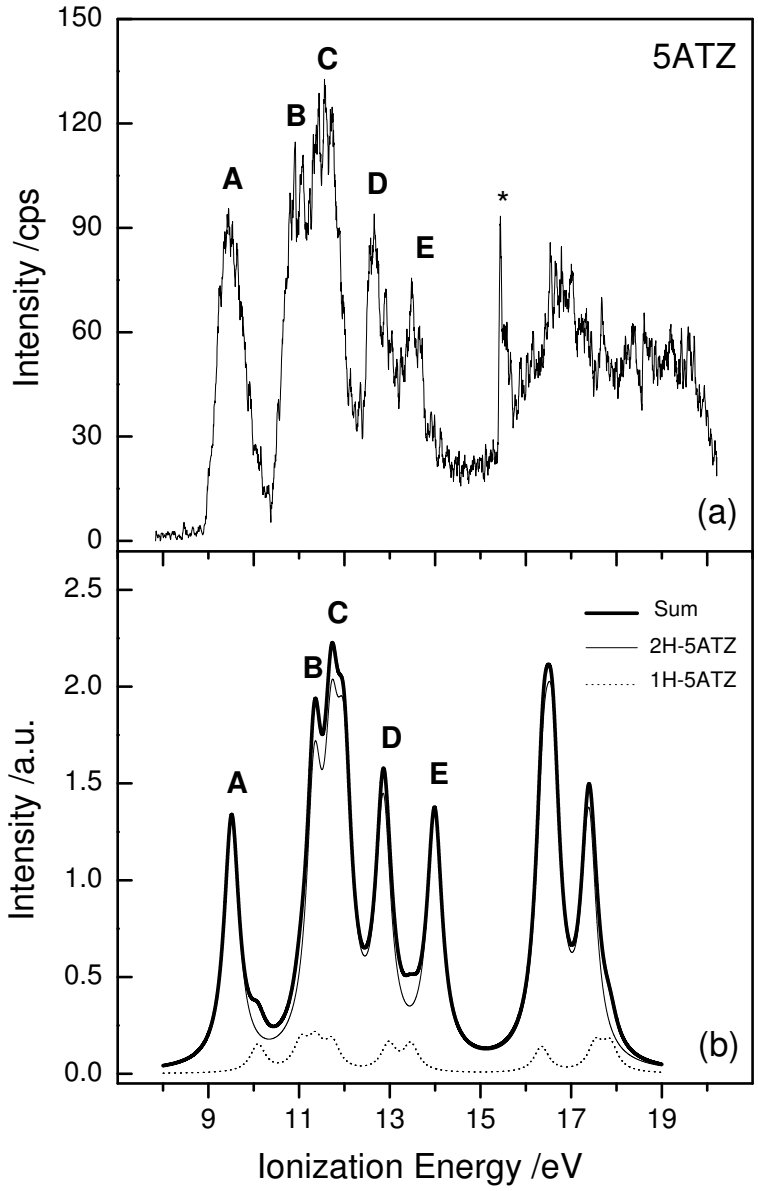

Figure 8.5: He(I) PE spectrum of 5ATZ, taken at 190 °C (a), and simulated outer-valence PE spectrum, based on P3/6-311++G(d,p) results (b). The asterisk marks the N_2 peak from a controlled leak.

5ATZ (195-205 °C). A typical thermal decomposition spectrum, taken at 245 °C, is shown in Fig. 8.6. Readily identified in this spectra are HN_3 and N_2, as the primary decomposition products, together with NH_2CN, HCN and 5ATZ vapour. A very low contribution from 5ATZ, which has its first broad band centred at 9.44 eV, indicates almost full decomposition.

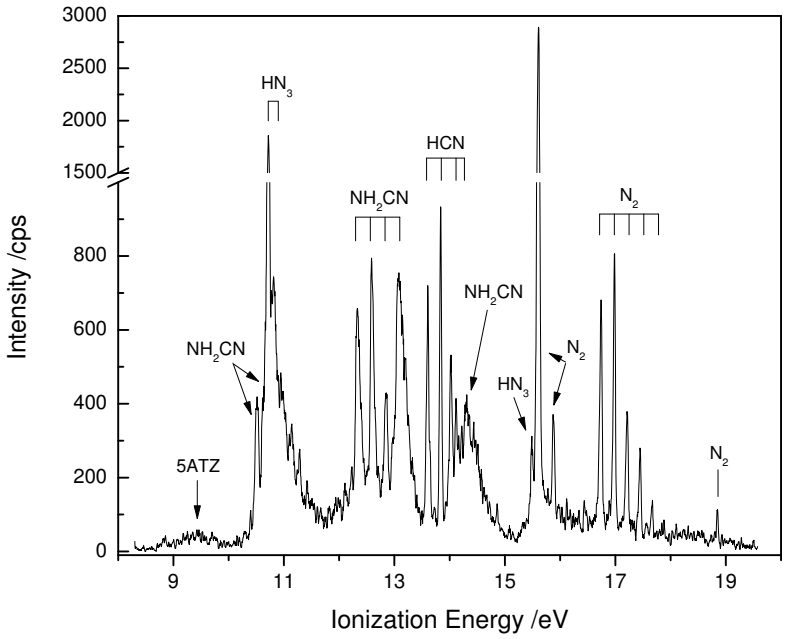

Figure 8.6: He(I) PE spectrum of the thermal decomposition of 5ATZ, taken at 245 °C.

Between 10 and 12 eV, the first bands of NH_2CN (VIE=10.65 eV[308]) and HN_3 (VIE=10.74 eV[309]) overlap, forming a wide band with a pronounced vibrational structure. Although the vibrational progression on top of this band appears to match the one from ammonia's first band (VIE=10.88 eV[310]), with an adiabatic ionization energy (AIE) of 10.15 eV[310] and vibrational spacing of 900 cm^{-1} [310], the excessive vibrational overlapping in this region does not allow us to unequivocally assign the progression to NH_3.

In the 12.0-13.5 IE range, there is a shoulder on the left side, followed by three sharp peaks and a narrow band. This shoulder corresponds to the second band of HN_3, centred at 12.2 eV, with 445 cm^{-1} vibrational intervals[309]. The three sharp peaks are associated with the ionization of the second HOMO of NH_2CN, centred at a 12.50 eV (middle peak, VIE) with associated vibrational structure appearing at $\pm$2080 cm^{-1} [308] from this value. Finally, the narrow band at 12.98 eV is also assigned to NH_2CN, and is ascribed to the ionization of a non-bonding orbital of cyanamide.

The needle like peaks starting at 13.60 ($\Delta\nu\approx$1800 cm^{-1}, due to the C$\equiv$N stretching) are unequivocally attributed to the ionization of HCN. The end of the vibrational progression of HCN is already on top of NH_2CN fourth band (VIE=14.23 eV[308]). Near the characteristic IE value of N_2 (15.60 eV[116]), one can also identify the third band of HN_3, at 15.47 eV[310].

These assignments of the thermal decomposition products for the overall spectral region are best interpreted in Fig. 8.7, where the individual contributions of each product can be seen.

Four different routes can be used to explain the direct formation of the detected

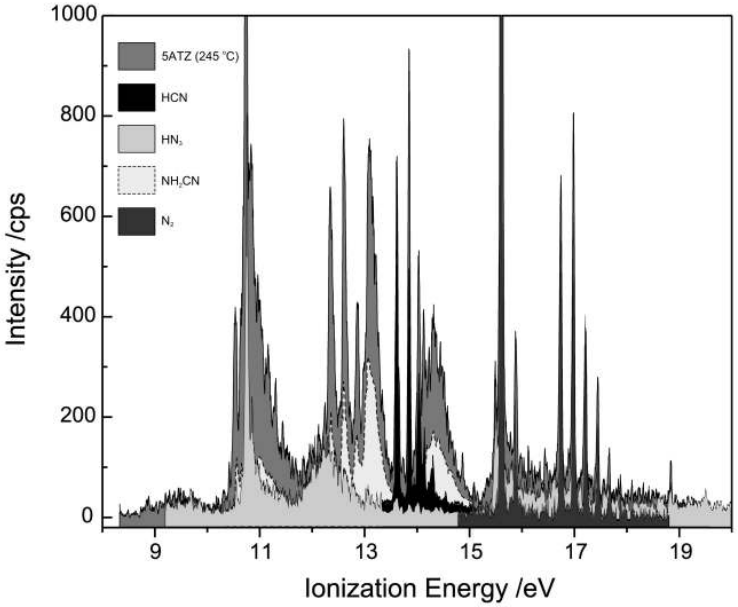

Figure 8.7: Detail of the He(I) PE spectrum of the thermal decomposition of 5ATZ (gray), taken at 245 °C, with estimated contributions from the decomposition species HCN (black), HN_3 (light gray), NH_2CN (lighter gray) and N_2 (dark gray).

products, two for each tautomer. The formation of N_2 and a metastable CH_3N_3 molecule implies the transformation of 1H-5ATZ into an azide (azido-methanimidamide), which readily loses N_2, by the usual nitrogen elimination process that accompanies the pyrolysis of almost all organic azides. The barriers involved in this route are depicted in the IRC calculations of Fig. 8.8 and Fig. 8.9.

The reaction path presented in Fig. 8.9 is very complex: the azide's NH_2 group undergoes rotation, followed by stretching of the N_2-N bond, which in turn breaks to give the unstable intermediate corresponding to the TS, 146.3 kJ/mol (calculated at the G2(MP2) level) above the energy of the initial azide. As N_2 moves farther away from the intermediate, the amino group bonds to the nitrogen end of the intermediate, stabilizing it and evolving to the final CH_3N_3 structure, a hydrazine derivative termed carboximidoylhydrazine. The sum of these two separated products is predicted to be more stable than the initial azide (-65.4 kJ/mol, from G2(MP2) results). This route clearly explains the formation of N_2 and the stable CH_3N_3 compound from 1H-5ATZ, but not the formation of HCN.

The direct formation of HN_3 and NH_2CN from the 1H-tautomer is explained by the elongation and breaking of the N3-N4 bond, followed by dissociation of the N1-C5 bond. Fig. 8.10 portrays this decomposition pathway, based on IRC calculations, obtained at the MP2(Full)/6-31G(d) level. Relatively to the initial product (1H-5ATZ) and the CH_3N_3 hydrazine from the previous route, N_2 plus cyanamide as final products are energetically less stable; in addition, the potential barrier for this reaction, calculated at the G2(MP2) level, is higher (204.7 kJ/mol) than the most energetic barrier calculated in the first decomposition route (146.3 kJ/mol).

Concerning 2H-5ATZ thermal decomposition, two routes can also be envisaged. In contrast with 1H-5ATZ, the N_2 elimination in the 2H-tautomer occurs in a direct way, without the formation of any stable intermediate. The process starts with the rotation of the NH_2 group towards the hydrogenated side of the tetrazole, followed by the dissociation of the N2-N3 bond and elongation of the N4-C5 bond. The N4-C5

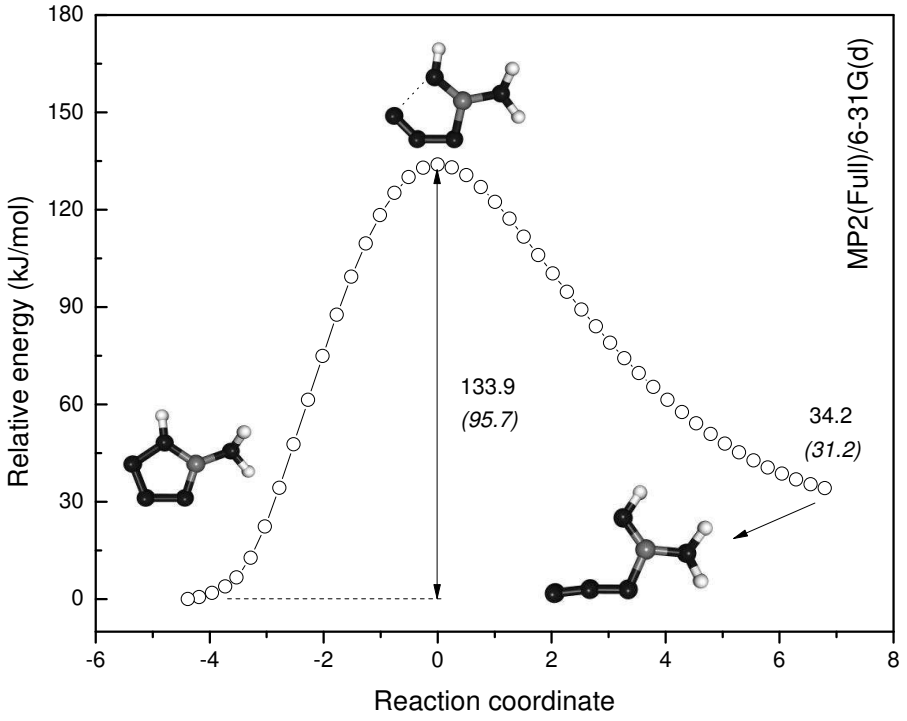

Figure 8.8: IRC calculations connecting 1H-5ATZ and the stable azide compound, obtained with MP2(Full)/6-31G(d). The relative energies of the TS and products, obtained with G2(MP2), are given in parentheses (in kJ/mol).

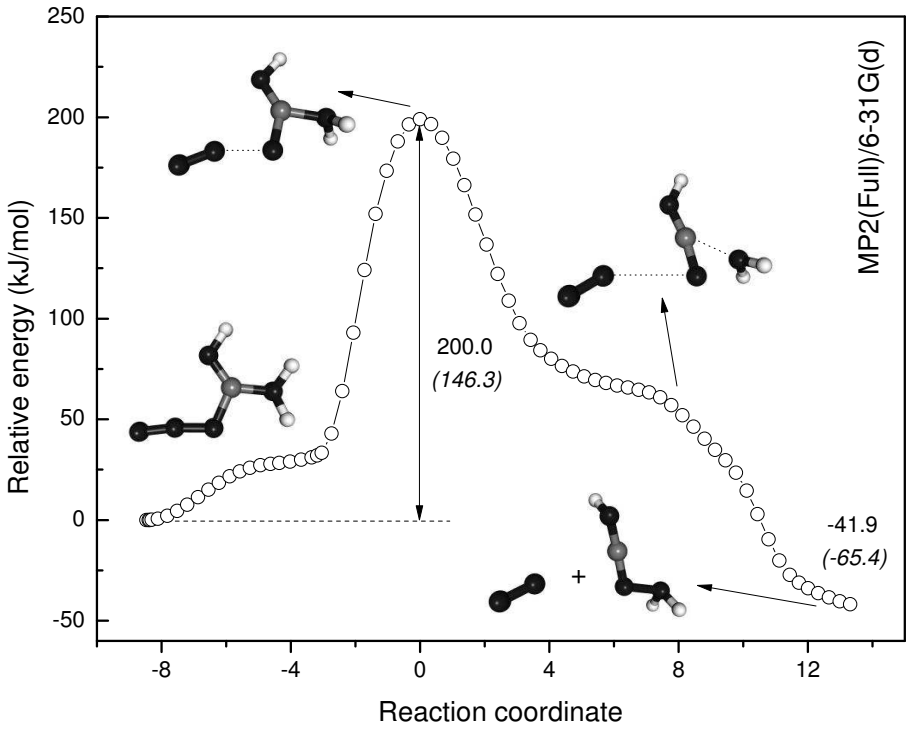

Figure 8.9: IRC calculations connecting the azide and N_2 plus the metastable CH_3N_3 compound, obtained with MP2(Full)/6-31G(d). The relative energies of the TS and products, obtained with G2(MP2), are given in parentheses (in kJ/mol).

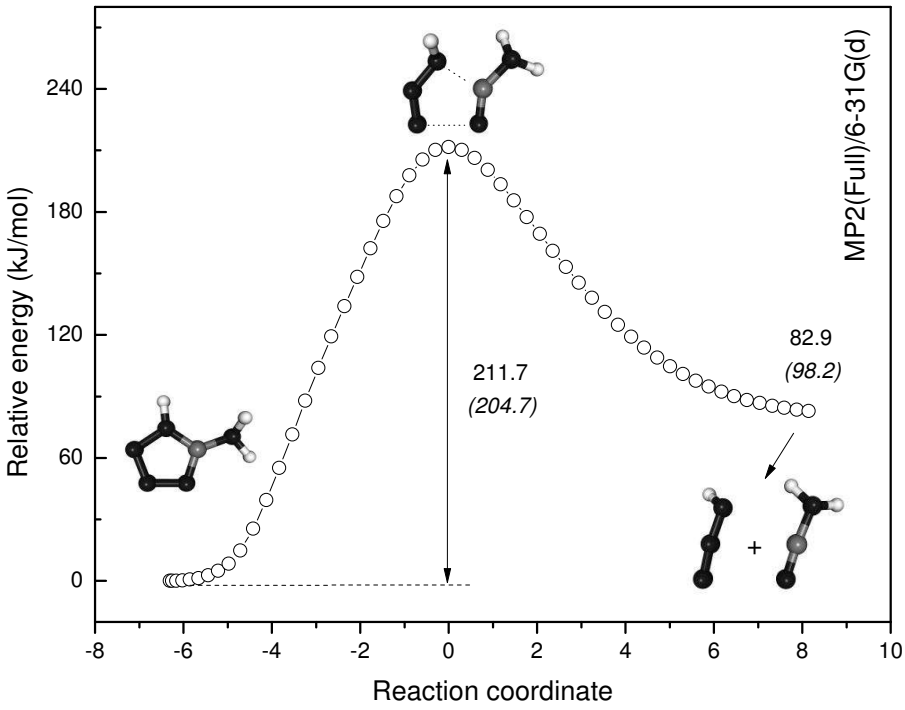

Figure 8.10: IRC calculations connecting 1H-5ATZ and HN_3 plus NH_2CN, obtained with MP2(Full) /6-31G(d). The relative energies of the TS and products, obtained with G2(MP2), are given in parentheses (in kJ/mol).

bond eventually breaks, releasing N_2 and leaving behind a short-lived CH_3N_3 carbene, named amino(diazenyl)methylidene. This reaction is depicted in the IRC of Fig. 8.11, where a potential barrier of approximately 149.6 kJ/mol (G2(MP2)) can be seen.

The formation of HN_3 from 2H-5ATZ decomposition is similar to the one from 1H-5ATZ. However, the dissociation starts from the hydrogenated side of the tetrazole instead, with the breaking of the N1-N2 bond, followed by elongation and breaking of the N4-C5 bond. The final products are again HN_3 and NH_2CN and the IRC pathway that follows this reaction is presented in Fig. 8.12, where a energy barrier of 228.0 kJ/mol (G2(MP2)) arises.

The sum of unimolecular processes that describe the thermal decomposition of 5ATZ is illustrated in Fig. 8.13. Associated with each step, we present the values for the potential energy barriers, obtained from the G2(MP2) energies at the stationary points of the PES, i.e. the energy differences between the reactants at each step and the corresponding TS. Also, the energies of all the products, relatively to the lowest energy tautomer 2H-5ATZ, are given above each structure. Results of our calculations are close to the data obtained by Kiselev and Gritsan[297], at the G3 level of theory.

The elimination of N_2 occurs as a one-step process in 2H-5ATZ, in contrast with the N_2 elimination from 1H-5ATZ. The latter implies ring opening of the tetrazole moiety and formation of an azide, through a 95.7 kJ/mol barrier, followed by the N_2 loss (implying the transposition of a 146.3 kJ/mol energy barrier) and formation of the metastable CH_3N_3 molecule. The formation of HN_3 from both tautomers is also a one-step process, but it involves approximately 23.3 kJ/mol more in the case of 2H-5ATZ. Thus, HN_3 is formed primarily by the decomposition of 1H-5ATZ.

A second thermal decomposition stage, which should include the self-reaction of cyanamide[293] and the decomposition of HN_3, is outside the scope of our theoretical investigations. However, some insight concerning the formation of HCN can be given,

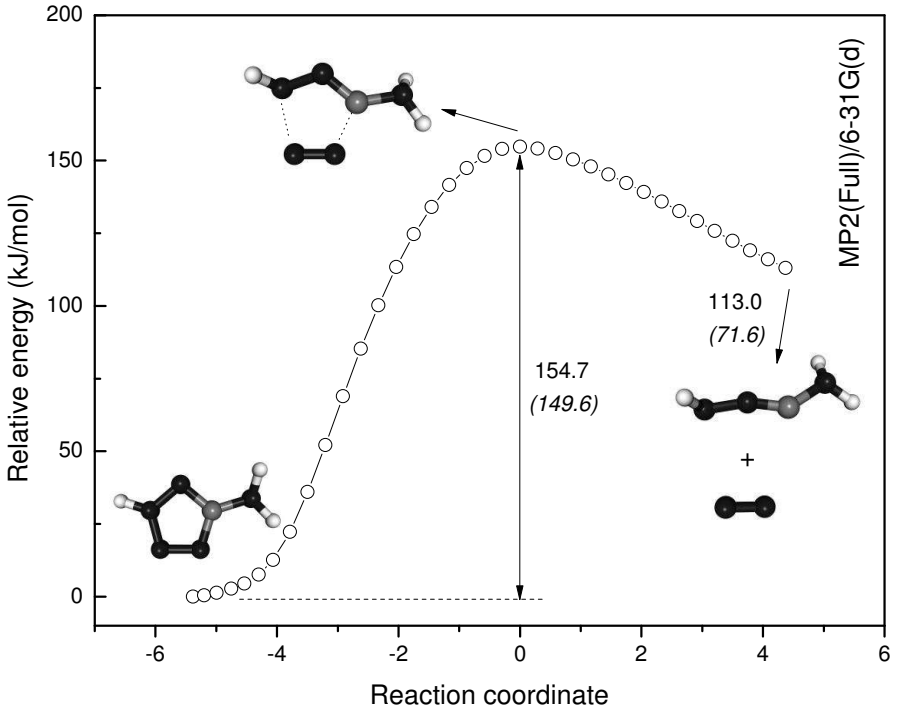

Figure 8.11: IRC calculations connecting 2H-5ATZ and N_2 plus amino(diazenyl) methylidene, obtained with MP2(Full)/6-31G(d). The relative energies of the TS and products, obtained with G2(MP2), are given in parentheses (in kJ/mol).

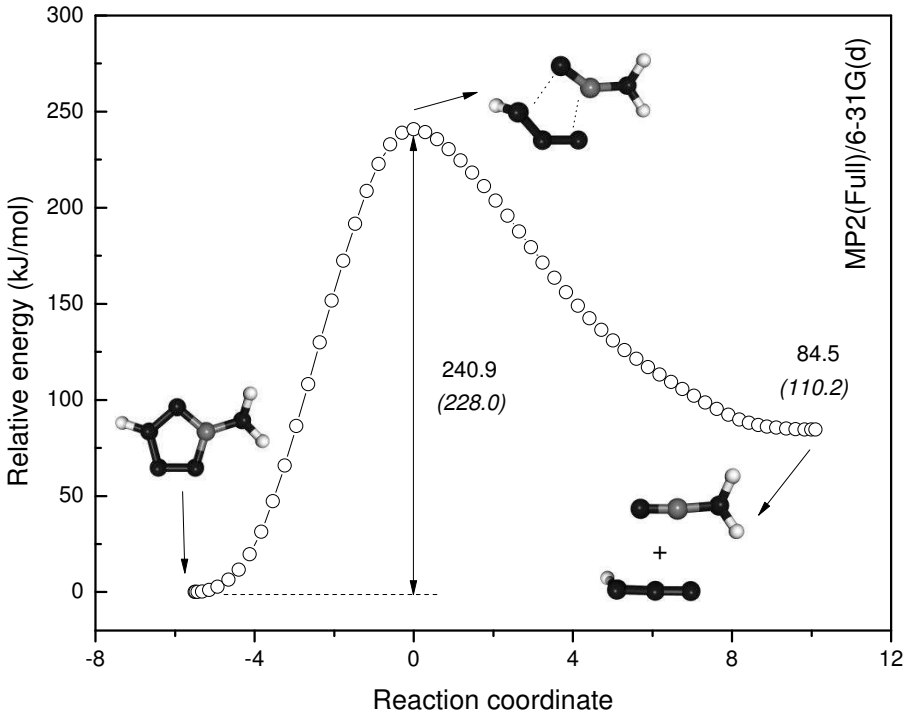

Figure 8.12: IRC calculations connecting 2H-5ATZ and HN_3 plus NH_2CN, obtained with MP2(Full) /6-31G(d). The relative energies of the TS and products, obtained with G2(MP2), are given in parentheses (in kJ/mol).

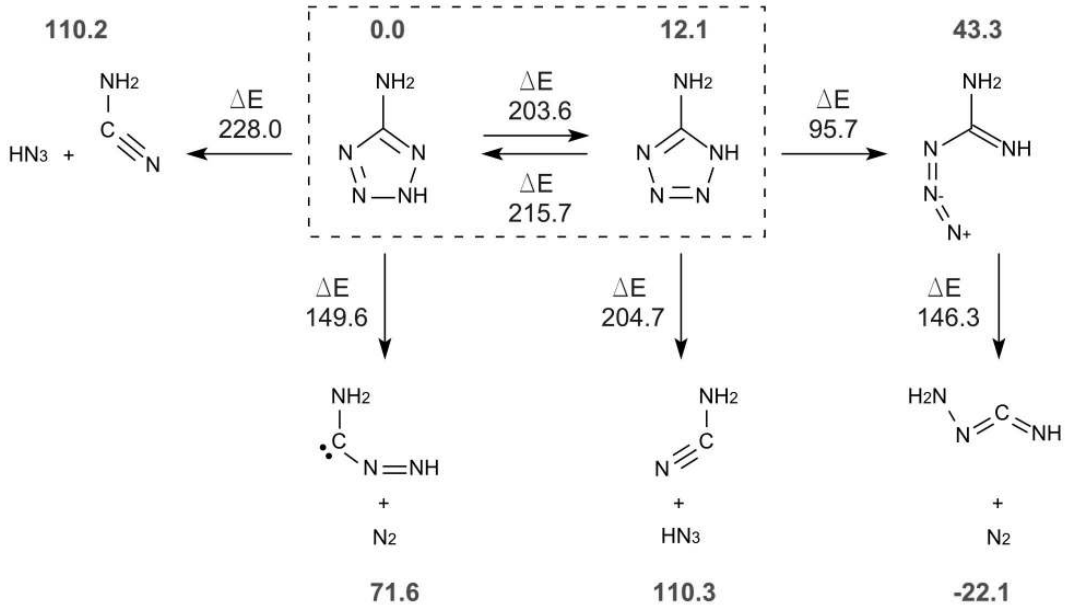

Figure 8.13: Proposed scheme for the thermal decomposition of gas-phase 5ATZ. G2(MP2) energies (in kJ/mol) relatively to the 2H-tautomer are given above each structure (in boldface type font). ΔE represents the G2(MP2) energy barriers (in kJ/mol) between the product(s) and the preceding reactant.

supporting its clear assignment in the thermal decomposition spectra. Bearing this in mind, we have carried out some calculations on the CH_3N_3 carbene (resulting from 2H-5ATZ degradation) and its possible thermal decomposition. Fig. 8.14 shows the IRC calculations connecting it, the TS and another CH_3N_3 isomer, which is different from the previous hydrazine derivative obtained from the decomposition of the azide compound. This reaction consists on the rotation of the amino group and migration of the hydrogen atom that it is closer to the central carbon, in order to form the more stable isomer N-imino-methanimidamide, which involves a energy barrier of approximately 223.7 kJ/mol (G2(MP2)).

Comparison of this route to the one that leads to HN_3 and NH_2CN from 2H-5ATZ, readily shows that the latter is energetically more expensive than the combined scheme that leads to the formation of N_2 in the first stage and N-imino-methanimidamide in the second stage.

From this reaction, N-imino-methanimidamide is formed 89.9 kJ/mol below the initial carbene isomer, adopting a conformation with C_s symmetry, with all the atoms lying in plane and the terminal hydrogens positioned in a *cis* configuration. If the hydrogen atom from the imino group is allowed to approach the central nitrogen, by excitation of one of the vibrational modes, a reaction similar to the one depicted in Fig. 8.15 is possible.

Afterwards, the migration of the second hydrogen leads to the direct formation of HCN and *cis*-diazene (HNNH), by elongation and breaking of the central N-C bond. This corresponds to a energy barrier of approximately 244.1 kJ/mol, calculated at the G2(MP2) level. Fig. 8.16 shows the mechanism underlying the proposed reaction scheme for the formation of HCN and HNNH. This is, in principle, a viable solution for the formation of HCN, as the maximum barrier involved in the mechanism is of the same order of magnitude as the other barriers present in the first stage of thermal decomposition of both tautomers. Finally, HNNH has a lifetime of the order of minutes

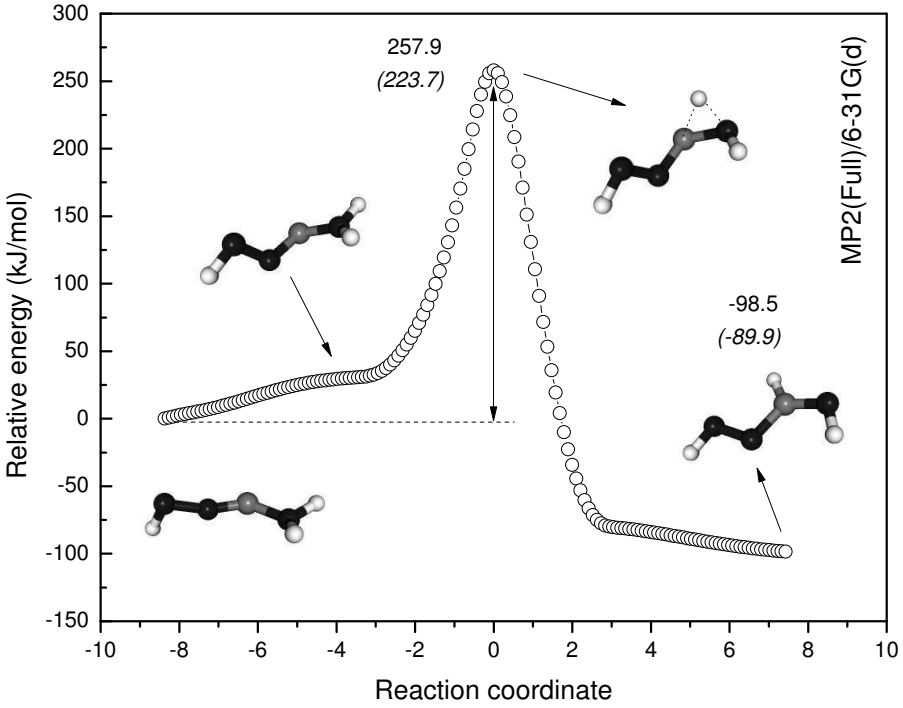

Figure 8.14: IRC calculations connecting the CH_3N_3 carbene (from 2H-5ATZ decomposition) and its isomer N-imino-methanimidamide, obtained with MP2(Full)/6-31G(d). The relative energies of the TS and products, obtained with G2(MP2), are given in parentheses (in kJ/mol).

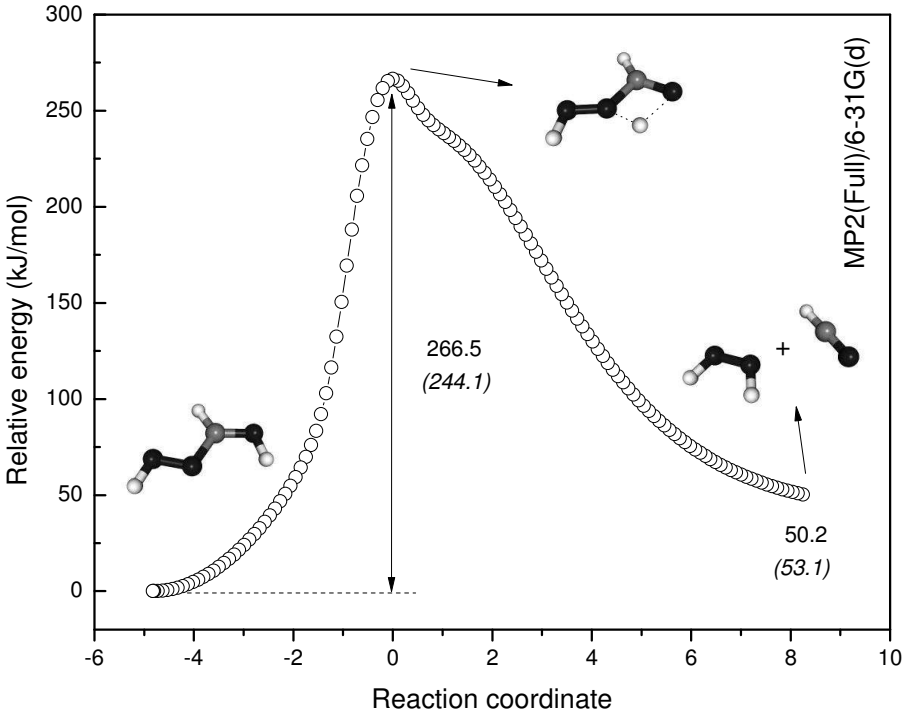

Figure 8.15: IRC calculations connecting N-imino-methanimidamide and HCN plus HNNH, obtained with MP2(Full)/6-31G(d). The relative energies of the TS and products, obtained with G2(MP2), are given in parentheses (in kJ/mol).

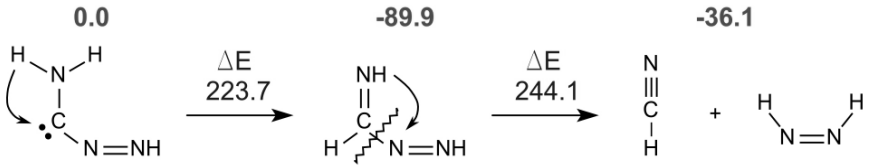

Figure 8.16: Proposed scheme for the thermal decomposition of the CH_3N_3 carbene. G2(MP2) energies (in kJ/mol) relatively to the carbene are given above each structure (in boldface type font). ΔE represents the G2(MP2) energy barriers (in kJ/mol) between the product(s) and the preceding reactant.

in the gas phase at low pressure and is known[311] to decompose into N_2 and H_2.

8.5 Conclusions

For the first time, the analysis of the gas-phase PE spectrum of 5ATZ was accomplished, taking into account contributions from both 1H and 2H tautomers. The information retrieved from the computational results obtained within the electron propagator theory, is unequivocal in considering that this molecule adopts almost exclusively the 2H-form. Its HOMO VIE is 9.44±0.04 eV, and relates to the ionization of a π MO originated in the tetrazole ring. The ionization of both tautomers leads to structural changes in the hydrogens from the amino group, placing them in plane with the tetrazole ring and raising the tautomers' symmetry to C_s (from the previous C_1, in the neutral ground state).

In terms of 5ATZ thermal decomposition, results taken at 245 °C revealed N_2, HCN, NH_2CN, HN_3 and 5ATZ vapor as the main gaseous final products. Formation of N_2 from 1H-5ATZ implies the formation of azido-methanimidamide, which evolves into molecular nitrogen and carboximidoylhydrazine (HN=C=N-NH_2). The azide formation from 1H-5ATZ involves a 95.7 kJ/mol barrier and the subsequent nitrogen elimination from the azide engages a 146.3 kJ/mol barrier. The formation of HN_3 plus NH_2CN directly from 1H-5ATZ/2H-5ATZ requires the transposition of 204.7/228.0 kJ/mol barriers, respectively. This and the fact that the energy required for the 2H-1H conversion is less than 228.0 kJ/mol, favors the formation of HN_3 from the thermal degradation of predominantly the 1H-tautomer.

N_2 is eliminated from 2H-5ATZ without the formation of any intermediate, through a 149.6 kJ/mol barrier. This reaction leaves behind a short-lived carbene (amino (diazenyl) methylidene), which transforms into the more stable N-imino-methanimidamide, through a 223.7 kJ/mol amino hydrogen migration. The C-N central bond of this latter compound is then compelled to break through another hydrogen migration (244.1 kJ/mol barrier), leaving HCN and *cis*-diazene as the final products of dissociation.

In summary, the routes concerning only 2H-5ATZ can be used to explain the unimolecular thermal decomposition of gas-phase 5ATZ, because all the observed final products were predicted by theoretical calculations on the 2H-tautomer only, through accessible energy barriers (150-250 kJ/mol).

Chapter 9

Electronic Structure and Thermal Decomposition of 5MTZ

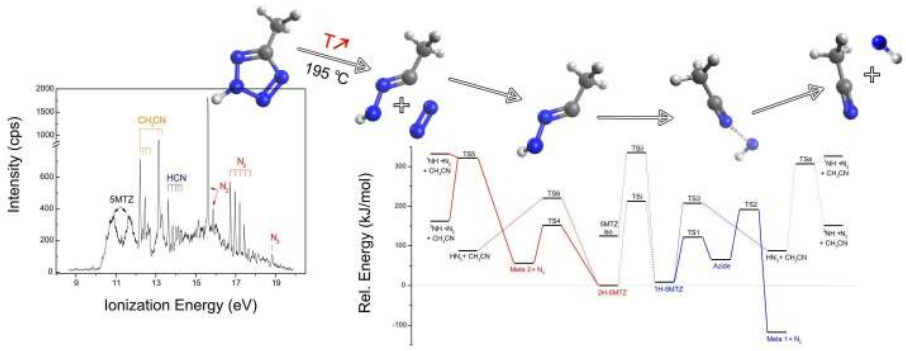

9.1 Introduction

Compounds containing the tetrazole ring (R-CN_4H) find their use disseminated among several areas of industry, as pyrotechnics[76], stabilizers in photography[4], gas generating agents in airbags[312] and precursors in organic synthesis[54]. Moreover, tetrazoles are also present in the synthesis of several anti-hypertensives drugs[73], where they are used as isosteric substituents of the carboxylic group (-CO_2H), protecting the drug from degradation arising from metabolic processes[72].

In gas-phase, the main research interest regarding tetrazoles relies in the study of its annular tautomerism and thermal decomposition. Tautomerism is an interesting subject *per se*, as certain molecules can have its functionality or physico-chemical activity altered by tautomeric changes. Furthermore, in the case of tetrazoles, tautomerism is linked to the aspect of thermal decomposition, because it influences profoundly the outcome of the thermal fragmentation: some pathways are only energetically accessible through specific tautomers[313].

The thermal decomposition of tetrazoles usually involves the elimination of N_2, accompanied by a high energy release[63], in a similar way to what occurs in the pyrolysis of the azido compounds (R-N_3)[33]. However, the products arising from the thermal

[†]Reproduced with permission from *Chem. Phys.* **2012**, *392*, 21-28.

decomposition of tetrazoles are considered environment-friendly[281], contrasting with the characteristic byproducts arising from azides' decomposition. Furthermore, the pyrolysis of tetrazoles can lead to the production of radicals and short-lived intermediates, whose characterization of the electronic structure constitutes a strong point of interest[314].

5-methyltetrazole (5MTZ, CH_3CN_4H, Fig. 9.1) was one of the first tetrazoles whose gas-phase tautomerism was investigated: Razynska *et al.*[65] studied the prototropic equilibrium of 5-methyltetrazole, using mass spectrometry and *ab initio* calculations. The authors of this study came to the conclusion that 5-methyltetrazole assumed predominantly the 2H-form.

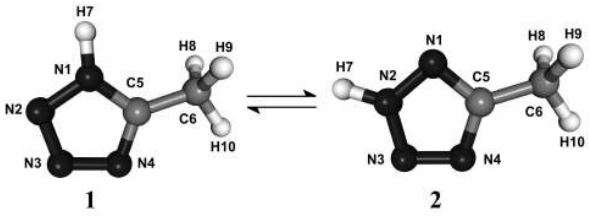

Figure 9.1: 1H-form and 2H-form of 5MTZ (**1** and **2**, respectively).

Palmer and co-workers[55–57] used UV photoelectron spectroscopy (UVPES) and *ab initio* calculations to study and assign the photoelectron spectra of the azoles. However, regarding the methylated tetrazole, only 1- and 2-methyltetrazole were studied, and not the 5-substituted species. More recently, the electronic structure of 5MTZ was studied by Novak *et al.*[299], using UVPES. In that work, the assignment of the photoelectron spectrum of 5MTZ was made on the basis of electronic structure calculations and the assumption that 5MTZ assumed almost exclusively the 2H-form. Contributions from the 1H-tautomer were deprecated, based on G3/B3LYP calculations which predicted that the 2H-tautomer was 36.7 kJ/mol more stable than the 1H-form.

To our knowledge, the gas-phase thermal decomposition of 5MTZ has not yet been studied, and no computational work regarding its thermal fragmentation pathways exists. Contrary to 5-aminotetrazole (5ATZ), there is an enormous literature gap regarding theoretical prediction of the thermal decomposition process and kinetics of 5MTZ.

Following our previous work on 5ATZ[315], the UVPES technique is used to study the electronic structure of and the gas-phase thermal decomposition of 5MTZ. In the same way, experimental data from both the electronic structure studies and the thermal decomposition work are rationalized in terms of results obtained from theoretical calculations.

9.2 Experimental method

The UV photoelectron spectrometer used in this work is described elsewhere[315]. Briefly, it operates under high vacuum conditions, and uses a large 150° spherical sector electrostatic analyser and a DC discharge lamp for producing He(I) radiation (21.22 eV). Typical working resolution is 30 meV full width at half maximum (FWHM) as measured for the $(3p)^{-1}\ ^2P_{3/2}$ Ar^+ ionization line.

A resistively heated oven, inside a reaction cell, was used to evaporate the sample, as 5MTZ is a crystalline white solid at room temperature. The internal space available for the evaporating charge is ca. 0.35 cm^3 and several tips (length = 20 mm) of different diameters (0.5-3.0 mm) and materials (copper and stainless steel) can be used. The

power supply system driving the oven heating resistance is very responsive and allows for a quick and controlled increment of the temperature (which remains stable within 0.2 °C around the desired temperature value).

In order to obtain photoelectron (PE) spectra of 5MTZ (*Aldrich*, 97%, mp = 147 °C), with no traces of thermal decomposition, the sample was heated at low heating rates (<60 °C/min), in 20 °C steps. At 110 °C, the signal was sufficient to record the spectra. Calibration of the spectra was achieved by addition of a small amount of argon (VIE = 15.76 eV) into the chamber and by traces of water (VIE = 12.62 eV) present in the sample[116].

In the thermal decomposition studies, two approaches were followed: (1) the sample was slowly heated from room temperature to 500 °C, at low heating rates (<60 °C/min), and spectra were recorded at each step of increasing temperature; (2) the sample was heated from room temperature to near its decomposition point (195 °C), at high heating rate (ca. 500 °C/min), and spectra at that final temperature were recorded. In these studies, the oven copper tip with the lowest internal diameter (0.5 mm) was used, in order to maintain the pressure below maximum workable values (ca. 2 x 10^{-2} Pa). The thermal decomposition spectra were calibrated using distinguishable ionization lines associated with known decomposition products (N_2, VIE = 15.60 eV, and CH_3CN, VIE = 12.21 eV)[116].

9.3 Computational details

All calculations were carried out using the Gaussian 09 software[206]. The structures and total energies presented in this work were obtained with the second-order Moller-Plesset (MP2) perturbation theory[172] and density-functional theory (DFT)[182], together with the split-valence double and triple-ζ basis set[200], with added diffuse and polarized functions, i.e. 6-31+G(d) and 6-311++G(d,p). The DFT results were obtained using Becke's hybrid three parameter exchange functional[189], along with the Lee, Yang and Parr correlation functional[190]. The frozen-core approximation was used throughout these calculations. Fully optimized geometries of both 5MTZ tautomers were obtained at the MP2/6-311++G(d,p) and DFT/6-311++G(d,p) levels of theory. Optimized geometries of the cations of both tautomers, 1H-5MTZ$^+$ and 2H-5MTZ$^+$, were obtained with the unrestricted B3LYP method using the 6-311++G(d,p) basis set. No symmetry restrictions were imposed during these calculations and the nature of the geometries was confirmed through vibrational analysis (no imaginary frequencies).

For the computation of the VIEs, the one-electron propagator formalism was adopted, and implemented at the level of the outer-valence Green's function (OVGF) and partial third-order (P3) schemes[176,177]. The OVGF/6-311++G(d,p) and P3/6-311++G(d,p) calculations were performed on the fully optimized geometries of both tautomers, obtained at the MP2/6-311++G(d,p) level of theory. Each ionization line was then convoluted with a Lorentzian function of 0.4 eV FWHM and made proportional to its pole strength. This value was chosen in order to accommodate the broadening due to the vibrational envelope associated with each transition and due to the experimental resolution of the apparatus. The set of convoluted VIEs of each tautomer were then summed over to generate the corresponding simulated spectrum.

The thermochemical data regarding 1H- and 2H-5MTZ were calculated with the G2(MP2) method[219]. Estimates of the relative populations of the tautomers, near their evaporation temperature, were based on the Boltzmann distribution formula,

$$n_i = \frac{e^{-(G_i - G_0)/kT}}{\sum_n e^{-(G_n - G_0)/kT}} \tag{9.1}$$

where n_i is the population ($\in [0,1]$) of the ith tautomer, G_i is the Gibbs energy of the ith tautomer, G_0 the Gibbs energy of the most stable tautomer and T the desired temperature. The resulting populations are designated by Boltzmann population ratios (BPR).

The computational study of the thermal decomposition of 5MTZ follows the same methodology as the one adopted in the work of 5ATZ[315]. Briefly, we scan the potential energy surface along a bond or migration of interest and then validate (only one imaginary frequency) and fully optimize a possible transition structure (TS). An intrinsic reaction coordinate computation follows, from this TS, in order to assure that the correct reactants and products are obtained. Finally, reactants, products and TS are fully optimized with the G2(MP2) method.

In order to aid the assignment of unknown ionization lines in the thermal decomposition spectra, the VIEs of some intermediates were computed with the ΔG2(MP2) approach[316]:

$$\mathrm{VIE[G2(MP2)]} = E[\mathrm{G2(MP2)}]_{n-1}^{CN} - E[\mathrm{G2(MP2)}]_n \tag{9.2}$$

where CN stands for clamped-nuclei and n is the number of electrons of the neutral molecule. This approach allows for orbital relaxation and correlation effects also in the cation, but preserves the geometry of the neutral species (thus, effectively estimating the VIE and not the adiabatic value).

9.4 Results and discussion

9.4.1 Structures and molecular orbitals of 5MTZ

The fully optimized structures of the two 5MTZ tautomers, 1H-5MTZ and 2H-5MTZ, in the neutral ground-state, obtained at the MP2/6-311++G(d,p) and B3LYP/6-311++G(d,p) levels of theory, are shown in Table 9.1. Both methods lead to similar geometries, in terms of the bond lengths in the tetrazole moiety. However, the in-plane hydrogen of the CH_3 group is located in the same side of the tetrazole hydrogen substituent (H7), in the case of 2H-5MTZ (*cis* geometry), and at the opposite side from it, in the case of 1H-5MTZ (*trans* geometry).

The position of the methyl group relatively to the plane containing the tetrazole ring (dihedral N4-C5-C6-H10) is differently predicted for 2H-5MTZ: B3LYP leads to C_s symmetry in both tautomers, whereas MP2 leads to C_s symmetry only in the 1H-form. With MP2, the geometry of the lowest energy conformer of 2H-5MTZ belongs to the C_1 group. The conformers are identified in Table 9.1: "A" designates the lowest energy conformer of 1H-5MTZ (equally determined by both methods), and "B1" and "B2" designate the lowest energy conformers of 2H-5MTZ as determined by MP2 and B3LYP, respectively.

This disagreement in predicting which structure lies lower in energy can be due to the fact that both MP2 and DFT/B3LYP are single-configuration methods and lack full accountancy for electron correlation, leading to symmetry-breaking instabilities[317]. This does not affect substantially the values from subsequent calculations in terms of the VIEs of 2H-5MTZ: either using the B3LYP C_s structure or the MP2 C_1 structure, MP2 or OVGF/P3 based VIEs do not vary more than our experimental resolution. Thus, all the calculations aimed at obtaining VIEs are based in the MP2 lowest energy structures of Table 9.1.

The optimized structures of the 1H- and 2H- cations were also computed (see Table 9.2). From these results, the ionization of both tautomers should be accompanied by a significant (ca. 0.16-0.22 Å) elongation of the N3-N4 bond and shortening of the substituent bond C5-R.

The contours of selected molecular orbitals (MOs) of 1H- and 2H-5MTZ are depicted in Fig. 9.2, as a result of calculations with MP2/6-311++G(d,p). The HOMO and the following three highest occupied orbitals follow exactly the same pattern as the corresponding MOs of 1H- and 2H-5ATZ[315]. In the following description of the electronic structure, the orbital notation characteristic of the C_s symmetry group (a″ and a′) was adopted for the two tautomers, in spite the slightly off-plane positioning of the methyl hydrogen in 2H-5MTZ.

Table 9.1: Calculated geometric parameters (Å, deg) for the 1H- and 2H-tautomer of 5MTZ, with two different methods and the 6-311++G(d,p) basis. The conformers A, B1 and B2 (see text for details) are indicated below each method.

	1H-5MTZ		2H-5MTZ	
	MP2	B3LYP	MP2	B3LYP
Parameter	(A)	(A)	(B1)	(B2)
r_{N1N2}	1.344	1.354	1.322	1.329
r_{N2N3}	1.317	1.285	1.334	1.324
r_{N3N4}	1.357	1.362	1.327	1.305
r_{N4C5}	1.329	1.317	1.355	1.363
r_{C5N1}	1.353	1.351	1.349	1.329
r_{NH7}	1.011	1.009	1.013	1.010
r_{CCH_3}	1.489	1.488	1.490	1.489
r_{CH}	1.093	1.093	1.093	1.092
α_{N1N2N3}	105.4	105.9	115.6	114.5
α_{N2N3N4}	110.9	111.2	104.6	105.6
α_{N3N4C5}	106.7	106.5	106.9	106.8
α_{N4C5N1}	107.1	107.3	112.2	111.7
α_{N1C5C6}	125.9	126.0	123.7	124.4
$\delta_{N4C5C6H10}$	0.6	0.5	80.0	59.5

Table 9.2: Differences between selected geometric parameters (Å) of the tautomers of 5MTZ in cationic and neutral ground states, obtained with B3LYP/6-311++G(d,p). R = CH_3.

Difference	1H-5MTZ$^+$	2H-5MTZ$^+$
Δr_{N1N2}	-0.056	-0.079
Δr_{N2N3}	0.154	0.218
Δr_{N3N4}	-0.099	-0.074
Δr_{N4C5}	0.072	0.043
Δr_{C5-R}	-0.035	-0.042

In the 1H-tautomer, HOMO 4a″ is a bonding orbital, originating from π orbitals established between N2 and N3 and between N4 and C5. The HOMO of 2H-5MTZ is also a π bonding orbital. In 1H-5MTZ, MO 3a″ is formed by a π lone pair (LP) originated from N1 (π_{LPN1}), plus the contribution of a π bonding orbital established between N3 and N4. MO 3a″ in 2H-5MTZ is formed from two bonding π orbitals ($\pi_{N1-N2,N3-N4}$). The following orbital, MO 18a′, originates from two σ lone pair orbitals ($\sigma_{LPN3,LPN4}$), in both tautomers. MO 17a′ of the 1H-tautomer also arises from the contribution of

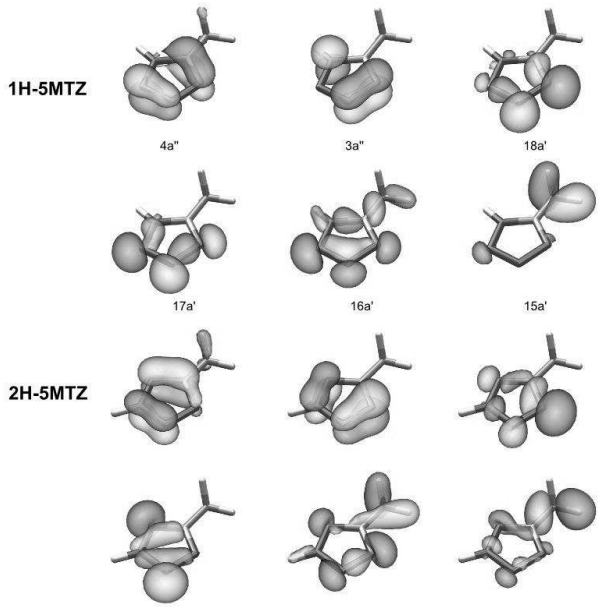

Figure 9.2: Molecular orbital contours (isovalue = 0.07) of 1H- and 2H-5MTZ, based on MP2/6-311++G(d,p) calculations.

nitrogen lone pair orbitals: three σ LPs from the N2, N3 and N4 atoms. In the 2H-tautomer, MO 17a′ is also composed of nitrogen LPs, although following a different pattern from the corresponding MO in 1H-5MTZ. The next orbital in both tautomers, MO 16a′, is formed from the three σ LPs related to the the nitrogens of the tetrazole moiety which are not bonded to the H7 atom. Finally, in both tautomers, 15a′ is a σ orbital, originated from a rotated p_z contribution of the C6 atom in the methyl group.

Table 9.3: Total (hartree) and relative (kJ/mol) electronic energies of 1H- and 2H-5MTZ, calculated at different levels of theory.

	Total Energy		ΔE_{1H-2H}
Method/basis	1H-5MTZ	2H-5MTZ	kJ/mol
MP2(Full)/6-31G(d)	-296.735628	-296.741037	14.20
MP2/6-311++G(d,p)	-296.859809	-296.866298	17.04
B3LYP/6-31G(d)[a]	-297.575900	-297.579180	8.61
B3LYP/6-31++G(d,p)[b]	-297.596603	-297.600457	10.12
B3LYP/6-311++G(d,p)	-297.659403	-297.663405	10.51
G2(MP2)	-297.099523	-297.102154	6.91

[a]Ref.[67]. [b]Ref.[304].

9.4.2 Total energies and thermochemistry

The total and relative electronic energies of 1H-5MTZ and 2H-5MTZ, obtained with different methods and basis are shown in Table 9.3. In order to extend the range of comparison, results from other studies were also included.

As with the majority of 5-substituted tetrazoles[284], the 2H-tautomer is predicted to be the predominant form adopted by the 5MTZ molecule, lying lower in energy than the 1H-tautomer. The MP2 method appears to overestimate the energy difference between

Table 9.4: Relative Gibbs free energies (ΔG, kJ/mol) and Boltzmann population ratios (BPR, %) of 1H- and 2H-5MTZ, based on G2(MP2) results.

	T=25 °C		T=140 °C	
Tautomer	ΔG	BPR	ΔG	BPR
2H-5MTZ	0.0	94.0	0.0	87.2
1H-5MTZ	6.8	6.0	6.7	12.8
5MTZ isomer	122.8	0	-	-

the tautomers, when compared with the values obtained with B3LYP. The G2(MP2) procedure yields a difference of 6.91 kJ/mol, between the 1H and 2H forms (the latter being the more stable).

Using the G2(MP2) Gibbs free energies and Eq. 9.1, the relative populations of 1H- and 2H-5MTZ are estimated to be ca. 6% and 94%, respectively, at room temperature. Near the temperature at which the spectra were obtained (ca. 140 °C), without thermal decomposition, the relative populations change: 13% of 5MTZ exists in the 1H-form and 87% in the 2H-form. Table 9.4 accounts for these values. Higher temperatures should benefit the highest energy tautomer, increasing its relative population, a fact which should be taken into account in the thermal decomposition studies.

9.4.3 Photoelectron spectrum of 5MTZ

The assignment of the experimental PE spectrum of 5MTZ is based on calculations performed at the OVGF/6-311++G(d,p)//MP2/6-311++G(d,p) and P3/6-311++G(d,p) //MP2/6-311++G(d,p) levels of theory, on both tautomers. All the resulting VIEs have pole strengths between 0.85 and 0.91, and therefore can be confidently related to direct one-electron ionizations only. Tables 9.5 and 9.6 show these VIEs, together with the main character of the valence orbitals and the MP2 VIEs, obtained via Koopmans' theorem.

Table 9.5: Calculated vertical ionization energies (VIE, in eV) of 1H-5MTZ

		MP2	OVGF B[a]	P3[a]
MO	Character	VIE	VIE	VIE
4a″	$\pi_{N2-N3,N4-C5}$	10.83	10.48	10.85
3a″	$\pi_{N3-N4,LPN1}$	12.30	10.75	10.96
18a′	$\sigma_{LPN3,LPN4}$	12.63	11.14	11.38
17a′	$\sigma_{LPN2,LPN3,LPN4}$	12.98	11.48	11.74
16a′	$\sigma_{LPN2,LPN3,LPN4}$	15.08	13.11	13.31
15a′	σ_{C6}	16.33	15.22	15.16
2a″	π_{C6}	16.38	15.30	15.25
14a′	σ	17.33	15.62	15.86
1a″	π	18.48	16.58	16.50

[a]On fully optimized MP2/6-311++G(d,p) geometry.

A typical PE spectrum of 5MTZ, taken at 140 °C, is shown in Fig. 9.3, section (a). Simulated spectra of 2H-5MTZ only, obtained with the P3 and OVGF B methods, are also shown for comparison. In the lower panel of Fig. 9.3 (section (d)), the VIEs calculated with the MP2 method clearly fail to predict the experimental values and

spectral pattern, specially when compared with the results from electron propagator methods.

When looking at Fig. 9.3, a striking difference is visible, regarding the simulated spectrum of 2H-5MTZ: the set of bands C, D and E appears to be correctly described, but slightly shifted to higher ionization energy values, and bands A and B (encompassing four ionizations) portray the wrong intensity relation, when compared to the experimental results. This suggests that the contribution of the 1H-tautomer is important for a correct assignment of the PE spectrum of 5MTZ. With this in mind, using the BPRs in Table 9.4, the simulated outer-valence PE spectrum of 5-methyltetrazole, containing contributions from the two tautomers, was produced (Fig. 9.4, panel (b)). The discrepancy of intensity between bands A and B is minimized by the 1H-contribution, but still persists in the simulated spectrum; this is due to differences between theoretical and experimental VIEs, regarding the most abundant tautomer (2H).

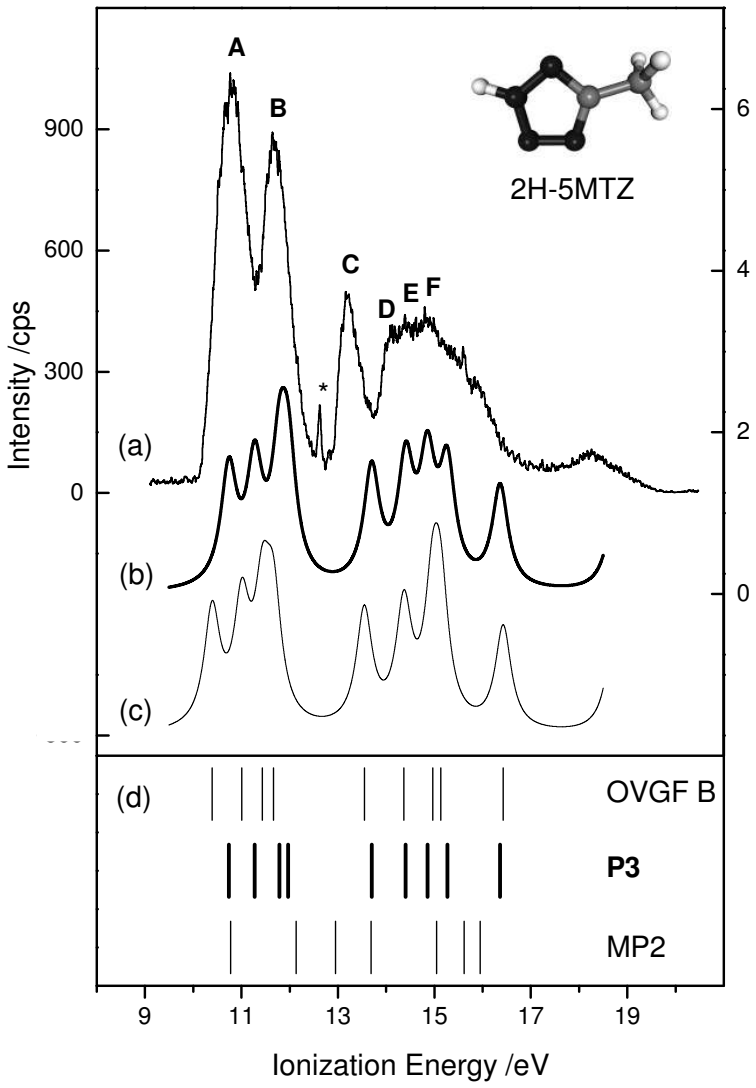

Figure 9.3: He(I) PE spectrum of 5MTZ, taken at 140 °C (a). The asterisk marks the H_2O characteristic ionization line. Simulated PE spectra of 2H-5MTZ, based on P3 (b) and OVGF B (c) results. VIEs of the 2H-5ATZ molecule, from MP2, P3 and OVGF B methods (d).

The first band appearing in the PE spectrum, band A, is centred at 10.82 eV, and results from the overlap of two peaks, related to the ionization of π orbitals 4a″

Table 9.6: Calculated vertical ionization energies (VIE, in eV) of 2H-5MTZ

		MP2	OVGF B[a]	P3[a]
MO	Character	VIE	VIE	VIE
4a″	$\pi_{N2-N3,C5-N1}$	10.78	10.39	10.74
3a″	$\pi_{N1-N2,N3-N4}$	12.14	11.01	11.27
18a′	σ_{LPN4}	12.95	11.44	11.79
17a′	$\sigma_{LPN1,LPN3}$	13.69	11.66	11.97
16a′	$\sigma_{LPN1,LPN3,LPN4}$	15.05	13.55	13.70
15a′	σ_{C6}	15.62	14.37	14.41
2a″	π_{C6}	15.95	14.96	14.86
14a′	σ	16.87	15.13	15.27
1a″	π	18.59	16.43	16.36

[a]On fully optimized MP2/6-311++G(d,p) geometry.

Table 9.7: Experimental and calculated vertical ionization energies (VIE, eV) for 5MTZ. MO stands for molecular orbital.

Band	MO	VIE	Previous[a]	Calc.[b]
A	4a″	10.82 ± 0.04	10.87	10.74
	3a″			11.27
B	18a′	11.68 ± 0.03	11.70	11.79
	17a′			11.97
C	16a′	13.19 ± 0.04		13.70
D	15a′	14.12 ± 0.04		14.41
E	2a″	14.41 ± 0.04		14.86
F	14a′	14.86 ± 0.05		15.27

[a]Ref.[299]. [b]P3 results on 2H-5MTZ.

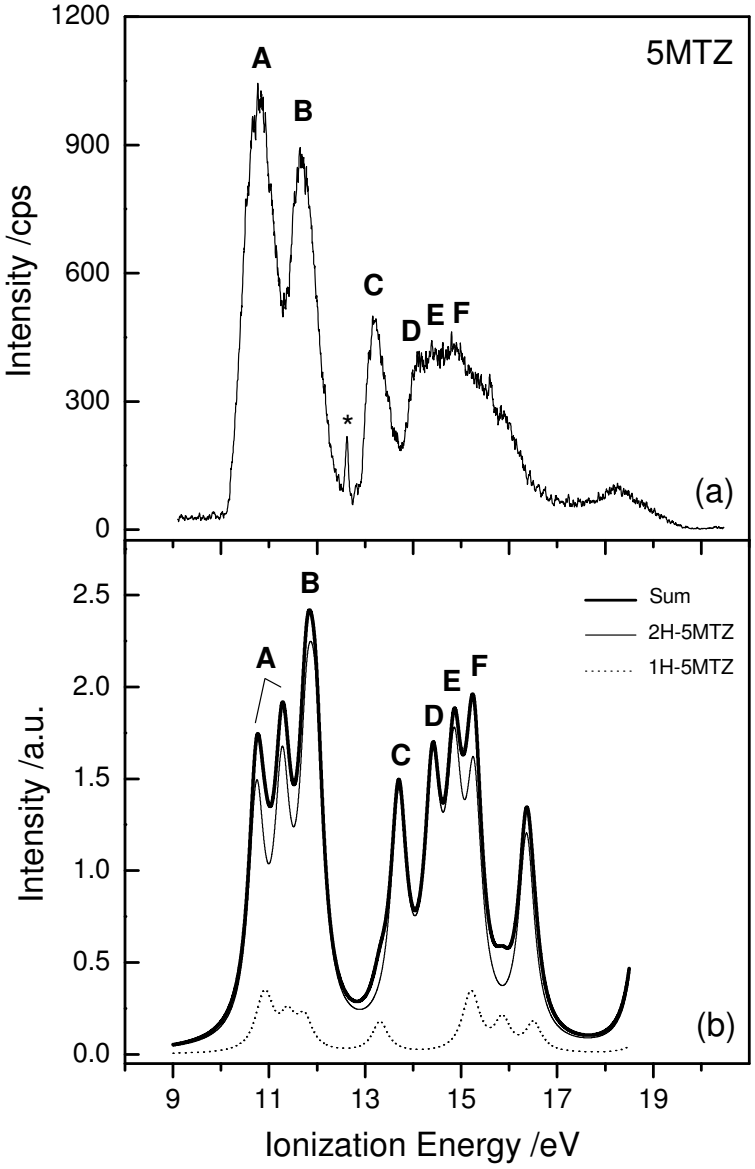

Figure 9.4: He(I) PE spectrum of 5MTZ, taken at 140 °C (a), and simulated outer-valence PE spectrum, based on P3/6-311++G(d,p) results (b). The asterisk marks the H_2O characteristic ionization line.

and 3a″. The P3 calculated VIEs yield 10.85 and 10.74 eV, for 1H- and 2H-5MTZ, respectively. These values are within ±0.08 eV of the experimental VIE, showing a very good agreement between experiment and theory.

The right hand-side of band A overlaps with band B (centred at 11.68 eV). The latter also arises from the overlap of two peaks, associated with the ionization of two σ lone pair orbitals, 18a′ and 17a′. Band C, centred at 13.19 eV, is related to the ionization of orbital 16a′, which is composed of nitrogen lone pairs, in both tautomers. The following three bands overlap: bands D and E, centred at 14.12 and 14.41 eV, respectively, can be associated with ionizations of orbitals belonging to the 2H-tautomer only (15a′ and 2a″), whereas band F (VIE = 14.86 eV) derives from the ionization of MO 14a′ of 2H-5MTZ and MO 15a′ of 1H-5MTZ.

Table 9.7 summarizes the values of the experimental VIEs of bands A-F, and the corresponding energy uncertainties, together with the predicted VIEs from P3 calculations on the 2H-5MTZ tautomer. Comparison between the experimental values and the computed VIEs on Tables 9.5 and 9.6 (considering only the first five HOMOs), leads to mean absolute differences of 1.25, 0.22 and 0.11 eV, for 1H-5MTZ, and 1.38, 0.20, and 0.30 eV, for 2H-5MTZ, from MP2, OVGF B and P3 calculations, respectively. It should be noted, however, that these values do not reflect qualitatively the adjustment of the theoretical methods (i.e. in terms of spectral band shape) to the experimental results.

9.4.4 Thermal decomposition of 5MTZ: UVPES results

The thermal decomposition studies were carried out at low (<60 °C/min) and high heating rates (ca. 500 °C/min). The first method is the one that more accurately mimics the thermal degradation of the sample, based on a succession of quasi-equilibrium thermodynamic states. On the other hand, fast heating usually leads to higher quantities of products formed from secondary reactions, in the early stages of the thermal decomposition process. Therefore, the two results are presented, although only one (at low heating rates) can be effectively rationalized in terms of our theoretical analysis.

5MTZ starts to decompose at ca. 195 °C, with the simultaneous appearance of the characteristic bands of CH_3CN (VIE = 12.21 eV[116]) and N_2 (VIE = 15.60 eV[116]). At ca. 250 °C, HCN starts to be formed, signalled by the appearance of its distinguishable peak at 13.60 eV[318]. From 250 °C to 450 °C, no changes occurred in the thermal decomposition spectra. Our evaporating system is limited by a maximum temperature of 500 °C, thus only partial decomposition was achieved: at 450 °C, the products HCN, N_2 and CH_3CN subsisted, alongside with the unchanged 5MTZ PE bands. Spectra taken at 195, 250 and 450 °C, are shown in Fig. 9.5.

The thermal decomposition of 5MTZ at high heating rates leads to the formation of the same decomposition products - HCN, N_2 and CH_3CN, but in higher quantities. Fig. 9.6 shows a typical PE spectrum, recorded shortly after heating of the sample from room temperature to ca. 195 °C, at 500 °C/min. The individual contributions of each product to the overall spectral band shape can best be seen in Fig. 9.7.

9.4.5 Thermal decomposition of 5MTZ: calculations results

In order to support the experimental evidence for the formation of acetonitrile, nitrogen and hydrogen cyanide, a thorough theoretical analysis was performed, covering almost all possible decomposition pathways for 5MTZ. The results are summarized in the potential energy diagram of Fig. 9.8, where several routes leading to the formation of the detected products are followed, starting from either 1H-5MTZ or 2H-5MTZ.

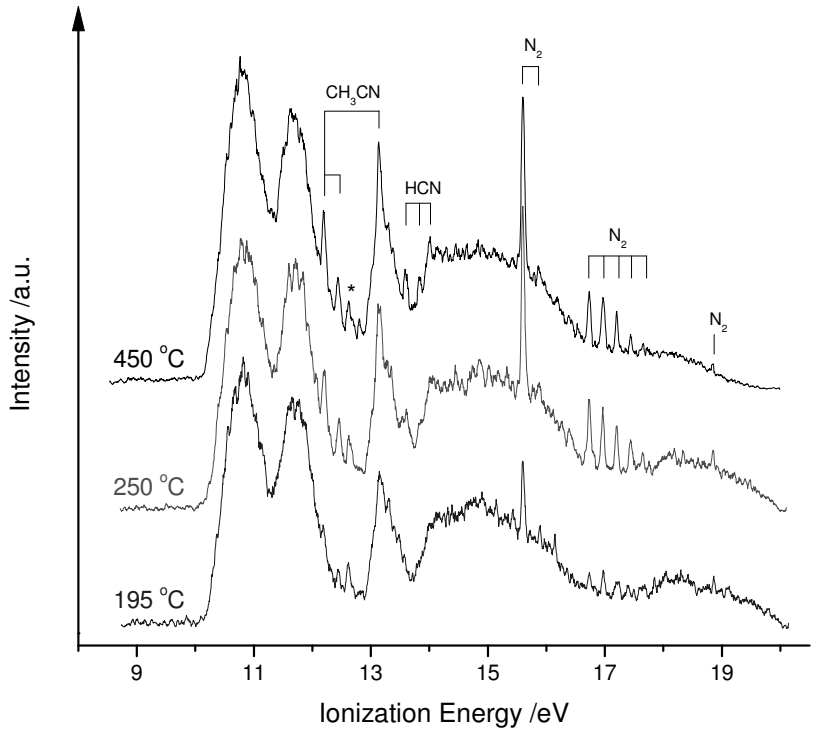

Figure 9.5: He(I) PE spectra of the thermal decomposition of 5MTZ, taken at 195, 250 and 450 °C (low heating rate). The asterisk marks the H_2O ionization line[116].

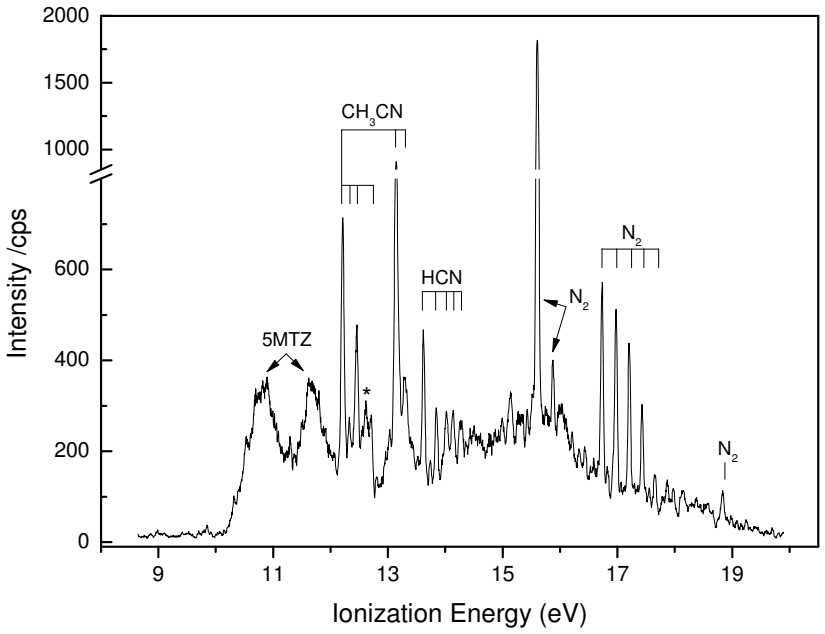

Figure 9.6: He(I) PE spectrum of the thermal decomposition of 5MTZ, taken at ca. 195 °C (high heating rate). The asterisk marks the H_2O ionization line[116].

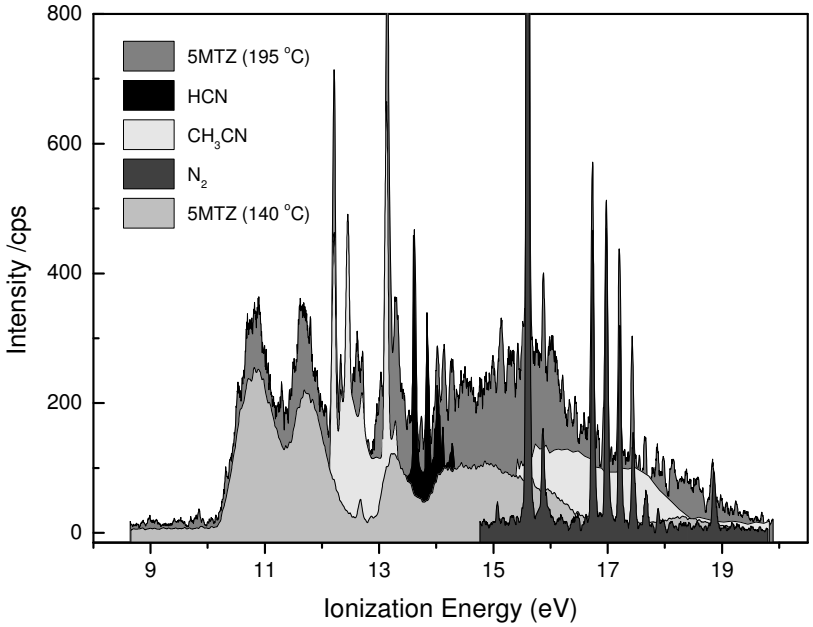

Figure 9.7: Detail of the He(I) PE spectra of the thermal decomposition (at high heating rate) of 5MTZ (grey), taken at ca. 195 °C, with estimated contributions from the decomposition products HCN (black), CH_3CN (lighter grey) and N_2 (dark grey). The contribution from 5MTZ at 140 °C is included (light grey).

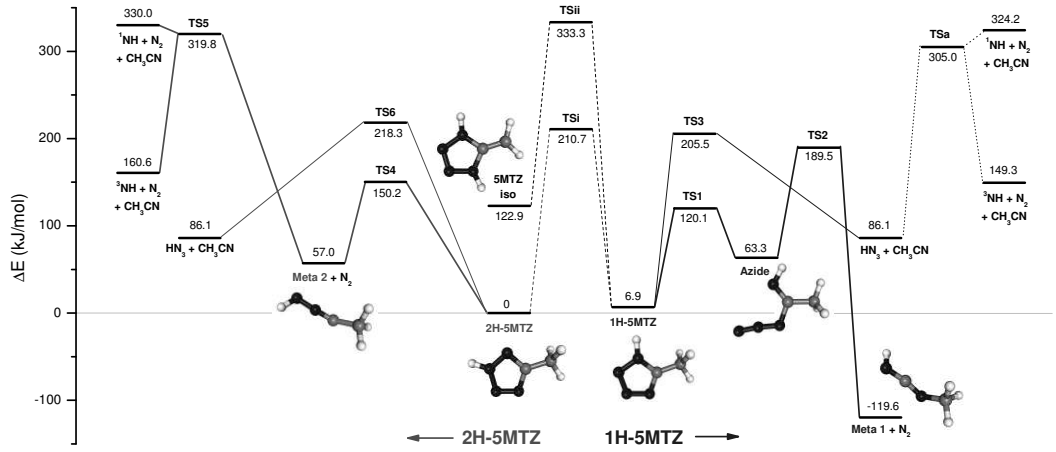

Figure 9.8: Potential energy diagram (in kJ/mol) for the thermal decomposition of 5MTZ, calculated with the G2(MP2) method. Decomposition pathways regarding the 1H-tautomer are shown at the right-hand side, whereas pathways relative to the 2H-tautomer are shown at the left-hand side. The results involving TSa and the decomposition of HN_3 are taken from the work of Besora and Harvey[319], calculated at the CCSD(T)/cc-pV∞Z level of theory. All other results are from these study.

In addition, activation barriers for tautomer interconversion between 1H-5MTZ and 2H-5MTZ and an isomer of 5MTZ are also presented (TSi and TSii).

9.4.5.1 Decomposition of the 1H-tautomer

The 1H-tautomer of 5MTZ can undergo ring opening (TS1) through a 113.2 kJ/mol barrier, and transformation into the corresponding azide (ethanecarbonimidoyl azide). Calculations using the ΔG2(MP2) procedure on the azide molecule (see Fig. 9.8, Azide), estimate a HOMO VIE of 9.87 eV. Looking into this ionization energy region in the spectrum of Fig. 9.7, one can see what almost appears as a band composed of three broad peaks, the most intense centred at 9.84 eV. We have tried to accumulate more data in this region, but the signal-to-noise ratio was simply not good enough for a detailed analysis. The fact that the azide is formed with high internal energy and that its presence in the thermal decomposition spectra is almost non-existent, leads to the conclusion that it quickly decomposes through N_2 elimination.

The N_2 elimination is followed by migration of the whole methyl group onto the electron deficient nitrogen atom, in what is known as a Type 2 mechanism[320], via a 126.2 kJ/mol energy barrier (TS2). This leads to the formation of a metastable compound (Fig. 9.8, Meta 1), HN=C=NCH_3 (termed carboximidoyl(methyl)amine). HN=C=NCH_3 has an estimated VIE of 10.30 eV, based on results from ΔG2(MP2) calculations. However, inspection of the thermal decomposition spectra of 5MTZ near this value did not reveal the presence of the compound, due perhaps to the extensive overlap from the 5MTZ bands. The overall route (azide formation plus azide decomposition), involving TS1 and TS2, can be used to explain the formation of N_2 from 1H-5MTZ, through accessible energy barriers.

From elongation and breaking of the C5-N1 and N3-N4 bonds (TS3), hydrogen azide (HN_3) and CH_3CN are formed. This fragmentation involves a barrier of 198.6 kJ/mol, which is almost twice as energetic as the barriers leading to the formation of HN=C=NCH_3 + N_2, and approximately equal to the barrier for the 1H-5MTZ → 2H-5MTZ tautomer conversion (203.8 kJ/mol).

Contrary to our study with 5ATZ[315], no clear evidence for the formation of HN_3 (VIE = 10.74 eV[309]) was found in the thermal decomposition spectra of 5MTZ. Taking into account that the temperature at which HN_3 was detected in 5ATZ (245 °C) is higher than the temperature at which CH_3CN is formed in 5MTZ thermal decomposition (195 °C), then HN_3 must be formed in a excited repulsive state, which possibly leads to its fragmentation.

The spin-forbidden thermolysis of HN_3 was recently revisited by Besora and Harvey[319] and by Knyazev and Korobeinichev[321], where the authors concluded that the spin-forbidden dissociation of HN_3 into the ^{3}NH radical plus N_2 dominates at lower energies. The theoretical results for the transition structure (TSa) and reactants relative energies (including ZPE corrections), calculated at the CCSD(T)/cc-pV∞Z level of theory[319], are also presented in Fig. 9.8, for comparison. However, the radical ^{3}NH (VIE = 13.49 eV[322]) was not detected experimentally, in our results.

9.4.5.2 Decomposition of the 2H-tautomer

The most stable tautomer, 2H-5MTZ, can also dissociate to form N_2 and an intermediate (Fig. 9.8, Meta 2): the carbene HNN-C̈-CH_3 is formed through a 150.2 kJ/mol barrier, via fragmentation of bonds N2-N3 and N4-C5 (TS4). The carbene + N_2 is energetically more stable than the azide formed from 1H-5MTZ, by approximately 7 kJ/mol. The first VIE for HNN-C̈-CH_3 was calculated at 8.65 eV (ΔG2(MP2)). In that ionization energy range, there is no risk of overlapping bands from other decomposition

products or even 5MTZ, but we found no traces of the carbene intermediate in the thermal decomposition spectra. The high reactivity of this compound, due to the unpaired electrons, probably leads to its structural rearrangement and further fragmentation.

The thermolysis of the carbene, through a spin-forbidden process, is represented in the left-hand side of Fig. 9.8. The singlet transition structure TS5 leads to the formation of CH_3CN (via an energy barrier of 262.8 kJ/mol) plus the singlet/ triplet NH radical, by elongation and breaking of the N=N bond of HNN-C̈-CH_3. Although CH_3CN is visible within the experimental results, in high quantities, the NH radical remains undetectable.

The formation of HN_3 and CH_3CN from the 2H-tautomer of 5MTZ is similar to the corresponding process in 1H-5MTZ. Breaking of two bonds in the tetrazole moiety, N1-N2 and N4-C5, leads to the formation of acetonitrile and hydrogen azide, through a 218.3 kJ/mol barrier (TS6). As stated before, the HN_3 molecule is then assumed to undergo subsequent thermolysis, decomposing into singlet/triplet NH + N_2.

9.4.5.3 Formation of HCN

Hydrogen cyanide in the thermal decomposition of 5MTZ is formed from secondary reactions. The evolution of the thermal decomposition spectra in Fig. 9.5 is clear regarding this point: the ionization lines of HCN only arise after the CH_3CN bands appear, and at a slightly higher temperature (250 °C) than the onset temperature for 5MTZ decomposition (195 °C). Thus, HCN must be formed from the thermal decomposition of either CH_3CN, the metastable compound HN=C=NCH_3 or the carbene HNN-C̈-CH_3.

The pyrolysis kinetics of CH_3CN has been studied in a stirred-flow reactor (880-960 °C) in helium[323], and in a tubular flow reactor (447-760 °C) in nitrogen[324]. In these studies, HCN and CH_4 were found as major pyrolysis products. The yield for HCN was found to increase with increasing temperature. Thus, it is possible that HCN is formed in the decomposition of 5MTZ, from the pyrolysis of CH_3CN. The lower temperature at which CH_3CN decomposes (comparing with the previous flow reactor experiments) can be regarded as a consequence of the high internal energy at which this product is initially formed.

The HN=C=NCH_3 intermediate can lead to the formation of hydrogen isocyanide and methanimine (HNC + CH_2NH, respectively), through cleavage of the C=N bond followed by a 1,2-H shift. This is depicted in the IRC calculations shown in Fig. 9.9. However, the energy barrier involved in the process is very high (464.4 kJ/mol, at the G2(MP2) level), rendering the reaction very unlikely or even impossible to occur. Furthermore, the methanimine molecule, a known intermediate resulting from azide's decomposition[32], is not present in our spectra. If actually formed, methanimine could decompose through several pathways, most of them yielding HCN (or HNC) and H_2 as final decomposition products. The theoretical study of Nguyen *et al.*[256] covers the latter subject in more detail.

At last, even though the carbene's decomposition could lead to HCN, modelling of such complex processes, most probably involving bimolecular reactions, is outside the scope of this work.

9.5 Conclusions

The electronic structure of 5-methyltetrazole was studied by UVPES and theoretical calculations. The He(I) spectrum of 5MTZ revealed six distinguishable bands in the 9-17 eV ionization energy range, and a HOMO VIE of 10.82±0.04 eV. Although it was

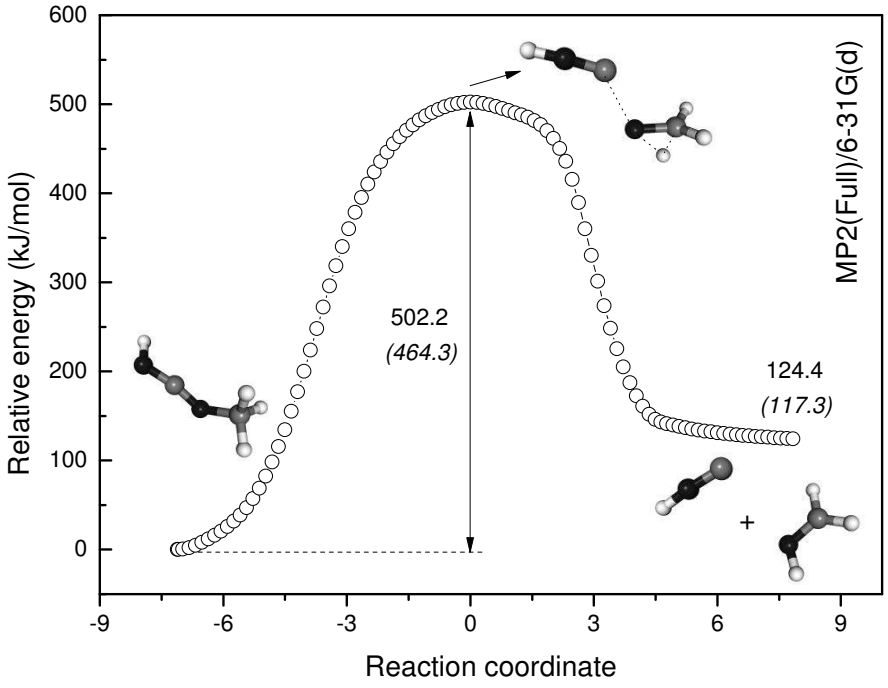

Figure 9.9: IRC calculations connecting the HN=C=NCH$_3$ (from 1H-5MTZ decomposition) and HNC plus CH$_2$CN, obtained at the MP2(Full)/6-31G(d) level of theory. The relative energies of the TS and the final dissociated products, obtained with the G2(MP2) method, are given in parentheses (kJ/mol).

found that gas-phase 5MTZ adopts mainly the 2H-tautomeric form, the UVPES results showed a noticeable contribution from the 1H-tautomer. The computational results obtained at the MP2/6-311++G(d,p) level of theory, predict a C_s symmetry structure for the 1H-form and a C_1 structure for the 2H-form. The latter is due to a slightly off-plane methyl H-atom. On the other hand, calculations with DFT B3LYP/6-311++G(d,p), predict that both tautomers belong to the C_s symmetry group. Calculated VIEs and simulated spectra based on the P3 approach showed a very good agreement with the experimental results. However, shake-up states above 15 eV can only be assigned on the basis of multi-configurational methods; this should accompany any future work on the electronic structure of tetrazoles.

The thermal decomposition of 5MTZ was also studied using UVPES. It was found that the onset of decomposition (at ca. 195 °C) was marked by the simultaneous appearance of N_2 and CH_3CN. At a latter stage of the decomposition (at ca. 250 °C), HCN was also found, most likely due to the thermolysis of CH_3CN. Results obtained at high heating rates, revealed the initial presence of N_2, CH_3CN and HCN in higher quantities, which lead to the conclusion that the thermal decomposition process of 5MTZ is strongly correlated with the heating rate.

The experimental findings were rationalized in terms of a potential energy diagram, calculated with the G2(MP2) method, regarding the several decomposition routes of 1H- and 2H-5MTZ. These results support the experimental evidence for the formation of N_2 and CH_3CN, through energy barriers below 150 and 220 kJ/mol, respectively. The direct formation of CH_3CN from the decomposition of both tautomers was found to be accompanied by the formation of HN_3. However, HN_3 compound was not found in our results, leading to the conclusion that it further decomposed into NH and N_2. Three intermediates were predicted by our calculations - an azide, a carbene and a metastable

$HN{=}C{=}NCH_3$ compound - which were not detected experimentally. The azide easily undergoes N_2 elimination and leads to the formation of the $HN{=}C{=}NCH_3$ compound. Furthermore, this compound was shown to decompose through a high barrier (ca. 460 kJ/mol), into CH_2CN and HCN. However, only HCN was found experimentally. In our opinion, future work regarding the decomposition of 5-methyltetrazole should be based on a technique which allows for molecular trapping and internal cooling of the nascent decomposition products, perhaps matrix isolation FTIR, in order to properly explore the high potential of this molecule as a radical source.

Chapter 10

Tautomerism in 5MTZ Studied by XPS and △SCF Calculations

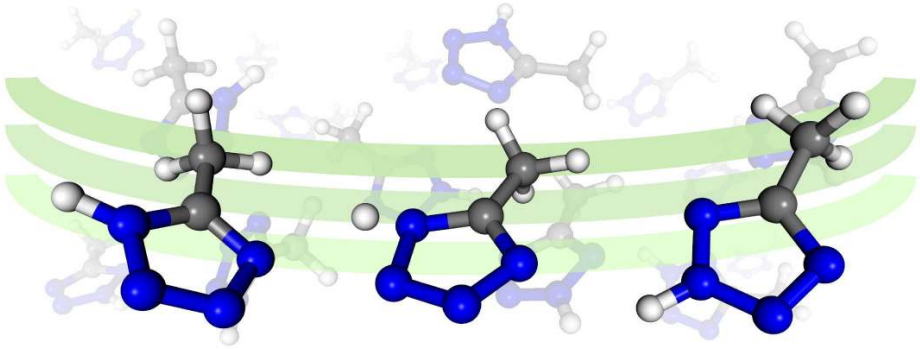

10.1 Introduction

The tautomerism of 5-substitued tetrazoles has remain an interesting subject, from the first studies with mass spectrometry and ^{15}N nuclear magnetic resonance (NMR) spectroscopy[288], almost 30 years ago, to the more recent investigations using high-level *ab initio* calculations[286,313] and matrix-isolation infrared spectroscopy[51,52].

The gas-phase tautomeric equilibria of tetrazoles is a key factor regarding the pyrolysis of these compounds: some decomposition pathways are only energetically accessible to specific tautomers[315,325], therefore the end products of any thermal degradation reaction involving tetrazoles is strongly correlated with the initial tautomeric population.

A very effective way of determining the gas-phase tautomeric population of a molecular compound with high accuracy is through high-resolution X-ray photoelectron spectroscopy (XPS), using synchrotron radiation. Recent examples are the determination of the oxo-hydroxy population ratio of 4-hydroxypyrimidine[326] and the evaluation of the tautomeric equilibria of nucleic acid bases[327–329].

In a XPS spectrum of a thermally evaporated compound, the sample is at thermal equilibrium, and the core-level photoemission intensities well above-threshold are directly proportional to the population of the corresponding chemical state. Through

[†]Reproduced with permission from *Chem. Phys. Lett.* **2011**, *516*, 149-153.

comparison with highly accurate theoretical calculations, it is possible to extract the population of the tautomers directly from the XPS data. The resulting information can also serve as a benchmark for several high-level quantum chemical methods.

In the present study, core-level photoelectron spectra of 5-methyltetrazole (5MTZ, CH_3CN_4H) were measured at the C and N 1s edges for the first time, using synchrotron radiation. The results have been further compared with accurate theoretical calculations, in order to gain information on the tautomeric equilibria of gas-phase 5MTZ.

10.2 Experimental details

The core-level photoelectron spectroscopy measurements were performed at the GAsPHase beamline of the Elettra synchrotron, in Trieste[135]. The apparatus used to obtain the spectra is described in detail elsewhere[327]. Briefly, it operates under high-vacuum conditions, and consists of a four-element electrostatic lens system, coupled to a 150 mm hemispherical electrostatic analyser equipped with six channel electron multipliers. The analyser is mounted at 54.7° with respect to the electric vector of the linearly polarized light, making the measurements insensitive to the β asymmetry parameter.

5-methyltetrazole was purchased from Sigma-Aldrich, with 97% purity, and used without any further purification. The sample was sublimated using a custom built resistively heated furnace, based on a stainless steel crucible, a Thermocoax® heating element and a type K thermocouple. The evaporation temperature for 5MTZ was ca. 313 K. The quality of the sample during the experiment was monitored by checking its valence photoelectron spectrum, taken at 99 eV photon energy, and further comparing it with the reference He(I) photoelectron spectrum of 5-methyltetrazole[325]. Calibration of the energy scale of the outer-valence spectra was achieved by admitting He (vertical ionization energy, VIE = 24.59 eV) into the ionization chamber and by traces of vaporized water (H_2O, VIE = 12.62 eV[116]) found in the system. Over the course of the whole experiment, the pressure at the ionization region remained constant and no evidence of thermal decomposition was found.

The core-level photoelectron spectra were measured with a total resolution (photon+analyser) of 0.25 and 0.35 eV at 382 (C 1s) and 495 eV (N 1s) photon energy values, respectively. The binding energy scale of the C 1s and N 1s photoelectron spectra were calibrated by admitting into the ionization chamber a small amount of CO_2 (C 1s VIE = 297.7 eV[330]) and N_2 (N 1s VIE = 409.9 eV[331]), respectively.

10.3 Computational methods

The thermochemistry data regarding the two tautomeric forms of 5MTZ were obtained using the composite Gaussian-n methods (Gn, n = 1, 2 and 3)[217,218,220] and the Complete Basis Set methods (CBS-4M and CBS-Q)[222,223], as implemented in the Gaussian 09 program package[206].

In order to calculate the core-electron binding energies (CEBEs), the delta self-consistent-field (ΔSCF) approach was used[211]. In this approximation, the energy required for removal of a core-electron is calculated as the difference in energy between the neutral and the core-ionized ground-states of the molecule. The readjustment of the electrons around the core-hole leads to a significant reduction of the binding energy. Thus, it is important to allow for relaxation of the other orbitals, maintaining the core-hole state. The relaxation energy $E_{\mathrm{relax}}(i)$ can be defined as the difference between a Koopmans' theorem binding energy, $E_{\mathrm{KT}}(i)$, and the binding energy $E_{\Delta\mathrm{SCF}}(i)$ obtained by an exact SCF approach using an Hartree-Fock total energy calculation for

both the initial and final states:

$$E_{\text{relax}}(i) = E_{\text{KT}}(i) - E_{\Delta\text{SCF}}(i). \tag{10.1}$$

Aiming to prevent the collapse of the core-hole during the SCF procedure, some constraints are usually adopted: forcing single occupancy of the core-orbital, making use of an intermediate optimization step (where the core-hole orbital is kept frozen) or restring orbital rotation.

The ΔSCF procedure, including orbital relaxation, was implemented using the Dalton program package[207]. The procedure implies an initial SCF calculation for the neutral ground-state of the molecule and several separate SCF calculations for each core-hole ground-state of the cation. In the case of the 1s ionizations of the C and N atoms of 5MTZ, six separate SCF calculations on each tautomer, plus one for the neutral ground-state are required. The computational cost for this task is therefore very high, specially if an extensive basis set analysis has to be performed.

All calculations regarding computation of the CEBEs by means of the ΔSCF approach, as well as geometry optimizations of the neutral tautomers, were performed with the Hartree-Fock (HF) method. The stationary nature of the geometries was confirmed by vibrational analysis (no imaginary frequencies). Several basis sets of increasing quality were experimented, ranging from standard 6-31G(d) to large correlation-consistent polarized triple-valence basis set (cc-pVTZ). However, for the sake of clarity, only results with Pople's 6-311++G(d,p)[200], Dunning's cc-pVTZ[202] and Ahlrichs' pVDZ[204] basis set are presented.

10.4 Results and discussion

10.4.1 Thermochemistry of 5MTZ

A set of high-accuracy quantum chemistry methods (estimated error ≤1 kcal/mol) was used to compute the relative Gibbs free energy between the 1H- and the 2H-tautomer of 5MTZ, at room temperature (298 K) and at the approximate vaporization temperature (313 K). The population of the tautomers was deemed to follow a Boltzmann distribution and the relative population of each tautomer was derived as a ratio of Boltzmann populations (BPR). The results from computations with the G1, G2 and G3 methods, together with results from the CBS-4M and CBS-Q methods, are shown in Table 10.1.

Table 10.1: Relative Gibbs free energy (kJ/mol) and Boltzmann population ratios (BPRs, %) of 1H-5MTZ and 2H-5MTZ, calculated with the Gaussian-n and Complete Basis Set methods.

	ΔG	BPR		ΔG	BPR	
	298 K	1H	2H	313 K	1H	2H
G1	7.98	3.8	96.2	7.98	4.5	95.5
G2	6.59	6.6	93.4	6.58	7.4	92.6
G3	7.15	5.4	94.7	7.14	6.0	94.0
CBS-4M	14.34	0.3	99.7	14.38	0.4	99.6
CBS-Q	9.84	1.9	98.1	9.83	2.2	97.8

All the methods yield 2H-5MTZ as the dominant tautomer. No differences above 1% exist between the BPRs calculated at 298 K and at 313 K, as expected. The results from the Gn methods are rather consistent being the lowest difference computed by the

G2 method, at 6.58 kJ/mol (313 K). This value corresponds to 5MTZ being composed of 93% of the 2H-tautomer and 7% of the 1H-tautomer. The CBS methods yield higher ΔG values, almost completely neglecting the 1H-tautomer in favor of the 2H-form: the more accurate CBS-Q method yields 97.8% of 2H-5MTZ and 2.2% of 1H-5MTZ (313 K).

10.4.2 Valence photoelectron spectrum

In order to monitor the integrity of the sample during the course of the experiment, valence photoelectron spectra were recorded and compared with our previous results obtained from conventional photoelectron spectroscopy and He(I) radiation[325]. Spectra obtained at 21.2, 40.8 and 99.0 eV photon energy values were compared with the reference spectrum taken at 21.2 eV, in our laboratory spectrometer, employing non polarized He(I) radiation from a DC discharge lamp. Fig. 10.1 presents these results. The spectra obtained with synchrotron radiation are in perfect agreement with the He(I) photoelectron spectrum of 5MTZ, revealing a first broad band centered at 10.82 eV (Fig. 10.1, band A), formed from the overlap of two peaks: $(4a'')^{-1}$ and $(3a'')^{-1}$, related to ionizations of π bonding molecular orbitals (MOs) in the tetrazole moiety.

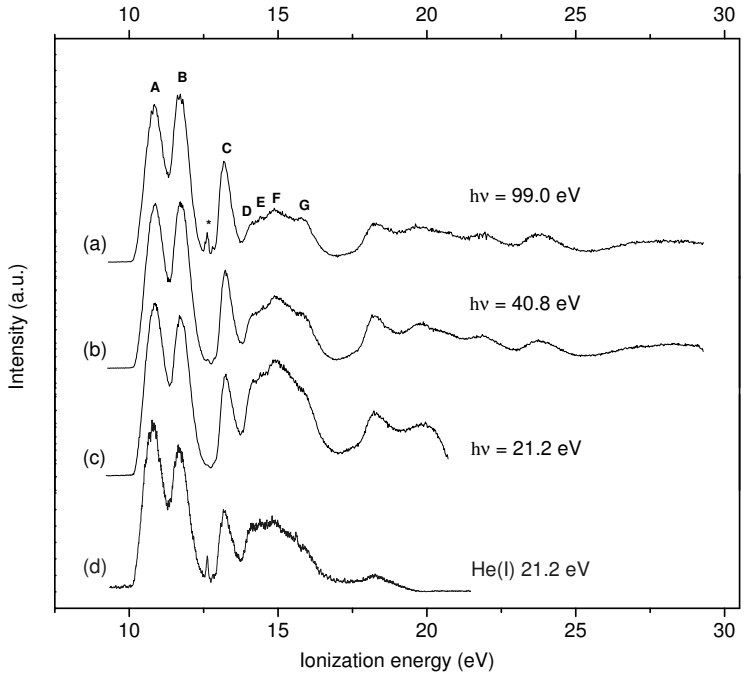

Figure 10.1: Valence photoelectron spectra of 5MTZ, recorded with synchrotron radiation at 99.0 (a), 40.8 (b) and 21.2 eV (c) photon energy values, at ca. 313 K, and reference He(I) photoelectron spectrum (d) (see Ref.[325]). The asterisk marks the ionization line of H_2O.

Even though quantitative analysis of the ionization cross-sections is outside the scope of this work, a note regarding this subject is mandatory, for the sake of clarity. The different relative intensities between the bands of the photoelectron spectra taken at distinct photon energies, are due to variations of the ionization cross-section with photon energy. This fact is readily noticeable in the relative intensity of bands A and B and between band C and the set of bands D, E, F and G: band B (lone-pair MOs) has a higher cross-section at higher photon energies, whereas bands D, E, F and G show lower cross-sections with higher photon energies, respectively. The assignment of the

main photoelectron bands in the 10-16 eV ionization energy region, together with the values of the VIEs, are summarized in Table 10.2. A complete description, including contributions from both tautomers, can be found in[325], and will not be given here.

Table 10.2: Experimental vertical ionization energies (VIE, eV) of the outer-valence ionization region (10-16 eV) of 5MTZ.

Band	MO	Character	VIE
A	4a″	$\pi_{N2-N3,C5-N1}$	10.82
	3a″	$\pi_{N1-N2,N3-N4}$	
B	18a′	σ_{LPN4}	11.68
	17a′	$\sigma_{LPN1,LPN3}$	
C	16a′	$\sigma_{LPN1,LPN3,LPN4}$	13.19
D	15a′	σ_{C6}	14.12
E	2a″	π_{C6}	14.41
F	14a′	σ	14.86
G	1a″	π	15.77

10.4.3 C 1s photoelectron spectrum

The C 1s XPS spectrum of 5MTZ recorded in gas-phase at a temperature of 313 K can be seen in Fig. 10.2 (a), together with the results from the ΔSCF calculations and different basis sets (Fig. 10.2, panels (b), (c) and (d)). Band A has its maximum at 291.35 eV, resulting from the $(1s)^{-1}$ ionization of the C6 carbon atom (-NN(C5)-**C6**-H_3), and encompasses contributions from both tautomers. The shoulder at the right-hand side is mainly due to vibrational structure from the methyl group, overlapped with a small contribution from the 1H-tautomer, ionized at the same site. Bands B (VIE = 292.65 eV) and C (VIE = 293.20 eV) are due to $(1s)^{-1}$ ionizations of the C5 carbon atom (-NN(**C5**)-C6-H_3), in the 2H and 1H tautomers, respectively. The chemical shift between bands A and B is estimated at 1.3 eV, and the tautomeric shift evaluated at bands B and C is ca. 0.55 eV.

The relative population of the tautomers can be estimated from the C 1s photoelectron spectra, by fitting the Franck-Condon envelope of band A with a Gaussian profile, and adding it to the final contribution from the 2H-tautomer. Therefore, we have fitted the C 1s XPS spectrum with five Gaussian functions, two for each tautomer, and an additional function encompassing the vibrational structure of band A. In this procedure, the mean widths and the energies were treated as free parameters.

The overall spectral pattern shows a very good agreement with the experimental results, and yields a 1H/2H tautomer population ratio of ca. 0.16/0.84. This ratio corresponds to a ΔG_{313K} of 4.32 kJ/mol, which is far from the predicted value of 6.58 kJ/mol, obtained with the G2 method. Qualitatively, the results obtained with the three basis sets fit reasonably well the experimental data. The less accurate quantitative results from both 6-311++G(d,p) and Ahlrichs-pVDZ basis sets are due to the insufficient number of functions of higher angular momentum (d and f), which would allow for extra spatial flexibility in the description of the C and N wave functions. In spite its high computational cost, the cc-pVTZ basis set yields a mean absolute deviation (MAD) of 0.22 eV, without *a posteriori* offset adjustment of the computed values.

The experimental and computed values for the CEBEs, as well as the KT and relaxation energies (regarding the values obtained with the cc-pVTZ basis set), are

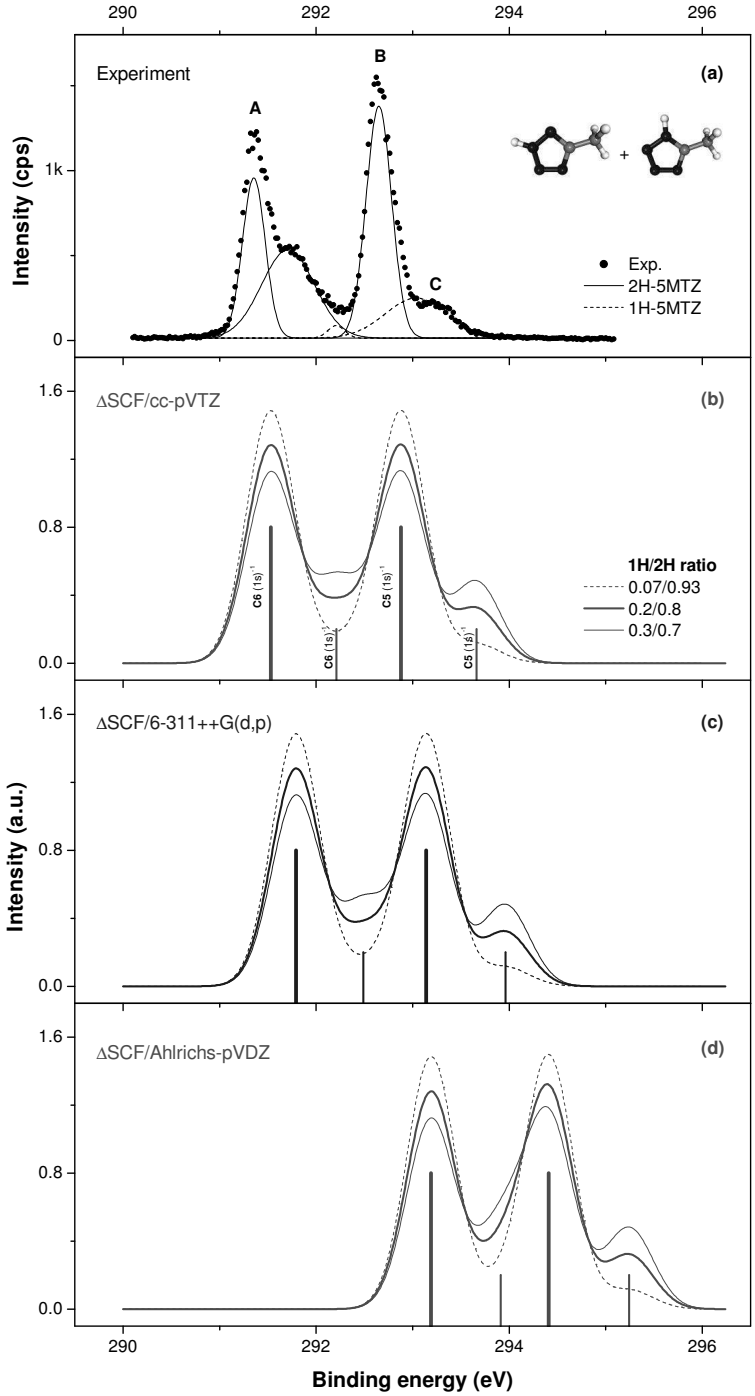

Figure 10.2: Experimental (a) and simulated C 1s photoelectron spectra of 5MTZ, based on ΔSCF calculations with cc-pVTZ (b), 6-311++G(d,p) (c) and Ahlrichs-pVDZ (d) basis sets. Simulated spectra include contributions from both tautomers and result from the convolution of the CEBEs with gaussian profiles (fwhm=0.5 eV). Simulations at different 1H/2H population ratios are also shown: 0.07/0.93 (dashed), 0.2/0.8 (thick, stick spectrum) and 0.3/0.7 (thin).

presented in the upper part of Table 10.3.

10.4.4 N 1s photoelectron spectrum

In comparison with the C 1s XPS spectrum of 5MTZ, the N 1s spectrum is more complex and difficult to analyse, due to the extensive overlap between peaks. Thus, determination of tautomer population from the N 1s spectrum can be regarded as less accurate than extraction from C 1s data. Fig. 10.3 (a) shows the N 1s XPS spectrum of 5MTZ, along with the results from different ΔSCF calculations (Fig. 10.3, panels (b), (c) and (d)). Although all the nitrogen atoms in both tautmeric forms of 5MTZ represent non-equivalent sites of ionization, the chemical shift between them is very small. Therefore, a thorough analysis and assignment can only be achieved on the basis of very accurate calculations.

Following the theoretical relative positions of the ionization lines, we fitted the experimental spectrum with eight gaussian functions, with widths and energies as free parameters. According to the obtained results, the 1H/2H area ratio is estimated as 0.21/0.79, which yields a ΔG_{313K} value of 3.45 kJ/mol, 0.87 kJ/mol below the value estimated from the C 1s XPS results.

Band A is assigned to the $(1s)^{-1}$ ionization of N4 (VIE = 406.05 eV) and overlaps with band B which results from the $(1s)^{-1}$ ionization of the N1 nitrogen (VIE = 406.45 eV), both from the 2H-tautomer. The measured chemical shift between these two nitrogens, N4 (C5–**N4**=N3) and N1 (N2–**N1**=C5), is evaluated at 0.4 eV, in good agreement with the calculated value of 0.36 eV. The contribution from the 1H-tautomer results in the broadening of band A/B. The small shoulder at the left-hand side of band A, centred at ca. 405.65 eV, originates from the $(1s)^{-1}$ ionization of the N4 nitrogen. The right-hand side broadening of band B is due to the ionization of the (1s) orbital of N3, centred at ca. 406.70 eV. The measured energy difference between the CEBEs of these two nitrogen atoms, N4 (C5=**N4**–N3) and N3 (N4–**N3**=N2), is approximately 1 eV, in contrast with the theoretical value of $\approx$ 1.5 eV.

The following broad feature, band C (VIE = 407.30 eV), is mainly due to the $(1s)^{-1}$ ionization of the N3 atom of 2H-5MTZ, although it also encompasses ionizations from the N2 and N1 atoms of the 1H-tautomer. On the basis of ΔSCF/cc-pVTZ results, the N3 and N1 $(1s)^{-1}$ ionization energies from the 2H- and 1H-tautomer, respectively, are almost degenerate. This is easily explained by looking at the neighbouring atoms at each ionization site: the N4=**N3**–N2 chain (in 2H-5MTZ) is almost equivalent to the N3=**N2**–N1 sequence (in 1H-5MTZ), in terms of the electronegativity of surrounding atoms. The difference between the corresponding CEBEs is estimated as 0.05 eV. However, this value is too low to be distinguishable in the experimental spectrum.

Finally, band D can be assigned almost exclusively to the $(1s)^{-1}$ ionization of the N2 atom of 2H-5MTZ, measured at 408.45 eV. As with the results recorded at the C 1s edge, the simulated N 1s photoelectron spectra of 5MTZ, based on ΔSCF/cc-pVTZ results, shows a very good agreement with the experimental data, both from a qualitatively and quantitatively point-of-view. The ordering of N 1s binding energies in 2H-5MTZ is N4<N1<N3<N2, whereas in 1H-5MTZ is N4<N3<N2<N1. In both tautomers, the NH fragment exhibits the highest N 1s binding energy, regarding other nitrogen atoms in the tetrazole moiety. A summary of these findings can be found in the lower part of Table 10.3.

Table 10.3: C 1s and N 1s calculated and measured CEBEs (eV) of 5MTZ. Calculated values are based on the ΔSCF approach with the cc-pVTZ (I), 6-311++G(d,p) (II) and Ahlrichs-pVDZ (III) basis set. Koopmans' theorem (KT) and relaxation energies (E_{relax}) regarding ΔSCF/cc-pVTZ are given in eV. Population ratios in %.

	Calculated								Measured		
	1H-5MTZ			2H-5MTZ							
Core level	I	II	III	I	II	III	KT	E_{relax}	VIE	Assign.	1H/2H
C 1s	293.66	293.96	295.24	292.88	293.14	294.41	307.41	-14.53	292.65	C5(B)	16/84
	292.21	292.49	293.91	291.53	291.79	293.19	305.74	-14.21	291.35	C6(A)	-
N 1s	407.28	407.54	408.86	408.61	408.89	410.30	427.13	-18.52	408.45	N2(D)	21/79
	406.98	407.22	408.54	407.69	407.96	409.30	426.11	-18.42	407.30	N3(C)	
	407.91	408.21	409.66	406.31	406.60	408.00	424.80	-18.49	406.45	N1(B)	
	405.51	405.78	407.17	405.96	406.24	407.63	424.35	-18.39	406.05	N4(A)	
	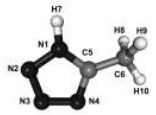			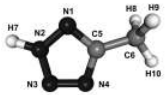							

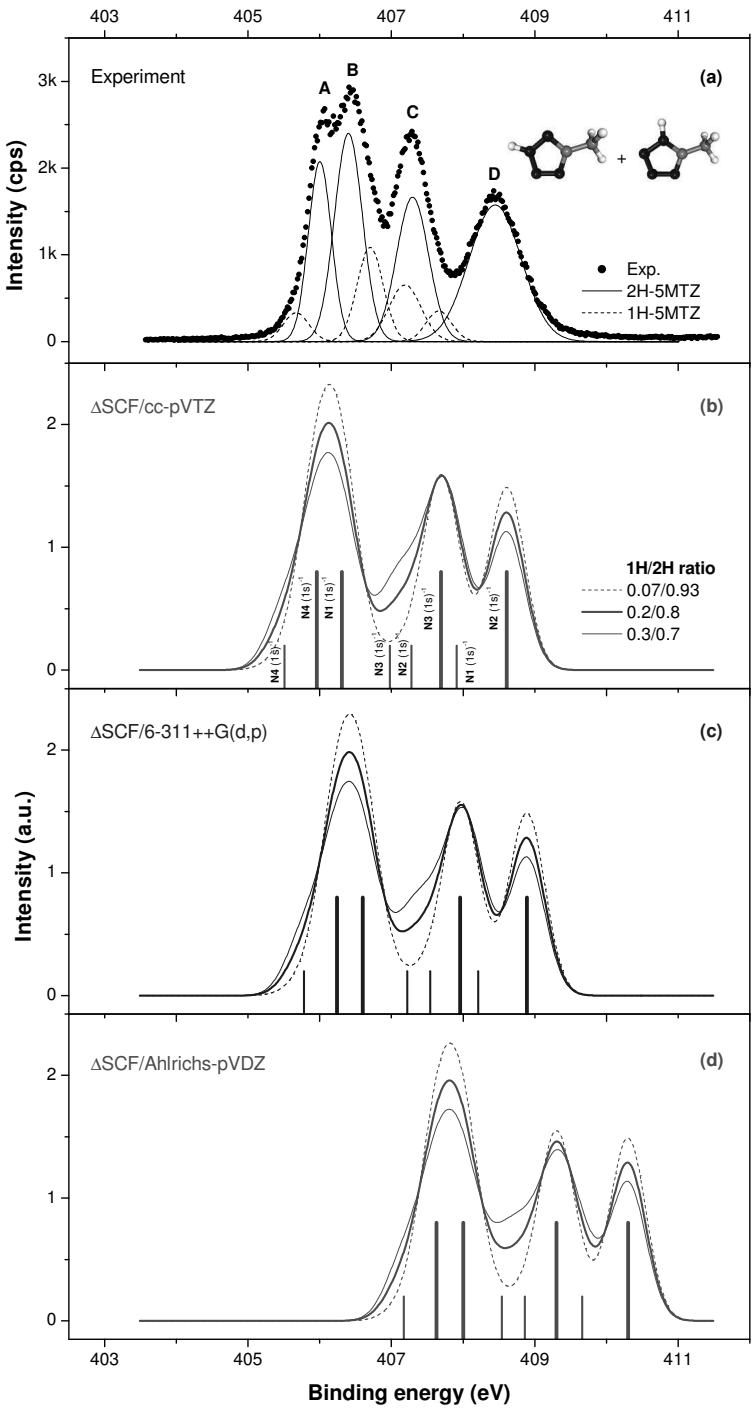

Figure 10.3: Experimental (a) and simulated N 1s photoelectron spectra of 5MTZ, based on ΔSCF calculations and cc-pVTZ (b), 6-311++G(d,p) (c) and Ahlrichs-pVDZ (d) basis sets. Simulated spectra include contributions from both tautomers and result from the convolution of the CEBEs with gaussian profiles (fwhm=0.5 eV). Simulations at different 1H/2H population ratios are also shown: 0.07/0.93 (dashed), 0.2/0.8 (thick, stick spectrum) and 0.3/0.7 (thin).

10.5 Conclusions

The gas-phase tautomeric equilibrium of 5-methyltetrazole has been estimated by high accuracy calculations and measured directly by high-resolution XPS using synchrotron radiation. Measurements at 313 K showed that the 2H-tautomer is predominant over the 1H-form, in agreement with the theoretical predictions. However, both Gn and CBS methods overestimate the energy difference, by at least 2 kJ/mol. Finally, the ΔSCF approach, together with the cc-pVTZ basis, revealed to be an excellent choice at predicting CEBEs within MADs of 0.2 eV.

Chapter 11

Tautomerism in 5ATZ Studied by XPS and △SCF Calculations

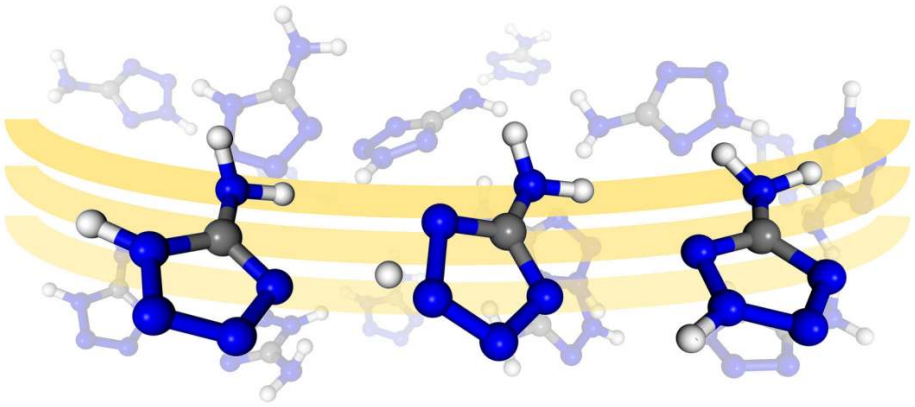

11.1 Introduction

Core-level photoelectron spectroscopy at high-resolution can be used to evaluate accurate relative populations of gas-phase molecules which exhibit tautomerism. The ability for discerning different tautomers is strongly dependent on the overall resolution of the apparatus. Thus, regarding standard synchrotron based photoelectron spectrometers, the electron energy analyser and the quality of the beam (brightness, stability and collimation properties) set the experimental detection limit for tautomeric shifts.

On the other hand, the type of tautomeric effect and the valence electronic distribution of the analysed samples can lead to large tautomeric shifts, and hence an easy detection, or to almost degenerate chemical states, which render detection very difficult. Keto-enol tautomerism can generate ca. 2 eV shifts in XPS O 1s spectra[326], whereas annular tautomerism can sometimes lead to 1.5 eV shifts in N 1s photoelectron spectra[332]. In the present study, a system exhibiting annular tautomerism – 5-aminotetrazole (5ATZ, NH_2CN_4H) – was investigated with a photoelectron spectrometer dedicated at unveiling tautomeric preferences[329,333], thus surpassing the inherent difficulty arising from experimental constraints.

[†]Reproduced with permission from *J. Electron Spectrosc. Relat. Phenom* **2012**, *185*, 13-17.

Regarding gas-phase, 5ATZ is a demanding case-study due to the fact that its thermal decomposition begins shortly above its melting point temperature – maintaining integrity of the sample during analysis is challenging[62]. It is also an interesting system: specific decomposition pathways can only be accessed through a given tautomer, therefore the decomposition end products are linked to the initial abundance of a given tautomeric form[297].

Core-level photoelectron spectra of 5ATZ were measured at the C 1s an N 1s edges for the first time, using synchrotron radiation. Assignment of the spectra is performed on the basis of accurate *ab initio* methods, and the tautomeric population is estimated and compared with results from composite methods of kcal mol^{-1} accuracy.

11.2 Experimental details

The core-level photoelectron spectroscopy measurements were performed at the GAsPHase (GAPH) beamline of the Elettra synchrotron, in Trieste[135]. The apparatus used to obtain the spectra is described in detail elsewhere[327]. Briefly, it operates under high-vacuum conditions, and consists of a four-element electrostatic lens system, coupled to a 150 mm hemispherical electrostatic analyser equipped with six channel electron multipliers. The analyser is mounted at 54.7° with respect to the electric vector of the linearly polarized light, making the measurements insensitive to the β asymmetry parameter.

5-aminotetrazole was purchased from Sigma-Aldrich, with 97% purity, and used without any further purification. The sample was sublimated using a custom built resistively heated furnace, based on a stainless steel crucible, a Thermocoax® heating element and a type K thermocouple. The evaporation temperature for 5ATZ was ca. 313 K. The quality of the sample during the experiment was monitored by checking its valence photoelectron spectrum, taken at 99 eV photon energy, and further comparing it with the reference He(I) photoelectron spectrum of 5-aminotetrazole[315]. Calibration of the energy scale of the outer-valence spectra was achieved by admitting He (vertical ionization energy, VIE = 24.59 eV) into the ionization chamber and by traces of vaporized water (H_2O, VIE = 12.62 eV[116]) found in the system. Over the course of the whole experiment, the pressure at the ionization region remained constant (ca. 3×10^{-5} Pa) and no evidence of thermal decomposition was found.

The core-level photoelectron spectra were measured with a total resolution (photon+analyser) of 0.25 and 0.35 eV at 382 (C 1s) and 495 eV (N 1s) photon energy values, respectively. The binding energy scale of the C 1s and N 1s photoelectron spectra were calibrated by admitting into the ionization chamber a small amount of CO_2 (C 1s VIE = 297.7 eV[330]) and N_2 (N 1s VIE = 409.9 eV[331]), respectively.

11.3 Computational methods

The thermochemistry data regarding the two tautomeric forms of 5ATZ were obtained using the composite Gaussian-*n* methods (G*n*, $n = 1$, 2 and 3)[217,218,220] and the Complete Basis Set methods (CBS-4M and CBS-Q)[222,223], as implemented in the Gaussian 09 program package[206].

In order to calculate the core-electron binding energies (CEBEs), the delta self-consistent-field (ΔSCF) approach was used[211]. In this approximation, the energy required for removal of a core-electron is calculated as the difference in energy between the neutral and the core-ionized ground-states of the molecule. The readjustment of the electrons around the core-hole leads to a significant reduction of the binding energy. The relaxation energy $E_{\mathrm{relax}}(i)$ can be defined as the difference between a Koopmans'

theorem binding energy, $E_{\mathrm{KT}}(i)$, and the binding energy $E_{\Delta\mathrm{SCF}}(i)$ obtained by an exact SCF approach using an Hartree-Fock total energy calculation for both the initial and final states:

$$E_{\mathrm{relax}}(i) = E_{\mathrm{KT}}(i) - E_{\Delta\mathrm{SCF}}(i). \tag{11.1}$$

The ΔSCF procedure, including orbital relaxation, was implemented using the DALTON program package[207]. The procedure implies an initial SCF calculation for the neutral ground-state of the molecule and several separate SCF calculations for each core-hole ground-state of the cation.

All calculations regarding computation of the CEBEs by means of the ΔSCF approach, as well as geometry optimizations of the neutral tautomers, were performed with the Hartree-Fock (HF) method. The stationary nature of the geometries was confirmed by vibrational analysis (no imaginary frequencies). Pople's 6-311++G(d,p)[200], Dunning's cc-pVTZ[202] and Ahlrichs' pVDZ[204] sets were chosen on the basis of our previous screening of basis sets influence on 5-aminotetrazole[332].

11.4 Results and discussion

11.4.1 Thermochemistry of 5MTZ

A set of high-accuracy quantum chemistry composite methods was used to compute the relative Gibbs free energy between the 1H- and the 2H-tautomer of 5ATZ, at room temperature (298 K) and at the experimental vaporization temperature (365 K). The population of the tautomers was deemed to follow a Boltzmann distribution and the relative population of each tautomer was derived as a ratio of Boltzmann populations (BPR). Results from computations with the G1, G2 and G3 methods, together with results from the CBS-4M and CBS-Q methods, are shown in Table 11.1.

Table 11.1: Relative Gibbs free energy (kJ/mol) and Boltzmann population ratios (BPRs, %) of 1H-5ATZ and 2H-5ATZ, calculated with the GAUSSIAN-n and Complete Basis Set methods.

	ΔG	BPR		ΔG	BPR	
	298 K	1H	2H	365 K	1H	2H
G1	12.32	0.7	99.3	12.17	1.2	98.2
G2	11.15	1.1	98.9	11.00	2.6	97.4
G3	11.51	1.0	99.0	11.37	2.3	97.7
CBS-4M	18.98	0	100.0	18.93	0.2	99.8
CBS-Q	12.86	0.6	99.4	12.72	1.5	98.5

All methods favour the 2H-form over 1H-5ATZ, in agreement with computational results from other authors. As expected, BPRs computed at vaporization temperature are only ca. 1.5% higher than the ones obtained at room temperature. Given the inherent uncertainty of the composite methods (ca. 4 kJ mol^{-1}), these values can only be regarded as gross estimates for the tautomers relative populations.

The lowest energy difference is computed as 11.0 kJ mol^{-1}, with the G2 procedure, and corresponds to an almost non-existent 1H-form rated at 2.6%. G1 and G3 methods give slightly higher differences, but within 1 kJ range of the G2 result. CBS-4M largely overestimates this difference, evaluating it at 18.93 kJ mol^{-1}, due to insufficient size of the basis sets used in the composite procedure. On the other hand, CBS-Q yields 12.72 kJ mol^{-1} between tautomers, favouring 2H-5ATZ in the same proportion as the Gn methods.

11.4.2 Valence photoelectron spectrum

In order to monitor the integrity of the sample during the course of the experiment, valence photoelectron spectra were recorded and compared with our previous results obtained from conventional photoelectron spectroscopy and He(I) radiation[315]. Spectra obtained at 21.2, 40.8 and 99.0 eV photon energy values were compared with the reference spectrum taken at 21.2 eV, in our laboratory spectrometer, employing non-polarized He(I) radiation from a DC discharge lamp. Fig. 11.1 presents these results. The VIEs for the main bands are shown in Tab. 11.2 and allow for correct identification of the compound.

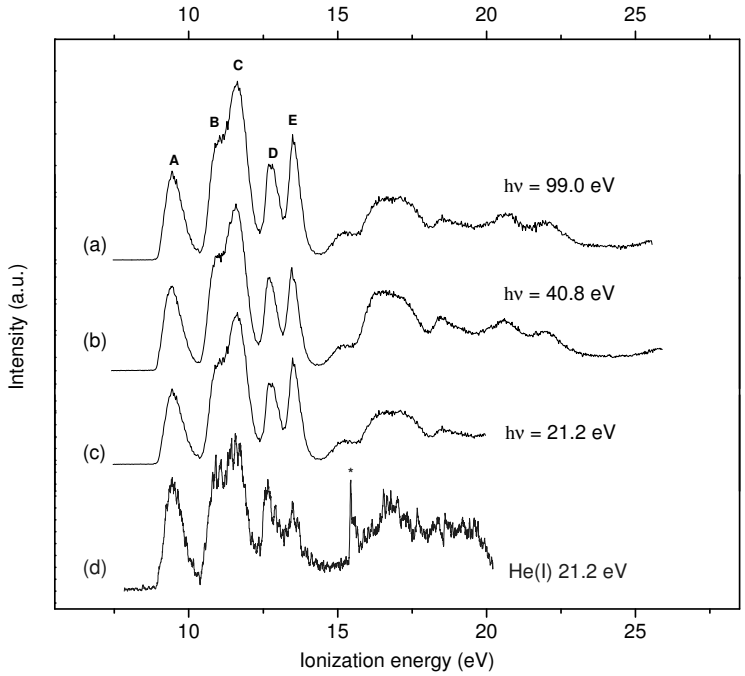

Figure 11.1: Valence photoelectron spectra of 5ATZ, recorded with synchrotron radiation at 99.0 (a), 40.8 (b) and 21.2 eV (c) photon energy values, at ca. 313 K, and reference He(I) photoelectron spectrum (d) (see Ref.[315]). The asterisk marks the ionization line due to a controlled N_2 leak.

Table 11.2: Experimental vertical ionization energies (VIE, eV) in the outer-valence ionization region (10-16 eV) of 5ATZ.

Band	MO	Character	VIE
A	22a	$\pi_{N4-C5,N2-N3}$	9.44
B	21a	$\pi_{N1-N2,N3-N4}$	10.85
C	20a	σ_{LPN4}	11.57
	19a	$\sigma_{LPN1,LPN3}$	
D	18a	π_{C5-N6}	12.66
E	17a	$\sigma_{LPN1,LPN3,LPN4}$	13.58

11.4.3 C 1s photoelectron spectrum

The C 1s XPS spectrum of gas-phase 5ATZ recorded at ca. 365 K is presented in Fig. 11.2a, together with the results from ΔSCF calculations with different basis sets (Fig. 11.2, panels a, b and c). The main peak (band A) is centred at 293.60 eV and is due to the $(1s)^{-1}$ ionization of the C5 carbon atom of the 2H-tautomer (N-**C5**(N)-N). The overlapping contribution (band B) at the right hand side of band A is due to the $(1s)^{-1}$ ionization of the C5 atom in the 1H-tautomer, and is centred at ca. 294.15 eV. The tautomeric shift between bands A and B is estimated at 0.55 eV, which is equal to the tautomeric shift evaluated at the same ionization site for 5-methyltetrazole (5MTZ), using the same technique and apparatus[332].

Although the contribution from the 1H-tautomer is very low, the relative population of the tautomers can be extracted from the C 1s photoelectron spectrum, by fitting two Gaussian functions to bands A and B. In this procedure, the mean widths and energies were treated as free parameters.

Peak A was adjusted to a single Gaussian function, and its mild asymmetric profile was accounted for by the shift of band B Gaussian function towards low binding energies. This represents a compromise between deconvolution accuracy and physical meaning of the fitting procedure: an additional Gaussian function to correct the slightly asymmetric profile of band A could only be justified if vibrational structure was present. Therefore, the reported CEBE for band B, based on the outcome of Gaussian peak fitting, is 293.85 eV, 0.25 eV below the effective centre deduced directly from the experimental spectrum. Therefore, the 1H/2H tautomeric ratio is largely overestimated: 0.29/0.7 from Gaussian peak fitting and 0.12/0.88 from the ratio of maximum height of peaks A and B. Without further discrimination of the spectra on the basis of Franck-Condon calculations, 0.12/0.88 is the most reasonable choice to follow.

The overall agreement between ΔSCF simulated spectra and the experimental data is good. However, absolute values for both tautomers CEBEs are only approximately reproduced at the ΔSCF/cc-pVTZ level of theory, with a mean absolute deviation (MAD) of 0.54 eV. MADs for results obtained with 6-311++G(d,p) and Ahlrichs-pVDZ basis sets rise to 0.85 and 2.1 eV, respectively. It is evident that the number of functions and quality of the basis set influences deeply the outcome of the calculation. In effect, the more 1s functions the basis set has after contraction, the more accurate the value for the $(1s)^{-1}$ ionization energy will be.

The experimental and computed CEBEs, together with the KT and relaxation energies (the latter two from results with the cc-pVTZ basis set only), can be consulted in the upper part of Table 11.3.

11.4.4 N 1s photoelectron spectrum

The N 1s XPS spectrum is over-crowded, when compared with the C 1s data. Due to the extensive overlap between peaks and the very low relative population of the 1H-tautomer, it is almost impossible to attempt any extraction of tautomeric ratios without assuming a disproportional uncertainty. Therefore, only 2H-5ATZ will be taken into account in the peak fitting procedure of the experimental spectrum.

Band A, centred at 406.15 eV, is composed of three lines which are associated with $(1s)^{-1}$ ionizations of the N4, N1 and N6 atoms of 2H-5ATZ, located at 405.90, 406.15 and 406.35 eV, respectively. N4 and N1 atoms share similar chemical environment (N3=**N4**-C and N2-**N1**=C) and their 1s states are almost degenerate, whereas 1s orbital of N6 is the one which contracts more due to charge withdrawal from neighbouring atoms (C5-**N6**(H)-H). Band B originates from a $(1s)^{-1}$ ionization of atom N3 (VIE = 407.15 eV) and band C is associated with the ionization of N2 (VIE = 408.25 eV).

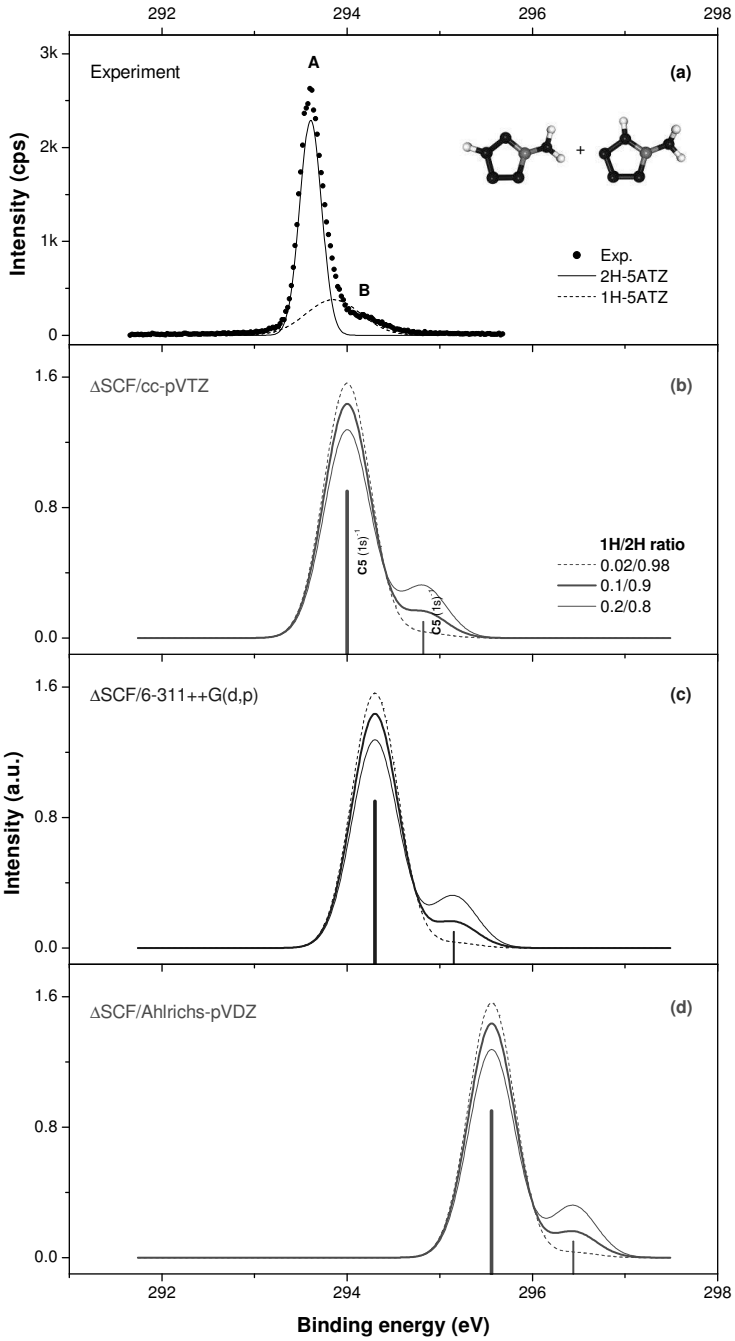

Figure 11.2: Experimental (a) and simulated C 1s photoelectron spectra of 5ATZ, based on ΔSCF calculations with cc-pVTZ (b), 6-311++G(d,p) (c) and Ahlrichs-pVDZ (d) basis sets. Simulated spectra include contributions from both tautomers and result from the convolution of the CEBEs with gaussian profiles (fwhm=0.5 eV). Simulations at different 1H/2H population ratios are also shown: 0.02/0.98 (dashed), 0.1/0.9 (thick, stick spectrum) and 0.2/0.8 (thin).

Table 11.3: C 1s and N 1s calculated and measured CEBEs (eV) of 5ATZ. Calculated values are based on the ΔSCF approach with the cc-pVTZ (I), 6-311++G(d,p) (II) and Ahlrichs-pVDZ (III) basis set. Koopmans' theorem (KT) and relaxation energies (E_{relax}) regarding ΔSCF/cc-pVTZ are given in eV. Population ratios in %.

	Calculated								Measured		
	1H-5MTZ			2H-5MTZ							
Core level	I	II	III	I	II	III	KT	E_{relax}	VIE	Assign.	1H/2H
C 1s	294.82	295.15	296.44	294.00	294.30	295.56	309.08	-15.08	293.60	C5(A)	29/71
									294.15	C5(B)	
N 1s	407.22	407.48	408.70	408.52	408.82	410.16	427.00	-18.48	408.25	N2(C)	-
	407.17	407.40	408.65	407.76	408.06	409.35	426.21	-18.45	407.15	N3(B)	
	406.91	407.18	408.63	406.17	406.41	407.82	423.84	-17.67	406.35	N6(A)	
	407.80	408.13	409.51	405.94	406.24	407.55	424.44	-18.50	406.15	N1(A)	
	405.51	405.57	406.88	405.81	406.11	407.43	424.21	-18.40	405.90	N4(A)	
	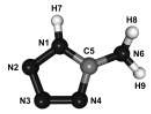										

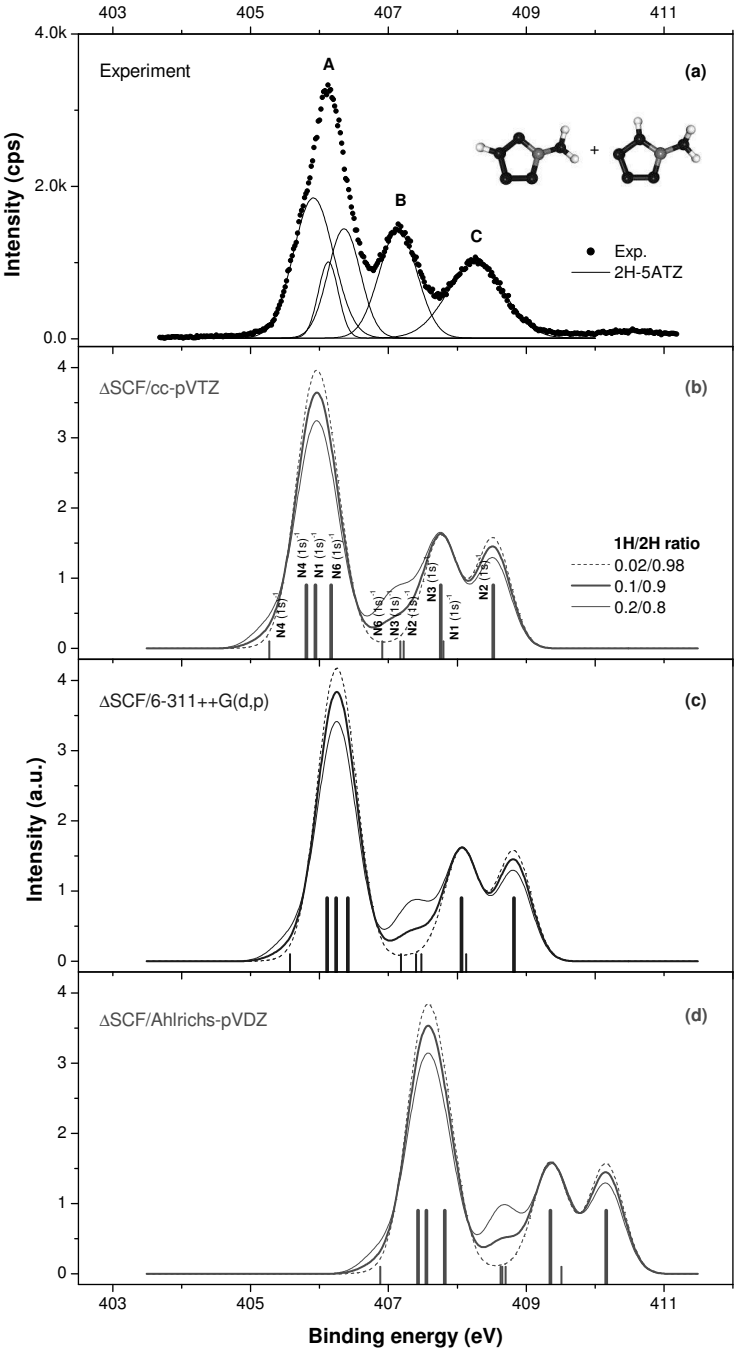

Figure 11.3: Experimental (a) and simulated N 1s photoelectron spectra of 5ATZ, based on ΔSCF calculations and cc-pVTZ (b), 6-311++G(d,p) (c) and Ahlrichs-pVDZ (d) basis sets. Simulated spectra include contributions from both tautomers and result from the convolution of the CEBEs with gaussian profiles (fwhm=0.5 eV). Simulations at different 1H/2H population ratios are also shown: 0.02/0.98 (dashed), 0.1/0.9 (thick, stick spectrum) and 0.2/0.8 (thin).

Contribution from 1H-5ATZ is not noticeable in the spectrum, but its spectral sequence from ΔSCF/cc-pVTZ results can be described as follows. The lowest CEBE appears at the left-hand side of band A, at 405.51 eV and it is associated with the $(1s)^{-1}$ ionization of the N4 nitrogen atom. Three lines are grouped between bands A and B, which relate to $(1s)^{-1}$ ionizations of the N6, N3 and N2 atoms, at 406.91, 407.17 and 407.22 eV, respectively. The last line is computed at 407.80 eV and regards ionization of the 1s orbital of nitrogen atom N1.

The ordering of N 1s binding energies, from ΔSCF results, is N4<N1<N6<N3<N2, for 2H-5ATZ, and N4<N6<N3<N2<N1, for 1H-5ATZ. In both tautomers, the 1s electrons of N4 require the least amount of energy to be ejected, whereas the NH fragment of the tetrazole moiety (N1 in 1H-, and N2 in 2H-) exhibits the highest N 1s binding energy.

Although the results obtained with the ΔSCF procedure agree reasonably well with the experimental values, with MADs of 0.27, 0.39 and 1.7 eV for cc-pVTZ, 6-311++G(d,p) and Ahlrichs-pVDZ, respectively, the simulated spectral pattern is not flawless. The line arising from the $(1s)^{-1}$ ionization of the N3 atom is shifted towards higher binding energies in all levels of theory. The same shift was registered in the XPS spectrum of 5MTZ[332], at the same ionization site. If this shift is due to large π electron delocalization[43] upon core-electron removal, then inclusion of valence correlation energy, by means of MP2 computations within the equivalent-core approach (also termed Z+1 approach)[334,335], can correct it.

The lower part of Table 11.3 shows the experimental and computed CEBEs, together with the KT and relaxation energies (the latter based on cc-pVTZ results only).

11.5 Conclusions

The gas-phase tautomeric equilibrium of 5-aminotetrazole has been investigated by high-accuracy *ab initio* methods and directly estimated from XPS data using synchrotron radiation. Spectra obtained at 365 K revealed almost exclusive predominance of 2H-5ATZ over the 1H-tautomer, in agreement with the G*n* and CBS composite methods. Gross peak height analysis of the XPS C 1s spectrum of 5ATZ indicates a 1H/2H tautomeric ratio of ca. 0.12/0.88, overestimating the BPRs predicted theoretically. The ΔSCF/cc-pVTZ approach estimates CEBEs with high-accuracy, within MADs of 0.3 and 0.5 eV, for N $(1s)^{-1}$ and C $(1s)^{-1}$ ionizations.

Chapter 12

Conclusions and Future Work

Analysis of the electronic structure and gas-phase thermal decomposition of nitrogen containing molecules of biological and industrial interest was successfully accomplished. The accumulated information will benefit future researchers who seek fundamental information on azides and tetrazoles, their gas-phase thermal decomposition, electronic structure and other molecular properties. Knowledge regarding the thermal stability and mechanisms behind the high-energy release and N_2 gas generation could be useful in new applications in the automotive industry, in pyrotechnics, in the research of new compounds for pharmaceutical use and in general organic synthesis.

Using different experimental techniques and computational methods, the following tasks on the nitrogen containing molecules under study – M2AP, BA, 2-MBA, 3-MBA, 4-MBA, 5ATZ and 5MTZ – were successfully completed:

- Characterization of the valence electronic structure.
- Characterization of the core electronic structure (tetrazoles only).
- Analysis of the gas-phase thermal decomposition.
- Identification of the final products of decomposition.
- Introduction of reaction schemes accounting for the detected products.
- Assessment of previously established mechanisms for the azido compounds.
- Evaluation of the 1H/2H gas-phase tautomeric equilibrium in the tetrazoles.

The intermediate species involved in the decomposition process of the molecules under study can be relevant for industrial/pharmaceutical applications: 5-oxazolidone (from M2AP decomposition) has significant antibacterial properties; N-methyleneaniline (from BA) is used as intermediate in dyes and rubber synthesis; cyanamide (from 5ATZ) can be applied as fertilizer.

From the experimental point-of-view, important objectives were reached, concerning the existing photoelectron spectrometer:

- Construction of a new sample introduction system, easier to assemble and clean.
- Construction of a new furnace system capable of achieving higher temperatures of pyrolysis (ca. 1000 K).
- Construction of an oven for vaporizing solid organic samples (to 800 K).
- Construction and design of a controllable power supply unit and software for driving the furnace/oven system.

Alongside with the scientific discoveries (see Table 12.1) and engineering creations, additional achievements should be emphasized. A classical spectroscopic technique was extended beyond its typical window of application, and used for real-time monitoring of

Table 12.1: Selected results obtained in the study of nitrogen containing molecules of biological and industrial interest. Experimental VIEs are in eV, and calculated activation energies (E_a) and reaction enthalpies ($\Delta_r H$) for exothermic N_2 elimination are in kJ/mol. Onset temperatures are expressed in °C.

	Electronic structure		Thermal decomposition[a,b]			
	HOMO	VIE	Onset	Main products	E_a	$\Delta_r H^{\phi}$
M2AP	$\pi^*_{N_3}$	9.60	400	CH_3OH, CH_3CN, N_2	161	-225
BA	$\pi_{C_6H_6}$	9.28	340	HCN, N_2, N-aniline	*c*)	*c*)
2-MBA	$\pi_{C_6H_6}$	9.03	200	HCN, N_2, isoindoline	*c*)	*c*)
3-MBA	$\pi_{C_6H_6}$	9.02	250	HCN, N_2, ring products	*c*)	*c*)
4-MBA	$\pi_{C_6H_6}$	8.89	300	HCN, N_2, ring products	*c*)	*c*)
5ATZ	π_{CN_4}	9.44	205	NH_2CN, HN_3, HCN, N_2	190	-22
5MTZ	π_{CN_4}	10.82	195	CH_3CN, HCN, N_2	190	-120

[a] E_a and $\Delta_r H$ on the azides are for a Type 1 mechanism (G3 results).
[b] E_a and $\Delta_r H$ on the tetrazoles are for N_2 elimination from the azide intermediate (G2(MP2) results.)
[c] To be evaluated in future computational work.

a thermodynamic process. A sturdy computational methodology for studying thermal decompositions was applied routinely, leading consistently to good results. Furthermore, synergy between UVPES and other important spectroscopic techniques, namely, matrix-isolation IR and EIMS, was demonstrated. Finally, the experimental and theoretical knowledge within the research group was renewed and extended.

On the overall, experimental and theoretical foundations for studying nitrogen containing molecules in the gas-phase were laid out, based mainly on the photoelectron spectroscopy technique and properly chosen computational methods. In the future, this framework can take advantage of both more sophisticated computational methods and experimental upgrades.

Calculation of rate constants associated with some decomposition pathways, from RRKM theory, could be helpful for other researchers performing thermogravimetry experiments on azides or tetrazoles. Regarding the design of potential energy diagrams for thermal decomposition processes, inclusion of computational methods (CASSCF, RASSCF) accounting for the multi-configuration character of some transition structures would lead to more reliable values for the activation energies. In terms of simulating the valence structure spectral patterns, inclusion of higher-order terms in the expansion of the self-energy matrix i.e. use of ADC4 or P4 methods, would definitely lead to better results, specially in the inner-valence region.

Experimentally, our standard He(I) photoelectron spectrometer would benefit from a radiation source capable of scavenging the inner-valence region, using radiation of higher energy e.g. from a He(II) optimized source. Inclusion of a quadrupole-based residual gas analyser would merit the overall experiment with the absolute evidence for the formation of some thermal decomposition products. Moreover, if the ion source from that analyser was removed, direct detection of photo-ions would allow for the implementation of the PIMS (photoionisation mass spectrometry) technique, as complementary technique to UVPES.

In all, there is a lot of work which can improve the current state of the experiment, and the quality of the information extracted from it.

Bibliography

[1] Patai, S. *The Chemistry of the Azido Group*; Interscience Publishers: New York, 1971.

[2] Bräse, S.; Banert, K. *Organic Azides: Syntheses and Applications*; John Wiley and Sons: Cambridge, 2010.

[3] Benson, F. R. *Chem. Rev.* **1947**, *41*, 1–61.

[4] Koldobskii, G. I.; Ostrovskii, V. A. *Russ. Chem. Rev.* **1994**, *63*, 797.

[5] Wittenberger, S. J. *Org. Prep. Proced. Int.* **1994**, *26*, 499–531.

[6] Turner, D. W.; Baker, C.; Baker, A. D.; Brundle, C. R. *Molecular photoelectron spectroscopy: a handbook of He 584 Å spectra*; John Wiley and Sons: New York, 1970.

[7] Grieß, P. *Liebigs Ann. Chem* **1865**, *135*, 121–121.

[8] Curtius, T. *Ber. Dtsch. Chem. Ges.* **1890**, *23*, 3023–3033.

[9] Sutton, L. E. *Nature* **1931**, *128*, 639.

[10] Schmidt, K. F. *Ber. Dtsch. Chem. Ges.* **1924**, *57*, 704–706.

[11] Scriven, E. F. V.; Turnbull, K. *Chem. Rev.* **1988**, *88*, 297–368.

[12] L'Abbe, G. *Chem. Rev.* **1969**, *69*, 345–363.

[13] Bräse, S.; Gil, C.; Knepper, K.; Zimmermann, V. *Angew. Chem. Int. Ed.* **2005**, *44*, 5188–5240.

[14] Kolb, H. C.; Finn, M. G.; Sharpless, K. B. *Angew. Chem. Int. Ed.* **2001**, *40*, 2004–2021.

[15] Rostovtsev, V.; Green, L.; Fokin, V.; Sharpless, K. *Angew. Chem. Int. Ed.* **2002**, *41*, 2596.

[16] Himo, F.; Lovell, T.; Hilgraf, R.; Rostovtsev, V. V.; Noodleman, L.; Sharpless, K. B.; Fokin, V. V. *J. Am. Chem. Soc.* **2005**, *127*, 210–216.

[17] Reiser, A.; Bowes, G.; Horne, R. J. *Trans. Faraday Soc.* **1966**, *62*, 3162–3169.

[18] Reiser, A.; Wagner, H. M.; Marley, R.; Bowes, G. *Trans. Faraday Soc.* **1967**, *63*, 2403–2410.

[19] Reiser, A.; Marley, R. *Trans. Faraday Soc.* **1968**, *64*, 1806–1815.

[20] Reiser, A.; Willets, F. W.; Terry, G. C.; Williams, V.; Marley, R. *Trans. Faraday Soc.* **1968**, *64*, 3265–3275.

[21] Smolinsky, G. *J. Org. Chem.* **1962**, *27*, 3557–3559.

[22] Bock, H.; Dammel, R.; Aygen, S. *J. Am. Chem. Soc.* **1983**, *105*, 7681–7685.

[23] Bock, H.; Dammel, R. *Angew. Chem. Int. Ed.* **1987**, *26*, 504–526.

[24] Bock, H.; Dammel, R. *J. Am. Chem. Soc.* **1988**, *110*, 5261–5269.

[25] Costa, M. L.; Ferreira, M. A. A. *J. Mol. Struct.* **1988**, *175*, 417 – 422.

[26] Costa, M. L.; Cabral, B. J. C.; Ferreira, M. A. A. *J. Mol. Struct.* **1990**, *220*, 315 – 319.

[27] Costa, M. L.; Cabral, B. J. C.; Ferreira, M. A. A. *J. Mol. Struct.* **1991**, *249*, 181 – 188.

[28] Whittle, E.; Dows, D. A.; Pimentel, G. C. *J. Chem. Phys.* **1954**, *22*, 1943–1943.

[29] Dyke, J. M.; Groves, A. P.; Morris, A.; Ogden, J. S.; Dias, A. A.; Oliveira, A. M. S.; Costa, M. L.; Barros, M. T.; Cabral, M. H.; Moutinho, A. M. C. *J. Am. Chem. Soc.* **1997**, *119*, 6883–6887.

[30] Dyke, J. M.; Groves, A. P.; Morris, A.; Ogden, J. S.; Catarino, M. I.; Dias, A. A.; Oliveira, A. M. S.; Costa, M. L.; Barros, M. T.; Cabral, M. H.; Moutinho, A. M. C. *J. Phys. Chem. A* **1999**, *103*, 8239–8245.

[31] Hooper, N.; Beeching, L. J.; Dyke, J. M.; Morris, A.; Ogden, J. S.; Dias, A. A.; Costa, M. L.; Barros, M. T.; Cabral, M. H.; Moutinho, A. M. C. *J. Phys. Chem. A* **2002**, *106*, 9968–9975.

[32] Dyke, J. M.; Levita, G.; Morris, A.; Ogden, J. S.; Dias, A. A.; Algarra, M.; Santos, J. P.; Costa, M. L.; Rodrigues, P.; Barros, M. T. *J. Phys. Chem. A* **2004**, *108*, 5299–5307.

[33] Dyke, J. M.; Levita, G.; Morris, A.; Ogden, J. S.; Dias, A. A.; Algarra, M.; Santos, J. P.; Costa, M. L.; Rodrigues, P.; Andrade, M. M.; Barros, M. T. *Chem. Eur. J.* **2005**, *11*, 1665–1676.

[34] Oliveira, A. M.; Barros, M. T.; Martins, A. M.; Cabral, M. A. R.; Dias, A. A.; Costa, M. L.; Cabral, M. H.; Moutinho, A. M. C.; Jennings, K. R. *Rapid Commun. Mass Spectrom.* **1999**, *13*, 559–561.

[35] Duarte, M. F.; Martins, F.; Fernandez, M. T.; Langley, G. J.; Rodrigues, P.; Barros, M. T.; Costa, M. L. *Rapid Commun. Mass Spectrom.* **2003**, *17*, 957–962.

[36] Barros, M.; Beyer, M.; Costa, M.; Duarte, M.; Fernandez, M.; Martins, F.; Rodrigues, P.; Watts, P. *Int. J. Mass Spec.* **2004**, *237*, 65 – 73.

[37] O'Keeffe, P.; Scotti, G.; Stranges, D.; Rodrigues, P.; Barros, M. T.; Costa, M. L. *J. Phys. Chem. A* **2008**, *112*, 3086–3093.

[38] Bladin, J. A. *Ber.* **1885**, *18*, 1544–1551.

[39] Bladin, J. A. *Ber.* **1892**, *25*, 1411–1413.

[40] Thiele, J. *Ann.* **1892**, *270*, 1–63.

[41] Dimroth, O.; Merzbacher, S. *Ber.* **1910**, *43*, 2899–2904.

[42] Mihina, J. S.; Herbst, R. M. *J. Org. Chem.* **1950**, *15*, 1082–1092.

[43] Raczyńska, E. D.; Kosińska, W.; Ośmialowski, B.; Gawinecki, R. *Chem. Rev.* **2005**, *105*, 3561–3612.

[44] Krygowski, T. M.; Cyrański, M. K. *Chem. Rev.* **2001**, *101*, 1385–1420.

[45] Katritzky, A.; Ramsden, C.; Joule, J.; Zhdankin, V. *Handbook of Heterocyclic Chemistry*; Elsevier, 2010.

[46] Joule, J.; Mills, K. *Heterocyclic Chemistry*; John Wiley & Sons, 2010.

[47] Koldobskii, G. I.; Ostrovskii, V. A.; Gidaspov, B. V. *Chem. Heteroc. Comp.* **1980**, *16*, 665–674.

[48] Gaponik, P. N.; Voitekhovich, S. V.; Ivashkevich, O. A. *Russ. Chem. Rev.* **2006**, *75*, 507.

[49] Demko, Z. P.; Sharpless, K. B. *J. Org. Chem.* **2001**, *66*, 7945–7950.

[50] Maier, G.; Eckwert, J.; Bothur, A.; Reisenauer, H. P.; Schmidt, C. *Liebigs Ann. Chem.* **1996**, *1996*, 1041–1053.

[51] Bugalho, S.; Maçôas, E.; Cristiano, M.; Fausto, R. *Phys. Chem. Chem. Phys.* **2001**, *3*, 3541–3547.

[52] Bugalho, S.; Serra, A.; Lapinski, L.; Cristiano, M.; Fausto, R. *Phys. Chem. Chem. Phys.* **2002**, *4*, 1725–1731.

[53] Bugalho, S.; Lapinski, L.; Cristiano, M.; Frija, L.; Fausto, R. *Vib. Spectrosc.* **2002**, *30*, 213–225.

[54] Frija, L. M. T.; Ismael, A.; Cristiano, M. L. S. *Molecules* **2010**, *15*, 3757–3774.

[55] Cradock, S.; Findlay, R. H.; Palmer, M. H. *Tetrahedron* **1973**, *29*, 2173 – 2181.

[56] Palmer, M. H.; Simpson, I.; Wheeler, J. R. *Z. Naturforsch. A* **1981**, *36*, 1246.

[57] Palmer, M. H.; Beveridge, A. J. *Chem. Phys.* **1987**, *111*, 249 – 261.

[58] Guimon, C.; Khayar, S.; Gracian, F.; Begtrup, M.; Pfister-Guillouzo, G. *Chem. Phys.* **1989**, *138*, 157 – 171.

[59] Lesnikovich, A.; Ivashkevich, O.; Lyutsko, V.; Printsev, G.; Kovalenko, K.; Gaponik, P.; Levchik, S. *Thermochim. Acta* **1989**, *145*, 195 – 202.

[60] Vyazovkin, S.; Lesnikovich, A.; Lyutsko, V. *Thermoch. Acta* **1990**, *165*, 17 – 22.

[61] Lesnikovich, A.; Ivashkevich, O.; Printsev, G.; Gaponik, P.; Levchik, S. *Thermochim. Acta* **1990**, *171*, 207 – 213.

[62] Lesnikovich, A. I.; Ivashkevich, O. A.; Levchik, S. V.; Balabanovich, A. I.; Gaponik, P. N.; Kulak, A. A. *Thermochim. Acta* **2002**, *388*, 233 – 251.

[63] Lesnikovich, A.; Levchik, S.; Balabanovich, A.; Ivashkevich, O.; Gaponik, P. *Thermochim. Acta* **1992**, *200*, 427 – 441.

[64] Prokudin, V. G.; Poplavsky, V. S.; Ostrovskii, V. A. *Russ. Chem. Bull.* **1996**, *45*, 2101–2104.

[65] Razynska, A.; Tempczyk, A.; Malinski, E.; Szafranek, J.; Grzonka, Z.; Hermann, P. *J. Chem. Soc., Perkin Trans. 2* **1983**, 379–383.

[66] Trifonov, R.; Ostrovskii, V. *Russ. J. Org. Chem.* **2006**, *42*, 1585–1605.

[67] Chen, F.-F.; Wang., F. *Molecules* **2009**, *14*, 2656–2668.

[68] Prescher, J. A.; Dube, D. H.; Bertozzi, C. R. *Nature* **2004**, *430*, 873–877.

[69] Li, Q. S.; Duan, H. X. *J. Phys. Chem. A* **2005**, *109*, 9089–9094.

[70] Meijer, E. W.; Nijhuis, S.; Vroonhoven, F. C. B. M. V. *J. Am. Chem. Soc.* **1988**, *110*, 7209–7210.

[71] Betterton, E. A. *Crit. Rev. Environ. Sci. Tech.* **2003**, *33*, 423–458.

[72] Herr, R. J. *Bioorg. Med. Chem.* **2002**, *10*, 3379 – 3393.

[73] Myznikov, L.; Hrabalek, A.; Koldobskii, G. *Chem. Heteroc. Comp.* **2007**, *43*, 1–9.

[74] Li, J.; Ren, T.; Liu, H.; Wang, D.; Liu, W. *Wear* **2000**, *246*, 130.

[75] Lee, J.-W.; Kang, M.-C.; Kim, J. J. *J. Electrochem. Soc.* **2005**, *152*, C827–C831.

[76] Steinhauser, G.; Klapötke, T. M. *Angew. Chem. Int. Ed.* **2008**, *47*, 3330–3347.

[77] Turner, D. W.; Al-Joboury, M. I. *J. Chem. Phys.* **1962**, *37*, 3007–3008.

[78] Muller-Dethlefs, K.; Schlag, E. W. *Ann. Rev. Phys. Chem.* **1991**, *42*, 109–136.

[79] Ellis, A. M.; Feher, M.; Wright, T. G. *Electronic and photoelectron spectroscopy: fundamentals and case studies*; Cambridge University Press: Cambridge, 2005.

[80] Duncan, M. A. *Int. J. Mass Spectrom.* **2000**, *200*, 545 – 569.

[81] Jonathan, N.; Morris, A.; Okuda, M.; Smith, D.; Ross, K. *Chem. Phys. Lett.* **1972**, *13*, 334 – 336.

[82] Dyke, J. M. *J. Chem. Soc., Faraday Trans. 2* **1987**, *83*, 69–87.

[83] Baker, J.; Barnes, M.; Cockett, M.; Dyke, J.; Ellis, A.; Fehr, M.; Lee, E.; Morris, A.; Zamanpour, H. *J. Electron Spectrosc. Relat. Phenom.* **1990**, *51*, 487 – 511.

[84] West, J. B.; Dyke, J. M.; Morris, A.; Wright, T. G.; Gamblin, S. D. *J. Phys. B* **1999**, *32*, 2763.

[85] Lenard, P. *Ann. Phys.* **1894**, *287*, 225–267.

[86] Einstein, A. *Ann. Phys.* **1905**, *322*, 132–148.

[87] Rabalais, J. W. *Principles of Ultraviolet Photoelectron Spectroscopy*; John Wiley and Sons: New York, 1977.

[88] Morse, P. M. *Phys. Rev.* **1929**, *34*, 57–64.

[89] Franck, J.; Dymond, E. G. *Trans. Faraday Soc.* **1926**, *21*, 536–542.

[90] Condon, E. *Phys. Rev.* **1926**, *28*, 1182–1201.

[91] IUPAC Compendium of Chemical Terminology – The Gold Book. 2009; http://goldbook.iupac.org/.

[92] Birge, R. T. *Phys. Rev.* **1926**, *28*, 1157–1181.

[93] Schönhense, G.; Heinzmann, U. *J. Phys. E* **1983**, *16*, 74.

[94] Ross, K. J.; Sonntag, B. *Rev. Sci. Instrum.* **1995**, *66*, 4409–4433.

[95] Purcell, E. M. *Phys. Rev.* **1938**, *54*, 818–826.

[96] Kuyatt, C. E.; Simpson, J. A. *Rev. Sci. Instrum.* **1967**, *38*, 103–111.

[97] Roy, D.; Tremblay, D. *Rep. Prog. Phys.* **1990**, *53*, 1621.

[98] Dogan, M.; Sise, O.; Ulu, M. *Rad. Phys. Chem.* **2007**, *76*, 445 – 449.

[99] Morris, A.; Jonathan, N.; Dyke, J. M.; Francis, P. D.; Keddar, N.; Mills, J. D. *Rev. Sci. Instrum.* **1984**, *55*, 172–181.

[100] Baltzer, P.; Wannberg, B.; Göethe, M. C. *Rev. Sci. Instrum.* **1991**, *62*, 643–654.

[101] Baltzer, P.; Karlsson, L.; Lundqvist, M.; Wannberg, B. *Rev. Sci. Instrum.* **1993**, *64*, 2179–2189.

[102] Dyke, J. M.; Gamblin, S. D.; Morris, A.; Wright, T. G.; Wright, A. E.; West, J. B. *J. Electron Spectrosc. Relat. Phenom.* **1998**, *97*, 5 – 14.

[103] Ralchenko, Y.; Kramida, A. E.; Reader, J.; NIST ASD Team, NIST Atomic Spectra Database (version 4.0). 2011; http://physics.nist.gov/asd, National Institute of Standards and Technology, Gaithersburg, MD.

[104] Samson, J. A. R. *Rev. Sci. Instrum.* **1969**, *40*, 1174–1177.

[105] Chambers, A. *Modern vacuum physics*; Masters series in physics and astronomy; Chapman & Hall/CRC, 2005.

[106] Clausing, P. *J. Vac. Sci. Technol.* **1971**, *8*, 636–646.

[107] Berman, A. S. *J. Appl. Phys.* **1965**, *36*, 3356–3356.

[108] Cole, R. J. *Progr. Astronaut. Aero.* **1977**, *51*, 261–272.

[109] DeSerio, R. *Rev. Sci. Instrum.* **1989**, *60*, 381–388.

[110] Browne, C. P.; Craig, D. S.; Williamson, R. M. *Rev. Sci. Instrum.* **1951**, *22*, 952–965.

[111] Barber, N. F. *Proc. Leeds Phil. Soc.* **1933**, *2*, 427.

[112] Zouros, T. J. M.; Benis, E. P. *J. Electron Spectrosc. Relat. Phenom.* **2002**, *125*, 221 – 248.

[113] Benis, E. P.; Zouros, T. J. M. *J. Electron Spectrosc. Relat. Phenom.* **2008**, *163*, 28 – 39.

[114] Sise, O.; Ulu, M.; Dogan, M.; Martinez, G.; Zouros, T. J. *J. Electron Spectrosc. Relat. Phenom.* **2010**, *177*, 42 – 51.

[115] Cristo, P. M. PSAS - Sistema de Aquisição para um Espectrómetro de Fotoelectrões. M.Sc. thesis, FCT-UNL, 2007.

[116] Kimura, K. *Handbook of HeI photoelectron spectra of fundamental organic molecules*; Halsted Press: Tokyo, 1981.

[117] Dyke, J. M.; Shaw, A. M.; Wright, T. G. *J. Phys. Chem.* **1994**, *98*, 6327–6331.

[118] Carnovale, F.; Peel, J. B.; Rothwell, R. G. *J. Chem. Phys.* **1991**, *95*, 1473–1478.

[119] Rademann, K.; Rech, T.; Kaiser, B.; Even, U.; Hensel, F. *Rev. Sci. Instrum.* **1991**, *62*, 1932–1941.

[120] Wang, D.; Li, C.; Qian, X.; Gamblin, S. D. *J. Electron Spectrosc. Relat. Phenom.* **1998**, *97*, 59 – 61.

[121] Butcher, V.; Costa, M.; Dyke, J.; Ellis, A.; Morris, A. *Chem. Phys.* **1987**, *115*, 261–267.

[122] Dyke, J.; Jonathan, N.; Lewis, A.; Morris, A. *Mol. Phys.* **1982**, *47*, 1231–1240.

[123] Dias, A. A. Fotoionização de Átomos e Moléculas. Ph.D. thesis, FCT-UNL, 2005.

[124] Elmer – a finite element multi-physics package. 2008; CSC – IT Center for Science, see http://www.csc.fi/english/pages/elmer.

[125] Geuzaine, C.; Remacle, J.-F. *Int. J. Numer. Meth. Eng.* **2009**, *79*, 1309–1331.

[126] Bulgin, D.; Dyke, J.; Goodfellow, F.; Jonathan, N.; Lee, E.; Morris, A. *J. Electron Spectrosc. Relat. Phenom.* **1977**, *12*, 67 – 76.

[127] Morris, A.; Dyke, J. M.; Josland, G. D.; Hastings, M. P.; Francis, P. D. *High Temp. Sci.* **1986**, *22*, 95 – 113.

[128] Siegbahn, K.; Nordling, C.; Johansson, G.; Hedman, J.; Hedé, P. F.; Hamrin, K.; Gelius, U.; Bergmark, T.; Werme, L. O.; Manne, R.; Baer, Y. *ESCA Applied to Free Molecules*; Elsevier: New York, 1969.

[129] Siegbahn, K.; Nordling, C.; Fahlman, A.; Nordberg, R.; Hamrin, K.; Hedman, J.; Johansson, G.; Bergmark, T.; Karlsson, S.-E.; Lindgren, I.; Lindberg, B. *ESCA - Atomic, Molecular and Solid State Structure Studied by Means of Electron Spectroscopy*; Elsevier: London, 1967.

[130] Briggs, D. *Handbook of X-Ray and Ultraviolet Photoelectron Spectroscopy*; Heyden and Son: London, 1978.

[131] Margaritondo, G. *Elements of synchrotron light: for biology, chemistry, and medical research*; Oxford University Press, 2002.

[132] Wiedemann, H. *Synchrotron radiation*; Advanced Texts in Physics; Springer, 2003.

[133] Samson, J. A.; Ederer, D. L. *Vacuum Ultraviolet Spectroscopy II*; Elsevier: London, 1999.

[134] Prince, K. C.; Blyth, R. R.; Delaunay, R.; Zitnik, M.; Krempasky, J.; Slezak, J.; Camilloni, R.; Avaldi, L.; Coreno, M.; Stefani, G.; Furlani, C.; de Simone, M.; Stranges, S. *J. Synchrotron Rad.* **1998**, *5*, 565–568.

[135] Blyth, R. et al. *J. Electron Spectrosc. Relat. Phenom.* **1999**, *101-103*, 959 – 964.

[136] Hoffmann, E.; Stroobant, V. *Mass spectrometry: principles and applications*; Wiley, 2001.

[137] Gross, J. *Mass Spectrometry: A Textbook*; Springer, 2011.

[138] Sparkman, O. *Mass spectrometry desk reference*; Global View Pub., 2000.

[139] Nier, A. O. *Rev. Sci. Instrum.* **1940**, *11*, 212–216.

[140] Nier, A. O. *Rev. Sci. Instrum.* **1947**, *18*, 398–411.

[141] Perutz, R. N. *Chem. Rev.* **1985**, *85*, 77–96.

[142] Perutz, R. N. *Chem. Rev.* **1985**, *85*, 97–127.

[143] Barnes, A. *J. Mol. Struct.* **1984**, *113*, 161 – 174.

[144] Andrews, L.; Moskovits, M. *Chemistry and Physics of Matrix-Isolated Species*; Elsevier, 1989.

[145] Fausto, R. *Low temperature molecular spectroscopy*; NATO ASI series: Mathematical and physical sciences; Kluwer Academic Publishers, 1996.

[146] Dunkin, I. *Matrix-isolation techniques: a practical approach*; The practical approach in chemistry series; Oxford University Press, 1998.

[147] Atkins, P.; Friedman, R. *Molecular quantum mechanics*; Oxford University Press, 1997.

[148] Jensen, F. *Introduction to computational chemistry*; John Wiley & Sons, 2007.

[149] Atkins, P.; Paula, J.; Walters, V. *Physical Chemistry*; W H Freeman & Co, 2006.

[150] Szabó, A.; Ostlund, N. *Modern quantum chemistry: introduction to advanced electronic structure theory*; Dover Publications, 1996.

[151] Schrödinger, E. *Phys. Rev.* **1926**, *28*, 1049–1070.

[152] Born, M.; Oppenheimer, R. *Ann. Phys.* **1927**, *389*, 457–484.

[153] Born, M.; Fock, V. *Z. Phys. A* **1928**, *51*, 165–180.

[154] Yarkony, D. R. *Rev. Mod. Phys.* **1996**, *68*, 985–1013.

[155] Worth, G. A.; Cederbaum, L. S. *Ann. Rev. Phys. Chem.* **2004**, *55*, 127–158.

[156] Baer, M. *Beyond Born-Oppenheimer: conical intersections and electronic nonadiabatic coupling terms*; Wiley, 2006.

[157] Greiner, W. *Quantum mechanics: an introduction*; Theoretical physics; Springer, 2001.

[158] Becke, A. D.; Dickson, R. M. *J. Chem. Phys.* **1990**, *92*, 3610–3612.

[159] Laaksonen, L.; Pyykka, P.; Sundholm, D. *Comp. Phys. Rep.* **1986**, *4*, 313 – 344.

[160] Roothaan, C. C. J. *Rev. Mod. Phys.* **1951**, *23*, 69–89.

[161] Hall, G. G. *Proc. Roy. Soc. London. A* **1951**, *205*, 541–552.

[162] Pople, J. A.; Nesbet, R. K. *J. Chem. Phys.* **1954**, *22*, 571–572.

[163] Pulay, P. *J. Comp. Chem.* **1982**, *3*, 556–560.

[164] Bacskay, G. B. *Chem. Phys.* **1981**, *61*, 385 – 404.

[165] Schlegel, H.; McDouall, J. In *Computational Advances in Organic Chemistry: Molecular Structure and Reactivity*; Ogretir, C., Csizmadia, I., Lang, E., Eds.; Nato Advanced Science Institutes Series, Series C, Mathematical and Physical Sciences; 1991; Vol. 330; pp 167–185, Nato Advanced Study Inst on Computational Advances in Organic Chemistry: Molecular Structure and Reactivity, Altinoluk, Turkey, Jul 31-Aug 12, 1989.

[166] Koopmans, T. *Physica* **1934**, *1*, 104 – 113.

[167] Veszprémi, T.; Fehér, M. *Quantum chemistry: fundamentals to applications*; Kluwer Academic/Plenum, 1999.

[168] Slater, J. C. *Phys. Rev.* **1929**, *34*, 1293–1322.

[169] Slater, J. C. *Phys. Rev.* **1931**, *38*, 1109–1144.

[170] Pople, J. A.; Head-Gordon, M.; Raghavachari, K. *J. Chem. Phys.* **1987**, *87*, 5968–5975.

[171] Sherrill, C. D.; III, H. F. S. In *The Configuration Interaction Method: Advances in Highly Correlated Approaches*; Per-Olov Löwdin, M. C. Z., John R. Sabin, Brändas, E., Eds.; Advances in Quantum Chemistry; Academic Press, 1999; Vol. 34; pp 143 – 269.

[172] Møller, C.; Plesset, M. S. *Phys. Rev.* **1934**, *46*, 618–622.

[173] Schrödinger, E. *Annalen der Physik* **1926**, *385*, 437–490.

[174] Raghavachari, K.; Trucks, G. W.; Pople, J. A.; Head-Gordon, M. *Chem. Phys. Lett.* **1989**, *157*, 479 – 483.

[175] Cederbaum, L. S. *J. Phys. B* **1975**, *8*, 290.

[176] von Niessen, W.; Schirmer, J.; Cederbaum, L. *Comp. Phys. Rep.* **1984**, *1*, 57 – 125.

[177] Ortiz, J. V. *J. Chem. Phys.* **1996**, *104*, 7599–7605.

[178] Linderberg, J.; Öhrn, Y. *Propagators in quantum chemistry*; Wiley-Interscience, 2004.

[179] Danovich, D. *Wiley Interdisciplinary Reviews: Computational Molecular Science* **2011**, *1*, 377–387.

[180] Dyson, F. J. *Phys. Rev.* **1949**, *75*, 1736–1755.

[181] Zakrzewski, V. G.; Ortiz, J. V.; Nichols, J. A.; Heryadi, D.; Yeager, D. L.; Golab, J. T. *Int. J. Quantum Chem.* **1996**, *60*, 29–36.

[182] Parr, R.; Yang, W. *Density-functional theory of atoms and molecules*; International series of monographs on chemistry; Oxford University Press, 1994.

[183] Parr, R. G.; Yang, W. *Ann. Rev. Phys. Chem.* **1995**, *46*, 701–728.

[184] Kohn, W.; Becke, A. D.; Parr, R. G. *J. Phys. Chem.* **1996**, *100*, 12974–12980.

[185] Geerlings, P.; De Proft, F.; Langenaeker, W. *Chem. Rev.* **2003**, *103*, 1793–1874.

[186] Sousa, S. F.; Fernandes, P. A.; Ramos, M. J. *J. Phys. Chem. A* **2007**, *111*, 10439–10452.

[187] Hohenberg, P.; Kohn, W. *Phys. Rev.* **1964**, *136*, B864–B871.

[188] Kohn, W.; Sham, L. J. *Phys. Rev.* **1965**, *140*, A1133–A1138.

[189] Becke, A. D. *J. Chem. Phys.* **1993**, *98*, 5648–5652.

[190] Lee, C.; Yang, W.; Parr, R. G. *Phys. Rev. B* **1988**, *37*, 785–789.

[191] Stephens, P. J.; Devlin, F. J.; Ashvar, C. S.; Chabalowski, C. F.; Frisch, M. J. *Faraday Discuss.* **1994**, *99*, 103–119.

[192] Stephens, P. J.; Devlin, F. J.; Chabalowski, C. F.; Frisch, M. J. *J. Phys. Chem.* **1994**, *98*, 11623–11627.

[193] Vosko, S. H.; Wilk, L.; Nusair, M. *Canad. J. Phys.* **1980**, *58*, 1200–1211.

[194] Becke, A. D. *Phys. Rev. A* **1988**, *38*, 3098–3100.

[195] Slater, J. C. *Phys. Rev.* **1929**, *34*, 1293–1322.

[196] Boys, S. F. *Proc. Roy. Soc. London. A* **1950**, *200*, 542–554.

[197] Hehre, W. J.; Ditchfield, R.; Pople, J. A. *J. Chem. Phys.* **1972**, *56*, 2257–2261.

[198] Hariharan, P. C.; Pople, J. A. *Theor. Chim. Acta* **1973**, *28*, 213–222.

[199] Clark, T.; Chandrasekhar, J.; Spitznagel, G. W.; Schleyer, P. V. R. *J. Comp. Chem.* **1983**, *4*, 294–301.

[200] Krishnan, R.; Binkley, J. S.; Seeger, R.; Pople, J. A. *J. Chem. Phys.* **1980**, *72*, 650–654.

[201] Gill, P. M.; Johnson, B. G.; Pople, J. A.; Frisch, M. J. *Chem. Phys. Lett.* **1992**, *197*, 499 – 505.

[202] Dunning, T. H. *J. Chem. Phys.* **1989**, *90*, 1007–1023.

[203] Kendall, R. A.; Dunning, T. H.; Harrison, R. J. *J. Chem. Phys.* **1992**, *96*, 6796–6806.

[204] Schaefer, A.; Horn, H.; Ahlrichs, R. *J. Chem. Phys.* **1992**, *97*, 2571–2577.

[205] Frisch, M. J. et al. Gaussian 03, Revision C.02. Gaussian, Inc., Wallingford, CT, 2004.

[206] Frisch, M. J. et al. Gaussian 09 Revision A.1. Gaussian Inc. Wallingford CT 2009.

[207] Angeli, C. et al. Dalton, a molecular electronic structure program, Release 2.0 (2005), see http://www.kjemi.uio.no/software/dalton/dalton.html.

[208] Simons, J. *An introduction to theoretical chemistry*; Cambridge University Press, 2003.

[209] Schlegel, H. B. *J. Comp. Chem.* **1982**, *3*, 214–218.

[210] Varetto, U. Molekel 5.4. Swiss National Supercomputing Centre: Manno (Switzerland).

[211] Bagus, P. S. *Phys. Rev.* **1965**, *139*, 619–634.

[212] Miller, W. H.; Handy, N. C.; Adams, J. E. *J. Chem. Phys.* **1980**, *72*, 99–112.

[213] Foresman, J.; Frisch, A.; Gaussian, I. *Exploring chemistry with electronic structure methods*; Gaussian, Inc., 1996.

[214] Fukui, K. *Acc. Chem. Res.* **1981**, *14*, 363–368.

[215] Hratchian, H. P.; Schlegel, H. B. *J. Chem. Theory Comput.* **2005**, *1*, 61–69.

[216] Hratchian, H. P.; Schlegel, H. B. *J. Chem. Phys.* **2004**, *120*, 9918–9924.

[217] Curtiss, L. A.; Jones, C.; Trucks, G. W.; Raghavachari, K.; Pople, J. A. *J. Chem. Phys.* **1990**, *93*, 2537–2545.

[218] Curtiss, L. A.; Raghavachari, K.; Trucks, G. W.; Pople, J. A. *J. Chem. Phys.* **1991**, *94*, 7221–7230.

[219] Curtiss, L. A.; Raghavachari, K.; Pople, J. A. *J. Chem. Phys.* **1993**, *98*, 1293–1298.

[220] Curtiss, L. A.; Raghavachari, K.; Redfern, P. C.; Rassolov, V.; Pople, J. A. *J. Chem. Phys.* **1998**, *109*, 7764–7776.

[221] Curtiss, L. A.; Redfern, P. C.; Raghavachari, K. *J. Chem. Phys.* **2007**, *126*, 084108.

[222] Montgomery, J. A.; Frisch, M. J.; Ochterski, J. W.; Petersson, G. A. *J. Chem. Phys.* **2000**, *112*, 6532–6542.

[223] Ochterski, J. W.; Petersson, G. A.; Montgomery, J. A. *J. Chem. Phys.* **1996**, *104*, 2598–2619.

[224] Nguyen, M. T.; Sengupta, D.; Ha, T.-K. *J. Phys. Chem.* **1996**, *100*, 6499–6503.

[225] Pinto, R.; Dias, A.; Costa, M. *J. Mol. Struct. (THEOCHEM)* **2009**, *894*, 80 – 87.

[226] Zaytseva, I. L.; Trofimov, A. B.; Schirmer, J.; Plekan, O.; Feyer, V.; Richter, R.; Coreno, M.; Prince, K. C. *J. Phys. Chem. A* **2009**, *113*, 15142–15149.

[227] Trofimov, A. B.; Schirmer, J.; Kobychev, V. B.; Potts, A. W.; Holland, D. M. P.; Karlsson, L. *J. Phys. B* **2006**, *39*, 305.

[228] Chrostowska, A.; Nguyen, T. X. M.; Dargelos, A.; Khayar, S.; Graciaa, A.; Guillemin, J. *J. Phys. Chem. A* **2009**, *113*, 2387–2396.

[229] Potts, A. W.; Holland, D. M. P.; Trofimov, A. B.; Schirmer, J.; Karlsson, L.; Siegbahn, K. *J. Phys. B* **2003**, *36*, 3129.

[230] Andersson, M. P.; Uvdal, P. *J. Phys. Chem. A* **2005**, *109*, 2937–2941.

[231] Nunes, Y.; Martins, G.; Mason, N. J.; Duflot, D.; Hoffmann, S. V.; Delwiche, J.; Hubin-Franskin, M.-J.; Limão Vieira, P. *Phys. Chem. Chem. Phys.* **2010**, *12*, 15734–15743.

[232] Francisco, J. S. *J. Am. Chem. Soc.* **2003**, *125*, 10475–10480.

[233] Metcalfe, W. K.; Simmie, J. M.; Curran, H. J. *J. Phys. Chem. A* **2010**, *114*, 5478–5484.

[234] Arenas, J. F.; Marcos, J. I.; López-Tocón, I.; Otero, J. C.; Soto, J. *J. Chem. Phys.* **2000**, *113*, 2282–2289.

[235] Sheppard, W. A. *J. Org. Chem.* **1962**, *27*, 3756–3759.

[236] L'vov, B. V. *Thermochimica Acta* **1997**, *291*, 179 – 185.

[237] Adam, D.; Holl, G.; Klapötke, T. M. *Heteroat. Chem.* **1999**, *10*, 548–553.

[238] Tokumoto, M.; Tanaka, Y.; Kinoshita, N.; Kinoshita, T.; Ishibashi, S.; Ihara, H. *J. Phys. Chem. Sol.* **1993**, *54*, 1667 – 1673.

[239] Jönsson, B.; Hakansson, K.; Liljas, A. *FEBS Letters* **1993**, *322*, 186 – 190.

[240] Merz, K. M.; Banci, L. *J. Phys. Chem.* **1996**, *100*, 17414–17420.

[241] Pieffet, G.; Petukhov, P. *J. Mol. Model.* **2009**, *15*, 1291–1297.

[242] Baruah, H.; Puthenveetil, S.; Choi, Y.-A.; Shah, S.; Ting, A. *Angew. Chem. Int. Ed.* **2008**, *47*, 7018–7021.

[243] Budyka, M. F.; Oshkin, I. V. *High Energy Chem.* **2005**, *39*, 216–223.

[244] Cordeiro, M. N. D. S.; Dias, A. A.; Costa, M. L.; Gomes, J. A. N. F. *J. Phys. Chem. A* **2001**, *105*, 3140–3147.

[245] Pepkin, V.; Matyushin, Y. N.; Khisamutdinov, G.; Slovetskii, V.; Fainzilberg, A. *Khim. Fiz.* **1993**, *12*, 1399–1403.

[246] Hillier, I. H.; Vincent, M. A.; Connor, J. A.; Guest, M. F.; MacDowell, A. A.; von Niessen, W. *J. Chem. Soc., Faraday Trans. 2* **1988**, *84*, 409–415.

[247] Hartree, D. R. *Proc. Cambridge Phil. Soc.* **1928**, *24*, 89–110.

[248] Fock, V. *Z. Phys. A* **1930**, *61*, 126–148.

[249] Slater, J. C. *Phys. Rev.* **1930**, *35*, 210–211.

[250] Dunning, T. H. *J. Chem. Phys.* **1971**, *55*, 716–723.

[251] Santos, J. P.; Costa, M. L.; Olariu, R. I.; Parente, F. *Eur. Phys. J. D* **2006**, *39*, 379–384.

[252] Zakrzewski, V. G.; Ortiz, J. V. *J. Phys. Chem.* **1996**, *100*, 13979–13984.

[253] Pinto, R. M.; Olariu, R. I.; Lameiras, J.; Martins, F. T.; Dias, A. A.; Langley, G. J.; Rodrigues, P.; Maycock, C. D.; Santos, J. P.; Duarte, M. F.; Fernandez, M. T.; Costa, M. L. *J. Mol. Struct.* **2010**, *980*, 163 – 171.

[254] Golas, P. L.; Tsarevsky, N. V.; Matyjaszewski, K. *Macromol. Rapid Commun.* **2008**, *29*, 1167–1171.

[255] Jones, G. O.; Houk, K. N. *J. Org. Chem.* **2008**, *73*, 1333–1342.

[256] Nguyen, D. P.; Lusic, H.; Neumann, H.; Kapadnis, P. B.; Deiters, A.; Chin, J. W. *J. Am. Chem. Soc.* **2009**, *131*, 8720–8721.

[257] Amblard, F.; Cho, J. H.; Schinazi, R. F. *Chem. Rev.* **2009**, *109*, 4207–4220.

[258] Song, Y.; Chan, J. M.; Tovian, Z.; Secrest, A.; Nagy, E.; Krysiak, K.; Bergan, K.; Parniak, M. A.; Oldfield, E. *Bioorg. Med. Chem.* **2008**, *16*, 8959 – 8967.

[259] Smith, A. B.; Safonov, I. G.; Corbett, R. M. *J. Am. Chem. Soc.* **2002**, *124*, 11102–11113.

[260] Niino, H.; Sato, T.; Yabe, A. *Appl. Phys. A: Mater. Sci. Process.* **1999**, *69*, 605–610.

[261] Fraser, R. T. M.; Paul, N. C.; Bagley, M. J. *Org. Mass Spec.* **1973**, *7*, 83–88.

[262] Martins, F.; Duarte, M. F.; Fernandez, M. T.; Langley, G. J.; Rodrigues, P.; Barros, M. T.; Costa, M. L. *Rapid Commun. Mass Spectrom.* **2004**, *18*, 363–366.

[263] Alvarez, S. G.; Alvarez, M. T. *Synthesis* **1997**, *1997*, 413–414.

[264] Gonzalez, C.; Schlegel, H. B. *J. Phys. Chem.* **1990**, *94*, 5523–5527.

[265] Bruins, A. P.; Jennings, K. R.; Evans, S. *Int. J. Mass Spectrom. Ion Processes* **1978**, *26*, 395–404.

[266] Karni, M.; Mandelbaum, A. *Org. Mass Spec.* **1980**, *15*, 53–64.

[267] Schwarz, H. *Organic Chemistry*; Topics in Current Chemistry; Springer Berlin / Heidelberg, 1978; Vol. 73; pp 231–263.

[268] Blachut, D.; Danikiewicz, W.; Olejnik, M.; Czarnocki, Z. *J. Mass Spectrom.* **2004**, *39*, 966–972.

[269] Pinto, R. M.; Dias, A. A.; Costa, M. L.; Santos, J. P. *J. Mol. Struct. (THEOCHEM)* **2010**, *948*, 15–20.

[270] Copeland, G.; Lee, E. P. F.; Dyke, J. M.; Chow, W. K.; Mok, D. K. W.; Chau, F. T. *J. Phys. Chem. A* **2010**, *114*, 1816–1825.

[271] Distefano, G.; Giumanini, A. G.; Modelli, A.; Poggi, G. *J. Chem. Soc., Perkin Trans. 2* **1985**, 1623–1627.

[272] Tian, Z.; Li, Y.; Zhang, T.; Zhu, A.; Cui, Z.; Qi, F. *Combust. Flame* **2007**, *151*, 347 – 365.

[273] T., K.; Nagakura, S. *Bull. Chem. Soc. Jpn.* **1974**, *47*, 2563–2572.

[274] Klasinc, L.; Kovac, B.; Gusten, H. *Pure Appl. Chem.* **1983**, *55*, 289–298.

[275] Maier, J. P.; Turner, D. W. *J. Chem. Soc., Faraday Trans. 2* **1973**, *69*, 521–531.

[276] D., R.; Smith, *Combust. Flame* **1979**, *35*, 179 – 190.

[277] Bally, T.; Haselbach, E.; Lanyiova, S.; Rossi, M.; Marschner, F. *Helv. Chim. Acta* **1976**, *59*, 486–498.

[278] Ostrovskii, V.; Koldobskii, G.; Trifonov, R. In *Comprehensive Heterocyclic Chemistry III*; in Chief: Alan R. Katritzky, E., Ramsden, C. A., Scriven, E. F., , Taylor, R. J., Eds.; Elsevier: Oxford, 2008; pp 257 – 423.

[279] Li, J.; Ren, T.; Liu, H.; Wang, D.; Liu, W. *Wear* **2000**, *246*, 130.

[280] Klapötke, T. M.; Sabate, C. M. *Chem. Mater.* **2008**, *20*, 3629.

[281] Klapötke, T. M.; Stierstorfer, J. *J. Am. Chem. Soc.* **2009**, *131*, 1122.

[282] Hashimoto, Y.; Ohashi, R.; Kurosawa, Y.; Minami, K.; Kaji, H.; Hayashida, K.; Narita, H.; Murata, S. *J. Cardiovasc. Pharmacol.* **1998**, *31*, 568–575.

[283] De Sarro, A.; Ammendola, D.; Zappala, M.; Grasso, S.; De Sarro, G. *Antimicrob. Agents Chemother.* **1995**, *39*, 232–237.

[284] Mazurek, A.; Sadlej-Sosnowska, N. *Chem. Phys. Lett.* **2000**, *330*, 212–218.

[285] Trifonov, R.; Alkorta, I.; Ostrovskii, V.; Elguero, J. *J. Mol. Struct.: Theochem* **2004**, *668*, 123–132.

[286] Balabin, R. M. *J. Chem. Phys.* **2009**, *131*, 154307.

[287] Elguero, J.; Marzin, C.; Roberts, J. D. *J. Org. Chem.* **1974**, *39*, 357–363.

[288] Wofford, D. S.; Forkey, D. M.; Russell, J. G. *J. Org. Chem.* **1982**, *47*, 5132–5137.

[289] Sokolova, M.; Melnikov, V.; Ostrovskii, V.; Koldobskii, G.; Melnikov, A.; Gidaspov, B. *Z. Organ. Khim.* **1975**, *11*, 1744–1749.

[290] Gómez-Zavaglia, A.; Reva, I. D.; Frija, L.; Cristiano, M. L.; Fausto, R. *J. Phys. Chem. A* **2005**, *109*, 7967–7976.

[291] Wong, M.; Leungtoung, R.; Wentrup, C. *J. Am. Chem. Soc.* **1993**, *115*, 2465–2472.

[292] Levchik, S.; Ivashkevich, O.; Balabanovich, A.; Lesnikovich, A.; Gaponik, P.; Costa, L. *Thermoch. Acta* **1992**, *207*, 115 – 130.

[293] Brill, T. B.; Ramanathan, H. *Combust. Flame* **2000**, *122*, 165–171.

[294] Paletsky, A. A.; Budachev, N. V.; Korobeinichev, O. P. *Kinet. Catal.* **2009**, *50*, 627–635.

[295] Sun, Z.; Zeng, X.-Q.; Wang, W.-G.; Ge, M.-F.; Wang, D.-X. *Acta Chim. Sinica* **2006**, *64*, 218–222.

[296] Zhang, J.; Feng, L.; Zhang, S.; Zheng, T.; Zheng, H. *J. Mol. Model.* **1992**, *14*, 403 – 408.

[297] Kiselev, V. G.; Gritsan, N. P. *J. Phys. Chem. A* **2009**, *113*, 3677–3684.

[298] Paul, K. W.; Hurley, M. M.; Irikura, K. K. *J. Phys. Chem. A* **2009**, *113*, 2483–2490.

[299] Novak, I.; Kovac, B.; Klasinc, L.; Ostrovskii, V. A. *Spectrochim. Acta A* **2003**, *59*, 1725–1731.

[300] Balabin, R. M. *J. Chem. Phys.* **2008**, *129*, 164101.

[301] Balabin, R. M. *J. Phys. Chem. A* **2010**, *114*, 3698–3702.

[302] Lendvay, G.; Mayer, I. *Chem. Phys. Lett.* **1998**, *297*, 365 – 373.

[303] Chen, Z. X.; Xiao, J. M.; Xiao, H. M.; Chiu, Y. N. *J. Phys. Chem. A* **1999**, *103*, 8062–8066.

[304] Chermahini, A. N.; Nasr-Esfahani, M.; Dalirnasab, Z.; Dabbagh, H. A.; Teimouri, A. *J. Mol. Struct. (THEOCHEM)* **2007**, *820*, 7–11.

[305] Sprenger, D.; Anderson, O. *Fresenius' Journal of Analytical Chemistry* **1991**, *341*, 116–120.

[306] Jr., J. D. A.; Grimm, F. A. *Chem. Phys. Lett.* **1979**, *66*, 72 – 78.

[307] Bravaya, K. B.; Kostko, O.; Dolgikh, S.; Landau, A.; Ahmed, M.; Krylov, A. I. *J. Phys. Chem. A* **2010**, *114*, 12305–12317.

[308] Stafast, H.; Bock, H. *Chem. Ber.* **1974**, *107*, 1882–1890.

[309] Eland, J. H. D. *Phil. Trans. Roy. Soc. Lond. A* **1970**, *268*, 87–96.

[310] Potts, A. W.; Price, W. C. *Proc. R. Soc. Lond. A.* **1972**, *326*, 181–197.

[311] Frost, D. C.; Lee, S. T.; McDowell, C. A.; Westwood, N. P. C. *J. Chem. Phys.* **1976**, *64*, 4719–4729.

[312] Miyata, Y.; Date, S.; Hasue, K. *Propell. Explos. Pyrot.* **2004**, *29*, 247–252.

[313] Kiselev, V. G.; Cheblakov, P. B.; Gritsan, N. P. *J. Phys. Chem. A* **2011**, *115*, 1743–1753.

[314] Butcher, V.; Cockett, M. C. R.; Dyke, J. M.; Ellis, A. M.; Feher, M.; Morris, A.; Zamanpour, H. *Phil. Trans. R. Soc. Lond. A* **1988**, *324*, 197–207.

[315] Pinto, R. M.; Dias, A. A.; Costa, M. L. *Chem. Phys.* **2011**, *381*, 49 – 58.

[316] Maksic, Z. B.; Vianello, R. *J. Phys. Chem. A* **2002**, *106*, 6515–6520.

[317] Crawford, T. D.; Stanton, J. F.; Allen, W. D.; Schaefer, H. F. *J. Chem. Phys.* **1997**, *107*, 10626–10632.

[318] Turner, D. *Phil. Trans. Roy. Soc. Lond. A.* **1970**, *268*, 7–31.

[319] Besora, M.; Harvey, J. N. *J. Chem. Phys.* **2008**, *129*, 044303.

[320] Pinto, R. M.; Dias, A. A.; Costa, M. L.; Rodrigues, P.; Barros, M. T.; Ogden, J. S.; Dyke, J. M. *J. Phys. Chem. A* **2011**, *115*, 8447–8457.

[321] Knyazev, V. D.; Korobeinichev, O. P. *J. Phys. Chem. A* **2010**, *114*, 839–846.

[322] Dunlavey, S. J.; Dyke, J. M.; Jonathan, N.; Morris, A. *Mol. Phys.* **1980**, *39*, 1121–1135.

[323] Asmus, T. W.; Houser, T. J. *J. Phys. Chem.* **1969**, *73*, 2555–2558.

[324] Metcalfe, E.; Booth, D.; McAndrew, H.; Wooley, W. D. *Fire Mater.* **1983**, *7*, 185–192.

[325] Pinto, R. M.; Dias, A. A.; Costa, M. L. *Chem. Phys.* **2011**, DOI: 10.1016/j.chemphys.2011.09.001.

[326] Giuliano, B. M.; Feyer, V.; Prince, K. C.; Coreno, M.; Evangelisti, L.; Melandri, S.; Caminati, W. *J. Phys. Chem. A* **2010**, *114*, 12725–12730.

[327] Plekan, O.; Feyer, V.; Richter, R.; Coreno, M.; de Simone, M.; Prince, K.; Trofimov, A.; Gromov, E.; Zaytseva, I.; Schirmer, J. *Chem. Phys.* **2008**, *347*, 360 – 375.

[328] Plekan, O.; Feyer, V.; Richter, R.; Coreno, M.; Vall-llosera, G.; Prince, K. C.; Trofimov, A. B.; Zaytseva, I. L.; Moskovskaya, T. E.; Gromov, E. V.; Schirmer, J. *J. Phys. Chem. A* **2009**, *113*, 9376–9385.

[329] Feyer, V.; Plekan, O.; Richter, R.; Coreno, M.; Vall-llosera, G.; Prince, K. C.; Trofimov, A. B.; Zaytseva, I. L.; Moskovskaya, T. E.; Gromov, E. V.; Schirmer, J. *J. Phys. Chem. A* **2009**, *113*, 5736–5742.

[330] Myrseth, V.; Bozek, J. D.; Kukk, E.; Sæthre, L. J.; Thomas, T. D. *J. Electron Spectrosc. Relat. Phenom.* **2002**, *122*, 57 – 63.

[331] Jolly, W. L.; Bomben, K. D.; Eyermann, C. J. *At. Data Nucl. Data Tables* **1984**, *31*, 433 – 493.

[332] Pinto, R. M.; Dias, A. A.; Coreno, M.; de Simone, M.; Giuliano, B. M.; Santos, J. P.; Costa, M. L. *Chem. Phys. Lett.* **2011**, *516*, 149–153.

[333] Feyer, V.; Plekan, O.; Kivimaki, A.; Prince, K. C.; Moskovskaya, T. E.; Zaytseva, I. L.; Soshnikov, D. Y.; Trofimov, A. B. *J. Phys. Chem. A* **2011**, *115*, 7722–7733.

[334] Ågren, H.; Jensen, H. J. A. *Chem. Phys.* **1993**, *172*, 45 – 57.

[335] Plashkevych, O.; Privalov, T.; Ågren, H.; Carravetta, V.; Ruud, K. *Chem. Phys.* **2000**, *260*, 11 – 28.